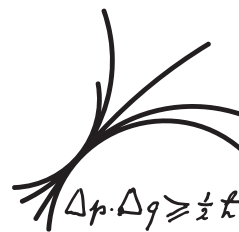# Electroweak Contributions to Squark-Pair Production Processes at the LHC

Jan Germer

Technische Universität München

Max-Planck-Institut für Physik
(Werner-Heisenberg-Institut)

Technische Universität München

Max-Planck-Institut für Physik
(Werner-Heisenberg-Institut)

Electroweak Contributions to Squark-Pair Production Processes at the LHC

Jan Germer

Vollständiger Abdruck der von der Fakultät für Physik
der Technischen Universität München
zur Erlangung des akademischen Grades eines
Doktors der Naturwissenschaften (Dr. rer. nat.)
genehmigten Dissertation.

Vorsitzender: Univ.-Prof. Dr. L. Oberauer

Prüfer der Dissertation: 1. Hon.-Prof. Dr. W. F. L. Hollik

2. Univ.-Prof. Dr. A. J. Buras

Die Dissertation wurde am 27. Januar 2011
bei der Technischen Universität München eingereicht und
durch die Fakultät für Physik am 28. April 2011 angenommen.

Zusammenfassung

Diese Arbeit beschäftigt sich mit den elektroschwachen Beiträgen zu Squark–Squark und Sbottom–Antisbottom Produktionsprozessen am LHC im Rahmen des minimalen supersymmetrischen Standardmodells. Um möglichst präzise theoretische Vorhersagen zu erhalten werden die elektroschwachen Beiträge sowohl auf Born-Niveau als auch in nächstführender Ordnung berücksichtigt. Diese Einschleifenbeiträge sind von der Ordnung $(\alpha_s^2 \alpha)$.

Die elektroschwache Wechselwirkung unterscheidet zwischen den unterschiedlichen Quark- bzw. Squark-Arten und -Chiralitäten, wodurch sich eine Vielzahl von Prozessen ergibt, welche zur Squarkproduktion beitragen. In dieser Dissertation werden alle benötigten technischen Details geliefert um die genannten Prozesse in nächstführender Ordnung zu berechnen. Dazu gehören unter anderem adäquate Regularisierungs- und Renormierungsvorschriften, als auch eine konsequente Behandlung von Massensingularitäten. Dies ist notwendig um ultraviolett-endliche sowie infrarot- und kollinear-sichere Observablen zu erhalten.

Sowohl Squark–Squark Produktion als auch deren ladungskonjugierten Prozesse setzen sich aus jeweils 36 Prozessen zusammen. Für all diese Prozesse werden die elektroschwachen Beiträge sowohl auf Born-Niveau $\mathcal{O}(\alpha_s \alpha + \alpha^2)$ als auch in nächstführender Ordnung $\mathcal{O}(\alpha_s^2 \alpha)$ berechnet. Abhängig von Art und Chiralität der produzierten Squarks müssen verschiedene Interferenzbeiträge aus elektroschwach und stark wechselwirkenden Diagrammen berücksichtigt werden. Während die $\mathcal{O}(\alpha_s \alpha + \alpha^2)$ Beiträge bis zu 20% des integrierten Born Wirkungsquerschnittes erreichen, reduzieren die $\mathcal{O}(\alpha_s^2 \alpha)$ Beiträge diesen um einige Prozent.

Die Berechnung der Wirkungsquerschnitte zu Sbottom–Antisbottom Produktion weist Besonderheiten auf, die sich grundlegend von der entsprechenden Berechnung für Squark–Antisquark und Stop–Antistop Produktion unterscheiden. Dazu gehören sowohl die Mischung der links- und rechts-chiralen schwachen Eigenzustände, die Renormierung des Sbottom Sektors, welche mit Vorsicht gewählt werden muss, als auch die für große Werte von $\tan\beta$-verstärkten Yukawakopplungen, welche resummiert werden müssen. Die elektroschwachen Beiträge zum Wirkungsquerschnitt werden bis zur Ordnung $\mathcal{O}(\alpha_s^2 \alpha)$ berechnet. Wir berücksichtigen dabei die bis dahin vernachlässigten Photon-induzierten Beiträge und liefern die erste vollständige Berechnung der elektroschwachen Beiträge in nächstführender Ordnung. Für die betrachteten Szenarien liegt der Beitrag der elektroschwachen Korrekturen zum inklusiven Wirkungsquerschnitt im Prozentbereich. In kinematischen Verteilungen kann dieser jedoch mehr als 10% des Born-Wirkungsquerschnittes ausmachen.

Abstract

We study the electroweak (EW) contributions to squark–squark and sbottom–anti-sbottom production processes at the LHC within the framework of the Minimal Supersymmetric Standard Model (MSSM). Aiming at precise theoretical predictions, the EW contributions are considered up to next-to leading order (NLO) which are of $\mathcal{O}(\alpha_s^2\alpha)$.

Since the EW interaction distinguishes flavor and chirality of the initial- and final-state quarks and squarks, respectively, the contributing processes are manifold and their interplay is non-trivial. All technical details needed in order to calculate the NLO EW contributions to the hadronic cross section for the abovementioned processes are given within this dissertation. This includes appropriate regularization and renormalization prescriptions and a proper treatment of mass singularities in order to get ultraviolet finite and infrared and collinear safe observables.

Squark–squark production consists of 36 processes and the same amount for anti-squark–anti-squark production. The tree-level EW contributions of $\mathcal{O}(\alpha_s\alpha + \alpha^2)$ and the NLO EW contributions are calculated for all processes. Depending on the flavor and chirality of the produced squarks, many interferences between EW-mediated and QCD-mediated diagrams give non-zero contributions at tree-level and NLO EW. While the tree-level EW contributions to the integrated cross section can reach the 20% level, the NLO EW corrections typically lower the LO prediction by a few percent.

Sbottom–anti-sbottom pair production exhibits specific features like left–right mixing and the renormalization of the sbottom sector which has to be chosen with care in order to get reliable predictions. In addition, Yukawa couplings get enhanced for large values of $\tan\beta$ with the related need of resummation. This renders the computation of the electroweak contributions substantially different from the corresponding computations for squark–anti-squark and stop–anti-stop production. The tree-level EW contributions to the cross section including the previously unknown photon-induced channel is calculated and we present the first complete computation of the NLO EW contributions. For the scenarios considered, the effect of the EW contributions on the inclusive cross section is at the percent region. However, in kinematical distributions they can exceed the LO contribution by 10%.

Table of Contents

1 Introduction

At the beginning of the 20th century, it was widely believed that all known physical phenomena could be described by Newton's laws of motion [1], Maxwell's equations [2], and the Lorentz force law. Together they form the foundation of classical mechanics and classical electrodynamics. However, technological improvements allowed for more and more precise measurements leading to observations that could not be explained within this framework and asked for two drastic changes in the fundamental concepts of physics. First of all, experiments like the Michelson–Morley experiment of 1887 [3] have shown that the speed of light is a constant independent of the reference frame. This was one basic ingredient for the formulation of special relativity by Einstein in 1905 [4], which dramatically changed the concept of simultaneity. Whether two events occur at the same time is no longer absolute since within this concept it depends on the inertial frame considered. Einstein extended the idea that physical laws apply equally in all inertial frames to gravity and formulated the famous theory of general relativity in 1915 [5], whose astonishing predictions such as the deflection of light were found to be correct and up to now no experiment contradicts its predictions. Sophisticated experiments examining the behavior of fundamental particles such as the Stern–Gerlach experiment on the deflection of particles in 1922 [6] asked for a second profound modification of the fundamental concepts of physics. It was discovered that electrons and atoms have intrinsic quantum properties and that measurements can affect the system being measured. In the mid-twenties, quantum mechanics was formulated. It postulates that the state of each particle can be described by a wavefunction which provides information about the particles probability to be at a specific location or state of motion. The most famous implication is given by the Heisenberg uncertainty principle which states that momentum and position of a particle cannot be measured simultaneously to arbitrary precision [7]. This is in striking contrast to classical mechanics where the trajectory of a particle can (at least in principle) be measured exactly.

After these two drastic changes in the description of modern physics, much effort was made in formulating a theory that incorporates both, the concept of special relativity and of quantum mechanics, which is nowadays successfully formulated in terms of relativistic quantum field theories. The first successful quantum field theory was quantum electrodynamics (QED) [8], which describes the interaction of electrons and positrons with the electromagnetic field, and is still among the most accurate physical theories known.

Numerous high-energy experiments were performed over the last decades in order to identify the elementary particles and forces. Quarks and leptons were found to be the fundamental constituents of matter which interact among each other via four fundamental forces: the gravitational, strong, weak, and electromagnetic force. Glashow, Salam, and Weinberg [9] managed to describe the short-ranged weak force and the long-ranged electro-

magnetic force in terms of an unified electroweak force. Together with the theory of the strong force [10] they are a basic ingredient for the formulation of the standard model of particle physics (SM). The SM is a relativistic quantum field theory which incorporates the quarks and leptons as well as the strong and electroweak force. It consists of 19 free independent parameters that have to be determined by experiments. Only one of those parameters, the one that parametrizes the mass of the Higgs boson [11], is a yet unknown quantity of the SM. Up to now, the standard model of elementary particles successfully describes all known high-energy phenomena to unexpected good accuracy.

Despite the success of the SM, there are several hints that it is only an effective theory in the sense that it correctly describes the electroweak and strong phenomena for currently available energies, but has to be extended by a more fundamental theory which manifests itself at higher energies. They arise from various theoretical as well as experimental observations such as the estimated amount of cold dark matter in the universe, the hierarchy problem related to the Higgs-boson mass, or gauge-coupling unification which is not possible with SM particle content only. Finally, an ultimate theory should also describe gravity.

Among the various possible extensions of the SM, a supersymmetric extension is of particular interest [12]. Supersymmetry (SUSY) is a space-time symmetry that relates particles that differ by spin $1/2$, i.e. bosons and fermions. In its simplest version, it postulates scalar partners to the SM fermions and spin-$1/2$ partners to the SM bosons. If the masses of the SUSY partners are at the TeV scale, one finds that the hierarchy problem is no longer present and that the particle content allows for gauge coupling unification of the strong, weak, and electromagnetic force. By introducing an additional discrete symmetry, the so-called $\mathcal{R}$ parity [13], one finds that the lightest supersymmetric particle (LSP) is stable at cosmological timescales and hence a cold dark matter candidate. Finally, supersymmetry has the potential to incorporate the gravitational interaction.

Up to now, there are only indirect hints that SUSY might be realized at the TeV scale, since no SUSY particle has ever been observed via direct production at high energy experiments. This non-observation can be translated into lower mass bounds on the SUSY particle spectrum [14]. Since an ultimate proof that SUSY is realized in the real world can only be given via direct SUSY particle production, the attention is currently turned to the Large Hadron Collider (LHC) at CERN. The LHC is a proton–proton collider which was built in order to probe TeV scale physics. If SUSY is realized at the TeV scale, colored SUSY particles, i.e. the superpartners of quarks and gluons which are commonly called squarks and gluinos, will be produced at a high rate. Unfortunately, a few weeks after the successful start-up in September 2008, the LHC was forced to shut down again due to magnetic quenching of about 100 superconducting solenoids. Since November 2009 the LHC is operating again. However, the center of mass energy is halved to 7 TeV for the first 18 month to two years, after which it will be shut down again to prepare for the 14 TeV collisions.

In this thesis we focus on colored SUSY particle production processes at the LHC within the framework of the minimal supersymmetric extension of the standard model (MSSM) [15,16] with SUSY masses realized at the TeV scale and $\mathcal{R}$-parity conservation. In order to analyze the data collected at collider experiments and to claim a discovery or to give reliable exclusion

bounds on the SUSY mass spectrum, precise theoretical predictions are needed. Due to the large interest in squark and gluino production processes at hadron colliders, much effort has been made in order to get reliable cross section predictions for squark and gluino production processes. First theoretical predictions based on leading order (LO) calculations were already made in the early '80s [17]. However, these LO QCD predictions suffer from large theoretical uncertainties and higher-order corrections have to be taken into account. The next-to leading order (NLO) QCD cross sections have been computed more than ten years ago [18, 19], considerably reducing the theoretical uncertainties. However, in order to obtain theoretical predictions that are competitive with the experimental statistical uncertainties, calculations beyond NLO QCD are necessary. These higher-order QCD contributions are investigated in [20–24] and are still subject of current research.

Besides the production of squarks and gluinos via the strong interaction, also electroweak (EW) production mechanisms are possible. For squark–(anti-)squark final states, EW contributions are already present at tree-level and one finds corrections to the LO cross section that amount to 10% to 20% [25] for specific final state configurations. In order to gain the same precision as obtained for the QCD predictions, one also has to take into account next-to leading order electroweak (NLO EW) contributions, which are formally of the same order than the beyond NLO QCD predictions. NLO EW contributions have in general a non-trivial structure, since as well the one-loop contribution as the real emission matrix elements can arise via various interference contributions. In addition one has to consider that due to QED evolution an effective photon density is generated inside the proton that can lead to photon-induced squark- and gluino-pair production. The NLO EW contributions to gluino-pair production, diagonal squark–anti-squark production, diagonal stop–anti-stop production, and squark–gluino production have been investigated in [26–29]. A wide class of the remaining processes, namely squark–squark and sbottom–anti-sbottom production are investigated within this thesis and have partly been published in [30–32].

The outline of this thesis is as follows: In Chapter 2 we introduce the building blocks and particle content of the SM and the MSSM. Some open questions of the SM are addressed and we argue that several of these weaknesses can be overcome by considering the minimal supersymmetric extension of the SM. Since the construction of supersymmetric field theories is quite involved we collect the fundamental concepts needed for the derivation of supersymmetric theories in Appendix D.

The aim of this thesis is to investigate the electroweak contributions to squark–squark and sbottom–anti-sbottom production processes. In Chapter 3 we give an overview over the current experimental and theoretical status to colored particle production. The lower mass bounds resulting from the non-observation of squarks and gluinos in collider experiments are given and we show the prospects for early SUSY discovery at the LHC. We compare the theoretical predictions to the production cross sections at the LHC for the various squark and gluino production processes and illustrate the impact of higher-order corrections. At the end of this chapter we summarize the status of higher-order corrections which demonstrates the importance of the NLO EW contributions to squark–squark and sbottom–anti-sbottom

production in order to have a complete knowledge of all relevant higher-order contributions.

In Chapter 4 we collect all technical issues needed in order to perform the NLO EW calculation to colored SUSY particle production processes at hadron colliders. Various QCD–EW interference contributions have to be taken into account at NLO EW. As a consequence, one has to renormalize the electroweak as well as the strong sector in order to obtain a ultraviolet (UV) finite result. In addition, one has to deal with infrared (IR) and collinear singularities arising from soft and collinear photons and gluons, respectively. In order to have a proper treatment of the UV divergences and IR and collinear singularities one has to define a regularization procedure. In this chapter, we give the regularization procedure used throughout this work and list the relevant renormalization constants needed in order to obtain a UV finite result. Afterwards, we show how IR and collinear singularities cancel for sufficient inclusive observables. Cross sections are finally derived via numerical integration of the squared matrix elements, which will be done using Monte Carlo methods. In order to allow for a stable integration, adequate phase-space parametrizations are needed, depending on the singular structure of the amplitude.

In Chapter 5 we consider the electroweak contributions to first and second generation squark–squark and anti-squark–anti-squark production processes up to order $(\alpha_s^2\alpha)$. Due to the large amount of possible final states that differ in flavor and chirality, respectively, squark–squark production consists of 36 processes and the same amount for anti-squark–anti-squark production. After classifying the various partonic production processes, we give the tree-level QCD and tree-level EW hadronic cross section including the analytic formulae. The NLO EW corrections are obtained by using the techniques presented in Chapter 4. We show the strategy and details of the calculation. In the following section we list the input parameters used in our numerical analysis and present hadronic cross sections and distributions for squark–squark production at the LHC with $\sqrt{S} = 14$ TeV and $\sqrt{S} = 7$ TeV. Different SUSY scenarios are considered and a scan over the squark and gluino masses is performed. We investigate the impact of reasonable phase-space cuts on the EW contributions.

The electroweak contributions to sbottom–anti-sbottom production processes up to order $(\alpha_s^2\alpha)$ are considered in Chapter 6. The production of third generation squark pairs is substantially different to squark–pair production of the first two generations due to the non-negligible mixing in the stop and sbottom sector. Moreover, b-tagging makes bottom- and top-squark production experimentally distinguishable from the production of squarks of the first two generations. In addition, the non-negligible Higgs-boson contributions and the enhanced Yukawa couplings for large values of $\tan\beta$ with the related need of resummation, render the computation of sbottom–anti-sbottom production substantially different from the corresponding computations for squark–anti-squark and stop–anti-stop production. The structure of this chapter is in close analogy to squark–squark production. However, it contains an additional section related to the enhanced bottom-quark Yukawa coupling for large values of $\tan\beta$.

We summarize and conclude in Chapter 7.

The conventions used throughout this work are collected in Appendix A. Explicit expressions for the counterterms needed in this work are listed in Appendix B. In Appendix C the $\tan\beta$ enhanced effects that alter the relation between the bottom-quark mass and its Yukawa coupling are explicitly resummed in SQCD. In addition the effective Higgs–bottom vertices are derived. The fundamental concepts for deriving supersymmetric theories are collected in Appendix D. After deriving the irreducible representations of the homogeneous Lorentz group, the supersymmetry algebra is written down. Afterwards the concept of superfields is introduced, in order to construct supersymmetric Lagrange densities.

2 From the Standard Model to the MSSM

2.1 The Standard Model of Particle Physics

The Standard Model of particle physics (SM) successfully describes all known elementary particles and their strong, weak, and electromagnetic interactions [9, 10, 33, 34]. It belongs to one of the best tested theories in physics [14].

The SM is given in terms of a renormalizable quantum field theory which is locally invariant under an internal $SU(3)_C \times SU(2)_L \times U(1)_Y$ symmetry group and globally invariant under the group of Poincaré space-time transformations. All known matter fields — the quarks and leptons — are described by spin-$1/2$ fermion fields. Forces are introduced within the concept of local gauge invariance under the internal symmetry group and give rise to gauge fields. The strong force is described by the $SU(3)_C$ gauge theory, called quantum chromodynamics (QCD), while the weak and electromagnetic force are unified into the electroweak force which is given in terms of the spontaneously broken $SU(2)_L \times U(1)_Y$ gauge theory. The symmetry is broken in such a way that the exact $U(1)_{\text{em}}$ symmetry remains which describes the electromagnetic phenomena via quantum electrodynamics (QED). In the SM the spontaneous symmetry breaking is achieved by a scalar field which develops a non-vanishing vacuum expectation value (vev), the so called Higgs field [11].

The internal symmetries of the SM can be described by the Lie algebra of the corresponding Lie group. Labeling the generators of $SU(3)_C$, $SU(2)_L$, and $U(1)_Y$ by T^a, I^a, and Y, respectively, their commutation relations are given by

$$[T^a, T^b] = \mathrm{i}f_{abc}T^c, \qquad [I^a, I^b] = \mathrm{i}\epsilon_{abc}I^c, \qquad [Y, Y] = 0, \tag{2.1}$$

with the totally antisymmetric structure constants f_{abc} and ϵ_{abc} of $SU(3)_C$ and $SU(2)_L$, respectively. Elements of the Lie group $S(x)$ are given by exponentiation of the generators,

$$S(x) = e^{-\mathrm{i}(\theta^a(x)T^a + \theta'^a(x)I^a + \theta''(x)Y)}, \tag{2.2}$$

with real spacetime dependent parameters $\theta^a(x)$, $\theta'^a(x)$, and $\theta''(x)$. Gauge transformations for fundamental fields Ψ and gauge fields $A_\mu = T^a A_\mu^a$ are defined by

$$\Psi \to \Psi' = S(x)\Psi, \tag{2.3}$$

$$A_\mu \to A'_\mu = S(x)\left(A_\mu + \mathrm{i}\partial_\mu\right)S^{-1}(x). \tag{2.4}$$

The gauge fields transform inhomogeneously under local gauge transformations.

Each SM field can be classified by its spin and its internal quantum numbers, corresponding to the representation of $SU(3)_C$, $SU(2)_L$, and $U(1)_Y$. The complete field content of the SM is summarized in Table 2.1. In the following we will further specify these fields.

Name	Fields	$SU(3)_C, SU(2)_L, U(1)_Y$
Quarks	$\binom{u}{d}_L, \binom{c}{s}_L, \binom{t}{b}_L$	$(\mathbf{3}, \mathbf{2}, \frac{1}{3})$
	u_R^c, c_R^c, t_R^c	$(\bar{\mathbf{3}}, \mathbf{1}, -\frac{4}{3})$
	d_R^c, s_R^c, b_R^c	$(\bar{\mathbf{3}}, \mathbf{1}, \frac{2}{3})$
Leptons	$\binom{\nu_e}{e}_L, \binom{\nu_\mu}{\mu}_L, \binom{\nu_\tau}{\tau}_L$	$(\mathbf{1}, \mathbf{2}, -1)$
	e_R^c, μ_R^c, τ_R^c	$(\mathbf{1}, \mathbf{1}, 2)$
Higgs-doublet	H	$(\mathbf{1}, \mathbf{2}, 1)$
Gauge bosons	G	$(\mathbf{8}, \mathbf{1}, 0)$
	W	$(\mathbf{1}, \mathbf{2}, 0)$
	B	$(\mathbf{1}, \mathbf{1}, 0)$

Table 2.1: Field content of the Standard model. The gauge group representation and charge of the SM fields are arranged as $(SU(3)_C, SU(2)_L, U(1)_Y)$. Quarks and leptons are fermions of spin-1/2 while the Higgs and gauge fields are bosons of spin-0 and spin-1, respectively. The label c on the right-handed particles denotes charge-conjugation, see also (D.79).

The fermion fields of the SM are constituted by quarks and leptons which are best described in terms of left- and right-handed Weyl spinors, cf. Appendix D.3.1. They can be grouped corresponding to their symmetry group representation:

- Quarks (up, down, charm, strange, top, and bottom):

$$Q^L = \left\{ \binom{u}{d}_L, \binom{c}{s}_L, \binom{t}{b}_L \right\}, \quad u_i^R = \{u_R, c_R, t_R, \}, \quad d_i^R = \{d_R, s_R, b_R\}. \quad (2.5)$$

- Leptons (electron, muon, tau, and the corresponding neutrinos):

$$L^L = \left\{ \binom{\nu_e}{e}_L, \binom{\nu_\mu}{\mu}_L, \binom{\nu_\tau}{\tau}_L \right\}, \quad l_i^R = \{e_R, \mu_R, \tau_R\}. \quad (2.6)$$

The subscripts L and R denote left- and right-handed spinors. All quarks are triplets of $SU(3)_C$ and therefore strongly interacting particles, while the leptons are singlets under $SU(3)_C$. Further, all left-handed fermions are doublets under $SU(2)_L$ while the right-handed fermions are singlets. As one can see from (2.6), right-handed neutrinos are not present in the SM. All fermions are charged under the $U(1)_Y$ hypercharge in such a way that the Gell–Mann–Nishijima relation for the generator of the electric charge holds,

$$Q = I^3 + \frac{Y}{2}. \quad (2.7)$$

The gauge fields of the SM are spin-1 fields and hence bosons, transforming under the adjoint representation of the respective gauge group. Therefore there are eight gauge fields G_μ^a corresponding to the strong interaction, three fields W_μ^i belonging to the weak-isospin, and the one belonging to the weak-hypercharge, called B_μ. With help of the gauge-covariant derivative, defined as

$$D_\mu = \partial_\mu + \mathrm{i}g_s T^a G_\mu^a + \mathrm{i}g_2 I^i W_\mu^i + \mathrm{i}g_1 \frac{Y}{2} B_\mu \,, \tag{2.8}$$

one can construct gauge and Lorentz invariant Lagrange densities (see also (D.72)),

$$\mathcal{L}_{\text{fermion}} = \sum_{\psi_L = Q^L, L^L} \psi_L^\dagger \bar{\sigma}^\mu D_\mu \psi_L + \sum_{\phi_R = u_i^R, d_i^R, l_i^R} \phi_R^\dagger \sigma^\mu D_\mu \phi_R. \tag{2.9a}$$

$$\mathcal{L}_{\text{gauge}} = -\frac{1}{4} G^{a\,\mu\nu} G_{\mu\nu}^a - \frac{1}{4} W^{a\,\mu\nu} W_{\mu\nu}^a - \frac{1}{4} B^{\mu\nu} B_{\mu\nu}, \tag{2.9b}$$

with the field-strength tensors $G_{\mu\nu}^a$, $W_{\mu\nu}^a$ and $B_{\mu\nu}$ defined as

$$G_{\mu\nu}^a = \partial_\mu G_\nu^a - \partial_\nu G_\mu^a - g_s f_{abc} G_\mu^b G_\nu^c \,, \tag{2.10a}$$

$$W_{\mu\nu}^a = \partial_\mu W_\nu^a - \partial_\nu W_\mu^a - g_2 \epsilon_{abc} W_\mu^b W_\nu^c \,, \tag{2.10b}$$

$$B_{\mu\nu} = \partial_\mu B_\nu - \partial_\nu B_\mu \,. \tag{2.10c}$$

The coupling between gauge fields and fermion fields is minimal in the sense that it is only mediated via the gauge-covariant derivative.

Explicit mass terms for gauge fields are forbidden by gauge invariance. Mass terms for fermion fields would also spoil either gauge or Lorentz invariance.[1] However, gauge invariance is crucial to guarantee the renormalizability of the theory [35]. Hence, mass terms for SM particles have to be generated dynamically in a gauge-invariant way. It is realized by the Higgs–Kibble mechanism [11], where a complex two-component scalar field $H^{\mathrm{T}} = (\phi^+, \phi^0)$ is postulated.[2] This field has a specific potential that allows for spontaneous symmetry breaking, and hence the realization of effective mass terms for gauge bosons and fermions. The introduced Higgs-doublet field H is a doublet under $SU(2)_L$ with hypercharge $Y = +1$. It has the following potential,

$$V(H) = -\mu^2 H^\dagger H + \frac{\lambda}{4} \left(H^\dagger H \right)^2 \,, \tag{2.11}$$

where $\mu^2, \lambda > 0$, i.e. it has a tachyonic mass term. The choice of the hypercharge $Y = +1$ further allows for Yukawa couplings, i.e. couplings between scalar and fermion fields in a gauge- and Lorentz-invariant way. The most general renormalizable Lagrangian, involving

---

[1]Dirac mass terms of two SM spinor fields ψ_L and ϕ_R are given by the Lorentz invariant contraction $\phi_R^\dagger \psi_L$ or its adjoint, which spoils $SU(2)$ invariance. The combination $\psi_L^\dagger \psi_L$ or $\phi_R^\dagger \phi_R$ would be conform with gauge invariance but is not Lorentz invariant. A gauge invariant Majorana mass term $\propto \psi_R^{\mathrm{T}} \sigma^2 \psi_R$ would only be possible for right-handed neutrinos, which are absent in the SM (see also Appendix D.3.1 f.).

[2]The labels + and 0 of the component fields ϕ denote the charge Q, eq. (2.7), of these components.

the scalar field H and further SM fields is given by

$$
\begin{aligned}
\mathcal{L}_{\text{Higgs}} = {} & (D^\mu H)^\dagger (D_\mu H) - V(H) \\
& - \sum_{i,j=1}^{3} \left[y_{ij}^d (Q_i^L)^\dagger H d_j^R + y_{ij}^u (Q_i^L)^\dagger H^c u_j^R + y_{ij}^e (L_i^L)^\dagger H l_j^R + \text{h.c.} \right],
\end{aligned}
\tag{2.12}
$$

with the charge-conjugated scalar field defined as $H^c = \mathrm{i}\sigma^2 H^*$. As mentioned above, the scalar-field self-interaction is chosen in such a way that spontaneous symmetry breaking can take place. The scalar potential (2.11) has a minimum for

$$
|\langle H \rangle|^2 = |H_0|^2 = \frac{2\mu^2}{\lambda} \equiv \frac{v^2}{2} \neq 0,
\tag{2.13}
$$

with the vacuum expectation value v. Since $U(1)_{\text{em}}$, whose generator is given by the electric charge operator (2.7), should remain an exact symmetry, H_0 is given up to a phase by $H_0^{\mathrm{T}} = (0, v/\sqrt{2})$. The Higgs doublet field can now be expanded about the classical ground state as

$$
H(x) = \begin{pmatrix} \phi^+(x) \\ \frac{1}{\sqrt{2}}[v + h(x) + \mathrm{i}\chi(x)] \end{pmatrix}, \qquad \phi^- = (\phi^+)^\dagger,
\tag{2.14}
$$

where $h(x)$, $\phi^\pm(x)$, and $\chi(x)$ have vanishing vacuum expectation values. The fields $\phi^\pm$ and χ, the would-be Goldstone fields of a broken global symmetry [36], are unphysical degrees of freedom in broken gauge symmetries. They disappear from the physical spectrum and some of the gauge bosons become massive. This can be seen by considering the so-called unitary gauge, where the unphysical fields are eliminated and only one physical field remains, the Higgs field $h(x)$.

Inserting the expanded Higgs-doublet field into the Higgs Lagrangian (2.12), one finds that the ground state is not $SU(2)_L \times U(1)_Y$ invariant anymore. Instead it is invariant under the (smaller) group $U(1)_{\text{em}}$ which is generated by the electric charge (2.7). The fields of the unbroken electroweak theory, W_μ^1, W_μ^2, W_μ^3 and B_μ, are no mass and charge eigenstates of $U(1)_{\text{em}}$. These eigenstates are simplest obtained in the unitary gauge, i.e. (2.14) for $\phi^+ = \chi = 0$, and are given by

$$
W^\pm = \frac{1}{\sqrt{2}} [W_\mu^1 \mp \mathrm{i} W_\mu^2],
\tag{2.15}
$$

$$
\begin{pmatrix} Z_\mu \\ \gamma_\mu \end{pmatrix} = \begin{pmatrix} \cos\theta_{\text{w}} & -\sin\theta_{\text{w}} \\ \sin\theta_{\text{w}} & \cos\theta_{\text{w}} \end{pmatrix} \begin{pmatrix} W_\mu^3 \\ B_\mu \end{pmatrix}.
\tag{2.16}
$$

with the weak mixing angle θ_{w} given by (2.18). Under $U(1)_{\text{em}}$ the eigenstates $W^\pm$ have charge ± 1 while Z and γ are uncharged. Three of the four eigenstates are massive. Their masses are given by

$$
M_W = g_2 \frac{v}{2}, \qquad\qquad\qquad M_Z = \frac{v}{2}\sqrt{g_1^2 + g_2^2}.
\tag{2.17}
$$

The weak mixing angle can also be expressed via the ratio of the heavy gauge boson masses

$$c_{\mathrm{w}} \equiv \cos \theta_{\mathrm{w}} = \frac{g_2}{\sqrt{g_1^2 + g_2^2}} = \frac{M_W}{M_Z} \,, \tag{2.18a}$$

$$s_{\mathrm{w}} \equiv \sin \theta_{\mathrm{w}} = \frac{g_1}{\sqrt{g_1^2 + g_2^2}} = \sqrt{1 - \left(\frac{M_W}{M_Z}\right)^2} \,. \tag{2.18b}$$

The remaining massless particle is identified as the photon γ, since it is the gauge boson of the unbroken $U(1)_{\mathrm{em}}$ which has to reproduce the observed low energy QED. Hence, the couplings g_1 and g_2 are related to the electric charge via $e = g_1 g_2 / \sqrt{g_1^2 + g_2^2}$.

The effective fermion masses are obtained by inserting (2.14) into the Yukawa part of the Higgs Lagrangian (2.12). The resulting mass matrix $M_{ij}^f = 1/\sqrt{2} y_{ij}^f v$ can be diagonalized by a bi-unitary transformation. The fermion mass eigenstates and corresponding eigenvalues are given by

$$f_i^{\prime L} = \sum_k U_{ik}^{f,L} f_k^L \,, \qquad\qquad f_i^{\prime R} = \sum_k U_{ik}^{f,R} f_k^R \,, \tag{2.19}$$

$$m_{f,i} = \frac{v}{\sqrt{2}} \sum_{k,m} U_{ik}^{f,L} y_{km}^f \left(U_{mi}^{f,R}\right)^\dagger = \frac{v}{\sqrt{2}} \lambda_i^f \,, \tag{2.20}$$

with the unitary matrices $U_{ik}^{f,L}$ and $U_{ik}^{f,R}$ for left- and right-handed fields $f = u_i, d_i, e_i$, respectively. Owing to their unitarity, the matrices $U_{ik}^{f,L}$ and $U_{ik}^{f,R}$ drop out of the interaction terms between fermions and neutral gauge bosons, when expressing the weak eigenstates in (2.9a) by the mass eigenstates (2.19). Therefore there are no flavor-changing neutral currents at tree-level [34]. However, since the quark–$W^\pm$-boson interaction connects up-type fermions with down-type fermions, a non-trivial matrix remains, the Cabbibo–Kobayashi–Maskawa (CKM) quark mixing matrix [37, 38]:

$$V_{\mathrm{CKM}} = U^{u,L} \left(U^{d,L}\right)^\dagger \,. \tag{2.21}$$

This matrix can be parametrized by four physical parameters, usually denoted by three mixing angles and a complex phase. The complex phase of the CKM matrix is the only source of CP-violation in the SM.

The potential $V(H)$ in (2.12) gives rise to the mass of the physical Higgs field $h(x)$:

$$M_h = \sqrt{2}\mu = \frac{v}{2}\sqrt{\lambda} \,, \tag{2.22}$$

i.e. the mass is a free parameter of the SM determined via the quartic coupling of the Higgs-doublet field. The Higgs-boson mass is a yet unknown quantity of the SM.

2.1.1 Open Questions of the Standard Model

Even though the SM is extremely successful in describing the electroweak and strong phenomena observed in nature, there are theoretical considerations as well as experimental observations that render the SM as a low energy effective field theory that gets modified when going to higher energies.

Theoretical Considerations

- The SM does not describe gravitational interactions. Macroscopically, gravitation is described by general relativity [5]. Since the gravitational coupling constant is many orders of magnitude weaker than the other known forces, it can be safely neglected for center-of-mass energies produced at high-energy colliders. However, at energies around the Planck scale, $\Lambda_{\text{Planck}} \sim 10^{19}$ GeV, gravity has to enter at the quantum level. A consistent quantum mechanical description of gravity is not known yet.

- In the SM, all fermions and gauge bosons are in principle massless due to gauge invariance. Since they obtain their masses via the Higgs mechanism, their masses have to be proportional to the electroweak breaking scale v. However, the SM Higgs-boson mass gets radiative corrections due to quartic Higgs–self-couplings and Higgs-couplings to massive gauge bosons and fermions. Cutting off the loop-momenta integral at the scale Λ_{cut} where new physics enters, one finds that the dominant corrections to the Higgs mass are given via

$$M_H^2 = (M_H^0)^2 + \frac{3\Lambda_{\text{cut}}^2}{8\pi v^2} \left(M_H^2 + 2M_W^2 + M_Z^2 - 4m_t^2 \right) , \qquad (2.23)$$

where M_H^0 is the bare mass of the unrenormalized Lagrangian, i.e. the bare Higgs mass squared is proportional to the cuttoff Λ_{cut}^2. If the SM is valid up to the GUT scale $\Lambda_{\text{GUT}} \sim 10^{15}$ GeV or the Planck scale, one would suppose that the electroweak scale is of the order of the cutoff scale. This problem is also known as the *naturalness* or *fine-tuning* problem.

- The electric charge of the quarks and leptons are related ($Q_e = 3Q_d = -3Q_u/2$) even though the charge is arbitrary in the SM. The quantization of the electric charge can be explained by the assumption that all three gauge groups of the SM are described by a *grand unified theory* (GUT). However, with the SM particle content only, one gets a wrong prediction of the weak mixing angle θ_{w} [39].

Experimental Observations

- From cosmological side one observes a large amount of weakly interacting cold dark matter (DM) in the universe. The most prominent hint for cold dark matter comes from the rotation curve of galaxies: instead of the expected behavior of the velocity of the stars $v^2 \propto 1/R$ at large distances, where R is the distance of the star to the center of the galaxy, one finds that the velocity is almost constant with respect to R. However, postulating dark matter that clumps inside the galaxies — and hence has to be cold, would explain this phenomenon. The only DM candidates in the SM is the neutrino since it is the only electrically neutral particle. However, neutrinos are hot DM and hence not a candidate for the cold DM in the universe. In addition, with the current upper bound for the neutrino mass $M_\nu < 2$ eV, the number of relict neutrinos is not sufficient to provide the observed amount of DM.

- To get the observed matter–anti-matter asymmetry the three Sakharov conditions have to be fulfilled [40]. These are a set of necessary conditions a baryon-generating interaction must satisfy:

  – Baryon number violation.

  – C-symmetry and CP-symmetry violation.

  – Interactions out of thermal equilibrium.

  At first glance, the SM seems to fulfill these conditions: Baryon number is violated via non-perturbative effects, the so called sphaleron processes [41]. C-symmetry is violated via the weak interaction, and CP-symmetry via the complex entry of the CKM matrix. The required interaction out of equilibrium is given by the time of electroweak symmetry breaking in the early universe. However, the amount of CP violation provided by the complex phase of the CKM matrix is far too small in order to obtain today's matter–anti-matter asymmetry.

- The SM neutrinos are massless. This contradicts the observed neutrino oscillation from solar, atmospheric and reactor neutrinos. The exact mass is not known, only an upper bound is given by direct measurement, $0 < M_\nu < 2$ eV. While it is possible to introduce a sterile right-handed neutrino and hence generate masses via the Higgs mechanism, it seems quite unnatural that the neutrino mass is so much smaller than all other fermion masses.

- The Higgs particle of the SM remains to be found. It is bounded from below by experimental searches, with the current limit $m_H > 114.4$ GeV/c^2 given by the LEP collaboration [42]. Theoretical considerations set additional bounds by requiring that the Higgs potential is bounded from below [43]. Even though the SM Higgs mechanism is not ruled out, the question arises whether it is the right description of the electroweak symmetry breaking.

- The anomalous magnetic moment of the muon, $(g-2)_\mu$, appears to differ by over three standard deviations from the best SM calculation based on low-energy e^+e^- data [44–50].

2.2 The Minimal Supersymmetric Standard Model

As shown at the end of last section, there are phenomena that cannot be explained within the SM. Therefore, one assumes that the SM is only a low-energy effective theory resulting from a yet unknown underlying theory. However, possible extensions of the SM have to fulfill the following restrictions:

1. The particle content and gauge group of the SM have to be incorporated in the new model.

2. The phenomenological observations, e.g. electroweak precision data and the proton lifetime have to be in accordance with the new model.

A possible extension of the SM which fulfills this criteria is provided by supersymmetry (SUSY) [12], especially by the Minimal Supersymmetric Standard Model (MSSM) [15,16]. In particle physics, supersymmetry is an extension of the Poincaré symmetry, whose symmetry generator Q when acting on particles changes its spin by a factor $1/2$ and hence relates bosons to fermions and vice versa. In the MSSM, each SM particle has a superpartner that differs by half-integer spin: The superpartners of the SM fermions are scalar bosons and the superpartners of the bosonic fields in the SM are given by spin-$1/2$ fermions.

2.2.1 Motivation

Coleman and Mandula showed in [51] that the most general Lie Algebra of symmetry operators that leave the S matrix invariant, are given by the direct product of an internal symmetry and the Poincaré symmetry, cf. Appendix D.2. The initial motivation for introducing supersymmetry into particle physics came from the observation that there are further symmetry generators that overcome this *no-go theorem* by requiring the algebra to be a graded Lie Algebra and hence being constituted by symmetry generators that fulfill commutations as well as anti-commutation relations. Such symmetries are called supersymmetries (see also Appendix D.5). From theoretical side, supersymmetries are appealing, since it is the only possible extension of the Poincaré spacetime-symmetry of the S matrix that allows for non-trivial scattering processes [52].

Apart from this this original motivation, supersymmetric field theories, especially the MSSM, were found to have many interesting phenomenological properties that may solve some of the beforehand mentioned weaknesses of the SM.

- An astonishing fact of supersymmetry is that the fine-tuning problem is not present in an exact supersymmetric version of the SM. The quadratically divergent radiative contributions to the Higgs mass are exactly canceled by the contributions arising from the supersymmetric partners.[3] In softly broken SUSY, radiative corrections are proportional to the squared-mass difference between the SUSY partners and only grow logarithmically with the cutoff scale,

$$M_H^2 = (M_H^0)^2 + \frac{m_{\text{f}}^2}{4\pi^2 v^2}\left(m_{\text{f}}^2 - m_{\text{s}}^2\right)\log\left(\frac{\Lambda_{\text{cut}}}{m_{\text{s}}}\right),\qquad(2.24)$$

with m_{f} being the fermion mass and m_{s} the mass of the corresponding supersymmetric partner. Therefore, in softly broken SUSY, the mass difference between the superpartners has to be of the order of the electroweak scale for not reintroducing the fine-tuning problem.

---

[3]This follows also from a more general statement of unbroken SUSY, the *non-renormalization theorem*. It states that all vacuum supergraphs vanish. [12, 53–56]

- Under the assumption of a GUT at high energies, the MSSM correctly predicts the weak mixing angle θ_w, provided the superpartner masses are not heavier than $\mathcal{O}(10 \text{ TeV})$ [39]. Turning the argument around, one finds that in the MSSM the three gauge couplings meet at one point, the GUT scale, which is found to be at roughly 10^{16} TeV.

- SUSY models can provide a massive, weakly interacting particle that is stable at cosmological timescales and therefore provides a candidate for cold DM. In the MSSM this is realized by the assumption that $\mathcal{R}$-parity is realized as a discrete symmetry, rendering the lightest SUSY particle stable.

- The MSSM is slightly preferred to the SM by electroweak precision data related to the weak mixing angle, the W-boson mass, and the top-quark mass [57]. Also the three-sigma standard deviation of the anomalous magnetic moment of the muon, $(g-2)_\mu$, can be explained within the MSSM [58]. Further, precision tests of the SM predict that the Higgs mass is smaller than ~ 200 GeV at the 99% confidence level (c.l.). The MSSM, which is a type-II two Higgs-doublet model, naturally predicts a light Higgs boson that cannot be heavier than ~ 140 GeV provided that the SUSY particles are not too heavy (i.e. at the TeV scale). A global fit to EW precision data slightly favors a Higgs boson within the MSSM [59].

2.2.2 The MSSM: Principles and Building Blocks

The MSSM is a $N = 1$ supersymmetric extension of the SM. The theoretical framework for describing supersymmetry and especially supersymmetric field theories is collected in Appendix D. The MSSM is based on the following principles:

- The field content of the MSSM is minimal in the sense that the least possible amount of new fields is introduced.

- The MSSM is invariant under the SM gauge groups.

- SUSY is softly broken, i.e. no new quadratic divergences arise from the breaking sector.

- $\mathcal{R}$-parity is conserved and defined in such a way, that all SM particles have $\mathcal{R}$-parity $+1$, while the SUSY partners have $\mathcal{R}$-parity -1.

- SUSY masses are close to the EW scale.

$N = 1$ SUSY has only one SUSY generator Q_A, which is a spinor doublet, cf. Appendix D.5. Different fields belonging to a supermultiplet, i.e. the irreducible representations of the SUSY algebra, hence differ by spin-$1/2$. With exact SUSY the masses of superpartners have to be the same. Hence, in any realistic supersymmetric extension of the SM as the MSSM, SUSY has to be broken. The SUSY breaking occurs in an a priori unknown sector and our ignorance of the breaking mechanism is parametrized by the so-called soft-breaking parameters. In order to construct the MSSM we make use of the concept of superfields, cf. Appendix D.6. The irreducible representations of $N = 1$ superfields can be used to

construct supersymmetric Lagrange densities. While chiral superfields describe fields of spin-0 and spin-1/2, vector superfields relate fields of spin-1/2 and spin-1. Hence all SM fermions and the scalar Higgs bosons have to be assigned to chiral superfields, while the gauge bosons are related to vector superfields. In order to obtain a supersymmetric version of the Higgs mechanism, two Higgs doublets are required, one with $U(1)_Y$ hypercharge $Y = +1$ generating masses for the up-type quarks, and one with hypercharge $Y = -1$ generating masses for the down-type quarks. The reason is twofold: Since the Higgs fields are in the $SU(2)_L$ doublet representation, their supersymmetric partners are chiral fermions. In order to cancel gauge anomalies, the hypercharge has to vanish when summing over all fermions [60–62]. Since the SM is anomaly-free, the contributions coming from the fermionic part of the Higgs sector have to cancel, i.e. the sum of their hypercharges has to vanish. The second reason is that in order to construct a supersymmetric version of the Higgs-fermion couplings, only analytic functions of combinations of chiral fields are allowed. A term like the one in (2.12) containing H and H^c in order to give masses to the up- and down-type fermions would spoil supersymmetry. Therefore two Higgs-doublet fields are needed, one developing its vev in the upper and one in the lower component. The field content of the MSSM is collected in Table 2.2. The names of superpartners of SM model particles are chosen such that spin-0 superpartner names correspond to the SM names with a prepended *s*, while spin-1/2 superpartners have an appended *ino*.

The supersymmetric Lagrange density of the MSSM can be written as

$$\mathcal{L}_{\text{MSSM}} = \mathcal{L}_{\text{SUSY}} + \mathcal{L}_{\text{soft}}, \tag{2.25}$$

where the first term is invariant under SUSY transformations while the latter contains the soft-breaking terms. The SUSY Lagrangian can be split into a kinetic term, a gauge term, and an interaction term, which are SUSY and gauge invariant by themselves. In accordance with Appendix D.7.1 these parts are given by

$$\mathcal{L}_{\text{kin}} = \int \mathrm{d}\theta^4 \Big\{ Q^\dagger e^{2(g_1 B + g_2 W + g_s G)} Q + \overline{U}^\dagger e^{2(g_1 B + g_s G)} \overline{U} + \overline{D}^\dagger e^{2(g_1 B + g_s G)} \overline{D}$$
$$+ L^\dagger e^{2(g_1 B + g_2 W)} L + \overline{E}^\dagger e^{2 g_1 B} \overline{E}$$
$$+ H_u e^{2(g_1 B + g_2 W)} H_u + H_d e^{2(g_1 B + g_2 W)} H_d \Big\}, \tag{2.26a}$$

$$\mathcal{L}_{\text{gauge}} = \frac{1}{16} \int \mathrm{d}\theta^2 \Big\{ \frac{1}{g_s^2} \text{Tr}\left[(W_G)^A (W_G)_A\right] + \frac{1}{g_2^2} \text{Tr}\left[(W_W)^A (W_W)_A\right]$$
$$+ \frac{1}{g_1^2} \text{Tr}\left[(W_B)^A (W_B)_A\right] + \text{h.c.} \Big\}, \tag{2.26b}$$

$$\mathcal{L}_{\text{int}} = \int \mathrm{d}\theta^2 \Big\{ \underbrace{\mu H_u \cdot H_d - y_{ij}^u \overline{U}_i Q_j \cdot H_u - y_{ij}^d \overline{D}_i Q_j \cdot H_d - y_{ij}^e \overline{E}_i L_j \cdot H_d}_{\mathcal{W}} + \text{h.c.} \Big\}. \tag{2.26c}$$

W_G, W_W, and W_B are the respective supersymmetric field strengths belonging to the vector superfields G, W, and B,

$$(W_G)_A = -\frac{1}{4} \bar{D}\bar{D} e^{-G} D_A e^G, \tag{2.27a}$$

	Name	Label	Bosonic Field	Fermionic Field	$SU(3)_C, SU(2)_L, U(1)_Y$
chiral superfields	(s)quarks	Q	$\tilde{q}_L = (\tilde{u}_L, \tilde{d}_L)$	$q_L = (u_L, d_L)$	$(\mathbf{3}, \mathbf{2}, +\frac{1}{3})$
		$\overline{U}$	$\tilde{u}_R^*$	$\bar{u}_L = u_R^c$	$(\bar{\mathbf{3}}, \mathbf{1}, -\frac{4}{3})$
		$\overline{D}$	$\tilde{d}_R^*$	$\bar{d}_L = d_R^c$	$(\bar{\mathbf{3}}, \mathbf{1}, +\frac{2}{3})$
	(s)leptons	L	$\tilde{l}_L = (\tilde{\nu}_L, \tilde{e}_L)$	$l_L = (\nu_L, e_L)$	$(\mathbf{1}, \mathbf{2}, -1)$
		$\overline{E}$	$\tilde{e}_R^*$	$\bar{e} = e_R^c$	$(\mathbf{1}, \mathbf{1}, +2)$
	Higgs(ino)	H_u	$h_u = (h_u^+, h_u^0)$	$\tilde{h}_u = (\tilde{h}_u^+, \tilde{h}_u^0)$	$(\mathbf{1}, \mathbf{2}, +1)$
		H_d	$h_d = (h_d^0, h_d^-)$	$\tilde{h}_d = (\tilde{h}_d^0, \tilde{h}_d^-)$	$(\mathbf{1}, \mathbf{2}, -1)$
vector superfields	gluon/gluino	G	g^a	$\tilde{g}^a$	$(\mathbf{8}, \mathbf{1}, 0)$
	W(ino)	W	W^i	$\tilde{W}^i$	$(\mathbf{1}, \mathbf{3}, 0)$
	B(ino)	B	B	$\tilde{B}$	$(\mathbf{1}, \mathbf{1}, 0)$

Table 2.2: Field content of the MSSM. Superfields are labeled with capital letters. The SUSY partners of the SM fields, cf. Table 2.1, are denoted with a tilde. The gauge group representation and charge of the fields are arranged as $(SU(3)_C, SU(2)_L, U(1)_Y)$. Generation and color indices for chiral superfields are suppressed. The index a and i enumerates the vector superfields of $SU(3)_C$ and $SU(2)_L$, respectively.

$$(W_W)_A = -\frac{1}{4}\bar{D}\bar{D}e^{-W}D_A e^W, \tag{2.27b}$$

$$(W_B)_A = -\frac{1}{4}\bar{D}\bar{D}e^{-B}D_A e^B. \tag{2.27c}$$

D_A and $\bar{D}_{\dot{A}}$ are the supersymmetric covariant derivatives defined in (D.119). The Yukawa couplings $y_{ij}^{u,d}$ appearing in (2.26c) are the same as the ones in (2.12). The dot-product in (2.26c) denotes the $SU(2)_L$-invariant contraction of two doublet fields, i.e. $A \cdot B = \epsilon_{ij}A^i B^j$. The μ parameter, describing the coupling between the two Higgs doublets, and after electroweak symmetry breaking also the ratio of the two Higgs vevs, $\tan\beta$, are the only new free parameters in $\mathcal{L}_{\text{SUSY}}$.

$\mathcal{R}$-Parity

The superpotential $\mathcal{W}$ is not the most general superpotential invariant under SUSY and gauge transformations. The possible terms have been constrained by the requirement of $\mathcal{R}$-parity (R_p) conservation. As shown in Appendix D.5.2, in $N = 1$ SUSY there is one $U(1)$ symmetry left that commutes non-trivial with the SUSY generators, called $\mathcal{R}$-symmetry. Under phase rotation of the Grassmann coordinates, $\theta \to e^{i\varphi}\theta$ and $\bar{\theta} \to e^{-i\varphi}\bar{\theta}$, one has $Q_A \to e^{-i\varphi}Q_A$ and $\bar{Q}_{\dot{A}} \to e^{i\varphi}\bar{Q}_{\dot{A}}$, (cf. (D.105)). One defines an $\mathcal{R}$-transformation on a

general left chiral superfield as

$$\Phi(x, \theta, \bar{\theta}) \to \Phi'(x, e^{i\varphi}\theta, e^{-i\varphi}\bar{\theta}) = e^{i\varphi R_\Phi}\Phi(x, \theta, \bar{\theta}), \tag{2.28}$$

i.e. the $\mathcal{R}$-charge of Φ is R_Φ. Considering a vector superfield V, its reality condition implies vanishing $\mathcal{R}$-charge. Turning to the component fields of Φ and V, eqs. (D.133) and (D.142), one gets the $\mathcal{R}$-charges of the component fields:

$$R(\varphi) = R_\Psi, \qquad R(\psi) = -R(\bar{\psi}) = R_\Phi - 1, \qquad R(F) = R_\Phi - 2, \tag{2.29a}$$
$$R(A_\mu) = 0, \qquad R(\lambda) = -R(\bar{\lambda}) = 1, \qquad R(D) = 0. \tag{2.29b}$$

Since the kinetic part of the SUSY Lagrangian is invariant under an $\mathcal{R}$-transformation, as well as the gauge part which is trivially invariant, one could think of $\mathcal{R}$-invariance as a symmetry of nature. However, an exact $\mathcal{R}$-symmetry is not possible for theoretical and phenomenological reasons.[4]

Its discrete $\mathbb{Z}_2$ subgroup for $\varphi = \pi$, called $\mathcal{R}$-parity, however, has been conjectured by [13] to be an exact symmetry in the multiplicative sense of the MSSM. It can be seen as the invariant remnant of a $U(1)_R$ gauge symmetry destroyed by anomalies, also called *discrete gauge symmetry* [64]. The value of $e^{i\pi R} = (-1)^R$ for a superfield is called matter parity (M_P), while the value of the component fields are called the $\mathcal{R}$-parity (R_P) of that field. Since R_P is always positive for a vector field whereas its fermionic partner is necessarily negative, the matter parity of the chiral fields of the MSSM are assigned such that all SM particles have positive $\mathcal{R}$-parity while their SUSY partners have negative $\mathcal{R}$-parity. This can be achieved by assigning $R_\Phi = 3(B - L)$, where B is the baryon number and L is the lepton number of the superfield Φ. With s being the spin of each particle, one can write the MSSM matter parity and $\mathcal{R}$-parity as

$$M_P = (-1)^{3(B-L)}, \tag{2.30a}$$
$$R_P = (-1)^{3(B-L)+2s}. \tag{2.30b}$$

In exact $\mathcal{R}$-parity conserving models as the MSSM the lightest R-odd state has to be stable. It is called lightest supersymmetric particle (LSP), which in many models serves as dark matter candidate. In addition, $\mathcal{R}$-parity does not allow for baryon and lepton number violating terms, which are potentially dangerous since they could lead to rapid proton decay.

For completeness we give the $\mathcal{R}$-parity violating terms which could in principle contribute to the superpotential and may be present in extensions of the MSSM,

$$\mathcal{W}_{\mathcal{R}} = -\epsilon_i L_i \cdot H_u + \frac{1}{2}\lambda_{ijk}L_i \cdot L_j\overline{E}_k + \lambda'_{ijk}L_i \cdot Q_j\overline{D}_k + \frac{1}{2}\lambda''_{ijk}\overline{U}_i\overline{D}_j\overline{D}_k. \tag{2.31}$$

---

[4] A $U(1)_R$ global symmetry would be destroyed by quantum anomalies [63]. Further a gaugino mass term would violate such a symmetry, however their non-observation at LEP/Tevatron renders them massive.

Soft SUSY-Breaking Terms

SUSY has to be broken in any realistic model, since it is manifestly not an exact symmetry of the known particle spectrum. In the MSSM, SUSY is explicitly broken and the breaking is parametrized by means of the soft breaking terms. The couplings of the soft breaking terms have positive mass dimension and only those terms are allowed that do not introduce new quadratic divergences.[5] The most general soft Lagrangian of the MSSM that is invariant under the SM gauge group is given by [65],

$$
\begin{aligned}
\mathcal{L}_{\text{soft}} = & -\tilde{q}_{iL}^{\dagger}(M_{\tilde{q}_L}^2)_{ij}\tilde{q}_{jL} - \tilde{u}_{iR}^{*}(M_{\tilde{u}_R}^2)_{ij}\tilde{u}_{jR} - \tilde{d}_{iR}^{*}(M_{\tilde{d}_R}^2)_{ij}\tilde{d}_{jR} \\
& -\tilde{l}_{iL}^{\dagger}(M_{\tilde{l}_L}^2)_{ij}\tilde{l}_{jL} - \tilde{e}_{iR}^{*}(M_{\tilde{e}_R}^2)_{ij}\tilde{e}_{jR} \\
& -\frac{1}{2}\left(M_1\tilde{B}\tilde{B} + M_2\tilde{W}^a\tilde{W}^a + M_3\tilde{g}^a\tilde{g}^a + \text{h.c.}\right) \\
& -m_{h_u}^2 h_u^{\dagger}h_u - m_{h_d}^2 h_d^{\dagger}h_d - (b\, h_u \cdot h_d + \text{h.c.}) \\
& -\left((a^u)_{ij}\tilde{u}_{iR}\,\tilde{q}_{jL} \cdot h_u + (a^d)_{ij}\tilde{d}_{iR}\,\tilde{q}_{jL} \cdot h_d + (a^e)_{ij}\tilde{e}_{iR}\,\tilde{l}_{jL} \cdot h_d + \text{h.c.}\right).
\end{aligned}
\tag{2.32}
$$

The allowed terms are squark and slepton mass terms (first and second line), gaugino mass terms (third line), Higgs-boson mass terms and bilinear couplings (fourth line), and trilinear Higgs–sfermion–sfermion interactions (last line). The i,j are generation indices and a runs from 1 to 8 for gluinos and from 1 to 3 for winos. The trilinear couplings $a_{ij}^{u,d,e}$ are usually expressed in terms of the Yukawa couplings $y_{ij}^{u,d,e}$,

$$
a_{ij}^{u,d,e} = (y^{u,d,e}A_{u,d,e})_{ij}.
\tag{2.33}
$$

The gaugino mass terms $M_{1,2,3}$ and the bilinear Higgs-boson coupling b are in general complex numbers, while the $m_{u,d}$ are real mass parameters. Further the sfermion masses $M_{\tilde{f}}^2$ and the trilinear couplings $a^{u,d,e}$ are hermitian 3×3 matrices in generation space. If one allows all parameters to be complex one would deal with 105 new unknown parameters. All but two, the μ parameter and $\tan\beta$, are coming from the soft-breaking terms. For comparison, the SM has 19 free parameters.

Constrained MSSM

Even though the MSSM in general introduces 105 new free parameters, an extensive range in parameter space is excluded phenomenologically. The main reason is that most of these parameters allow for flavor-changing neutral currents (FCNC) or introduce new sources of CP violation, which are both not observed so far [66–69]. The concept of minimal flavor violation assumes that the only source of CP violation is given by the CKM matrix or rather the Yukawa couplings $y^{u,d}$, and that the sfermion mass matrices $M_{\tilde{f}}^2$ and the trilinear

---

[5]Positive mass dimension of the couplings is a necessary but not sufficient condition for not having quadratic divergences. For example, a term such as $d_{ijk}\phi_i^*\phi_j\phi_k$ generally tends to generate quadratic divergences from loops.

couplings A_f are diagonal in flavor space so that FCNC are absent at tree-level,

$$(M_{\tilde{f}}^2)_{ij} = \delta_{ij} M_{\tilde{f}_i}^2 \,, \qquad\qquad (A_f)_{ij} = \delta_{ij} A_{f_i} \,, \qquad (2.34)$$

with $\tilde{f} = \{\tilde{q}, \tilde{u}, \tilde{d}, \tilde{l}, \tilde{e}\}$ and $f = \{u, d, e\}$ and the generation indices $i, j = 1, 2, 3$.

The parameters can be further restricted in constrained SUSY models, where assumptions about the SUSY breaking at high scales and their mediation to the visible sector are made. The most prominent symmetry breaking mechanisms are *gravity mediated* (mSUGRA) [70, 71], *gauge mediated* (GMSB) [72–74], and *anomaly mediated* (AMSB) supersymmetry breaking [75, 76]. In all these models the parameters appearing in (2.32) have a particular simple form at the GUT scale. Renormalization group equations can then be used to run them down to the electroweak scale.

The constrained MSSM (CMSSM) is obtained by assuming that the MSSM breaking parameters can be described by such universal braking mechanisms. However, referring to the CMSSM without specifying the underlying mechanism commonly denotes the mSUGRA scenario.

2.2.3 The Particle Spectrum of the MSSM

In the following we want to discuss the particle spectrum of the MSSM. If SUSY would be unbroken, it would be a very economic theory, since all sfermion and gaugino masses would be identical to their SM partners. The only difference would occur in the Higgs sector, since now one has a two Higgs-doublet model instead of a single Higgs field. After eliminating the auxiliary fields appearing in $\mathcal{L}_{\text{SUSY}}$ eqs. (2.26a)–(2.26c), see also Appendix D.7.1, one gets the mass terms of the various particles which have to be diagonalized in order to obtain mass eigenstates.

Higgs Bosons

The MSSM Higgs sector is constituted by two (complex) Higgs-doublet fields with opposite hypercharge. Hence, the Higgs sector has eight free parameters. As well as in the SM Higgs mechanism, after developing its vacuum expectation value, the three would-be Goldstone bosons vanish from the physical spectrum, giving mass to the W and Z bosons. Therefore there are five physical Higgs bosons: three neutral Higgs bosons, two of them CP-even, h^0 and H^0, and one CP-odd, A^0, as well as two charged Higgs bosons, $H^\pm$. The Higgs potential of the MSSM has the following form,

$$\begin{aligned} V_H = {}& (|\mu|^2 + m_{h_d}^2) h_d^\dagger h_d + (|\mu|^2 + m_{h_u}^2) h_u^\dagger h_u + (b\, h_u \cdot h_d + \text{h.c.}) \\ & + \frac{g_1^2 + g_2^2}{8} \left[h_d^\dagger h_d - h_u^\dagger h_u \right]^2 + \frac{g_2^2}{2} |h_d^\dagger h_u|^2. \end{aligned} \qquad (2.35)$$

Comparing this with the SM Higgs potential (2.11) one finds that the Higgs self-interaction terms of the MSSM are no longer free parameters. Instead they are given by the gauge couplings g_1 and g_2. In analogy to the Higgs mechanism in the SM, the Higgs fields are required

to have non-vanishing vacuum expectation values that are annihilated by the generator Q of the electric charge (2.7),

$$\langle h_d \rangle = \frac{1}{\sqrt{2}} \begin{pmatrix} v_1 \\ 0 \end{pmatrix}, \qquad \langle h_u \rangle = \frac{1}{\sqrt{2}} \begin{pmatrix} 0 \\ v_2 \end{pmatrix}. \tag{2.36}$$

The requirement of electroweak symmetry breaking for nonzero vacuum expectation values $v_{1,2}$ and the condition that the Higgs potential has to be bounded from below impose the following conditions on the parameters of the Higgs potential

$$m_{h_u}^2 + m_{h_d}^2 + 2|\mu|^2 > 2|b|\,, \tag{2.37a}$$

$$(m_{h_u}^2 + |\mu|^2)(m_{h_d}^2 + |\mu|^2) < b^2\,. \tag{2.37b}$$

These relations link electroweak symmetry breaking of the MSSM to the breaking of supersymmetry, since in an unbroken theory (i.e. $m_{h_u}^2 = m_{h_d}^2 = b = 0$) eqs. (2.37a,b) cannot be fulfilled simultaneously.

Expanding the two Higgs fields about the classical ground state, they can be written as

$$h_d = \begin{pmatrix} \frac{1}{\sqrt{2}}(v_1 + \phi_1 + i\chi_1) \\ h_1^- \end{pmatrix} = \begin{pmatrix} \frac{1}{\sqrt{2}}(v\cos\beta + \phi_1 + i\chi_1) \\ h_1^- \end{pmatrix},$$

$$h_u = \begin{pmatrix} h_2^+ \\ \frac{1}{\sqrt{2}}(v_2 + \phi_2 + i\chi_2) \end{pmatrix} = \begin{pmatrix} h_2^+ \\ \frac{1}{\sqrt{2}}(v\sin\beta + \phi_2 + i\chi_2) \end{pmatrix}, \tag{2.38}$$

where $v = \sqrt{v_1^2 + v_2^2} \approx 246$ GeV and $\tan\beta = v_2/v_1$ with $0 < \beta < \pi/2$. The minimization condition leading to (2.36) can be written as

$$b = -\frac{(m_{h_d}^2 - m_{h_u}^2)\tan 2\beta + M_Z^2 \sin 2\beta}{2}, \tag{2.39a}$$

$$|\mu|^2 = \frac{m_{h_u}^2 \sin^2\beta - m_{h_d}^2 \cos^2\beta}{\cos 2\beta} - \frac{M_Z^2}{2}. \tag{2.39b}$$

The mass-squared matrix of the Higgs bosons are obtained by inserting (2.38) into (2.35) and taking only the terms quadratic in the fields. After some simplification, it is given by

$$V_H^{\text{quadratic}} = (\phi_1,\ \phi_2) \begin{pmatrix} m_{A^0}^2 \sin^2\beta + M_Z^2 \cos^2\beta & -(m_{A^0}^2 + M_Z^2)\sin\beta\cos\beta \\ -(m_{A^0}^2 + M_Z^2)\sin\beta\cos\beta & m_{A^0}^2 \cos^2\beta + M_Z^2 \sin^2\beta \end{pmatrix} \begin{pmatrix} \phi_1 \\ \phi_2 \end{pmatrix}$$

$$+ b\,(\chi_1,\ \chi_2) \begin{pmatrix} v_2/v_1 & 1 \\ 1 & v_1/v_2 \end{pmatrix} \begin{pmatrix} \chi_1 \\ \chi_2 \end{pmatrix} \tag{2.40}$$

$$+ \left(b + \frac{v_1 v_2}{4} g_2^2\right)(h_1^+,\ h_2^+) \begin{pmatrix} v_2/v_1 & 1 \\ 1 & v_1/v_2 \end{pmatrix} \begin{pmatrix} h_1^- \\ h_2^- \end{pmatrix}.$$

with $m_{A^0}^2 = 2b/\sin 2\beta$.[6] The mass eigenstates are obtained by performing the following unitary transformations

$$\frac{1}{\sqrt{2}} \begin{pmatrix} H^0 \\ h^0 \end{pmatrix} = \begin{pmatrix} \cos\alpha & \sin\alpha \\ -\sin\alpha & \cos\alpha \end{pmatrix} \begin{pmatrix} \phi_1 \\ \phi_2 \end{pmatrix}, \tag{2.41}$$

$$\frac{1}{\sqrt{2}} \begin{pmatrix} G^0 \\ A^0 \end{pmatrix} = \begin{pmatrix} -\cos\beta & \sin\beta \\ \sin\beta & \cos\beta \end{pmatrix} \begin{pmatrix} \chi_1 \\ \chi_2 \end{pmatrix}, \tag{2.42}$$

$$\begin{pmatrix} G^\pm \\ H^\pm \end{pmatrix} = \begin{pmatrix} -\cos\beta & \sin\beta \\ \sin\beta & \cos\beta \end{pmatrix} \begin{pmatrix} h_1^\pm \\ h_2^\pm \end{pmatrix}. \tag{2.43}$$

The tree-level masses of the five physical Higgs bosons and would-be Goldstone bosons are then given by

$$m_{h^0,H^0}^2 = \frac{1}{2} \left(m_{A^0}^2 + M_Z^2 \mp \sqrt{(m_{A^0}^2 + M_Z^2)^2 - 4M_Z^2 m_{A^0}^2 \cos^2 2\beta} \right), \tag{2.44a}$$

$$m_{A^0}^2 = \frac{2b}{\sin 2\beta}, \tag{2.44b}$$

$$m_{H^\pm}^2 = m_{A^0}^2 + M_W^2, \tag{2.44c}$$

$$m_{G^0}^2 = m_{G^\pm}^2 = 0. \tag{2.44d}$$

The mixing angle α obeys the relation

$$\sin 2\alpha = -\frac{m_{H^0}^2 + m_{h^0}^2}{m_{H^0}^2 - m_{h^0}^2} \sin 2\beta. \tag{2.45}$$

The Higgs mass spectrum is determined by only two new parameters, as one can see from (2.44). Usually, they are taken to be m_{A^0} and $\tan\beta$. It follows that the CP-even and charged Higgs-boson tree-level masses are no longer free parameters of the theory and underlie the following constrains that emerge from (2.44),

$$m_{h^0} < \min(m_{A^0}, M_Z), \tag{2.46a}$$

$$m_{H^0} > \max(m_{A^0}, M_Z), \tag{2.46b}$$

$$m_{H^\pm} > \max(m_{A^0}, M_W). \tag{2.46c}$$

One remarkable prediction is that the tree-level mass of the lightest CP-even Higgs boson h^0 is lower than the Z mass. This bound has of course already been exceeded by the current experimental lower bound from LEP, $m_H > 114.4$ GeV 95% c.l. [42].[7] However,

---

[6]Identifying the mass of the CP-odd Higgs boson with m_{A^0} will be validated below.

[7]This lower bound was derived by the negative search of Higgs bremstrahlung from Z bosons. In modified Higgs models this coupling can get altered, e.g. in the MSSM the $h^0 ZZ$ coupling is suppressed via a factor $\sin(\beta - \alpha)$ which in principle lowers the mass bound depending on the precise value of α and β. However, in the decoupling limit, $m_{A^0} \gg M_Z$, one has $m_{A^0} \sim m_{H^0} \sim m_{H^\pm}$ and $\beta - \alpha \to \pi/2$ and the lightest Higgs becomes SM like while the others decouple.

since the CP-even Higgs mass is not a free parameter of the theory, it gets altered by radiative corrections [77, 78]. Owing to the large top-quark–Higgs Yukawa coupling the radiative corrections are dominated by the incomplete cancellation of loops involving top quarks t and its SUSY partners, the stops $\tilde{t}_\alpha$. In the limit of exact supersymmetry, the Higgs masses are protected by the non-renormalization theorem, hence the corrections have to be proportional to $\ln(m_S/m_t)$, with m_S being of the order of the soft breaking scale. By neglecting squark-mixing effects for simplicity, the shift of the mass bound can be estimated and is given via

$$m_{h^0}^2 < m_Z^2 + \frac{3m_t^4}{2\pi^2 v^2} \ln \frac{m_S}{m_t}, \tag{2.47}$$

i.e. the corrections go with the fourth power of the top mass. This shows that in the MSSM it is crucial to have a heavy fermion, since otherwise radiative corrections would not be able to shift the Higgs mass above the experimental bound.

The relations for the gauge bosons, eqs. (2.15–2.17), also hold in the MSSM with $v = \sqrt{v_1^2 + v_2^2}$. The SM fermions obtain their masses in much the same way as in the SM, however since in the MSSM h_u can only couple to up-type fermions while h_d couples to the down-type fermions, the relation between masses and Yukawa couplings becomes

$$\frac{\lambda_u}{\sqrt{2}} = \frac{m_u}{v_2} = \frac{m_u}{v\sin\beta}, \qquad \frac{\lambda_d}{\sqrt{2}} = \frac{m_d}{v_1} = \frac{m_d}{v\cos\beta}, \qquad \frac{\lambda_e}{\sqrt{2}} = \frac{m_e}{v_1} = \frac{m_e}{v\cos\beta}. \tag{2.48}$$

Comparing this with the Yukawa couplings in the SM, eq. (2.20) one finds an additional factor of $1/\cos\beta$ or $1/\sin\beta$, respectively. Hence, down-type Yukawa couplings can be considerably enhanced for large values of $\tan\beta$.

Even though true at tree-level, the relations (2.48) between masses and Yukawa couplings get spoiled by radiative corrections. These allow for an effective coupling of down-type quarks to the vev v_2 of h_u while up-type quarks get an effective coupling to v_1 [79]. While the former corrections are enhanced by $\tan\beta$, the latter are suppressed by $1/\tan\beta$. The induced effective couplings are closely related to the soft breaking parameters, as expected due to the non-renormalization theorem. The $\tan\beta$ enhanced contributions can be resummed to all orders [79–84]

$$\frac{v\lambda_b^0}{\sqrt{2}} = \frac{m_b}{1 + \Delta m_b}, \tag{2.49}$$

where λ_b^0 denotes the bare Yukawa coupling and Δm_b contains all $\tan\beta$ enhanced terms. Further details on the effective Yukawa couplings are be given in Section 6.2 and Appendix C.

Sfermions

In principle all particles with the same spin, $SU(3)_C \times U(1)_{\text{em}}$ quantum numbers, and $\mathcal{R}$-parity can mix with each other. Since sfermions of different families can mix via the soft breaking terms, this would lead to 6×6 mixing matrices for up-type squarks, down-type squarks, and charged sleptons and to a 3×3 mixing matrix for the sneutrinos. As mentioned before, family mixing is strongly constrained by phenomenological observations. Therefore

in the following minimal flavor violation is assumed, resulting in reducible 6×6 matrices whose irreducible elements are 2×2 matrices for up-type squarks, down-type squarks, and charged sleptons, describing left-right mixing between each generation. Since only left-handed sneutrinos are included in the MSSM, no mixing takes place in this sector. In the gauge eigenstate basis $(\tilde{f}_L, \tilde{f}_R)$, the sfermion mass matrix can be written as

$$\mathcal{M}_{\tilde{f}} = \begin{pmatrix} M_{\tilde{f}_L}^2 + m_f^2 + M_Z^2 \cos(2\beta)(I_f^3 - Q_f s_w^2) & m_f(A_f^* - \mu\kappa) \\ m_f(A_f - \mu^*\kappa) & M_{\tilde{f}_R}^2 + m_f^2 + Q_f M_Z^2 \cos(2\beta) s_w^2 \end{pmatrix}, \quad (2.50)$$

where $\kappa = \cot\beta$ for up-type squarks and $\kappa = \tan\beta$ for down-type squarks and electron-type sleptons. The chirality eigenstates can be rotated into the mass eigenstates with help of a unitary matrix $U_{\tilde{f}}$,

$$\begin{pmatrix} \tilde{f}_1 \\ \tilde{f}_2 \end{pmatrix} = U_{\tilde{f}} \begin{pmatrix} \tilde{f}_L \\ \tilde{f}_R \end{pmatrix} \qquad \Rightarrow \qquad \mathcal{D}_{\tilde{f}} \equiv U_{\tilde{f}} \mathcal{M}_{\tilde{f}} U_{\tilde{f}}^\dagger = \begin{pmatrix} m_{\tilde{f}_1}^2 & 0 \\ 0 & m_{\tilde{f}_2}^2 \end{pmatrix}. \quad (2.51)$$

The sfermion mass eigenvalues are given by

$$m_{\tilde{f}_{1,2}}^2 = \frac{1}{2}(M_{\tilde{f}_L}^2 + M_{\tilde{f}_R}^2) + m_f^2 + \frac{1}{2}I_f^3 M_Z \cos(2\beta) \qquad (2.52)$$
$$\mp \frac{1}{2}\sqrt{\left[M_{\tilde{f}_L}^2 - M_{\tilde{f}_R}^2 + M_Z^2 \cos(2\beta)(I_f^3 - 2Q_f s_w^2)\right]^2 + 4m_f^2|A_f - \mu\kappa|^2},$$

with the convention $m_{\tilde{f}_1} < m_{\tilde{f}_2}$. The sfermion matrix (2.50) can be expressed in terms of the unitary matrix $U_{\tilde{f}}$ and the physical sfermion masses

$$\mathcal{M}_{\tilde{f}} = \begin{pmatrix} (U_{\tilde{f}11})^2 m_{\tilde{f}_1}^2 + (U_{\tilde{f}21})^2 m_{\tilde{f}_2}^2 & U_{\tilde{f}11} U_{\tilde{f}12} m_{\tilde{f}_1}^2 + U_{\tilde{f}21} U_{\tilde{f}22} m_{\tilde{f}_2}^2 \\ U_{\tilde{f}11} U_{\tilde{f}12} m_{\tilde{f}_1}^2 + U_{\tilde{f}21} U_{\tilde{f}22} m_{\tilde{f}_2}^2) & (U_{\tilde{f}12})^2 m_{\tilde{f}_1}^2 + (U_{\tilde{f}22})^2 m_{\tilde{f}_2}^2 \end{pmatrix}. \quad (2.53)$$

$U_{\tilde{f}}$ can be parametrized by a mixing angle $\theta_{\tilde{f}}$,

$$U_{\tilde{f}} = \begin{pmatrix} \cos\theta_{\tilde{f}} & \sin\theta_{\tilde{f}} \\ -\sin\theta_{\tilde{f}} & \cos\theta_{\tilde{f}} \end{pmatrix}, \qquad \text{or} \quad U_{\tilde{f}} = \begin{pmatrix} -\sin\theta_{\tilde{f}} & \cos\theta_{\tilde{f}} \\ \cos\theta_{\tilde{f}} & \sin\theta_{\tilde{f}} \end{pmatrix}. \quad (2.54)$$

Depending on the precise value of the parameters in (2.50) one has to choose $\det(U_{\tilde{f}}) = \pm 1$ in order to realize $m_{\tilde{f}_1} < m_{\tilde{f}_2}$. Comparing $(\mathcal{M}_{\tilde{f}})_{1,2}$ of (2.50) and (2.53) and using the explicit expression for $U_{\tilde{f}}$ given by (2.54), relates the mixing angle to the soft breaking parameters,

$$\sin 2\theta_{\tilde{f}} = \det(U_{\tilde{f}}) \frac{2m_f(A_f^* - \mu\kappa)}{m_{\tilde{f}_1}^2 - m_{\tilde{f}_2}^2}. \quad (2.55)$$

The soft breaking parameter $M_{\tilde{f}_L}^2$ is the same for up- and down-type quarks of the same generation due to $SU(2)_L$ invariance, relating the squark masses within one generation.

Comparing the $(\mathcal{M}_{\tilde{f}})_{1,1}$ of (2.50) and (2.53) one finds for each generation following relation between the four mass eigenvalues:

$$(U_{\tilde{d}11})^2 m_{\tilde{d}_1}^2 + (U_{\tilde{d}12})^2 m_{\tilde{d}_2}^2 = (U_{\tilde{u}11})^2 m_{\tilde{u}_1}^2 + (U_{\tilde{u}12})^2 m_{\tilde{u}_2}^2 + m_d^2 - m_u^2 - M_W^2 \cos 2\beta \,. \quad (2.56)$$

For each generation there are five independent parameters related to the squark sector, M_L^2, $M_{\tilde{u}_R}^2$, $M_{\tilde{d}_R}^2$, A_u, and A_d (with $M_L^2 = M_{\tilde{u}_L}^2 = M_{\tilde{d}_L}^2$). All other parameters are already determined from other sectors. Depending on the parametrization used, these parameters can be related to the ones appearing in (2.53), namely three out of the four fermion masses $m_{\tilde{u}_1}^2$, $m_{\tilde{u}_2}^2$, $m_{\tilde{d}_1}^2$ and $m_{\tilde{d}_2}^2$ and the two mixing angles $\theta_{\tilde{u}}$, $\theta_{\tilde{d}}$.

The sfermion mixing is proportional to the corresponding fermion mass. Hence for the third generation huge mixing effects take place, while for the first two generations mixing effects can be safely neglected leading to trivial mixing matrices. In the squark sector the number of free parameters is then reduced from five to three for the first and second generation, namely M_L^2, $M_{\tilde{u}_R}^2$, and $M_{\tilde{d}_R}^2$.

Neutralinos and Charginos

The neutral higgsinos h_u^0 and h_d^0, and the neutral gauginos $\tilde{B}$ and $\tilde{W}^0$ mix and form four mass eigenstates, the neutralinos. They are Majorana fermions, in the sense that their left- and right-handed component are related via $\Psi_R = -i\sigma^2 \Psi_L$ (cf. (D.59) and (D.81)). In the basis

$$\Psi_i^0 = (\tilde{B}, \tilde{W}^0, \tilde{h}_u^0, \tilde{h}_d^0)^{\mathrm{T}}, \quad (2.57)$$

their mass matrix is given by,

$$M_N = \begin{pmatrix} M_1 & 0 & -M_Z s_{\mathrm{w}} \cos\beta & M_Z s_{\mathrm{w}} \sin\beta \\ 0 & M_2 & M_Z c_{\mathrm{w}} \cos\beta & M_Z c_{\mathrm{w}} \sin\beta \\ -M_Z s_{\mathrm{w}} \cos\beta & M_Z c_{\mathrm{w}} \cos\beta & 0 & -\mu \\ M_Z s_{\mathrm{w}} \sin\beta & M_Z c_{\mathrm{w}} \sin\beta & -\mu & 0 \end{pmatrix}. \quad (2.58)$$

Without electroweak symmetry breaking, this matrix would be block diagonal, and gauginos would not mix with the higgsinos. Due to the fact that Ψ_i^0 are Majorana particles, M_N has to be symmetric and can be diagonalized with help of a unitary matrix N. Defining the mass eigenstates as

$$\begin{pmatrix} \tilde{\chi}_1^0 \\ \tilde{\chi}_2^0 \\ \tilde{\chi}_3^0 \\ \tilde{\chi}_4^0 \end{pmatrix} = N \begin{pmatrix} \tilde{B} \\ \tilde{W}^0 \\ \tilde{h}_u^0 \\ \tilde{h}_d^0 \end{pmatrix}, \quad (2.59)$$

the diagonalized mass matrix is given by

$$M_{\tilde{\chi}^0} = N^* M_N N^\dagger \,. \quad (2.60)$$

N can be chosen such that all entries are non-negative and the neutralino masses obey $m_{\tilde{\chi}_1^0} < m_{\tilde{\chi}_2^0} < m_{\tilde{\chi}_3^0} < m_{\tilde{\chi}_4^0}$. The diagonalization of the neutralino mass matrix is usually done numerically.

The positive and negative charged higgsinos and winos $(\tilde{W}^+, \tilde{h}_u^+)$ and $(\tilde{W}^-, \tilde{h}_d^-)$, with $\tilde{W}^\pm = \frac{1}{\sqrt{2}}(\tilde{W}^1 \mp \tilde{W}^2)$, can mix, and their mass eigenstates are called charginos. With help of the electric charge eigenstates

$$\Psi^+ = \begin{pmatrix} \tilde{W}^+ \\ \tilde{h}_u^+ \end{pmatrix}, \qquad \Psi^- = \begin{pmatrix} \tilde{W}^- \\ \tilde{h}_d^- \end{pmatrix}, \tag{2.61}$$

the chargino mass term of the Lagrangian can be written as

$$-\frac{1}{2}\left[(\Psi^+)^{\mathrm{T}} M_C^{\mathrm{T}} \Psi^- + (\Psi^-)^{\mathrm{T}} M_C \Psi^+ \right] + \text{h.c.}, \tag{2.62}$$

with the mass matrix

$$M_C = \begin{pmatrix} M_2 & \sqrt{2} M_W \sin\beta \\ \sqrt{2} M_W \cos\beta & \mu \end{pmatrix}. \tag{2.63}$$

As in the neutralino case, the mixing is due to the electroweak symmetry breaking. This matrix can be diagonalized by a bi-unitary transformation. Since Ψ^+ and Ψ^- are independent states, they can be separately rotated. Defining the mass eigenstates as

$$\begin{pmatrix} \tilde{\chi}_1^+ \\ \tilde{\chi}_2^+ \end{pmatrix} = V \begin{pmatrix} \tilde{W}^+ \\ \tilde{h}_u^+ \end{pmatrix}, \qquad \begin{pmatrix} \tilde{\chi}_1^- \\ \tilde{\chi}_2^- \end{pmatrix} = U \begin{pmatrix} \tilde{W}^- \\ \tilde{h}_d^- \end{pmatrix}, \tag{2.64}$$

the diagonalized mass matrix is obtained by

$$M_{\tilde{\chi}^\pm} = U^* M_C V^\dagger. \tag{2.65}$$

This yields the following chargino masses,

$$
\begin{aligned}
m_{\tilde{\chi}_{1,2}^\pm}^2 = {} & \frac{1}{2}\left(M_2^2 + \mu^2 + 2M_W^2 \right) \\
& \mp \frac{1}{2}\sqrt{\left(M_2^2 + \mu^2 + 2M_W^2 \right)^2 - 4\left(\mu M_2 - M_W^2 \sin 2\beta \right)^2}.
\end{aligned}
\tag{2.66}
$$

Gluino

The gluino $\tilde{g}$ is the superpartner of the gluon and hence a color octet fermion. Due to its unique color and spin quantum number it cannot mix with any other particle in the MSSM. Its Majorana mass arises from the soft SUSY breaking gluino mass term,

$$m_{\tilde{g}} = M_3. \tag{2.67}$$

In supersymmetric GUT theories the three gaugino breaking parameters are related to each other since they have to unify at the GUT scale Λ_{GUT}. Running the scale down to low energies with help of the renormalization-group equation (RGE), this results in

$$M_3 = \frac{\alpha_s}{\alpha}\sin^2\theta_{\mathrm{w}} M_2 = \frac{5}{3}\frac{\alpha_s}{\alpha}\cos^2\theta_{\mathrm{w}} M_1. \tag{2.68}$$

3 Squark and Gluino Production at Hadron Colliders

Having introduced the MSSM in the last chapter, we now want to discuss its phenomenological implications for collider physics. Up to now, no direct evidence for supersymmetric particles (sparticles) has been found, resulting in lower mass bounds for these particles. However, as motivated in Section 2.2.1, there are several indications that SUSY might be realized at the TeV scale, and hence should become detectable at the Large Hadron Collider (LHC) at CERN.

The LHC is a proton–proton collider with a design center of mass energy (c.m.) of 14 TeV with two high luminosity experiments, ATLAS [85] and CMS [86], aiming to a peak luminosity of L = 10^{34} cm^{-2}s^{-1} = 100 pb^{-1}s^{-1}, and two low luminosity experiments, LHCb [87] and ALICE [88]. ATLAS and CMS are multi-purpose experiments designed for the searches of new particles, LHCb investigates CP-asymmetry in B-meson systems while ALICE looks towards the quark–gluon plasma induced by heavy-ion collisions.

Unfortunately, a few weeks after the successful start-up in September 2008, the LHC was forced to shut down again due to magnetic quenching of about 100 of the superconducting solenoids. Since November 2009 the LHC is operating again. However, the center of mass energy is halved to 7 TeV for the first 18 month to two years, after which it will be shut down again to prepare for the 14 TeV collisions.

If SUSY is realized at the TeV scale, colored SUSY particles, i.e. squarks and gluinos, are expected to be produced at a high rate, since it proceeds via the strong interaction. In $\mathcal{R}$-parity conserving models, like the MSSM, SUSY particles can only be produced in pairs. Studies for the 14 TeV LHC, based on Monte Carlo simulations have shown that there is the possibility of early SUSY discovery within 1 fb^{-1} of data in the inclusive jet plus missing energy channel, provided that the SUSY particles are not too heavy (i.e. below 2 TeV) [89]. Precise theoretical predictions for squark and gluino pair production are crucial for the analysis of the LHC data and extraction of the SUSY parameters.

Among the final-state squarks one distinguishes the production of light-flavor squarks, i.e. squarks belonging to the first and second generation, and the third generation squarks, the top-squark $\tilde{t}$ and the bottom-squark $\tilde{b}$. The reasons are the following: First, in contrast to the light-flavor squarks, the decay of top- and bottom-squarks proceeds via the decay into a bottom-quark. Hence these processes can be triggered via B-tagging. Second, in many SUSY models, e.g. mSUGRA, when running the common parameters from the high scale down to the TeV scale, the third generation Yukawa-couplings have to be taken into account in the RGE running, which drives the masses of the third generation squarks to a lower value. Further, the left-right mixing is proportional to the Yukawa coupling, which

implies a large mass splitting for the third generation squarks. Hence in many models one of the top-squarks is the lightest squark.

Since the light-flavor squark mass-eigenstates are in a good approximation given by their flavor eigenstates, their states will be denoted as $\tilde{q}_L$ and $\tilde{q}_R$ for the left- and right handed squarks, respectively. In contrast top- and bottom-squarks will be labeled as $\tilde{t}_\alpha$ and $\tilde{b}_\alpha$, respectively, with $\alpha = 1, 2$ denoting the mass eigenstates.

3.1 Experimental Searches

The negative search results for SUSY particles leads to lower mass bounds on the SUSY spectrum by comparing theoretical predictions with experimental observations. These lower mass bounds are usually defined at the 95% confidence level (c.l.). Obviously, the so derived exclusion bounds usually depend on the underlying parameter space. Due to the huge parameter space in the MSSM where the SUSY breaking is parametrized by more than hundred parameters, a scan through all these parameters is not possible. Even when assuming a breaking mechanism, where the total spectrum can be derived by a few parameters, a sampling of these parameters is beyond present capabilities for phenomenological studies, especially when it comes to simulating experimental signatures within detector simulation. Therefore one defines benchmark scenarios such as the snowmass points and slopes (SPS) [90] which exhibit specific characteristics of the MSSM. Such benchmark points are then used for the analysis or as starting point of a one- or two-dimensional analysis.

In the following we will constrain our discussion to the $\mathcal{R}$-parity conserving MSSM. The expected signal for squark and gluino production is characterized by the presence of multiple jets of hadrons from their cascade decays and large missing transverse energy $\not{E}_T$ from the presence of two LSPs in the final state.

3.1.1 Light-Flavor Squarks

The search strategy and mass reconstruction for the various SUSY particles are described in e.g. [91] and references therein. Since the LSP will escape detection, it is not straightforward to reconstruct SUSY events. A possible approach is to use kinematic edges of distributions [92]. However, the search strategies are strongly model dependent. For example, in a scenario with squark masses $m_{\tilde{q}}$ significantly larger than the gluino mass $m_{\tilde{g}}$, at least four jets in the final state are expected, while for $m_{\tilde{g}} > m_{\tilde{q}}$ dijet configurations dominate. Further the decay chains of light-flavor squarks often depend on its chirality. For example, in the SPA1a benchmark point the second neutralino $\tilde{\chi}_2^0$ is wino like while the first (i.e. the LSP) $\tilde{\chi}_1^0$ is bino like. Consequently, while a right handed squark decays directly into the LSP and a quark, a left handed squark can decay into the LSP via a decay chain with the $\tilde{\chi}_2^0$ as intermediate state,

$$\tilde{q}_R \to q \, \tilde{\chi}_1^0 \,, \tag{3.1a}$$

$$\tilde{q}_L \to \tilde{\chi}_2^0 \, q \to q \, \tilde{l} \, l \to q \, l^+ \, l^- \, \tilde{\chi}_1^0 \,, \tag{3.1b}$$
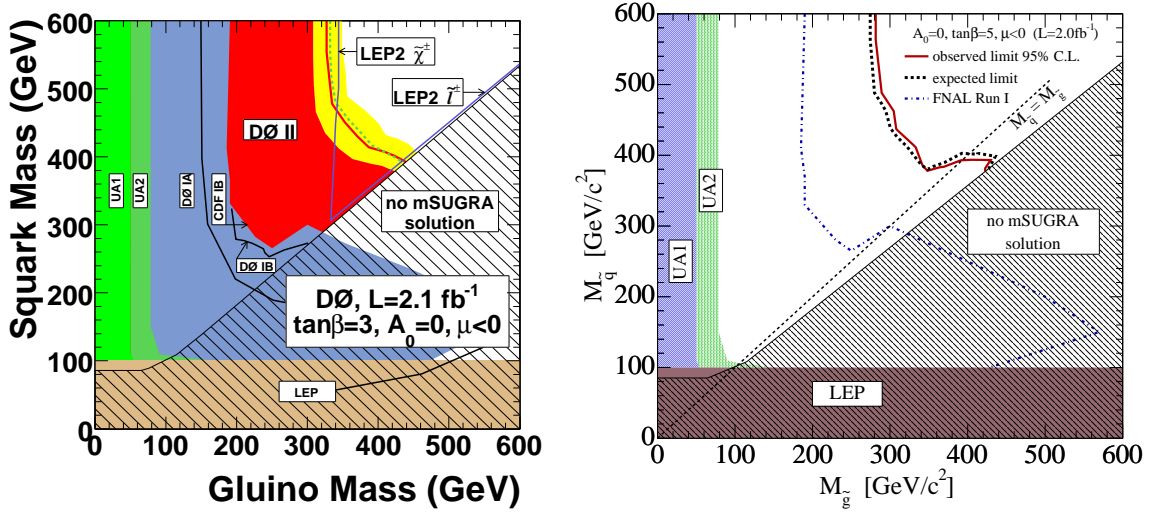
Figure 3.1: Exclusion plane at 95% c.l. as a function of squark and gluino masses by direct searches in the mSUGRA framework. Results from previous experiments are included. The regions where no mSUGRA solution is possible are black shaded. The referred "squark mass" is the average mass of all squarks considered in the analysis. DØ (left plot): All squarks other than stops are considered. The red shaded region shows the most conservative exclusion bound, which is given by the red line combining with the expected uncertainties, shown by the yellow region [93]. CDF (right plot): Stop pair production processes are not considered and the contribution from hard processes involving sbottom production is not included in the analysis. The red solid line shows the observed upper mass limit including all uncertainties [94].

making left- and right-handed squarks distinguishable due to the two extra leptons in the final state.

The most stringent bounds for light-flavor squark and gluino masses are obtained from the DØ and CDF collaboration [93,94] as a result on an inclusive search for squarks and gluinos in proton–anti-proton collisions at the Tevatron at a c.m. energy of $\sqrt{S} = 1.96$ TeV in events with large $\not{E}_T$ and multiple jets in the final state, based on 2 fb^{-1} of CDF Run II data and 2.1 fb^{-1} of DØ data, respectively. The analysis was performed in both cases within mSUGRA scenarios fixing the high scale parameters A_0, $\tan\beta$, and $\text{sign}(\mu)$ and varying M_0 and $M_{1/2}$ which results in a scan over the squark and gluino masses. The analysis performed by the DØ collaboration was done for $A_0 = 0$, $\tan\beta = 3$, and $\text{sign}(\mu) < 0$, and the one performed by CDF is done in the same region but for $\tan\beta = 5$. The exclusion plane as a function of the squark and gluino masses derived by both experiments are shown in Figure 3.1. The squark and gluino lower mass bounds from DØ (CDF) are given by $m_{\tilde{q}} > 392$ GeV (392 GeV) and $m_{\tilde{g}} > 327$ GeV (340 GeV). Taking theoretical uncertainties into account by allowing for a factor of two in the choice of factorization and renormalization scale and considering uncertainties in the parton distribution functions (PDFs), these lower mass bounds are reduced to $m_{\tilde{q}} > 379$ GeV and $m_{\tilde{g}} > 308$ GeV. This points out the importance of accurate theoretical predictions for precise experimental analysis.
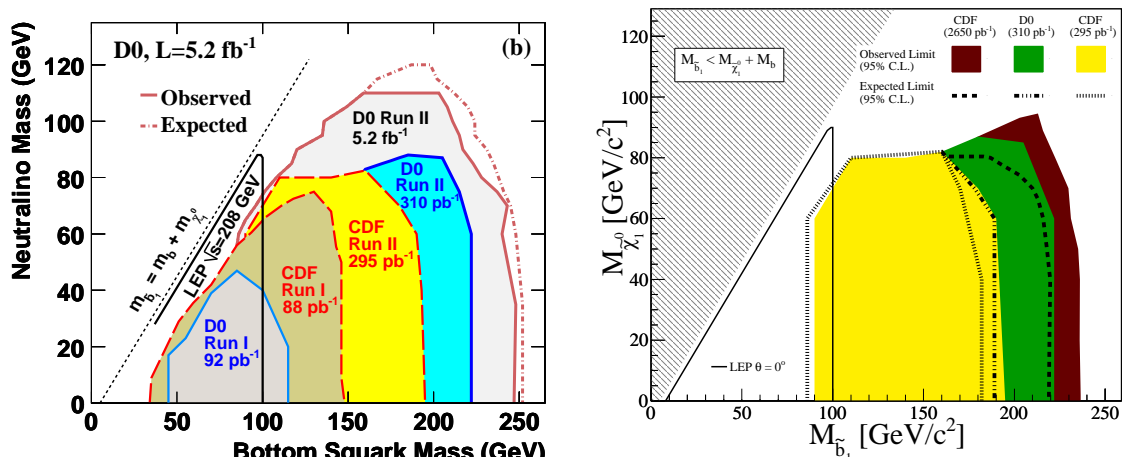
Figure 3.2: Exclusion plane at the 95% c.l. as a function of sbottom and neutralino mass. The observed and expected upper limits from the new DØ [97] (left) and CDF [98] (right) analysis are compared to the previous results from DØ and CDF experiments, and from LEP experiments with squark mixing angle $\theta_{\tilde{b}} = 0$. Due to the much larger data set used in the DØ analysis, higher exclusion bounds are obtained.

3.1.2 Bottom-Squarks

Since the bottom-squark sector is connected to the top-squark sector, often a combined analysis is performed, with a stop and a sbottom in the final state. Even though SUSY particles have to be pair-produced, a mixed stop–sbottom final state can occur via W-boson production or via gluino-pair production and subsequent decay into a stop and a sbottom, if kinematically allowed. The relevant decay modes, which in general have to be considered are

$$\tilde{b}_1 \rightarrow b\,\tilde{\chi}_j^0\,(\rightarrow b\,l^+\,l^-\,\tilde{\chi}_1^0)\,, \tag{3.2a}$$

$$\tilde{b}_i \rightarrow W\,\tilde{t}_1 \rightarrow b\,W\,\tilde{\chi}_j^\pm\,, \tag{3.2b}$$

$$\tilde{b}_i \rightarrow t\,\tilde{\chi}_j^\pm\,, \tag{3.2c}$$

$$\tilde{t}_1 \rightarrow t\,\tilde{\chi}_j^0\,(\rightarrow b\,l^+\,l^-\,\tilde{\chi}_1^0)\,, \tag{3.2d}$$

$$\tilde{t}_1 \rightarrow b\,\tilde{\chi}_j^\pm\,, \tag{3.2e}$$

where the subsequent chargino decay is not written explicitly. Depending on the decay chain, different strategies are used for the analysis. The decay of the lighter bottom-squark $\tilde{b}_1$ is often studied through the decay mode (3.2a). The analysis used is similar to the one used for the light-flavor squarks, cf. (3.1). Another analysis method is proposed in e.g. Refs. [95, 96], by measuring the edge position of the invariant mass distribution of the final-state top- and bottom-quarks, m_{tb}, coming from decay modes (3.2b) and (3.2c). As for the light-flavor squarks, the most stringent bounds are obtained from the DØ and CDF collaboration [97–99]. The expected signal for direct sbottom production is characterized

by the presence of two energetic jets from the hadronization of the bottom quarks and large missing transverse energy $\not{E}_T$. The analysis makes use of b-tagging, based on the presence of a displaced vertex due to the decay of a b-hadron inside the jet. Special kinematical cuts on the pseudo-rapidity and transverse energy of the leading jet are required. The analysis is based on 2.65 fb^{-1} of CDF Run II data and 5.1 fb^{-1} of DØ data, respectively, collected at the $\sqrt{S} = 1.96$ TeV Tevatron. In contrast to light-flavor squark searches, the analysis is not restricted to a specific mSUGRA model. It is done in a generic MSSM with $\mathcal{R}$-parity conservation assuming a mass hierarchy such that the sbottom decays exclusively as $\tilde{b} \rightarrow b \tilde{\chi}_1^0$, i.e. corresponding to (3.2a). The exclusion planes as a function of the sbottom mass $m_{\tilde{b}}$ and LSP mass $\tilde{\chi}_1^0$ derived by DØ and CDF are shown in Figure 3.2. The sbottom lower mass bound strongly depends on the LSP mass. For $m_{\tilde{\chi}_1^0} < 70$ GeV, sbottom masses up to 240 GeV (230 GeV) are excluded by the DØ (CDF) experiment. For a heavier LSP, these bounds are not so stringent. For $m_{\tilde{\chi}_1^0} \gtrsim 110$ GeV ($m_{\tilde{\chi}_1^0} \gtrsim 95$ GeV) the only constraint on the sbottom mass is given by the requirement of being heavier than its decay products, $m_{\tilde{b}} > m_{\tilde{\chi}_1^0} + m_b$.

3.1.3 Prospects for the LHC

By using indirect experimental and cosmological information, the likely range of the parameters of the mSUGRA scenario are estimated using a Markov-chain Monte Carlo (MCMC) technique to sample the parameter space [100]. Most of the constraints on new physics beyond the SM are negative, in the sense that the data is in agreement with the SM predictions, and hence set lower limits on SUSY particles. However, the anomalous magnetic moment of the muon $(g-2)_\mu$ that differs by over three standard deviations from the best SM calculations based on e^+e^- collider data [44–50], and the cold matter density Ω_{CMD} [101] which has no origin in the SM, may be used to set upper limits on the possible masses of supersymmetric particles. To be consistent with current precision data, any such analysis should also take into account the constraints imposed by electroweak precision observables (EWPO) and B-physics observables (BPO) such as the branching ratio $b \rightarrow s\gamma$. The so achieved likely range can then be compared with the expected discovery reach at the LHC.

The left plot of Figure 3.3 shows that the 95% c.l. area in the $(m_0, m_{1/2})$ plane of the CMSSM (red area) lies largely within the region that could be explored with 1 fb^{-1} of integrated LHC luminosity at 14 TeV, indicated by the 5σ discovery contours published by the ATLAS and CMS collaboration [102, 103]. For the same data set, a same sign dilepton signal could as well be visible in the 68% c.l. area. A parameter scan through the whole MSSM parameter space is not possible for such a large amount of free parameters which cannot be explored with the MCMC approach due to limited available CPU power. However, one might wonder to what extend the conclusions are valid for more general scenarios. To get an idea, a simple extension of the CMSSM is considered, in which the high scale soft breaking parameter for the Higgs masses differ to those of the squarks and sleptons, the so-called non-universal Higgs model 1 (NUHM1) [104]. The results of the scan including an additional parameter m_ϕ are shown on the right plot of Figure 3.3. The general sizes of the
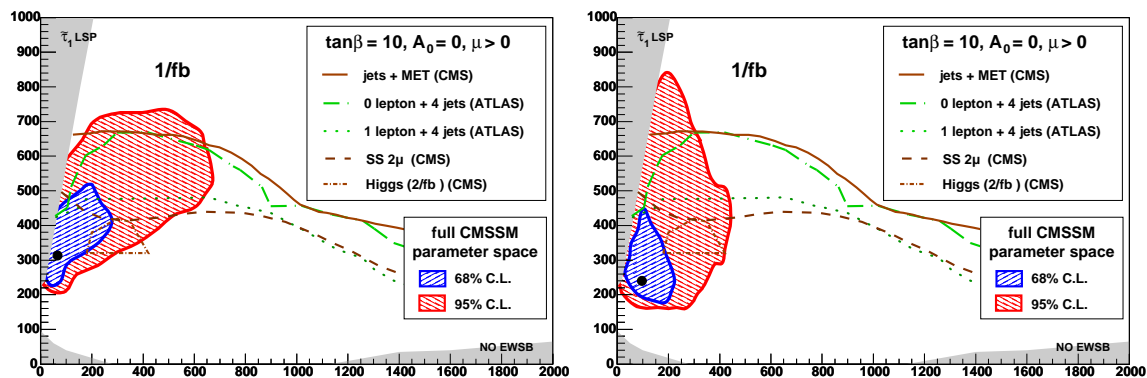
Figure 3.3: The 95% and 68% confidence level in the $(m_0, m_{1/2})$ plane of the CMSSM for $\tan \beta = 10$ and $A_0 = 0$ [100]. The dark shaded area are excluded due to a scalar tau LSP and the absence of electroweak symmetry breaking. Left: The best fit point is indicated by a filled circle, and the 68% (95%) c.l. contours from the fit are given by the blue (red) areas scanned over all $\tan \beta$ and A_0 values. The $5\,\sigma$ discovery contours for various observables at ATLAS and CMS for $1\,\mathrm{fb}^{-1}$ of data as well as the Higgs-boson discovery via sparticle decay for $2\,\mathrm{fb}^{-1}$ of data at CMS are shown. Right: same as left plot, but the best fit point and the 68% (95%) c.l. contours from the fit are given for the NUHM1 scenario.

68% and 95% c.l. regions are the same as in the CMSSM, though the best fit point and the 68% c.l. region is lowered a bit and the 95% c.l. region is enlarged in $m_{1/2}$. Again, a large (whole) range of the 95% (68%) c.l. area lies within the region that can be explored with $1\,\mathrm{fb}^{-1}$ of integrated LHC luminosity at 14 TeV.

In summary one can say that there are good prospects that the initial runs of the LHC will determine the (non)-existence of many low energy SUSY models.

3.2 Theoretical Predictions

In order to obtain reliable exclusion bounds or to claim a discovery of new SUSY particles, precise theoretical predictions for the production cross sections and kinematical distributions are crucial. In the event of discovering SUSY, one would like to trace back the underlying model by measuring the low energy breaking parameters and evolve them via RGE running to a high scale. To achieve this, experimental as well as theoretical uncertainties have to be as small as possible. In the following we will give an overview over the status of the work that has been done in order to get precise predictions for the cross section at hadron colliders.

When making predictions for hadronic collision, i.e. proton–proton (PP) collisions or proton–anti-proton ($\mathrm{P\overline{P}}$) collisions, one makes use of the factorization theorem which states, that the cross section can be written as a long distance part and a short distance part, and is the basis of perturbative QCD [105]. The long distance part is then given by the parton distribution function (PDF), that depends on the external hadron and the interacting parton. The PDF requires experimental inputs, since it cannot be calculated from first principles
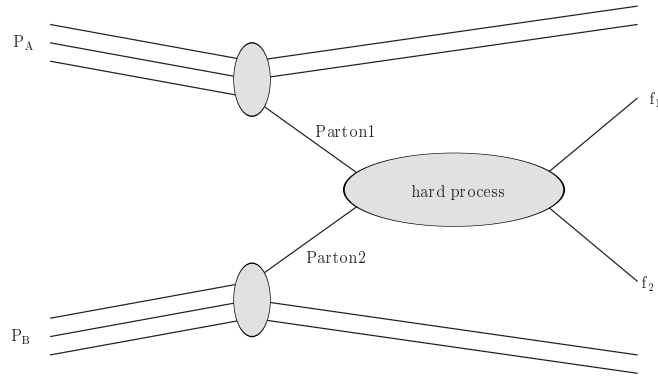
Figure 3.4: Factorization of the hard process from the hadrons P_A and P_B. The hard process leading to the final states f_1 and f_2 can be calculated in perturbation theory.

in perturbation theory. The short distant part, also called the hard scattering process, can then be calculated in perturbation theory. Since the separation into a long distance part and a short distance part is not unique, the separation requires the definition of a soft-hard scale parameter, the factorization scale. The choice of this scale is to a large extend arbitrary and is a source of theoretical uncertainties. The concept of factorization is schematically depicted in Figure 3.4. A more detailed discussion of the parton model will be postponed to Section 4.2.

3.2.1 QCD Contributions

The dominant production mechanism for squarks and gluinos is via the strong interaction. Due to the large interest in squark and gluino production processes first theoretical cross section predictions based on leading order (LO) calculations, which are of $\mathcal{O}(\alpha_s^2)$, were already made in the early '80s [17]. The processes contributing at LO can be classified by their final-state content:

$\tilde{g}\tilde{g}$: Gluino–pair production proceeds at the partonic level via two initial-state gluons or quark–anti-quark annihilation.

$\tilde{q}\tilde{g}$: Squark–gluino production (and its charge-conjugated process) only take place via the partonic process with a quark and a gluon in the initial state.

$\tilde{q}\tilde{q}$: Squark–squark production proceeds via t- and u-channel exchange of a gluino, and is only possible if the initial- and final-state flavors are identical. However, any combination of final-state flavors and chiralities are possible, i.e. $\tilde{u}_{i\alpha}\tilde{u}_{j\beta}$, $\tilde{d}_{i\alpha}\tilde{d}_{j\beta}$, $\tilde{u}_{i\alpha}\tilde{d}_{j\beta}$, with $i, j \in \{1, 2\}$ and $\alpha, \beta \in \{L, R\}$.

$\tilde{q}\tilde{q}^*$: Squark–anti-squark is initiated at the partonic level via gluon fusion, quark–anti-quark annihilation, and via t-channel gluino exchange in the case where the initial-state flavor equals the final-state favor. Due to this last production channel, any combination of final-state flavors and chiralities are possible at leading order.
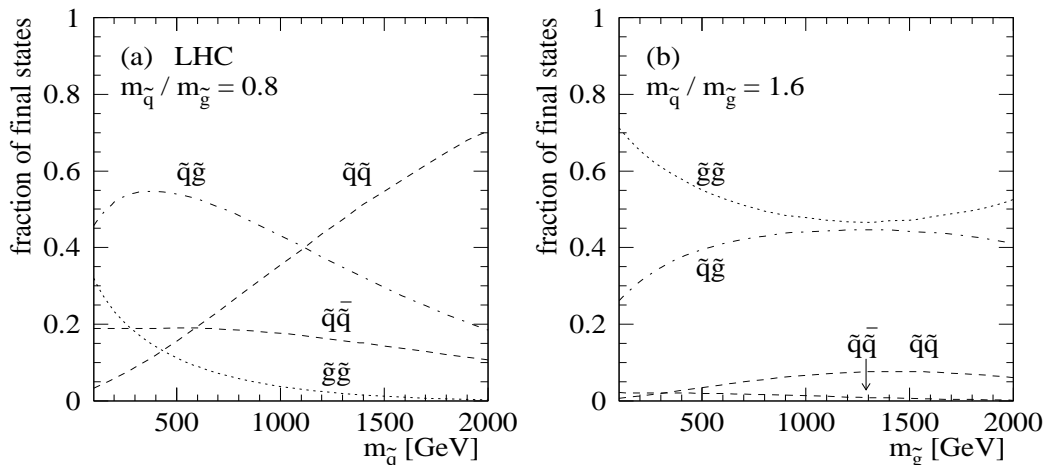
Figure 3.5: The relative yields of light-flavor squarks and gluinos at the 14 TeV LHC. The squark masses are set to a common value $m_{\tilde{q}}$. The ratio $m_{\tilde{q}}/m_{\tilde{g}}$ is chosen to be 0.8 (1.6) left (right) plot. Renormalization and factorization scale are set to $\mu = m_{\tilde{q}}$ for squarks, $\mu = m_{\tilde{g}}$ for gluinos and $\mu = (m_{\tilde{q}} + m_{\tilde{g}})/2$ for squark–gluino pairs [18].

$\tilde{t}\tilde{t}^*$: Stop–anti-stop production proceeds at LO in a similar way as $\tilde{q}\tilde{q}^*$ production. The only exception is that the t-channel gluino exchange is absent, due to the vanishing top-quark density inside the proton. Hence only diagonal $\tilde{t}\tilde{t}^*$ occurs at LO. Due to the non-trivial mixing and the fact that top-squarks are experimentally distinguishable to light-flavor squarks this process has to be examined separately.

$\tilde{b}\tilde{b}^*$: Sbottom–anti-sbottom production has the same production channels as $\tilde{q}\tilde{q}^*$ production. In former analysis bottom-squark production was treated for simplicity inclusively with light-flavor squark production, neglecting left-right mixing. However, in many scenarios, neglecting flavor mixing is not a good approximation. In addition, bottom-squarks are, as the top-squarks, experimentally distinguishable from light-flavor squarks.

The production of non-diagonal top-squark pairs and mixed stop–sbottom pairs is not possible at lowest order in QCD.

One might wonder, which of these processes contributing at LO QCD are most relevant, i.e. have the highest cross section. This question cannot be answered in a general way, since the production cross sections strongly depends on the sparticle masses (i.e. on the underlying parameter space), on the available c.m. energy and whether PP or $P\overline{P}$ collisions are considered. Further, the production of gluinos differs from squark production, due to the Majorana nature of the gluino and being in a color octet representation. One also has to consider that light-flavor squarks have a high multiplicity which considerably alters the $\tilde{q}\tilde{q}$ production cross section. And as already mentioned, in many models one of the stops is the lightest colored sparticle, relatively enhancing its production cross section. However, to get an idea how the relative cross section behaves when varying the masses, in Figure 3.5 one finds the relative yields for $\tilde{g}\tilde{g}$, $\tilde{q}\tilde{g}$, $\tilde{q}\tilde{q}^*$, and $\tilde{q}\tilde{q}$ production at the 14 TeV LHC for two

different ratios of $m_{\tilde{q}}/m_{\tilde{g}}$ [18]. In this scan, all light-flavor masses, including the sbottom mass, are set to a common value $m_{\tilde{q}}$. One can see that in the case of the squark being lighter than the gluino (left plot) the production of $\tilde{q}\tilde{g}$ is most significant if the squarks have low masses (in the example below 1200 GeV), while for heavier squark masses $\tilde{q}\tilde{q}$ production dominates. $\tilde{g}\tilde{g}$ production becomes almost negligible for high squark masses. This behavior changes completely when considering a scenario where the gluino is lighter than the squark. Now $\tilde{g}\tilde{g}$ and $\tilde{q}\tilde{g}$ production are most important while $\tilde{q}\tilde{q}$ and especially $\tilde{q}\tilde{q}^*$ only have a small production yield.

Since the leading order QCD cross section suffers from large renormalization and factorization scale uncertainties, higher-order corrections have to be taken into account. The next-to leading order (NLO) QCD cross sections, which are of $\mathcal{O}(\alpha_s^3)$, have been computed more than ten years ago in [18,19] and are publicly available in the code PROSPINO [106]. It was shown that the scale uncertainties are considerably reduced by taking into account the NLO corrections. While at LO the cross section increases by about 35% when changing the scale from $\mu = m$ to $\mu = m/2$, at NLO the variation is only $5 - 10\%$. Here m is the average mass of the produced particles. At NLO the dependence on the factorization scale is very mild and the residual scale dependence is dominated by α_s. To quantitatively compare the LO and NLO cross section one defines the ratio

$$K = \sigma^{\mathrm{NLO}}/\sigma^{\mathrm{LO}}, \tag{3.3}$$

usually referred to as the K-factor. Obviously, the K-factor depends on the scale chosen. For the scale $\mu \sim (0.4 \text{ to } 0.5)\, m$ one finds a ratio of $K = 1$, i.e. LO and NLO cross sections coincide. The K-factors at the scale $\mu = m$ for the various final states for different squark and gluino masses are shown in Figure 3.6. One finds that the K-factor varies in a wide range, being biggest for $\tilde{g}\tilde{g}$ production going up to $K = 2$ for heavy gluinos while for $\tilde{q}\tilde{q}$ the NLO contribution rises the LO cross section by only a few percent up to 20%, depending on the precise squark/gluino mass ratio.

The origin of such large higher-order QCD corrections in hadro-production of heavy colored particles is well known, since it is related to universal QCD dynamics. As a typical pattern so-called Sudakov logarithms show up which originate from soft gluon emission in regions of phase space near the production threshold. These logarithms depend on the particle velocity $\beta^2 = (1 - 4m^2/\hat{s})$ and hence become large for c.m. energies $\sqrt{\hat{s}}$ near the threshold, $\hat{s} \simeq 4m^2$. Therefore, in order to further reduce remaining scale uncertainties, the resummation of soft gluon emission from squark and gluino hadro-production was performed at next-to-leading-logarithmic (NLL) accuracy [20–23], for all processes contributing at LO QCD. The relative NLL K-factor is shown in Figure 3.7 for various production processes. At the LHC, the scale uncertainty is reduced in the case of $\tilde{g}\tilde{g}$ production, while the improvement for the other processes is quite mild. For squark and gluino masses below 1 TeV the NLO cross section increases due to NLL resummation by $1 - 5\%$ for $\tilde{g}\tilde{g}$, $\tilde{q}\tilde{g}$ and $\tilde{q}\tilde{q}^*$ production and is less than 1% in the case of $\tilde{q}\tilde{q}$, $\tilde{t}\tilde{t}$ and $\tilde{b}\tilde{b}$ production. For very heavy squarks and gluinos i.e. masses between 2000 and 3000 TeV the NLL resummation gets more pronounced and can become up to 35% (18%) of the NLO cross section in the case of $\tilde{g}\tilde{g}$ ($\tilde{q}\tilde{g}$)
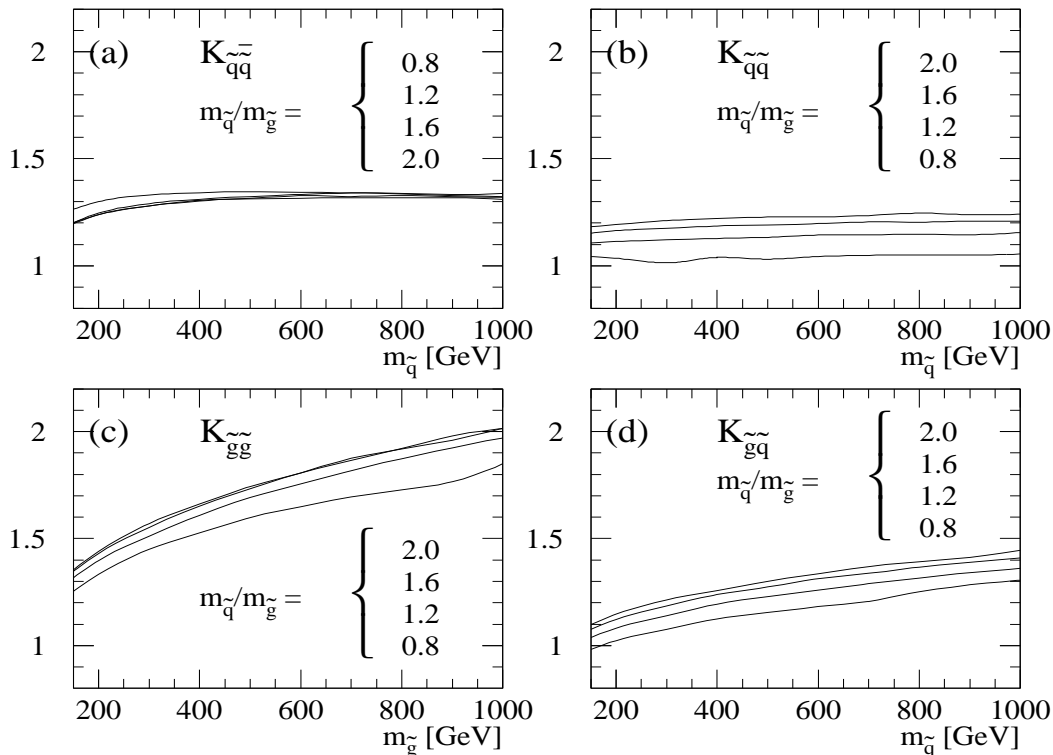
Figure 3.6: The K-factors for the 14 TeV LHC at the scale $\mu = m$ [18].

production. Such a behavior is expected due to the large Sudakov logarithms at threshold. A second approach to reduce remaining scale uncertainties was done by taking approximate next-to-next-to-leading order (NNLO) QCD effect into account [24]. In practice, Sudakov resummation was employed to generate approximate NNLO QCD predictions which are accurate in all $\log \beta$-enhanced terms at two loops. Moreover, the complete two-loop Coulomb corrections as well as the exact dependence on the renormalization and factorization scale are included. However, this was only performed for $\tilde{q}\tilde{q}^*$ production. These results are compatible to the ones obtained by NLL resummation.

For completeness one should mention that the strong production of non-diagonal stop- and sbottom-pairs, $\tilde{t}_\alpha \tilde{t}_\beta$ and $\tilde{b}_\alpha \tilde{b}_\beta$ for $(\alpha \neq \beta)$, require at least one-loop diagrams and are studied in [107, 108]. These contributions are of $\mathcal{O}(\alpha_s^4)$ and therefore suppressed via the coupling constant and powers of inverse squark masses stemming from the loop integral. Additionally these contributions suffer from large scale uncertainties induced by the scale choice of α_s.
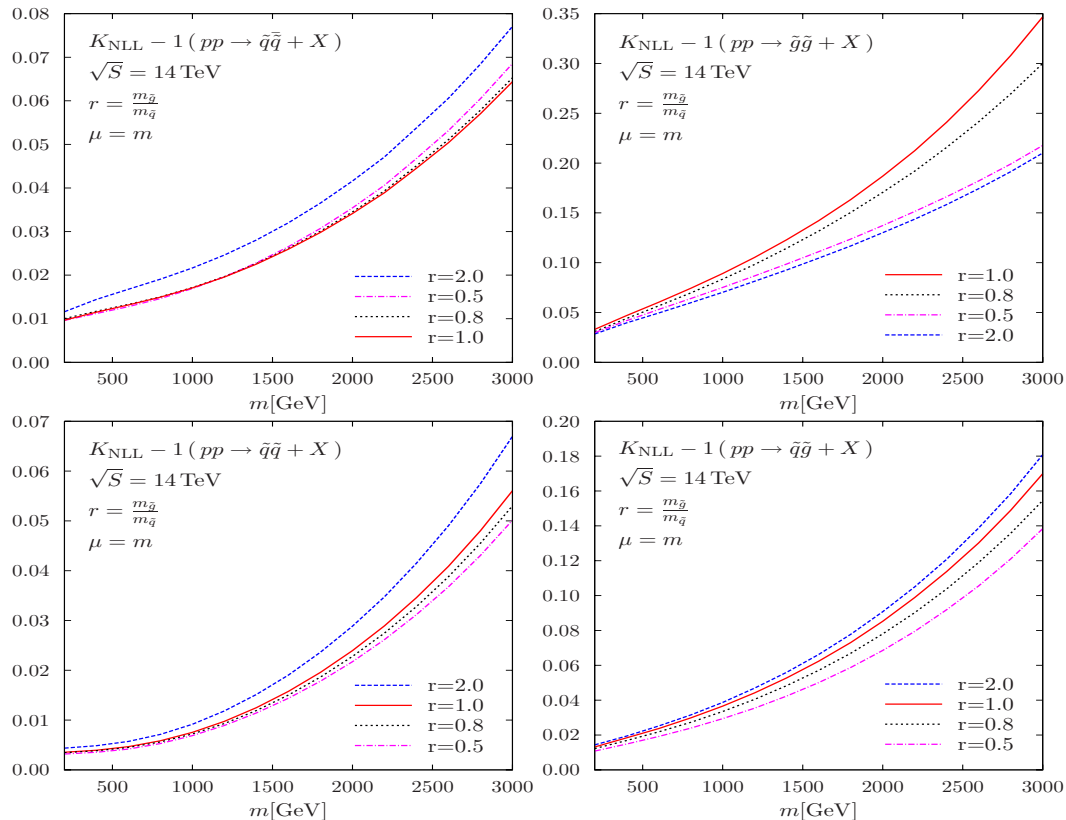
Figure 3.7: The relative NLL K-factor $K_{\mathrm{NLL}} - 1 = \sigma^{\mathrm{NLL+NLO}}/\sigma^{\mathrm{NLO}} - 1$ for squark and gluino pair-production processes at the Tevatron as a function of the average sparticle mass m. Shown are results for various mass ratios $r = m_{\tilde{g}}/m_{\tilde{q}}$ [22]. $\sigma^{\mathrm{NLL+NLO}}$ denotes the sum of NLL-resummed cross section matched with the complete NLO result.

3.2.2 Electroweak Contributions

In addition to the production of squarks and gluinos via the strong interaction, also electroweak (EW) production mechanisms are possible. For squark–(anti-)squark final states, EW contributions are already present at tree-level, and due to the chiral nature of the EW couplings also non-diagonal squark–pairs can be produced, in contrast to squark-pair production at LO, $\mathcal{O}(\alpha_s^2)$. Even though EW contributions are usually expected to be small due to the roughly ten times smaller EW coupling constant α, these contributions can have a relatively high impact on the total cross section. In particular processes with non-vanishing QCD–EW interference terms at tree-level, which are of $\mathcal{O}(\alpha_s\alpha)$, can get a significant production yield.

EW contributions to squark production was first considered in [107], focusing on flavor observables. A consistent treatment of all light-flavor squark-pair processes contributing at LO EW is given in [25].[1] The size of EW contributions strongly depends on the chirality

---

[1]However, the analytic results of [25] contain some incorrect color factors, giving wrong results for the $\mathcal{O}(\alpha^2)$ contribution. For $\tilde{q}\tilde{q}$ production the impact of these wrong factors is rather small, while for $\tilde{q}\tilde{q}^*$

of the produced squarks. LO EW contributions were found to be quite small in the case of squark production with at least one right-handed squark. However, considering only left-handed squark production, one finds corrections to the LO cross section that amount to 10% to 20% for typical mSUGRA scenarios. The main part contributing to the EW cross section, is given by the non-vanishing interference terms of $\mathcal{O}(\alpha_s\alpha)$. Investigating left-handed squark production exclusively is justified by the fact that squarks of different chirality can be distinguished experimentally.

EW contributions to the production of third-generation squarks have further been considered by [108]. Besides the loop-induced contributions for non-diagonal stop/sbottom production, also Higgs-boson exchange at tree level owing to initial-state bottom-quarks is taken into account. However, contributions due to Higgs-boson exchange only become significant for resonant intermediate Higgs bosons or for a negative μ parameter, eq. (2.26c), which is disfavored by the anomalous magnetic moment of the muon, $(g-2)_\mu$.

Finally, one also has to consider the electroweak contribution at NLO EW, $\mathcal{O}(\alpha_s^2\alpha)$, which is formally of the same order as the NNLO and NLL-resummed QCD correction discussed last section and hence are expected to have contributions of the same size. NLO EW contributions have in general a non-trivial structure, since they can arise via various interference contributions, as well for the one-loop contribution as for the real emission matrix elements. Since the EW interaction is not flavor diagonal and distinguishes between different chiralities, many production channels have to be treated separately. This leads to effects at NLO EW which strongly depend on the initial- and final-state particle flavor and chirality. The NLO EW contributions for gluino-pair production, diagonal squark–anti-squark production, diagonal stop–anti-stop production and squark–gluino production have been investigated in [26–29]. Two of the remaining processes, namely squark–squark and sbottom–anti-sbottom production are investigated within this thesis and partly published in [30–32]. As expected the analysis shows that the NLO EW contributions are competitive with QCD corrections beyond NLO. Interestingly, NLO EW contributions often tend to be more important for processes where the impact of NLO QCD corrections is rather small and less important for processes that get huge QCD corrections. For example, on the one hand, $\tilde{g}\tilde{g}$ production has a NLO K-factor of $1.5 - 2$, cf. Figure 3.6, and at NLL it gets corrections of $5 - 35\%$, depending on the gluino mass, while the NLO EW contributions are completely negligible. On the other hand, $\tilde{q}\tilde{q}$ production gets only mild corrections at NLO with a K-factor of $1.1 - 1.2$ and NLL corrections of less than 1% for squark masses below 1 TeV, while the EW contributions up to $\mathcal{O}(\alpha_s^2\alpha)$ can be as high as 20%. Moreover, for processes with huge tree-level contributions originating from QCD–EW interferences, NLO EW contributions are needed to reduce the scale uncertainties and make the electroweak prediction reliable. Further details on this topic will be given in the following sections, when the production of squark pairs is considered.

A summary of the status of higher-order corrections for the various squark and gluino production processes, including references, is given in Table 3.1. As one can see from the

---

production the EW contribution to the cross section even changes sign.

		α_s^2	α_s^3	NLL	NNLO	LO(α_s^4)	$\alpha_s\alpha$	α^2	$\alpha_s^2\alpha$
	$\tilde{g}\,\tilde{g}$	[17]	[18]	[20–22]	×	–	–	–	[29]
	$\tilde{g}\,\tilde{q}_\alpha$	[17]	[18]	[22]	×	–	–	–	[28]
$\alpha,\beta \in \{1,2\}$	$\tilde{q}_\alpha\,\tilde{q}_\alpha^*$	[17]	[18]	[20–22]	[24]	–	[25]	[25]	[27]
	$\tilde{b}_\alpha\,\tilde{b}_\alpha^*$	[17]	[18]	[23]	×	–	[108]	[108]	[32]
	$\tilde{t}_\alpha\,\tilde{t}_\alpha^*$	[17]	[19]	[23]	×	–	–	[108]	[26]
	$\tilde{q}_\alpha\,\tilde{q}'_\beta$	[17]	[18]	[22]	×	–	[25]	[25]	[30]
	$\tilde{t}_\alpha\,\tilde{b}_\beta^{(*)}$	–	–	–	–	–	–	[107, 108]	–
$q_\alpha \neq q'_\beta$	$\tilde{q}_\alpha\,\tilde{q}'^*_\beta$	[17]	[18]	[23]	×	–	[25]	[25]	×
	$\tilde{b}_\alpha\,\tilde{b}^{(*)}_\beta$	[17]	[18]	–	–	[107, 108]	–	[107, 108]	–
	$\tilde{t}_\alpha\,\tilde{t}^{(*)}_\beta$	–	–	–	–	[19, 107, 108]	–	[107, 108]	–

Table 3.1: Summary of all squark and gluino production processes and status of higher-order corrections. Given are the corresponding references. A "−" indicates that this process does not contribute at the corresponding order or its contribution has been estimated as negligible, while "×" indicates that it has not been calculated yet. NLL refers to next-to leading log resummation as described in the text and NNLO are approximate next-to-next-to-leading order results. In contrast LO(α_s^4) only refers to processes that are LO one-loop induced.

last column, the processes presented in this dissertation, i.e. the NLO EW contributions to squark–squark production and to sbottom–anti-sbottom production, provide an important contribution to the knowledge of all relevant EW contributions.

4 Colored SUSY Particle Production at Electroweak NLO

The NLO EW contributions to colored particle production are given by the radiative corrections of $\mathcal{O}(\alpha_s^2\alpha)$. At this order in perturbation theory, one has to take one-loop virtual corrections into account, as well as real photon, gluon, and quark radiation. When calculating higher-order corrections, one has to deal with ultraviolet (UV) divergences as well as infrared (IR) and collinear singularities. The UV divergences arise from very short distance physics, i.e. infinite momentum configurations. For renormalizable theories they can consistently be absorbed by redefining the fundamental parameters of the theory, usually referred to as renormalization. The IR singularities originate from the radiation or exchange of massless particles with arbitrary small energy, while collinear singularities arise from the splitting of a massless particle into two massless (virtual or real) collinear particles. However, for inclusive enough observables, these so called mass singularities cancel order-by-order in perturbation theory, i.e. after combining virtual and real contributions.

In this chapter, the technical details needed in order to perform a NLO EW calculation are given. At first, the basic principles of particle scattering are reviewed in Section 4.1. In Section 4.2 it is shown how hadronic cross sections can be calculated via factorization of long- and short-distance physics. Afterwards, the technical issues needed in order to obtain the (finite) cross section at $\mathcal{O}(\alpha_s^2\alpha)$ to colored SUSY particle production are given. In Section 4.3 and 4.4 the regularization and renormalization procedure used in this work are presented. The treatment of mass singularities due to massless photons, gluons, and quarks is discussed in Section 4.5. Finally, the parametrization for the numerical integration for the four and five particle phase-space is given in Section 4.6. It is shown how the final-state kinematics can be parametrized in order to take the singular behavior into account.

4.1 Preliminaries

In this section, the basic principles needed for calculating cross sections at high-energy colliders are summarized and some useful notation used throughout this work is introduced. Further details can be found in standard textbooks, e.g. in [109–112].

Generally, cross sections are obtained from the matrix element of the scattering matrix also called the S matrix, which transforms incoming states into outgoing states. The formal definition of S is given by the infinite-time limit of the time-evolution operator T in the interaction picture and is related to the interaction Lagrangian $\mathcal{L}_I$ via the formal power series

$$S = T \exp\left[\mathrm{i} \int \mathrm{d}^4 x \, \mathcal{L}_I \right] . \tag{4.1}$$

The probability for an incoming state $|i\rangle$ to evolve into an outgoing state $|f\rangle$ is given by the absolute square of the S matrix element $\langle f|S|i\rangle$. This definition also contains the trivial case of no scattering at all. Hence, for in- and outgoing momentum eigenstates $|i\rangle$ and $|f\rangle$ with momenta p_i and p_f one defines the invariant matrix element $\mathcal{M}_{fi}$ by

$$\langle f|S|i\rangle = \langle f|i\rangle + \mathrm{i}(2\pi)^4 \delta^{(4)}(p_i - p_f)\mathcal{M}_{fi}\,. \tag{4.2}$$

The delta function reflects momentum conservation of the scattering processes. The cross section σ is defined as the number of scattering events divided by the flux of the incoming particles. For two incoming particles with momenta p_1 and p_2 and masses m_1 and m_2 scattering into $n-2$ particles with momenta $p_3, \ldots, p_n$, the differential cross section is given by the squared invariant matrix element divided by the flux of the incoming particles and multiplied with the phase-space density of the outgoing particles,

$$\mathrm{d}\sigma = \frac{(2\pi)^4 \delta^{(4)}(p_1 + p_2 - \sum_{i=3}^n p_i)}{4\sqrt{(p_1 p_2)^2 - m_1^2 m_2^2}} |\mathcal{M}_{fi}|^2 \frac{\mathrm{d}^3 \mathbf{p}_3}{(2\pi)^3 2E_3} \cdots \frac{\mathrm{d}^3 \mathbf{p}_n}{(2\pi)^3 2E_n}\,. \tag{4.3}$$

In the case of two final-state particles, it is common to parameterize the kinematics in terms of the Mandelstam variables,

$$s = (p_1 + p_2)^2, \quad t = (p_1 - p_3)^2, \quad u = (p_1 - p_4)^2. \tag{4.4}$$

In terms of these variables, the phase-space integration takes a simple form and the differential cross section can be written as

$$\mathrm{d}\sigma = |\mathcal{M}_{fi}|^2 \frac{\mathrm{d}t}{16\pi s^2}\,. \tag{4.5}$$

In many cases, initial and final states are degenerate, and one has to average over the initial-state quantum numbers and sum over the final-state quantum numbers. In practice, these quantum numbers are often given by color and spin, since it is not possible to measure the color quantum number of colored particles, and one often also is not interested in the precise spin-state of the particles. In this case, the differential cross section is given in terms of the squared matrix element, averaged over initial-state spin and color and summed over final-state spin and color,

$$\mathrm{d}\sigma = \overline{\sum} |\mathcal{M}_{fi}|^2 \frac{\mathrm{d}t}{16\pi s^2}\,. \tag{4.6}$$

In order to calculate cross sections for the scattering of elementary particles, we use the framework of perturbation theory. In this approach, the gauge couplings are used as ordering parameters of a perturbative expansion. Matrix elements, and hence cross sections, can then be calculated order-by-order in the gauge couplings. In particular in the SM and the MSSM, the ordering parameters are the strong coupling constant α_s and the fine-structure constant α of the electromagnetic interaction. In the following we will denote matrix elements calculated at a given order $\alpha_s^a \alpha^b$ by $\mathcal{M}^{a,b}$. In the same way $\sigma^{a,b}$ denotes the cross section at order $\alpha_s^a \alpha^b$.
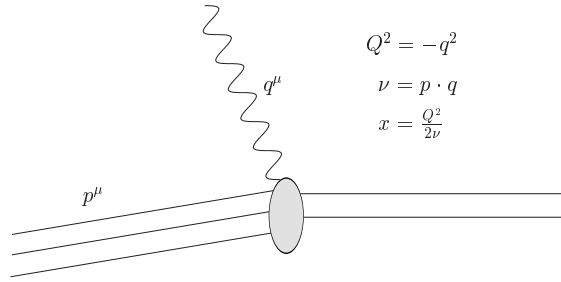
Figure 4.1: Scattering of partons inside a hadron. q is the momentum transfer and p the momentum of the hadron.

4.2 Hadronic Cross Section, Factorization, and the PDFs

In the definition of the invariant matrix element (4.2), the initial and final states are asymptotic states. However, when considering processes with $SU(3)_C$ color charged particles in the initial and/or final state, no such asymptotic states for elementary particles can be formulated due to color confinement of QCD. In order to make theoretical predictions at hadron colliders, the cross section is factorized into a long-distance part and a short-distance part [105], cf. Figure 3.4. The long-distance part contains the physics in the regime where the coupling constant of QCD becomes strong and hence cannot be calculated in perturbation theory. However, at short distances, i.e. high energies, the constituents of the hadrons can approximately be described by free point-like particles, and the concepts of the parton model can be applied [113, 114]. The basic assumption of the *naive* parton model is that at high energies the hadron acts like an ensemble of free massless particles, the partons. The momentum of the hadron $\mathbf{p}$ is distributed over the parton momenta $\hat{\mathbf{p}}_i$, with i labeling the parton. The scattering is considered in the infinite-momentum frame in which the mass of the hadron can be neglected. In this limit the hadron, and therefore also the partons, can be regarded as moving at speed of light and the parton i carries the fraction ξ_i of the four-momentum of the hadron, $\hat{p}_i^\mu = \xi_i p^\mu$. Defining the kinematics of the scattering as depicted in Figure 4.1, one finds that in the Bjorken limit, defined by $Q^2, \nu \to \infty$ with $x = Q^2/(2\nu)$ fixed, the on-shell constraint for the outgoing parton in the infinite-momentum frame implies that $\xi_i = x$. The cross section can then be calculated by the incoherent sum of the parton–parton cross section $\hat{\sigma}$ multiplied by the parton distribution function (PDF) $f_i^H(x)$, where $f_i^H(x)$ is the probability density to find a parton i with momentum fraction x inside the hadron H. The hadron–hadron cross section σ of hadron A and B is hence given by summing over all partons ζ_i and integrating over all momentum fractions x_i,

$$\sigma = \sum_{\zeta_1, \zeta_2} \int_0^1 \mathrm{d}x_1 \int_0^1 \mathrm{d}x_2 \, \frac{\hat{\sigma}_{\zeta_1, \zeta_2}}{1 + \delta_{\zeta_1, \zeta_2}} \left(f_{\zeta_1}^A(x_1, \mu) f_{\zeta_2}^B(x_2, \mu) + f_{\zeta_1}^A(x_2, \mu) f_{\zeta_2}^B(x_1, \mu) \right) \qquad (4.7)$$

The PDFs contain the long-distance physics and hence cannot be calculated in perturbation theory. However, these functions are universal and can be extracted from experiments like deep inelastic lepton–hadron scattering. The key point for the extraction of the PDFs is that

the double differential lepton–hadron cross section can be factorized into a leptonic and a hadronic piece

$$\frac{\mathrm{d}\sigma}{\mathrm{d}x\mathrm{d}y} \propto L_{\alpha\beta}W^{\alpha\beta}, \tag{4.8}$$

where the structure of the leptonic tensor $L_{\alpha\beta}$ is completely determined by the EW interaction and $y = (p \cdot q)/(k \cdot p)$ with k being the momenta of the incoming lepton. The hadronic tensor has the following Lorentz decomposition

$$W^{\alpha\beta} = \left(g^{\alpha\beta} - \frac{q^\alpha q^\beta}{q^2}\right) F_1(x, Q^2) + \left(p^\alpha + \frac{1}{2x}q^\alpha\right)\left(p^\beta + \frac{1}{2x}q^\beta\right)\frac{1}{\nu}F_2(x, Q^2), \tag{4.9}$$

with the structure functions F_1 and F_2. In the parton model, the structure function is directly related to the PDF. Assuming photon exchange only, one finds for a spin-$1/2$ parton of charge e_q

$$F_2 \equiv e_q^2\, x\, q(x)\,. \tag{4.10}$$

In the naive parton model the structure function and hence the PDFs scale, i.e. they depend only on x and are independent of Q and the Callan–Gross relation $F_2 = 2\, x\, F_1$, a characteristic of the spin-$1/2$ nature of the constituents, is recovered.

In the SM the partons are identified with the quarks and gluons. The quark and anti-quark distribution functions, $q(x)$ and $\bar{q}(x)$, can be extracted directly from the structure function of deep-inelastic scattering experiments, whereas the gluon distribution function $g(x)$ is obtained by the condition that the hadron momentum equals the sum of the momenta of the partons,

$$\sum_q \int_0^1 \mathrm{d}x\, x\, [q(x) + \bar{q}(x)] + \int_0^1 \mathrm{d}x\, x\, g(x) = 1\,. \tag{4.11}$$

In contrast to the naive parton model above, when applying it to QCD one finds that the scaling is broken by logarithms of Q^2. These come from the fact that a quark can emit a gluon and acquire large transverse momentum k_T with probability proportional to $\alpha_s \mathrm{d}k_T^2/k_T^2$ at large k_T^2, contradicting the basic assumption of the parton model that $\hat{p} \propto p$. This integral breaks up at the kinematical limit $k_T^2 \sim Q^2$ and gives a contribution proportional to $\alpha_s \log Q^2$ to the quark distribution function. Including higher-order contributions to the structure function F_2, in particular gluon radiation off a quark leg, one finds the following expression

$$F_2(x, Q^2) = x\sum_{q,\bar{q}} e_q^2\left[q_0(x) + \frac{\alpha_s}{2\pi}\int_x^1 \frac{\mathrm{d}\xi}{\xi}q_0(\xi)\left\{P\left(\frac{x}{\xi}\right)\log\frac{Q^2}{\kappa^2} + C\left(\frac{x}{\xi}\right)\right\} + \dots\right]. \tag{4.12}$$

P is known as the splitting function and C is a rational function. When calculating F_2 one has to regularize the long-distance physics that are determined by non-perturbative effects. They arise for $k_T^2 \to 0$ and are called collinear singularities. In the expression above this was achieved by introducing a small momentum cut-off κ^2. The "bare" distribution q_0 in (4.12) is not a measurable quantity. Absorbing the collinear singularities into the bare distribution

at a factorization scale μ, one can define a renormalized distribution $q(x, \mu)$ by

$$q(x, \mu^2) = q_0(x) + \frac{\alpha_s}{2\pi} \int_x^1 \frac{\mathrm{d}\xi}{\xi} q_0(\xi) \left\{ P\left(\frac{x}{\xi}\right) \log \frac{\mu^2}{\kappa^2} + C'\left(\frac{x}{\xi}\right) \right\} + \dots . \qquad (4.13)$$

$F_2(x, Q^2)$ can be written in terms of (4.13). For $C' = C$ it is given by

$$F_2(x, Q^2) = x \sum_{q,\bar{q}} e_q^2 \left[q(x, \mu^2) + \frac{\alpha_s}{2\pi} \int_x^1 \frac{\mathrm{d}\xi}{\xi} q(\xi, \mu^2) \left\{ P\left(\frac{x}{\xi}\right) \log \frac{Q^2}{\mu^2} \right\} + \dots \right] . \qquad (4.14)$$

As before, the distributions $q(x, \mu^2)$ cannot be calculated in perturbation theory by first principles. However, it can be determined from structure-function data at any particular scale, since

$$F_2(x, Q^2) = x \sum_{q,\bar{q}} e_q^2 \, q(x, Q^2) . \qquad (4.15)$$

The factorization provides a prescription how to deal with the collinear singularities, however there is an arbitrariness in how the finite contributions C' of (4.13) are treated. How much of the finite contribution is factored out defines the "factorization scheme". In (4.14) all of the finite contribution was absorbed into the quark distribution, corresponding to the DIS scheme. A more common choice is the $\overline{\text{MS}}$ scheme, in which in addition to the divergent piece regularized in dimensional regularization, only a universal contribution, $\log(4\pi) - \gamma_E$ is absorbed.[1] It is important that once a scheme has been fixed, it has to be used in all cross-section calculations.

The quark distribution function gets also a contribution from the splitting of a gluon in a quark–anti-quark pair. In the same way, the gluon distribution function gets QCD corrections from gluon–gluon splitting and gluon radiation off a quark leg. After extracting the distribution functions at a given scale, one can use the fact that the structure function (4.14) has to be independent of the factorization scale μ to determine the scale dependence. These differential equations, determining the scale dependence of the distribution functions are called the Dokshitzer–Gribov–Lipatov–Altarelli–Parisi (DGLAP) equations [115–118]. The DGLAP equations have been calculated up to NNLO QCD [119–125]. At LO QCD they are given by

$$\mu^2 \frac{\partial}{\partial \mu^2} q_i(x, \mu^2) = \frac{\alpha_s}{2\pi} \int_x^1 \frac{\mathrm{d}z}{z} \left(P_{qq}(z) \, q_i(\frac{x}{z}, \mu^2) + P_{qg}(z) \, g(\frac{x}{z}, \mu^2) \right) , \qquad (4.16\text{a})$$

$$\mu^2 \frac{\partial}{\partial \mu^2} g(x, \mu^2) = \frac{\alpha_s}{2\pi} \int_x^1 \frac{\mathrm{d}z}{z} \left(P_{qg}(z) \sum_j q_j(\frac{x}{z}, \mu^2) + P_{gg}(z) \, g(\frac{x}{z}, \mu^2) \right) , \qquad (4.16\text{b})$$

---

[1] Further details on dimensional regularization and the $\overline{\text{MS}}$ scheme are postponed to Section 4.3 f.

with the splitting functions

$$P_{qq}(z) = C_F \left[\frac{1+z^2}{(1-z)_+} + \frac{3}{2}\delta(1-z) \right] , \qquad (4.17a)$$

$$P_{qg}(z) = \frac{1}{2} \left[z^2 + (1-z)^2 \right] , \qquad (4.17b)$$

$$P_{gq}(z) = C_F \left[\frac{1+(1-z)^2}{z} \right] , \qquad (4.17c)$$

$$P_{gg}(z) = 2C_A \left[\frac{z}{(1-z)_+} + \frac{(1-z)(1+z^2)}{z} + \delta(1-z)\frac{11C_A - 2n_f}{6} \right] . \qquad (4.17d)$$

The $[\ldots]_+$ description is defined such that the integral with any sufficiently smooth function g is given by

$$\int_0^1 \mathrm{d}x \, [f(x)]_+ \, g(x) = \int_0^1 \mathrm{d}x f(x) \left[g(x) - g(1) \right] . \qquad (4.18)$$

When considering EW contributions at hadron colliders, large logarithmic corrections proportional to $\alpha \log(Q^2/m^2)$ arise from photons emitted off incoming quark lines, the analogue of the $\alpha \log(Q^2/m_e^2)$ initial-state corrections in e^+e^- collisions. Taking these explicitly into account would require a precise knowledge of the incoming quark masses. Furthermore, due to the high Q^2 values probed at hadron colliders, one should in principle resum these logarithms. Instead of doing so, one can also use the fact that the factorization theorem of QCD also applies in QED and absorb such photon-induced collinear singularities into the PDFs. In doing so, first of all, the normal DGLAP evolution equations are slightly modified, since the photon carries away some of the quark momenta. This leads to isospin violation since up- and down-type quarks evolve differently. Second, a "photon distribution" of the hadron $\gamma(x, \mu^2)$ is generated. This gives rise to new production channels, with photons in the initial state. Taking QED evolution of the partons into account, the DGLAP equations (4.16) get the following $\mathcal{O}(\alpha)$ contributions,

$$\mu^2 \frac{\partial}{\partial \mu^2} q_i(x, \mu^2) = \frac{\alpha}{2\pi} \int_x^1 \frac{\mathrm{d}z}{z} \left(\widetilde{P}_{qq}(z) \, e_i^2 q_i(\frac{x}{z}, \mu^2) + P_{q\gamma}(z) \, e_i^2 \gamma(\frac{x}{z}, \mu^2) \right) , \qquad (4.19a)$$

$$\mu^2 \frac{\partial}{\partial \mu^2} \gamma(x, \mu^2) = \frac{\alpha}{2\pi} \int_x^1 \frac{\mathrm{d}z}{z} \left(P_{\gamma q}(z) \sum_j e_j^2 q_j(\frac{x}{z}, \mu^2) + P_{\gamma\gamma}(y) \gamma(\frac{x}{z}, \mu^2) \right) , \qquad (4.19b)$$

where,

$$\begin{aligned} \widetilde{P}_{qq} &= C_F^{-1} P_{qq} , & P_{\gamma q} &= C_F^{-1} P_{gq} , \\ P_{q\gamma} &= 2P_{qg} , & P_{\gamma\gamma} &= -\frac{2}{3} \sum_i e_i^2 \delta(1-y) . \end{aligned} \qquad (4.20)$$

Currently, the only PDF set that consistently determines a new set of QED corrected partons from an overall best fit to data is the MRST2004QED [126]. The effect on the quark distribution was found to be small when comparing with NNLO QCD contributions on the distribution. For obvious reasons, the gluon evolution is largely unaffected by the QED corrections. Figure 4.2 shows the parton distribution function of the proton calculated at
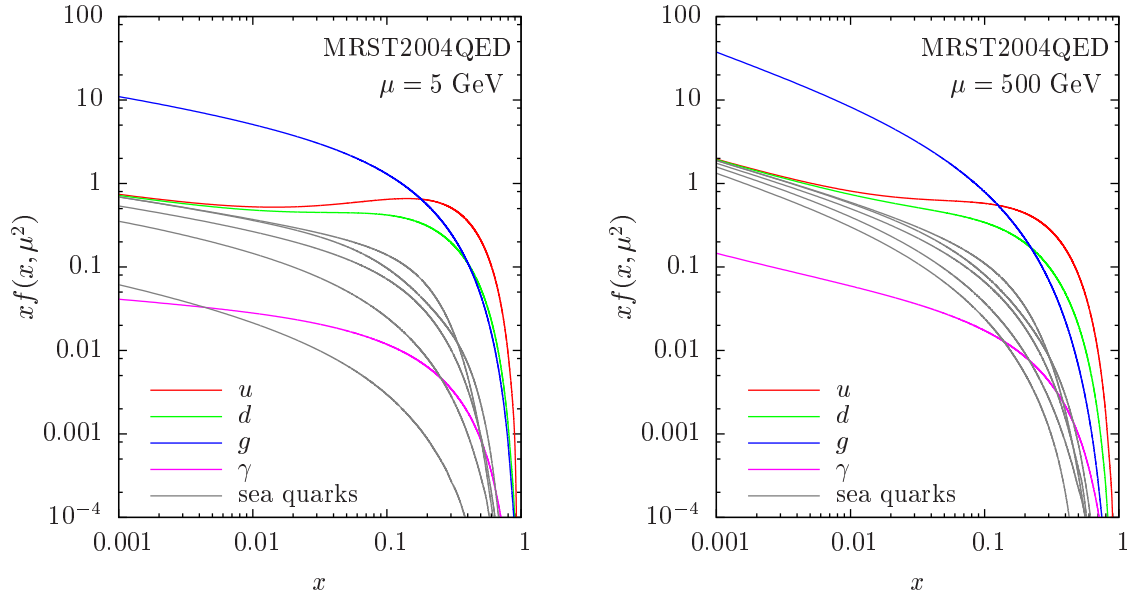
Figure 4.2: Parton distribution functions of the proton for the MRSTQED set at $\mu = 5$ GeV (left) and $\mu = 500$ GeV (right). The sea-quark distributions correspond to $\bar{u}$, $\bar{d}$, s, c, b, with the b distribution being the smallest. The photon distribution tends to a significant yield for low values of x. The difference between the two plots is due to scaling violations, calculated at NLO QCD + LO QED.

NLO QCD + LO QED, resulting from the global fit performed by the MRST collaboration for two different factorization scales. For $x < 0.1$ one finds mainly gluons inside the proton, while for $x > 0.1$ the up- and down-quarks have the highest yield. The sea quarks and the photon distribution become relatively more important for low values of x and at high factorization scales. The bottom distribution, which is the sea quark with the smallest yield, is strongly suppressed at $\mu = 5$ GeV, while for $\mu = 500$ GeV it gets close to the other sea quarks. This is not surprising, since the lower scale is of the scale of the bottom-quark mass itself, while for high scales $\mu \gg m_b$ differences due to the masses become small.

For heavy final-state particles, the production threshold has to be taken into account. It is convenient to define $(\tau, x) = (x_1 x_2, x_1)$. With this definition, the partonic c.m. energy $\hat{s}$ is related to the hadronic c.m. energy via

$$\hat{s} = \tau S. \tag{4.21}$$

For two massive particles in the final state with masses m_3 and m_4, the production threshold is given by $\tau = \tau_0 = (m_3 + m_4)^2/S$. Putting all together, the hadronic cross section at $\mathcal{O}(\alpha_s^a \alpha^b)$, is given by

$$\sigma^{a,b}(S) = \sum_{\xi_i \xi_j} \int_{\tau_0}^1 d\tau \frac{dL_{\xi_i \xi_j}}{d\tau} \hat{\sigma}_{\xi_i, \xi_j}^{a,b}(\hat{s}), \tag{4.22}$$

with the parton luminosity

$$\frac{\mathrm{d}L_{\xi_i \xi_j}}{\mathrm{d}\tau} = \frac{1}{1 + \delta_{\xi_i \xi_j}} \int_\tau^1 \frac{\mathrm{d}x}{x} \left[f_{\xi_i}^A\left(\frac{\tau}{x}, \mu\right) f_{\xi_j}^B(x, \mu) + f_{\xi_i}^A(x, \mu) \, f_{\xi_j}^B\left(\frac{\tau}{x}, \mu\right) \right] . \qquad (4.23)$$

$f_{\xi_i}^A$ denotes the parton distribution function for a parton ξ_i in hadron A. One has to take into account that a parton ξ_i with momentum fraction x can evolve from hadron A as well as from hadron B. The Kronecker-delta in the denominator prevents double counting for the case $\xi_i = \xi_j$.

The LO and NLO QCD cross sections described in Section 3.2 are in this nomenclature given by $\sigma^{2,0}$ and $\sigma^{3,0}$, respectively. The LO EW contributions are labeled by $\sigma^{0,2}$ and $\sigma^{1,1}$, the latter being the QCD–EW interference contribution, while the NLO EW contributions are given by $\sigma^{2,1}$.

4.3 Regularization

In order to consistently treat UV divergences and IR singularities that appear in the loop momenta and phase-space integration, one has to define a regularization procedure. These are purely mathematical prescriptions with no physical meaning. The singular or divergent parts manifest by some parameter introduced by the prescription and are recovered in specific limits of these parameters. This allows for an analytical treatment of the UV divergences and IR singularities. The former can then be consistently removed by the concept of renormalization (cf. Section 4.4), while the latter cancel in sufficient inclusive observables (cf. Section 4.5). However, care has to be taken in order to obtain a regularized amplitude that respects all the underlying symmetries of the theory. This can be achieved either by taking a regularization scheme that preserves the symmetry relation by itself, or if the symmetry is broken, by adding a (unique) symmetry restoring contribution to the amplitude. The basic symmetry that has to hold in supersymmetric theories are the Slavnov–Taylor identities, which incorporate the gauge symmetries and supersymmetry [127, 128]. The most naive attempt to regularize the divergent integrals is imposing a cutoff on the momenta. However, this already spoils QED gauge invariance. A more sophisticated method is the Pauli–Villars regularization prescription, introducing some fictitious fields whose masses regularize the divergent integral. However, several sets of fields would be necessary and this regularization method also potentially spoils gauge invariance of non-Abelian gauge symmetries. The regularization procedures applied in this work are dimensional regularization and dimensional reduction in order to regularize the UV divergences. Soft and collinear singularities are regularized via mass regularization, i.e. giving a fictitious mass to the massless particles.

Dimensional Regularization

In dimensional regualrization (DREG) the calculations are performed in D instead of 4 dimensions [35, 129]. A precise definition of dimensional regularization can be found in [130]. It is based on the observation that UV divergent loop diagrams converge for small enough

dimension D. The analytic structure of the loop integrals such as linearity, translational, and rotational invariance allows for analytic continuation to arbitrary complex values of D. In DREG spacetime coordinates, momenta, γ-matrices, and the quantum fields are treated in D dimensions. This D-dimensional space is only realized formally as an infinite dimensional vector space on which one defines a metric operator with all desired properties that resemble D-dimensional behavior. Care has to be taken when generalizing γ_5 to D spacetime dimensions. By changing the value of the dimension of the integral an arbitrary mass parameter μ has to be introduced, in order to retain the correct dimension of the coupling constant. This method of regularizing the divergent integrals has the advantage that it respects Lorentz and gauge invariance. The UV divergences manifest themselves as poles at integer values of D. At one loop, one finds that in the limit $D \to 4$ all divergent integrals have a part proportional to

$$\Delta = \frac{1}{\epsilon} - \gamma_E + \log 4\pi \,, \qquad D = 4 - 2\epsilon \,. \tag{4.24}$$

However, DREG explicitly breaks supersymmetry since the number of degrees of freedom of gauge bosons and gauginos does not match for $D \neq 4$.

Dimensional Reduction

Dimensional reduction (DRED) is a variant of DREG proposed in order to avoid direct supersymmetry breaking [131]. Originally, in DRED only momenta are treated in D dimensions whereas γ-matrices and gauge fields remain ordinary 4-vectors. However, this naive definition leads to mathematical inconsistencies [132]. A consistent definition of DRED is given in [133]. The idea is to realize the 4-dimensional space as a "quasi-4-dimensional" space that retains essential 4-dimensional properties but is in fact infinite-dimensional. It was shown that it is possible to construct such a space that contains the D-dimensional subspace. As in DREG, γ_5 has to be treated carefully. It was proven that DRED preserves supersymmetry at the one-loop level. A general prove to all orders is still missing.

Mass Regularization

In much the same way as for the UV divergences one finds that the IR and collinear singularities are not present for $D > 4$. Hence, they can be regularized by taking $\epsilon < 0$ in eq. (4.24). Another regularization method is given by means of mass regularization, in which the particles that cause these singularities, light-flavor quarks and massless gauge bosons, obtain a fictitious mass. All symmetries are preserved as long as no gauge-boson self-interactions are considered. This is the case for all processes considered in this work.

4.4 Renormalization

When performing a calculation beyond tree level, higher-order contributions often have divergent parts. After regularizing these, they have to be absorbed by redefining the bare

parameters. Moreover, the relation between the parameters in the Lagrangian and the observables changes. The original parameters, the "bare" parameters, are no longer directly related to physical quantities. In addition, also the normalization of the state vectors is modified by higher-order corrections. This has to be taken into account by renormalization of the external fields and state vectors. In a renormalizable theory all divergences can be absorbed order-by-order in perturbation theory and only a finite number of renormalization conditions is needed up to all orders. The SM as well as the MSSM are renormalizable theories [35, 127, 128].

The concept of renormalization is best illustrated when considering a theory described by only one field ψ_0 and some parameter g_0 with the Lagrangian $\mathcal{L}(\psi_0, g_0)$. Quantities with a zero as suffix are bare quantities. By measurements one can relate the bare parameter g_0 to an observable $\mathcal{O}_1 = \sigma_1(g_0)$, where σ_1 is a calculable prediction, and hence determine $g_0 = \sigma_1^{-1}(\mathcal{O}_1)$. For n observables $\mathcal{O}_i$ one has now $n - 1$ calculable predictions $\sigma_i(g_0)$ of the theory, that can be compared to measured values yielding $n - 1$ test of the theory. The parameter g_0 has no ad-hoc physical meaning. However, it can be replaced by another parameter that has a more direct physical connection. This is achieved by introducing an appropriate new parameter g and substituting $g_0 = g_0(g)$. Under this reparametrization, which can be also extended to the fields ψ_0, one has the same relations for the theoretical predictions: $\sigma_i(g) = \sigma_i(g_0(g))$. In practice one introduces well-defined quantities that have been measured with high precision as parameters of the Lagrangian. When performing higher-order corrections, in addition one has to introduce a regularization parameter ϵ whose precise form depends on the regularization scheme. Consequently the prediction is given by $\sigma_i = \sigma_i(g_0, \epsilon)$. When determining the bare parameter g_0 via σ_1 and $\mathcal{O}_1$ one obtains a value of g_0 that depends on this regularization parameter and can be ultraviolet divergent: $g_0 = \sigma^{-1}(\mathcal{O}_1, \epsilon)$. Therefore the bare quantity evidently has no direct physical meaning. However, once g_0 is fixed via σ_1 and $\mathcal{O}_1$ one gets theoretical predictions for $\sigma_i = \sigma_i(\sigma^{-1}(\mathcal{O}_1, \epsilon), \epsilon)$, $i \neq 1$, that are finite in the limit $\epsilon \to \epsilon_0$, where ϵ_0 corresponds to the absence of regularization. As a consequence, the bare quantities are regularization scheme dependent, while the relations between different observables are not. The choice of taking $\mathcal{O}_1$ to fix g_0 defines the renormalization scheme. One can define other schemes, i.e. by relating g_0 to $\mathcal{O}_2$. Then one gets predictions $\tilde{\sigma}_i = \tilde{\sigma}_i(\tilde{\sigma}^{-1}(\mathcal{O}_2, \epsilon), \epsilon)$, that can differ by higher-order corrections to σ_i, leading to unavoidable scheme dependencies of the calculation. One has to make sure that the residual renormalization scheme dependence in σ_i is small in order to make a reliable prediction for the observables $\mathcal{O}_i$.

Counterterm Formalism

An efficient way for renormalizing amplitudes is the counterterm formalism, which has the advantage that it can be formalized quite easy. It is realized via a suitable parametrization of the bare parameters by introducing multiplicative renormalization constants that include the divergent parts. For a bare Lagrangian with a field ψ_0 of mass m_0 and a coupling

constant g_0 one defines

$$g_0 = Z_g \, g \,, \qquad m_0 = Z_m \, m \,, \qquad \psi_0 = Z_\psi^{1/2} \, \psi \,. \tag{4.25}$$

Applied to the Lagrangian one obtains

$$\mathcal{L}(\psi_0, m_0, g_0) = \mathcal{L}(Z_\psi^{1/2} \, \psi, Z_m \, m, Z_g \, g) \,. \tag{4.26}$$

In perturbation theory these Z factors can be expanded into a power series of the ordering parameter, in the SM and the MSSM the coupling constants α and α_s,

$$Z_n = 1 + \delta Z_n = 1 + \sum_{i,j=1}^{\infty} \delta Z_n^{i,j} \,, \tag{4.27}$$

with $\delta Z_n^{i,j}$ being of order $\alpha_s^i \alpha^j$. Inserting this expansion in (4.25), the bare quantities are given by

$$g_0 = \left(1 + \delta Z_g^{1,0} + \delta Z_g^{0,1} + \delta Z_g^{2,0} + \delta Z_g^{0,2} + \delta Z_g^{1,1} + \dots \right) g = g + \delta g^{1,0} + \delta g^{0,1} \dots \,, \tag{4.28}$$

$$m_0 = \left(1 + \delta Z_m^{1,0} + \delta Z_m^{0,1} + \delta Z_m^{2,0} + \delta Z_m^{0,2} + \delta Z_m^{1,1} + \dots \right) m = m + \delta m^{1,0} + \delta m^{0,1} \dots \,,$$

$$\psi_0 = (1 + \frac{1}{2} \left[\delta Z_\psi^{1,0} + \delta Z_\psi^{0,1} \right] + \frac{1}{2} [\delta Z_\psi^{2,0} + \delta Z_\psi^{0,2} + \delta Z_\psi^{1,1} - \frac{1}{4} (\delta Z_\psi^{1,0} + \delta Z_\psi^{0,1})^2] + \dots) \, \psi \,.$$

This relates the bare fields and parameters ψ_0, m_0 and g_0 to the renormalized quantities ψ, m and g and the renormalization constants $\delta Z^{i,j}$, $\delta m^{i,j}$ and $\delta g^{i,j}$. The Lagrangian (4.26) can be written with help of (4.27) as the sum of a tree-level Lagrangian that contains only the renormalized fields and couplings, and a counter-term part which in addition contains the renormalization constants

$$
\begin{aligned}
\mathcal{L}(\psi_0, m_0, g_0) = {} & \mathcal{L}(\psi, m, g) \\
& + \mathcal{L}_{\text{CT}}^{1,0}(\psi, m, g, \delta Z_\psi^{1,0}, \delta m^{1,0}, \delta g^{1,0}) \\
& + \mathcal{L}_{\text{CT}}^{0,1}(\psi, m, g, \delta Z_\psi^{0,1}, \delta m^{0,1}, \delta g^{0,1}) \\
& + \mathcal{L}_{\text{CT}}^{2,0}(\psi, m, g, \delta Z_\psi^{1,0}, \delta m^{1,0}, \delta g^{1,0} \delta Z_\psi^{2,0}, \delta m^{2,0}, \delta g^{2,0}) \\
& + \dots \,.
\end{aligned}
\tag{4.29}
$$

For the one-loop calculations considered in this work, counterterms of order α_s and α are needed in order to obtain UV finite results. Hence the renormalization constants are required to be evaluated at order α_s and α, respectively.

4.4.1 Renormalization Schemes

The renormalization constants have to be such that the absorption of the UV divergences is guaranteed. However, this determines those only up to finite parts. To fix the finite part, one has to define a renormalization scheme which specifies the precise definition of physical parameters such as the particle masses and coupling constants and allows for a convenient normalization of the fields. In the following we list the schemes used in this work.

On-shell scheme: In the on-shell (OS) scheme the renormalization constants are defined in such a way that the renormalized quantities are directly related to physical observables order-by-order in perturbation theory. The renormalized OS mass is given by defining the physical mass as the real part of the pole of the propagator. The field renormalization constants are fixed by proper normalization of the renormalized fields, e.g. requiring the pole of the renormalized propagator to have residue unity. For mass matrices, the corresponding mass eigenvalues are taken and one further requires the renormalized fields to be diagonal at all orders in perturbation theory. Hence, mixing is not changed by higher-order corrections. In the OS scheme, the coupling constant α of QED is fixed by the requirement that the renormalized vertex function at zero momentum transfer reproduces the Thomson cross section. Such a definition is not applicable to the strong coupling constant α_s of QCD since in this regime it becomes strong and perturbation theory breaks down. Therefore a different renormalization scheme is required in the case of QCD. The OS renormalization has been formulated in the SM [134, 135] and generalized to the MSSM [136].

$\overline{\text{MS}}$ scheme: The renormalization in the modified minimal-subtraction ($\overline{\text{MS}}$) scheme [137] relies on dimensional regularization. In this scheme the renormalization constants absorb only the divergences plus the universal remnants of this regularization prescription, eq. (4.24). As a consequence, when performing a fixed order calculation, the renormalized amplitudes still depend on the mass scale μ introduced by this renormalization scheme. This leads to a residual scale dependence of the cross section, namely the renormalization scale dependence, which enters logarithmically and is proportional to the pole structure of the amplitude. Obviously this scale dependence is unphysical. It gets reduced when including higher-order corrections and ultimately drops out in an "all order" calculation. Hence, the scale dependence of a given (calculated) cross section gives a hint to the remaining uncertainties coming from higher-order corrections. The $\overline{\text{MS}}$ scheme is commonly used for the strong coupling constant α_s of QCD. This scheme is related to the minimal-subtraction scheme (MS) [138], in which only the divergent $1/\epsilon$ poles are subtracted, via a change in the scale μ,

$$\log \mu_{\text{MS}}^2 - \gamma_E + \log 4\pi = \log(4\pi e^{-\gamma_E} \mu_{\text{MS}}^2) \to \log \mu_{\overline{\text{MS}}}^2. \tag{4.30}$$

In calculations μ usually enters in the form $\log \mu^2/Q^2$ where Q is set by the kinematics of the process. Thus, μ should be chosen to be of the energy scale of the process, in order to keep these logarithms small. In contrast to the $\overline{\text{MS}}$ scheme, in the on-shell scheme no scale dependence is left, since in this scheme a natural scale is set by the masses of the renormalized particles and by defining the coupling constant α of QED at zero momentum transfer.

$\overline{\text{DR}}$ scheme: The $\overline{\text{DR}}$ scheme is defined in much the same way as the $\overline{\text{MS}}$ scheme. The regularization procedure has to be performed in dimensional reduction and again only the divergent part plus the universal remnant (4.24) are absorbed by the renormalization constants. Since DRED preserves SUSY (at least at the one-loop level) this scheme is commonly used in supersymmetric higher-order calculations.

4.4.2 Renormalization Conditions

In the following we give the renormalization conditions for the sectors needed for the NLO EW corrections to squark–squark and sbottom-pair production. It consists of the wavefunction renormalization of quarks, squarks, and gluinos, the mass renormalization of the squarks and gluinos, as well as the renormalization of the strong coupling constant. The Feynman rules for the relevant counterterms needed in our NLO EW calculations are explicitly listed in Appendix B.

Renormalization of the Quark Sector

The Fourier-transformed bare kinetic Lagrangian for a quark q after electroweak symmetry breaking is given by

$$\mathcal{L}^0_{\text{quark}} = \bar{q}^0(\slashed{p} - m_0)q^0, \qquad \text{with } q = \begin{pmatrix} q_L \\ q_R \end{pmatrix}. \tag{4.31}$$

Here $q = u_i, d_i$ are the Dirac fermion fields with generation index $i = 1, 2, 3$. We neglect mixing between generations, i.e. suppose a diagonal CKM matrix. The left- and right-handed states q_L and q_R can be projected out with help of the projection operators

$$P_L := \frac{1}{2}(1 - \gamma_5), \qquad P_R := \frac{1}{2}(1 + \gamma_5). \tag{4.32}$$

Splitting the bare masses and fields into renormalized quantities plus counterterms according to (4.28),

$$P_L\, q^0 \to P_L(1 + \frac{1}{2}\delta Z^q_L)\, q\,, \tag{4.33a}$$

$$P_R\, q^0 \to P_R(1 + \frac{1}{2}\delta Z^q_R)\, q\,, \tag{4.33b}$$

$$m_0 \to m + \delta m\,, \tag{4.33c}$$

one gets the tree-level (first line) and counterterm Lagrangian (second and third line),

$$\begin{aligned}
\mathcal{L}^0_{\text{quark}} =\ & \bar{q}_L\slashed{p}q_L + \bar{q}_R\slashed{p}q_R - m_q(\bar{q}_Rq_L + \bar{q}_Lq_R) \\
& + \frac{1}{2}\bar{q}_L\slashed{p}\left(\delta Z^q_L + \delta Z^{q\dagger}_L\right)q_L + \frac{1}{2}\bar{q}_R\slashed{p}\left(\delta Z^q_R + \delta Z^{q\dagger}_R\right)q_R \\
& - \bar{q}_R\left(\frac{m_q}{2}\left(\delta Z^q_L + \delta Z^{q\dagger}_R\right) + \delta m\right)q_L - \bar{q}_L\left(\frac{m_q}{2}\left(\delta Z^q_R + \delta Z^{q\dagger}_L\right) + \delta m\right)q_R\,.
\end{aligned} \tag{4.34}$$

With the following Lorentz decomposition of the Fourier-transformed self-energy (cf. Appendix A.4),

$$\Sigma(p) = \slashed{p}P_L\Sigma^L(p^2) + \slashed{p}P_R\Sigma^R(p^2) + P_L\Sigma^{SL}(p^2) + P_R\Sigma^{SR}(p^2)\,, \tag{4.35}$$

the scalar coefficients of the renormalized self-energy are given by

$$\hat{\Sigma}^L(p^2) = \Sigma^L(p^2) + \frac{1}{2}\left(\delta Z_L^q + \delta Z_L^{q\dagger}\right), \tag{4.36a}$$

$$\hat{\Sigma}^R(p^2) = \Sigma^R(p^2) + \frac{1}{2}\left(\delta Z_R^q + \delta Z_R^{q\dagger}\right), \tag{4.36b}$$

$$\hat{\Sigma}^{SL}(p^2) = \Sigma^{SL}(p^2) - \left(\frac{m}{2}\left(\delta Z_L^q + \delta Z_R^{q\dagger}\right) + \delta m\right), \tag{4.36c}$$

$$\hat{\Sigma}^{SR}(p^2) = \Sigma^{SR}(p^2) - \left(\frac{m}{2}\left(\delta Z_L^q + \delta Z_R^{q\dagger}\right) + \delta m\right). \tag{4.36d}$$

The renormalization conditions for the masses and fields are fixed by on-shell renormalization conditions, i.e. imposing that the masses correspond to the real part of the pole of the propagator with residue unity,

$$\widetilde{\mathrm{Re}}\left[\hat{\Sigma}(p)\right]u(p)\Big|_{p^2=m^2} = 0\,, \qquad \lim_{p^2\to m^2}\frac{1}{\not{p}-m}\widetilde{\mathrm{Re}}\left[\hat{\Sigma}(p)\right]u(p) = 0\,, \tag{4.37}$$

with $u(p)$ being the particle wavefunction of q. $\widetilde{\mathrm{Re}}$ is defined such that only the real parts of the loop integrals L_i are selected while all other expressions c_i like e.g. coupling constants remain complex, $\widetilde{\mathrm{Re}}\sum c_i L_i = \sum c_i \mathrm{Re} L_i$. The renormalization constants can be evaluated by inserting (4.35) and (4.36) into (4.37) and are given by

$$\delta m = \frac{1}{2}\left(m\widetilde{\mathrm{Re}}\left[\Sigma^L(m^2) + \Sigma^R(m^2)\right] + \widetilde{\mathrm{Re}}\left[\Sigma^{SL}(m^2) + \Sigma^{SR}(m^2)\right]\right), \tag{4.38a}$$

$$\delta Z^{L/R} = -\widetilde{\mathrm{Re}}\left[\Sigma^{L/R}(m^2) + m^2\left(\Sigma^{L'}(m^2) + \Sigma^{R'}(m^2)\right) + m\left(\Sigma^{SL'}(m^2) + \Sigma^{SR'}(m^2)\right)\right]. \tag{4.38b}$$

with $\Sigma'(m^2) = \frac{\partial}{\partial p^2}\Sigma(p^2)|_{p^2=m^2}$. Only light-flavor quarks appear as external particles in our NLO EW calculations. Since light-flavor quark masses are not observable in squark and gluino production processes, they will be neglected everywhere, except in collinear singular regions where its mass is kept in order to regularize the singularities.

In contrast, the top-quark pole mass is related to experimental data. Due to the large top-quark width of $\Gamma_t \approx 1.5$ GeV, the top quark typically decays before it can hadronise [139]. The mass measurement proceeds via kinematic reconstruction from the decay products and comparison to Monte Carlo simulations. Currently, a value of $m_t = 173.1\pm1.3$ GeV is quoted for the mass of the top quark [140], which amounts to an experimental uncertainty of less than 1%. However, there are conceptual problems with the determination of the top-quark mass from the kinematic reconstruction. It is not completely clear, how to interprete the quantity measured at the Tevatron in terms of a parameter of the SM Lagrangian. In order to circumvent this problem, in [141,142] the running top-quark mass in the $\overline{\mathrm{MS}}$ scheme was related to the total $t\bar{t}$ production cross section. The best estimate for the running mass, $m_t^{\overline{\mathrm{MS}}}(m_t) = 160.0 \pm 3.3$ GeV, corresponds to a pole mass of $m_t = 168.9 \pm 3.5$ GeV and is consistent with the current world average.

For the bottom-quark mass, non-perturbative effects are much more profound. In order to circumvent this problem, theoretical prediction often use a running bottom-quark mass

defined in the $\overline{\text{MS}}$ scheme. Therefore, the parameter extracted from the comparison of theory and experiment is not the bottom-quark pole mass. The value of the bottom mass is usually given in the $\overline{\text{MS}}$ scheme with renormalization scale chosen at the bottom-quark mass, i.e. $m_b^{\overline{\text{MS}}}(m_b^{\overline{\text{MS}}})$. For the calculation of squark-squark production, the bottom mass parameter only enters at NLO, hence different definitions of the mass give contributions that are formally of higher order. However, for sbottom-pair production a precise definition of the bottom-quark mass is necessary. An appropriate treatment of the mass parameter for NLO calculations within the MSSM is to define the bottom-quark mass in the $\overline{\text{DR}}$ scheme within the MSSM, which determines the mass counterterm by the expression

$$\delta m_b^{\overline{\text{DR}}} = \frac{1}{2}\left(m_b\widetilde{\text{Re}}\left[\Sigma_{\text{div}}^L(m_b^2) + \Sigma_{\text{div}}^R(m_b^2)\right] + \widetilde{\text{Re}}\left[\Sigma_{\text{div}}^{SL}(m_b^2) + \Sigma_{\text{div}}^{SR}(m_b^2)\right]\right), \qquad (4.39)$$

where Σ_{div} only takes the divergent part proportional to Δ (cf. (4.24)). In order to determine $m_b^{\overline{\text{DR}}}(\mu^{\overline{\text{DR}}})$ from the value $m_b^{\overline{\text{MS}}}(\mu^{\overline{\text{MS}}})$ extracted from experiment, one has to notice that the definition of $m_b^{\overline{\text{DR}}}$ needed for calculations in the MSSM sector contains all MSSM contributions at $\mathcal{O}(\alpha_s, \alpha)$, while $m_b^{\overline{\text{MS}}}$ contains only $\mathcal{O}(\alpha_s)$ SM corrections. However, both definitions can easily be related to the pole mass m_b^{OS} which is scheme invariant. Hence, for any renormalization scheme "RS", the on-shell mass is given by[2]

$$m_b^{\text{OS}} = m_b^{\text{RS}}(\mu^{\text{RS}}) - \frac{1}{2}\left(m_b\widetilde{\text{Re}}\left[\hat{\Sigma}_{\text{RS}}^L(m_b^2) + \hat{\Sigma}_{\text{RS}}^R(m_b^2)\right] + \widetilde{\text{Re}}\left[\hat{\Sigma}_{\text{RS}}^{SL}(m_b^2) + \hat{\Sigma}_{\text{RS}}^{SR}(m_b^2)\right]\right), \quad (4.40)$$

with the self-energy being renormalized in the RS-scheme. Taking RS $= \overline{\text{DR}}$ and calculating the OS mass from $m_b^{\overline{\text{MS}}}(M_Z)$,

$$m_b^{\text{OS}} = m_b^{\overline{\text{MS}}}(M_Z)\left[1 + \frac{\alpha_s}{\pi}\left(\frac{4}{3} - \log\frac{(m_b^{\overline{\text{MS}}}(M_Z))^2}{M_Z^2}\right)\right] = m_b^{\overline{\text{MS}}}(M_Z)b^{\text{shift}}, \qquad (4.41)$$

the running $\overline{\text{DR}}$ bottom quark mass is evaluated as

$$m_b^{\overline{\text{DR}}}(\mu^{\overline{\text{DR}}}) = m_b^{\overline{\text{MS}}}(M_Z)b^{\text{shift}} + \frac{1}{2}\left(m_b\left[\hat{\Sigma}_{\text{div}}^L(m_b^2) + \hat{\Sigma}_{\text{div}}^R(m_b^2)\right] + \hat{\Sigma}_{\text{div}}^{SL}(m_b^2) + \hat{\Sigma}_{\text{div}}^{SR}(m_b^2)\right). \tag{4.42}$$

Renormalization of the Squark Sector (Light Flavor)

The bare kinetic Lagrangian for a squark $\tilde{q}$ can be written as follows,

$$\mathcal{L}_{\text{squark}}^0 = (\tilde{q}_L^{0\dagger}, \tilde{q}_R^{0\dagger})(p^2 - \mathcal{M}_{\tilde{q}}^0)\begin{pmatrix}\tilde{q}_L^0\\\tilde{q}_R^0\end{pmatrix}, \qquad (4.43)$$

with the squark mass matrix $\mathcal{M}_{\tilde{q}}$ given in (2.50). For light-flavor squarks the corresponding quark masses are set to zero, neglecting left-right mixing effects,

$$\mathcal{M}_{\tilde{q}} = \begin{pmatrix} M_{\tilde{q}_L}^2 + M_Z^2\cos(2\beta)(I_q^3 - Q_q s_{\text{w}}^2) & 0 \\ 0 & M_{\tilde{q}_R}^2 + Q_q M_Z^2\cos(2\beta)s_{\text{w}}^2 \end{pmatrix} = \begin{pmatrix} m_{\tilde{q}_L}^2 & 0 \\ 0 & m_{\tilde{q}_R}^2 \end{pmatrix}.$$

---

[2]This expression can also be derived by noticing that the bare mass has to be the same in all renormalization schemes, and hence for two different renormalization schemes RS1 and RS2 one has, $m_b^{\text{RS1}} + \delta m_b^{\text{RS1}} = m_b^{\text{RS2}} + \delta m_b^{\text{RS2}}$.

Hence, for each generation, there are three free parameters corresponding to this sector, $M_L^2 = M_{\tilde{u}_L}^2 = M_{\tilde{d}_L}^2$, $M_{\tilde{u}_R}^2$ and $M_{\tilde{d}_R}^2$. Splitting the bare quantities into a renormalized part plus counterterm,

$$\mathcal{M}_{\tilde{q}}^0 = \mathcal{M}_{\tilde{q}} + \delta\mathcal{M}_{\tilde{q}} = \begin{pmatrix} m_{\tilde{q}_L}^2 & 0 \\ 0 & m_{\tilde{q}_R}^2 \end{pmatrix} + \begin{pmatrix} \delta m_{\tilde{q}_L}^2 & 0 \\ 0 & \delta m_{\tilde{q}_R}^2 \end{pmatrix}, \qquad (4.44a)$$

$$\begin{pmatrix} \tilde{q}_L^0 \\ \tilde{q}_R^0 \end{pmatrix} = (1 + \tfrac{1}{2}\delta Z^{\tilde{q}}) \begin{pmatrix} \tilde{q}_L \\ \tilde{q}_R \end{pmatrix}, \qquad \text{with} \quad \delta Z^{\tilde{q}} = \begin{pmatrix} \delta Z_{LL}^{\tilde{q}} & \delta Z_{LR}^{\tilde{q}} \\ \delta Z_{RL}^{\tilde{q}} & \delta Z_{RR}^{\tilde{q}} \end{pmatrix}, \qquad (4.44b)$$

with

$$\delta m_{\tilde{q}_L}^2 = \delta M_{\tilde{q}_L}^2 + (I_q^3 - Q_q s_{\mathrm{w}}^2)(\delta M_Z^2 \cos(2\beta) + M_Z^2 \delta\cos(2\beta)) - M_Z^2 \cos(2\beta) Q_q \delta s_{\mathrm{w}}^2, \quad (4.44c)$$

$$\delta m_{\tilde{q}_R}^2 = \delta M_{\tilde{q}_R}^2 + Q_q \delta M_Z^2 \cos(2\beta) s_{\mathrm{w}}^2 + Q_q M_Z^2 \delta\cos(2\beta) s_{\mathrm{w}}^2 + Q_q M_Z^2 \cos(2\beta) \delta s_{\mathrm{w}}^2, \quad (4.44d)$$

the bare Lagrangian becomes

$$\begin{aligned} \mathcal{L}_{\mathrm{squark}}^0 = &\, (\tilde{q}_L^\dagger, \tilde{q}_R^\dagger)(p^2 - \mathcal{M}_{\tilde{q}}) \begin{pmatrix} \tilde{q}_L \\ \tilde{q}_R \end{pmatrix} \\ &+ (\tilde{q}_L^\dagger, \tilde{q}_R^\dagger) \left[\tfrac{1}{2}(\delta Z^{\tilde{q}} + \delta Z^{\tilde{q}\dagger})p^2 - \tfrac{1}{2}(\delta Z^{\tilde{q}\dagger}\mathcal{M}_{\tilde{q}} + \mathcal{M}_{\tilde{q}}\delta Z^{\tilde{q}}) - \delta\mathcal{M}_{\tilde{q}} \right] \begin{pmatrix} \tilde{q}_L \\ \tilde{q}_R \end{pmatrix}. \end{aligned} \qquad (4.45)$$

The renormalized squark self-energy is therefore given by

$$\left[\hat{\Sigma}_{ij}^{\tilde{q}}(p^2) \right] = \left[\Sigma_{ij}^{\tilde{q}}(p^2) \right] + \left[\tfrac{1}{2}(\delta Z^{\tilde{q}} + \delta Z^{\tilde{q}\dagger})p^2 - \tfrac{1}{2}(\delta Z^{\tilde{q}\dagger}\mathcal{M}_{\tilde{q}} + \mathcal{M}_{\tilde{q}}\delta Z^{\tilde{q}}) - \delta\mathcal{M}_{\tilde{q}} \right]_{ij}. \qquad (4.46)$$

$\Sigma_{ij}^{\tilde{q}}$ corresponds to the self-energy of $\tilde{q}_i \to \tilde{q}_j$. Due to $SU(2)$ invariance, there are only three independent mass parameters in the squark sector. Hence one can impose only three on-shell conditions on the squark masses, while one squark mass remains a dependent quantity. The left-handed down-type squark will be taken as the dependent quantity. With the squark fields renormalized on-shell one has the following renormalization conditions,

$$\lim_{p^2 \to m_{\tilde{q}}^2} \frac{1}{p^2 - m_{\tilde{q}}^2} \widetilde{\mathrm{Re}} \left[\hat{\Sigma}_{ii}^{\tilde{q}}(p^2) \right] = 0, \qquad (4.47a)$$

$$\widetilde{\mathrm{Re}} \left[\hat{\Sigma}_{12}^{\tilde{q}}(m_{\tilde{q}_i}^2) \right] = 0, \qquad\qquad \widetilde{\mathrm{Re}} \left[\hat{\Sigma}_{21}^{\tilde{q}}(m_{\tilde{q}_i}^2) \right] = 0, \qquad (4.47b)$$

$$\widetilde{\mathrm{Re}} \left[\hat{\Sigma}_{ii}^{\tilde{q}}(m_{\tilde{q}_i}^2) \right] = 0, \qquad \text{for } \tilde{q} \neq \tilde{d}_L. \qquad (4.47c)$$

The diagonal field renormalization constants follow from the first condition by requiring the diagonal self-energies to have residue unity. The absence of the transition between different mass eigenstates fixes the non-diagonal field renormalization constants. The last condition fixes the mass renormalization constants for the three independent squark masses. Inserting (4.46) into (4.47) the explicit form of the renormalization constant for the independent mass

parameter and of the field renormalization constants are obtained,

$$\delta m_{\tilde{q}_i} = \widetilde{\mathrm{Re}} \left[\Sigma_{ii}^{\tilde{q}}(m_{\tilde{q}_i}^2) \right], \qquad \text{for} \quad \tilde{q}_i = \tilde{u}_L, \tilde{u}_R, \tilde{d}_R, \tag{4.48a}$$

$$\delta Z_{ii}^{\tilde{q}} = -\frac{\partial}{\partial p^2} \widetilde{\mathrm{Re}} \left[\Sigma_{ii}^{\tilde{q}}(p^2) \right] \Big|_{p^2 = m_{\tilde{q}}^2}, \tag{4.48b}$$

$$\delta Z_{ij}^{\tilde{q}} = \frac{2}{m_{\tilde{q}_i}^2 - m_{\tilde{q}_j}^2} \widetilde{\mathrm{Re}} \left[\Sigma_{ij}^{\tilde{q}}(m_{\tilde{q}_j}) \right], \qquad i \neq j. \tag{4.48c}$$

The renormalization constants of the mass parameters originally appearing in the Lagrangian are related to the squark mass renormalization constants via (4.44). The renormalization constant of the dependent squark mass $\delta m_{\tilde{d}_L}$ can be expressed in terms of the independent ones,

$$\delta m_{\tilde{d}_L}^2 = \delta m_{\tilde{u}_L}^2 + c_{\mathrm{w}}(\delta M_Z^2 \cos(2\beta) + M_Z^2 \delta \cos(2\beta)) + M_Z^2 \cos(2\beta) \delta s_{\mathrm{w}}^2. \tag{4.48d}$$

Hence, the pole mass of the left-handed down-type squark receives a shift due to radiative corrections,

$$(m_{\tilde{d}_L}^{\mathrm{pole}})^2 = m_{\tilde{d}_L}^2 + \left(\delta m_{\tilde{d}_L}^2 - \widetilde{\mathrm{Re}} \Sigma_{LL}^{\tilde{d}}(m_{\tilde{d}_L}^2) \right). \tag{4.49}$$

Renormalization of the Squark Sector (3rd Generation)

For the third generation, the corresponding quark masses cannot be neglected and left-right mixing of the squarks has to be taken into account. In the real MSSM the mass matrix has the following structure (cf. (2.50)),

$$\mathcal{M}_{\tilde{q}} = \begin{pmatrix} M_{\tilde{q}_L}^2 + m_q^2 + M_Z^2 \cos(2\beta)(I_q^3 - Q_q s_{\mathrm{w}}^2) & Y_{\tilde{q}} \\ Y_{\tilde{q}} & M_{\tilde{q}_R}^2 + m_q^2 + Q_q M_Z^2 \cos(2\beta) s_{\mathrm{w}}^2 \end{pmatrix}, \tag{4.50}$$

with the off-diagonal entries $Y_{\tilde{q}}$ given by

$$Y_{\tilde{t}} = m_t(A_t - \mu \cot \beta), \qquad Y_{\tilde{b}} = m_b(A_b - \mu \tan \beta). \tag{4.51}$$

Using the definition (2.51), $\mathcal{D}_{\tilde{q}} = U_{\tilde{f}} \mathcal{M}_{\tilde{f}} U_{\tilde{f}}^\dagger = \mathrm{diag}(m_{\tilde{q}_1}, m_{\tilde{q}_2})$, the bare Lagrangian can be written as

$$\mathcal{L}_{\mathrm{squark}}^0 = (\tilde{q}_1^{0\dagger}, \tilde{q}_2^{0\dagger})(p^2 - \mathcal{D}_{\tilde{q}}^0) \begin{pmatrix} \tilde{q}_1^0 \\ \tilde{q}_2^0 \end{pmatrix} \tag{4.52}$$

$$= (\tilde{q}_1^\dagger, \tilde{q}_2^\dagger)(p^2 - \mathcal{D}_{\tilde{q}}) \begin{pmatrix} \tilde{q}_1 \\ \tilde{q}_2 \end{pmatrix} \tag{4.53}$$

$$+ (\tilde{q}_1^\dagger, \tilde{q}_2^\dagger) \left[\frac{1}{2}(\delta Z^{\tilde{q}} + \delta Z^{\tilde{q}\dagger})p^2 - \frac{1}{2}(\delta Z^{\tilde{q}\dagger} \mathcal{D}_{\tilde{q}} + \mathcal{D}_{\tilde{q}} \delta Z^{\tilde{q}}) - \delta \mathcal{D}_{\tilde{q}} \right] \begin{pmatrix} \tilde{q}_1 \\ \tilde{q}_2 \end{pmatrix}, \tag{4.54}$$

where in the second line the bare fields and masses are split into renormalized quantities and counterterms according to

$$\mathcal{D}_{\tilde{q}}^0 = \mathcal{D}_{\tilde{q}} + \delta \mathcal{D}_{\tilde{q}} \equiv \mathcal{D}_{\tilde{q}} + U_{\tilde{q}} \delta \mathcal{M}_{\tilde{q}} U_{\tilde{q}}^\dagger, \tag{4.55a}$$

$$\begin{pmatrix} \tilde{q}_1^0 \\ \tilde{q}_2^0 \end{pmatrix} = (1 + \frac{1}{2} \delta Z_{ij}^{\tilde{q}}) \begin{pmatrix} \tilde{q}_1 \\ \tilde{q}_2 \end{pmatrix}, \qquad \text{with} \quad \delta Z^{\tilde{q}} = \begin{pmatrix} \delta Z_{11}^{\tilde{q}} & \delta Z_{12}^{\tilde{q}} \\ \delta Z_{21}^{\tilde{q}} & \delta Z_{22}^{\tilde{q}} \end{pmatrix}. \tag{4.55b}$$

Using the explicit parametrization of $U_{\tilde{q}}$ in terms of a mixing angle $\theta_{\tilde{q}}$, eq. (2.54), the counterterm $\delta\mathcal{D}_{\tilde{q}}$ is explicitly given by

$$\delta\mathcal{D}_{\tilde{q}} = \begin{pmatrix} \delta m_1^2 & (m_1^2 - m_2^2)\det(U_{\tilde{q}})\,\delta\theta_{\tilde{q}} \\ (m_1^2 - m_2^2)\det(U_{\tilde{q}})\,\delta\theta_{\tilde{q}} & \delta m_2^2 \end{pmatrix}. \tag{4.56}$$

The entry $(\delta\mathcal{D}_{\tilde{q}})_{12} = (\delta\mathcal{D}_{\tilde{q}})_{21}$ is conveniently defined as

$$\delta Y_{\tilde{q}} \equiv (U_{\tilde{q}}\delta\mathcal{M}_{\tilde{f}}U_{\tilde{q}}^{\dagger})_{12} = (m_1^2 - m_2^2)\det(U_{\tilde{q}})\,\delta\theta_{\tilde{q}}. \tag{4.57}$$

The counterterms for $\delta\mathcal{M}$ and $\delta\mathcal{D}$ can be related mutually via (4.55a). In particular the off-diagonal entries are related via

$$\begin{aligned}(\delta\mathcal{M}_{\tilde{q}})_{12} &= (A_q^* - \mu\,\kappa)\delta m_q + m_q(\delta A_q^* - \mu\,\delta\kappa - \kappa\,\delta\mu) \\ &= U_{\tilde{q}11}U_{\tilde{q}12}(\delta m_{\tilde{q}_1}^2 - \delta m_{\tilde{q}_2}^2) + (U_{\tilde{q}11}U_{\tilde{q}22} + U_{\tilde{q}12}U_{\tilde{q}21})\delta Y_{\tilde{q}}.\end{aligned} \tag{4.58}$$

In total one has five parameters describing the heavy squark sector, two more compared to the non-mixing case. The new parameters are given by A_t and A_b, or equivalently by $\theta_{\tilde{t}}$ and $\theta_{\tilde{b}}$, since these two quantities are related via (2.55). The renormalized self-energies are now given by

$$\left[\hat{\Sigma}_{11}^{\tilde{q}}(p^2)\right] = \left[\Sigma_{11}^{\tilde{q}}(p^2)\right] + \frac{1}{2}(p^2 - m_{\tilde{q}_1}^2)\left[\delta Z_{11}^{\tilde{q}} + \delta Z_{11}^{\tilde{q}*}\right] - \delta m_{\tilde{q}_1}^2, \tag{4.59a}$$

$$\left[\hat{\Sigma}_{22}^{\tilde{q}}(p^2)\right] = \left[\Sigma_{22}^{\tilde{q}}(p^2)\right] + \frac{1}{2}(p^2 - m_{\tilde{q}_2}^2)\left[\delta Z_{22}^{\tilde{q}} + \delta Z_{22}^{\tilde{q}*}\right] - \delta m_{\tilde{q}_2}^2, \tag{4.59b}$$

$$\left[\hat{\Sigma}_{12}^{\tilde{q}}(p^2)\right] = \left[\Sigma_{12}^{\tilde{q}}(p^2)\right] + \frac{1}{2}(p^2 - m_{\tilde{q}_1}^2)\delta Z_{12}^{\tilde{q}} + \frac{1}{2}(p^2 - m_{\tilde{q}_2}^2)\delta Z_{21}^{\tilde{q}*} - \delta Y_{\tilde{q}}, \tag{4.59c}$$

$$\left[\hat{\Sigma}_{21}^{\tilde{q}}(p^2)\right] = \left[\Sigma_{21}^{\tilde{q}}(p^2)\right] + \frac{1}{2}(p^2 - m_{\tilde{q}_1}^2)\delta Z_{12}^{\tilde{q}*} + \frac{1}{2}(p^2 - m_{\tilde{q}_2}^2)\delta Z_{21}^{\tilde{q}} - \delta Y_{\tilde{q}}. \tag{4.59d}$$

As in the non-mixing case, the fields are renormalized on-shell. Again, the requirement that the real part of the residua of the propagators have unity value fixes the diagonal Z-factors, while the non-diagonal Z-factors are fixed by the condition that for on-shell squarks no transition from one squark to another occurs,

$$\lim_{p^2 \to m_{\tilde{q}}^2} \frac{1}{p^2 - m_{\tilde{q}}^2}\widetilde{\mathrm{Re}}\left[\hat{\Sigma}_{ii}^{\tilde{q}}(p^2)\right] = 0, \tag{4.60a}$$

$$\widetilde{\mathrm{Re}}\left[\hat{\Sigma}_{12}^{\tilde{q}}(m_{\tilde{q}_i}^2)\right] = 0, \qquad \widetilde{\mathrm{Re}}\left[\hat{\Sigma}_{21}^{\tilde{q}}(m_{\tilde{q}_i}^2)\right] = 0. \tag{4.60b}$$

The field renormalization constants for the third generation squarks are given by

$$\delta Z_{ii}^{\tilde{q}} = -\frac{\partial}{\partial p^2}\widetilde{\mathrm{Re}}\left[\Sigma_{ii}^{\tilde{q}}(p^2)\right]\Big|_{p^2 = m_{\tilde{q}}^2}, \tag{4.61a}$$

$$\delta Z_{ij}^{\tilde{q}} = 2\frac{\widetilde{\mathrm{Re}}\left[\Sigma_{ij}^{\tilde{q}}(m_{\tilde{q}_j}^2)\right] - \delta Y_{\tilde{q}}}{(m_{\tilde{q}_i}^2 - m_{\tilde{q}_j}^2)}, \qquad i \neq j. \tag{4.61b}$$

From (4.50) one finds that in addition to the parameters of the squark sector, M_L, $M_{\tilde{b}_R}$, $M_{\tilde{t}_R}$, A_t, and A_b also the quark masses m_b and m_t enter. Hence, when considering a renormalization scheme for the stop/sbottom sector one also has to consider the renormalization of the top and bottom mass parameter. There are several ways of fixing the parameters in this sector, depending on the precise parametrization chosen. The most physical one is to define the masses and the mixing angle via on-shell conditions. For the top/stop sector this is done by imposing

$$\delta m_{\tilde{t}_i} = \widetilde{\mathrm{Re}}\left[\Sigma_{ii}^{\tilde{t}}(m_{\tilde{t}_i}^2)\right], \tag{4.62}$$

$$\delta Y_{\tilde{t}} = \frac{1}{2}\widetilde{\mathrm{Re}}\left[\Sigma_{12}^{\tilde{t}}(m_{\tilde{t}_1}^2) + \Sigma_{12}^{\tilde{t}}(m_{\tilde{t}_2}^2)\right], \tag{4.63}$$

and the on-shell condition (4.38) for the top-quark mass. $\delta Y_{\tilde{t}}$ is obtained from (4.59c) and (4.60b) and the additional condition $\delta Z_{12}^{\tilde{q}} = \delta Z_{21}^{\tilde{q}*}$ as proposed in [143]. The counterterm for the mixing angle $\delta\theta_{\tilde{t}}$ is directly related to $\delta Y_{\tilde{t}}$ via (4.57). The counterterm for the trilinear coupling δA_t remains a dependent quantity. It is obtained by solving (4.58),

$$\delta A_t = \frac{1}{m_t}\left[U_{\tilde{t}11}U_{\tilde{t}12}\left(\delta m_{\tilde{t}_1}^2 - \delta m_{\tilde{t}_2}^2\right) + \left(U_{\tilde{t}11}U_{\tilde{t}22} - U_{\tilde{t}12}U_{\tilde{t}21}\right)\delta Y_{\tilde{t}} - (A_t - \mu\cot\beta)\delta m_t\right]$$
$$+ \delta\mu\cot\beta - \mu\cot^2\beta\,\delta\tan\beta\,. \tag{4.64}$$

In the bottom/sbottom sector, only one mass can be treated as independent quantity due to $SU(2)$ invariance, in the same way as in the light-flavor case. Apart from that, in principle an analogue on-shell definition as for the top/stop sector is possible, i.e. imposing on-shell renormalization conditions on one of the bottom-squark masses, the bottom-squark mixing angle, and the bottom-quark mass. In the following we will impose the on-shell renormalization condition on the heavier bottom squark $\tilde{b}_2$ which renders $\tilde{b}_1$ as an dependent quantity,[3]

$$\delta m_{\tilde{b}_2} = \widetilde{\mathrm{Re}}\left[\Sigma_{22}^{\tilde{b}}(m_{\tilde{b}_2}^2)\right]. \tag{4.65}$$

The counterterm for the dependent parameter A_b is then given via

$$\delta A_b = \frac{1}{m_b U_{\tilde{b}11}}\Big[-U_{\tilde{b}12}\delta m_{\tilde{b}_2}^2 + U_{\tilde{b}22}\delta Y_{\tilde{b}} - \left(U_{\tilde{b}11}(A_b - \mu\tan\beta) - 2U_{\tilde{b}12}m_b\right)\delta m_b$$
$$+ U_{\tilde{b}12}\left(U_{\tilde{t}11}^2\delta m_{\tilde{t}_1}^2 + U_{\tilde{t}12}^2\delta m_{\tilde{t}_2}^2 - U_{\tilde{t}12}U_{\tilde{t}22}\delta Y_{\tilde{t}}\right) - 2U_{\tilde{b}12}m_t\delta m_t - U_{\tilde{b}12}\cos 2\beta\,\delta M_W^2$$
$$+ \left(U_{\tilde{b}12}4M_W^2\frac{\tan\beta}{(1+\tan^2\beta)^2} + m_b U_{\tilde{b}11}\mu\right)\delta\tan\beta + m_b U_{\tilde{b}11}\tan\beta\,\delta\mu\Big]. \tag{4.66}$$

However, this scheme was found to be unreliable for large values of $\tan\beta$, in particular when $(\mu\tan\beta \gg A_b)$ [144]. The reason is that δA_b contains a contribution

$$\delta A_b = \frac{1}{m_b}\left[-(A_b - \mu\tan\beta)\delta m_b + \ldots\right]. \tag{4.67}$$

Hence, in parameter regions where $(\mu\tan\beta)$ is much larger than A_b, the counterterm receives a large finite shift when derived from the $Y_{\tilde{b}}$, i.e. the sbottom mixing angle. This is not an

---

[3]This is always possible as long as $\tilde{b}_2 \neq \tilde{b}_R$, which is always true for non-trivial mixing.

issue in the stop sector, since there only the combination $\mu \cot \beta$ arises which is strongly suppressed for large values of $\tan \beta$. The problem of large finite contributions to the counterterm can be avoided by changing to an appropriate renormalization scheme. There are several possibilities, e.g. one can either impose on-shell conditions directly on A_b or by defining A_b or $Y_{\tilde{b}}$ in the $\overline{\text{DR}}$ scheme. Another possibility is to define the bottom-quark mass in the $\overline{\text{DR}}$ scheme, since by definition, $\delta m_b^{\overline{\text{DR}}}$ does not lead to a finite contribution. In addition, as discussed in the section of quark renormalization, by using the running bottom-quark mass parameter defined in the $\overline{\text{DR}}$ scheme, potential problems with the bottom-pole-mass definition can be avoided. Besides m_b, we will also define the trilinear coupling A_b in the $\overline{\text{DR}}$ scheme to avoid further potential problems due to renormalization of the mixing angle. $\delta A_b^{\overline{\text{DR}}}$ is obtained from (4.66) by inserting the renormalization constants obtained from (4.59) in the $\overline{\text{DR}}$ condition,

$$\widetilde{\text{Re}} \hat{\Sigma}^{\overline{\text{DR}}}(m^2) = \widetilde{\text{Re}} \Sigma(m^2) - \widetilde{\text{Re}} \Sigma(m^2)|_{\text{div}},$$

with $\Sigma(m^2)|_{\text{div}}$ being the divergent part of the self-energy regularized within dimensional reduction (i.e. the part proportional to Δ, (4.24)).

$$
\begin{aligned}
\delta A_b^{\overline{\text{DR}}} = \frac{1}{m_b U_{\tilde{b}11}} \Big[&- U_{\tilde{b}12} \widetilde{\text{Re}} \Sigma_{22}^{\tilde{b}}(m_{\tilde{b}_2}^2)|_{\text{div}} + \frac{U_{\tilde{b}22}}{2} \left(\widetilde{\text{Re}} \Sigma_{12}^{\tilde{b}}(m_{\tilde{b}_1}^2)|_{\text{div}} + \widetilde{\text{Re}} \Sigma_{12}^{\tilde{b}}(m_{\tilde{b}_2}^2)|_{\text{div}} \right) \\
&- \left(U_{\tilde{b}11}(A_b - \mu \tan \beta) - 2U_{\tilde{b}12} m_b \right) \widetilde{\text{Re}} \Sigma^b(m_b^2)|_{\text{div}} \\
&+ U_{\tilde{b}12} \Big(U_{\tilde{t}11}^2 \widetilde{\text{Re}} \Sigma_{11}^{\tilde{t}}(m_{\tilde{t}_1}^2)|_{\text{div}} + U_{\tilde{t}12}^2 \widetilde{\text{Re}} \Sigma_{22}^{\tilde{t}}(m_{\tilde{t}_2}^2)|_{\text{div}} \\
&\qquad - \frac{U_{\tilde{t}12} U_{\tilde{t}22}}{2} \left(\widetilde{\text{Re}} \Sigma_{12}^{\tilde{t}}(m_{\tilde{t}_1}^2)|_{\text{div}} + \widetilde{\text{Re}} \Sigma_{12}^{\tilde{t}}(m_{\tilde{t}_2}^2)|_{\text{div}} \right) \Big) \\
&- 2U_{\tilde{b}12} m_t \widetilde{\text{Re}} \Sigma^t(m_t^2)|_{\text{div}} - U_{\tilde{b}12} \cos 2\beta \, \delta M_W^2|_{\text{div}} \\
&+ \left(U_{\tilde{b}12} 4M_W^2 \frac{\tan \beta}{(1 + \tan^2 \beta)^2} + m_b U_{\tilde{b}11} \mu|_{\text{div}} \right) \delta \tan \beta + m_b U_{\tilde{b}11} \tan \beta \, \delta \mu|_{\text{div}} \Big].
\end{aligned}
\tag{4.68}
$$

The dependent counterterms for $m_{\tilde{b}_1}$ and $Y_{\tilde{b}}$ can be expressed through the independent ones and are given by

$$
\begin{aligned}
\delta m_{\tilde{b}_1}^2 = \frac{1}{U_{\tilde{b}11}^2} \Big[&U_{\tilde{b}12}^2 \delta m_{\tilde{b}_2}^2 + \left(2U_{\tilde{b}11} U_{\tilde{b}12}(A_b - \mu \tan \beta) + 2m_b(1 - 2U_{\tilde{b}12}^2) \right) \delta m_b \\
&+ \left(1 - 2U_{\tilde{b}12}^2 \right) \left(U_{\tilde{t}11}^2 \delta m_{\tilde{t}_1}^2 + U_{\tilde{t}12}^2 \delta m_{\tilde{t}_2}^2 - 2U_{\tilde{t}12} U_{\tilde{t}22} \delta Y_{\tilde{t}} - 2m_t \delta m_t - \cos 2\beta \delta M_W^2 \right) \\
&+ \left(4M_W^2 \frac{\tan \beta}{(1 + \tan^2 \beta)^2} \left(1 - 2U_{\tilde{b}12}^2 \right) - 2U_{\tilde{b}11} U_{\tilde{b}12} m_b \mu \right) \delta \tan \beta \\
&- 2U_{\tilde{b}11} U_{\tilde{b}12} m_b \tan \beta \delta \mu \Big],
\end{aligned}
\tag{4.69}
$$

$$
\begin{aligned}
\delta Y_{\tilde{b}} = \frac{1}{U_{\tilde{b}22}} \Big[&U_{\tilde{b}12} \delta m_{\tilde{b}_2}^2 + U_{\tilde{b}11} m_b \delta A_b + \left(U_{\tilde{b}11} (A_b - \mu \tan \beta) - 2U_{\tilde{b}12} m_b \right) \delta m_b \\
&+ U_{\tilde{b}12} \left(-U_{\tilde{t}11}^2 \delta m_{\tilde{t}_1}^2 - U_{\tilde{t}12}^2 \delta m_{\tilde{t}_2}^2 + 2U_{\tilde{t}12} U_{\tilde{t}22} \delta Y_{\tilde{t}} + 2m_t \delta m_t \right) \\
&- U_{\tilde{b}11} m_b \tan \beta \, \delta \mu + U_{\tilde{b}12} \cos 2\beta \, \delta M_W
\end{aligned}
$$

$$- \left(U_{\tilde{b}11} m_b \mu + 4 U_{\tilde{b}12} M_W^2 \frac{\tan \beta}{(1 + \tan^2 \beta)^2} \right) \delta \tan \beta \Big] . \tag{4.70}$$

As in the light-flavor case, the dependent mass parameter gets a finite shift. The pole mass of the lightest bottom squark is hence given via

$$(m_{\tilde{b}_1}^{\text{pole}})^2 = m_{\tilde{b}_1}^2 + \left(\delta m_{\tilde{b}_1}^2 - \widetilde{\text{Re}} \Sigma_{11}^{\tilde{b}}(m_{\tilde{b}_1}^2) \right) . \tag{4.71}$$

Besides this choice of fixing the counterterms in the sbottom sector, there are other possibilities corresponding to different renormalization schemes. Different choices of renormalization conditions have been investigated in [144] and [145], while in the latter a further renormalization condition was imposed to fix the mass of the dependent bottom-squark on its mass shell. The "$m_b^{\overline{\text{DR}}}$ and $A_b^{\overline{\text{DR}}}$" scheme given above was found to be reliable for the investigated parameter spaces. Nevertheless, when considering NLO EW calculations for sbottom-pair production, we will check whether the renormalization scheme considered is reliable by comparing the finite contribution of the dependent counterterms to their tree-level value.

In Chapter 6 we deal with final-state bottom squarks, which have to fulfill on-shell properties. Using the "$m_b^{\overline{\text{DR}}}$ and $A_b^{\overline{\text{DR}}}$" scheme, $\tilde{b}_2$ is defined on-shell by (4.65) fixing its on-shell (pole) mass to be the tree-level mass at all orders in perturbation theory. Due to (4.71) the $\tilde{b}_1$ pole-mass differs from its tree-level mass and the finite mass-shift has to be taken into account when $\tilde{b}_1$ appears in an external line. However, using the $\tilde{b}_1$ pole-mass everywhere, i.e. also for the internal bottom-quark propagators, spoils the tree-level relations of this sector which are crucial to guarantee the cancellation of the UV divergences. A naive solution to this problem would be to use different mass values $m_{\tilde{b}_1}$ and $m_{\tilde{b}_1}^{\text{pole}}$ as internal and external mass parameters. However, this leads to inconsistencies related to the IR structure of the virtual and real amplitudes. As we will see in Section 4.5, IR singularities have to cancel in sufficient inclusive observables. Supposing soft photon emission, the matrix element in the singular region becomes proportional to the tree-level cross section (cf. (4.88)) times a universal factor which contains the singularity with the actual value depending on the mass of the particle that emits the soft photon (cf. (4.91)). Using a different mass for the evaluation of the virtual amplitudes than used for the external particle, obviously spoils the cancellation of the IR singularities. In addition, if the on-shell mass is lighter than the tree-level mass, one has to deal with unphysical resonances in the real-emission amplitudes due to the "decay" $\tilde{b}_1^{\text{tree}} \to \tilde{b}_1^{\text{pole}} \gamma$.

One approach to circumvent this problem is to use the pole-mass everywhere for the real emission amplitudes which solves the problem of unphysical resonances. For the virtual amplitudes one can use the fact that the IR behavior manifests itself in some scalar loop-integral functions. The tree-level mass is used everywhere as internal mass-parameter except for the IR singular functions which have to be evaluated using the pole-mass. By doing so, as well the UV divergences as the IR singularities cancel.

A second approach is to impose an additional renormalization condition which ensures the $\tilde{b}_1$ mass to be on-shell as suggested in [145].[4] This requires an input that restores

---

[4]This extra condition overconstraints the bottom-squark sector.

symmetries, i.e. this imposes $M_{\tilde{t}_L}^2 \neq M_{\tilde{b}_L}^2$ in (4.50). It has the advantage that the sbottom-mass mixing-matrix correctly rotates the pole masses (instead of the tree-level masses).

In the case of $\tilde{b}_\alpha \tilde{b}_\alpha^*$ production we use an approach similar to the first one, i.e. using two different masses in the virtual contributions for the internal and external $\tilde{b}_1$. For the processes considered at NLO EW, besides field renormalization only the sbottom mass has to be renormalized. In particular we do not need to renormalize the sbottom mixing-matrix. The tree-level relations requiring a tree-level sbottom mass in order to cancel the UV divergences hence are only needed for the renormalized sbottom self-energy, eq. (4.59a) for $\tilde{q} = \tilde{b}$. Therefore, we calculate the analytic expression for the renormalized self-energy $\hat{\Sigma}_{11}^{\tilde{b}}$ by using the tree-level sbottom mass. After expressing the amplitude in terms of renormalized quantities only, we can safely exchange $\tilde{b}_1^{\text{tree}} \to \tilde{b}_1^{\text{pole}}$. In practice, we hence use the tree-level mass only for calculating the analytic expression for $\hat{\Sigma}_{11}^{\tilde{b}}$ and use the pole mass elsewhere. In particular we also use the pole mass in the internal sbottom propagator at tree-level. This introduces a contribution to the tree-level cross section which is formally one-loop,

$$\frac{1}{p^2 - m_{\tilde{b}_1}^2 - \delta m_{\tilde{b}_1}^2 + \widetilde{\text{Re}}\Sigma_{11}^{\tilde{b}}} = \frac{1}{p^2 - m_{\tilde{b}_1}^2} - \frac{-\delta m_{\tilde{b}_1}^2 + \widetilde{\text{Re}}\Sigma_{11}^{\tilde{b}}}{(p^2 - m_{\tilde{b}_1}^2)^2} + \dots . \tag{4.72}$$

The structure of the last term in (4.72) is exactly the same as the one originating from the counterterm contribution. Hence the one-loop contribution induced by using the pole mass in the LO amplitude is correctly taken into account by means of the following shift,

$$\delta m_{\tilde{b}_1}^2 \to \widetilde{\text{Re}}\Sigma_{11}^{\tilde{b}}. \tag{4.73}$$

Renormalization of the Glunio Sector

The gluino is renormalized on-shell. Since the gluino mass is determined through the soft breaking parameter M_3, cf. (2.67), imposing renormalization conditions on the gluino mass $m_{\tilde{g}}$ is equivalent to imposing them on M_3. After splitting the bare gluino field and mass into renormalized quantities plus counterterms,

$$m_{\tilde{g}}^0 = m_{\tilde{g}} + \delta m_{\tilde{g}} , \tag{4.74a}$$

$$\tilde{g}^0 = (1 + \frac{1}{2}\delta Z^{\tilde{g}})\tilde{g} , \qquad \text{with } \Psi_{\tilde{g}} = \begin{pmatrix} \tilde{g} \\ \bar{\tilde{g}} \end{pmatrix}, \tag{4.74b}$$

the Lagrangian reads (with a factor 1/2 because of the Majorana nature of the gluino)

$$\begin{aligned} \mathcal{L}_{\tilde{g}}^0 = {}& \frac{1}{2}\bar{\Psi}_{\tilde{g}}(\not{p} - m_{\tilde{g}})\Psi_{\tilde{g}} \\ & + \frac{1}{2}\bar{\Psi}_{\tilde{g}}\left[\frac{1}{2}\not{p}(\delta Z^{\tilde{g}} + \delta Z^{\tilde{g}*}) - m_{\tilde{g}}(\delta Z^{\tilde{g}}P_L + \delta Z^{\tilde{g}*}P_R) - \delta m_{\tilde{g}}\right]\Psi_{\tilde{g}} . \end{aligned} \tag{4.75}$$

The renormalized self-energies are then given by

$$\hat{\Sigma}^{\tilde{g}}_{L/R}(p^2) = \Sigma^{\tilde{g}}_{L/R}(p^2) + \frac{1}{2}\left(\delta Z^{\tilde{g}} + \delta Z^{\tilde{g}*}\right), \tag{4.76a}$$

$$\hat{\Sigma}^{\tilde{g}}_{SL}(p^2) = \Sigma^{\tilde{g}}_{SL}(p^2) - \left(m_{\tilde{g}}\delta Z^{\tilde{g}} + \delta m_{\tilde{g}}\right), \tag{4.76b}$$

$$\hat{\Sigma}^{\tilde{g}}_{SR}(p^2) = \Sigma^{\tilde{g}}_{SR}(p^2) - \left(m_{\tilde{g}}\delta Z^{\tilde{g}*} + \delta m_{\tilde{g}}\right). \tag{4.76c}$$

Due to the Majorana nature of the gluino one finds in the CP-conserving case that $\Sigma^{\tilde{g}}_L = \Sigma^{\tilde{g}}_R$ and $\Sigma^{\tilde{g}}_{SL} = \Sigma^{\tilde{g}}_{SR}$. Imposing the on-shell conditions analogously to the quark case, cf. (4.37), the renormalization constants are given via

$$\delta m_{\tilde{g}} = m_{\tilde{g}}\widetilde{\mathrm{Re}}\left[\Sigma^{\tilde{g}}_L(m_{\tilde{g}}^2)\right] + \widetilde{\mathrm{Re}}\left[\Sigma^{\tilde{g}}_{SL}(m_{\tilde{g}}^2)\right], \tag{4.77a}$$

$$\delta Z^{\tilde{g}} = -\widetilde{\mathrm{Re}}\Sigma^{\tilde{g}}_L(m_{\tilde{g}}^2) + 2m_{\tilde{g}}^2\frac{\partial}{\partial p^2}\widetilde{\mathrm{Re}}\Sigma^{\tilde{g}}_L(p^2)\Big|_{p^2=m_{\tilde{g}}^2} + 2m_{\tilde{g}}\frac{\partial}{\partial p^2}\widetilde{\mathrm{Re}}\Sigma^{\tilde{g}}_{SL}(p^2)\Big|_{p^2=m_{\tilde{g}}^2}. \tag{4.77b}$$

Renormalization of the Strong Coupling Constant

The strong coupling constant g_s of QCD grows large at large distances which renders an on-shell renormalization at zero-momentum transfer not well-defined. However, due to asymptotic freedom of QCD, perturbation theory can be applied for scales at which the strong fine structure constant $\alpha_s = g_s^2/4\pi$ is smaller than one. The running of α_s from a given scale M to a scale μ is at one-loop determined via

$$\alpha_s(\mu^2) = \frac{\alpha_s(M^2)}{1 + \frac{\alpha_s(M^2)}{4\pi}\beta_0\log\frac{\mu^2}{M^2}}, \tag{4.78}$$

with β_0 depending on the particle content of the theory. (4.78) gets additional terms when higher order contributions are taken into account. The most precise value of the parameter α_s extracted from comparison of experimental data to theoretical predictions is given in the $\overline{\mathrm{MS}}$ scheme at the scale $\mu = M_Z$ [146],

$$\alpha_s(M_Z^2) = 0.1184 \pm 0.0007. \tag{4.79}$$

This value together with the running of α_s taking into account five active flavors, is widely used for fits and extraction of data in QCD, as e.g. the extraction of the PDFs. Taking into account only five active flavors is possible due to the so-called decoupling theorem [147,148]. It states that at scales much lower than the particle mass, its contribution to β_0 and hence the change in the running of α_s is not observable at low energies since it can be absorbed via a redefinition of α_s.

In order to be consistent when calculating hadronic cross sections, in particular when folding the PDFs with the calculated matrix element, cf. (4.22), it is crucial to use the same definition of the strong coupling constant. Defining the renormalized coupling constant via

$$g_s^0 = Z_{g_s}g_s = (1 + \delta Z_{g_s})g_s, \tag{4.80}$$

heavy-flavor effects can be excluded by a proper definition of the counterterm. In particular, the mass of the top quark, the gluinos, and the squarks has to be excluded from the running in order to retain five-flavor running within the MSSM. The corresponding counterterm reads

$$\delta Z_{g_s} = -\frac{\alpha_s}{4\pi}\left[\Delta\frac{\beta_0}{2} + \frac{1}{3}\ln\frac{m_t^2}{\mu^2} + \frac{N}{3}\ln\frac{m_{\tilde{g}}^2}{\mu^2} + \frac{1}{12}\sum_{\tilde{q}}\ln\frac{m_{\tilde{q}}^2}{\mu^2}\right],\tag{4.81}$$

$$\beta_0 = \Big(\underbrace{\frac{11}{3}N - \frac{2}{3}n_f}_{\text{light particles}}\Big) + \Big(\underbrace{-\frac{2}{3} - \frac{2}{3}N - \frac{n_f+1}{3}}_{\text{heavy particles}}\Big) = 3\,,\tag{4.82}$$

with $N = 3$ for $SU(3)$ and $n_f = 5$ active flavors. The contribution to β_0 can be divided into a part with contributions from light particles, the gluons and five light quarks, and a contribution from heavy particles, the top quark, the gluinos, and the squarks.

In supersymmetric QCD (SQCD) the qqg and $\tilde{q}\tilde{q}g$ coupling strength is given by g_s while the $q\tilde{q}\tilde{g}$ coupling is given by $\hat{g}_s$. The supersymmetric Slavnov–Taylor identities require that $g_s = \hat{g}_s$. However, performing the regularization in DREG to obtain the $\overline{\text{MS}}$ definition of α_s spoils SUSY and in particular the relation between the coupling constants. This is cured by renormalizing g_s and $\hat{g}_s$ independently and introducing a symmetry restoring counterterm for the strong scalar coupling $\hat{g}_s$ [18],

$$\hat{g}_s^0 = Z_{\hat{g}_s}\,\hat{g}_s = (1 + \delta Z_{\hat{g}_s})\,\hat{g}_s\,,\tag{4.83a}$$

$$\delta Z_{\hat{g}_s} = \delta Z_{g_s} + \frac{\alpha_s}{3\pi}\,.\tag{4.83b}$$

4.5 Infrared and Collinear Singularities

The UV divergences of last section arise from infinite loop-momenta and are therefore short distance effects. They display our ignorance on physics at high energies and have to be removed by renormalization. Besides these, quantum field theories contain singularities related to finite momenta. In particular, some of these singularities occur independently of the external momenta and are related to vanishing masses. Such singularities are generally called *mass singularities*. They result from loop integrals as well as from integrating the phase space of massless particles originating from real radiation processes. There are two types of mass singularities:

- *Infrared* or *soft singularities* are related to vanishing momenta and thus long-distance effects, i.e. when a (massive or massless) particle emits or absorbs a massless particle.

- *Collinear singularities* are related to collinear light-like momenta, i.e. when a massless particle emits or absorbs two massless collinear particles.

The physical origin of mass singularities is the presence of degeneracies in the initial and final states, respectively. In QED, for example, the states of a charged particle with an arbitrary number of soft photons are nearly degenerate, giving rise to IR singularities. They are

indistinguishable in real detectors due to its finite energy resolution. In the case of collinear singularities, the state of a light-like particle with momenta p is degenerate with the states of an arbitrary number of light-like particles with the same overall quantum numbers and momenta p_i if $p = \sum p_i$. These states are indistinguishable for a detector with finite angular resolution. In sufficient inclusive observables, all these states contribute simultaneously and the singularities cancel.

In the case of QED with finite fermion masses, the Bloch–Nordsieck theorem [149] states that for the cancellation of IR singularities it is sufficient to sum over all degenerate final states, i.e. all states with an arbitrary number of soft photons in the final state. A more general theorem, the Kinoshita–Lee–Nauenberg (KLN) theorem [150], states that as a consequence of unitarity, transition amplitudes are finite when summed over all degenerate initial and final states. Both theorems hold order-by-order in perturbation theory for unrenormalized and renormalized quantities as long as the renormalization schemes do not introduce mass singularities via the renormalization constants.

The cancellation of singularities arising from virtual corrections and real radiation is a non-trivial task since they originate from different phase-space regions. The most prominent methods to deal with this are phase-space slicing, see e.g. [135] and dipole subtraction [151–153].[5] In the phase-space slicing method, the soft and collinear regions of the phase-space are split off by introducing phase-space cut parameters. The singular region can then be integrated analytically and is added to the virtual contribution leading to a finite result. The hard real-emission contribution can be integrated numerically. The dependence on the cutoff parameters cancel in the sum of soft and hard real emission, provided the cutoff parameters are small enough. The dipole-subtraction method uses a completely different approach. The general idea of this method is to introduce a set of functions that have the same pointwise singular behavior as the real-emission contribution to the differential cross section. These so-called "dipoles" act as local counterterms and can be integrated analytically over the one-particle phase space. One now adds and subtracts these dipoles twice, once to the virtual contribution and once for the real-emission contribution to the differential cross section, and hence effectively adds a zero contribution. Each part is now finite and can be integrated numerically. The advantage of the dipole method is that no cutoff has to be introduced, with the result that the integration error within this method is typically one order of magnitude smaller, depending on the number of external particles. However, for two-to-two processes, as considered in this work, the accuracy derived using the phase-space-slicing method is by far sufficient, which renders the implementation of the far more sophisticated dipole method dispensable. As already mentioned in the last section, the mass singularities will be regularized by means of mass regularization, i.e. introducing a fictitious mass for the massless particles. Of course, the physical amplitude has to be independent of this introduced mass parameter since it has no physical meaning. The independence of the calculated cross section on the regularization and cutoff parameters can be used as a consistency check.

---

[5]Further details on the difference between these both methods can be found in [154].

4.5.1 Soft and Collinear Photon Emission

The real photon radiation processes considered in this work are of the form

$$a(p_1)\, b(p_2) \rightarrow c(p_3)\, d(p_4)\, \gamma(k), \tag{4.84}$$

with massless incoming particles a and b and massive outgoing particles c and d and the photon γ. At $\mathcal{O}(\alpha_s^2 \alpha)$ it is given by the squared matrix element of a QCD tree-level diagram with an external photon attached, $|\mathcal{M}_{ab \rightarrow cd\gamma}^{1,\frac{1}{2}}|^2$. Initial-state radiation only contributes if at least one of the partons is charged, i.e. either a quark or an anti-quark. The external states considered in this work are squarks, and therefore charged and massive.

Using the method of phase-space slicing, one can divide real photon emission into singular and non-singular regions. The non-singular regions are finite and can be integrated directly. In the singular regions, one has to introduce regulators in order to regularize the mass singularity and the integration is performed analytically. Soft singularities arise for $k^0 \rightarrow 0$ and collinear singularities for $p_i \cdot k \rightarrow 0$ for $i = \{1, 2\}$ since the other outgoing particles are massive. The soft-singular region is defined by the region where the energy of the photon is smaller than the cutoff $\Delta E = \delta_s \sqrt{\hat{s}}/2$, with the dimensionless parameter δ_s. The collinear region is defined as the region in which the angle between the charged particle and the emitted (hard) photon is smaller than an angular cutoff $\Delta\theta$, i.e. the photon is emitted collinear (but not soft). For practical reasons it is convenient to define $\delta_\theta = \cos(\Delta\theta)$, since the collinear region is then given via $|\cos(\theta)| < 1 - \delta_\theta$ which can be implemented easily in the numerical integration. The partonic cross section can be decomposed into a soft, a collinear, and a finite part

$$\mathrm{d}\hat{\sigma}_{12 \rightarrow 34\gamma}^{2,1} = \mathrm{d}\hat{\sigma}_{12 \rightarrow 34\gamma}^{2,1}\big|_{\mathrm{soft}} + \mathrm{d}\hat{\sigma}_{12 \rightarrow 34\gamma}^{2,1}\big|_{\mathrm{coll}} + \mathrm{d}\hat{\sigma}_{12 \rightarrow 34\gamma}^{2,1}\big|_{\mathrm{finite}}. \tag{4.85}$$

The considered process is given as a subscript for clarification and particles are labeled by $i = 1 \ldots 4$ according to the definition of momenta p_i in (4.84). In the soft and collinear region, the squared matrix element $|\mathcal{M}^{1,\frac{1}{2}}|^2$ factorizes into universal factors times the lowest order matrix element squared $|\mathcal{M}^{1,0}|^2$. The five-particle phase-space also factorizes into the four-particle phase-space of the particles $i = 1 \ldots 4$ times the photon phase-space. In the soft region, the matrix element of a photon emitted from particle i factorizes according to

$$\mathcal{M}_{12 \rightarrow 34\gamma}^{1,\frac{1}{2}}\big|_{\mathrm{soft}} = \mathcal{M}_{12 \rightarrow 34}^{1,0} \sum_{i=1}^{4} \frac{2 e e_i\, p_i \epsilon_\lambda^*}{\sigma_i 2 p_i k + \mathrm{i}\epsilon}, \tag{4.86}$$

with $\sigma_i = \pm 1$ depending on whether the particle is incoming or outgoing, respectively. e_i is the charge of the ith particle in terms of the positron charge e and ϵ_λ is the polarization vector of the emitted photon. Since $p_i^2 \neq 0$, the denominator is always non-zero and the $\mathrm{i}\epsilon$ can be omitted.[6] The cross section in the soft region is obtained by squaring the matrix element (4.86). Since the soft photons are not detected, one has to sum over their polarizations and

---

[6] In the case of a massless particle i, one obtains contributions that are soft and collinear. These are regularized by introducing a fictitious particle mass m_i.

integrate their momenta over the available phase space. Owing to charge conservation, the gauge dependent parts of the polarization sum (A.16) vanish and one is left with

$$\sum_{\lambda=1}^{2} \epsilon_\mu^*(k,\lambda)\epsilon_\nu(k,\lambda) = -g_{\mu\nu} \,. \tag{4.87}$$

Regularizing the IR-singular phase-space integral by a small photon mass λ_γ, and hence $E_\gamma = \sqrt{k^2 + \lambda_\gamma^2}$, the partonic differential cross section in the soft-photon approximation is given by

$$\mathrm{d}\hat\sigma_{12\to34\gamma}^{2,1}\big|_{\mathrm{soft}} = -e^2 \mathrm{d}\hat\sigma_{12\to34}^{2,1} \int_{|\vec{k}|\le\Delta E} \frac{\mathrm{d}^3k}{(2\pi)^3 2E_\gamma} \sum_{i,j=1}^{4} e_i e_j \sigma_i \sigma_j \frac{p_i p_j}{p_i k \, p_j k} \tag{4.88}$$

$$= -\frac{\alpha}{2\pi} \mathrm{d}\hat\sigma_{12\to34}^{2,1} \sum_{i,j=1;i<j}^{4} e_i e_j \sigma_i \sigma_j \mathcal{I}_{ij} \,, \tag{4.89}$$

with the symmetric phase-space integrals $\mathcal{I}_{ij}$,

$$\mathcal{I}_{ij} = \int_{|\vec{k}|\le\Delta E} \frac{\mathrm{d}^3k}{2\pi E_\gamma} \frac{p_i p_j}{p_i k \, p_j k} \,. \tag{4.90}$$

The general expressions of these integrals are given in [135]. In the limit of vanishing initial-state masses (and two massive final-state particles), i.e. $m_{1,2} \ll \sqrt{S}$, they can be further simplified and are given by (with $\lambda = \lambda_\gamma$)

$$
\begin{aligned}
\mathcal{I}_{ii} &= \ln\left(\frac{4(\Delta E)^2}{\lambda^2}\right) + \ln\left(\frac{m_i^2}{\hat{s}_{12}}\right), && \text{for } i = \{1,2\}, \\
\mathcal{I}_{ii} &= \ln\left(\frac{4(\Delta E)^2}{\lambda^2}\right) + \frac{1}{\beta_i}\ln\left(\frac{1-\beta_i}{1+\beta_i}\right), && \text{for } i = \{3,4\}, \\
\mathcal{I}_{12} &= \sum_{i=1,2}\left[\ln\left(\frac{\hat{s}_{12}}{m_i^2}\right)\ln\left(\frac{4(\Delta E)^2}{\lambda^2}\right) - \frac{1}{2}\ln^2\left(\frac{\hat{s}_{12}}{m_i^2}\right) - \frac{\pi^2}{3}\right], \\
\mathcal{I}_{34} &= \frac{1}{v_{34}}\sum_{i=3,4}\left[\ln\left(\frac{1+\beta_i}{1-\beta_i}\right)\ln\left(\frac{4(\Delta E)^2}{\lambda^2}\right) - 2\mathrm{Li}_2\left(\frac{2\beta_i}{1+\beta_i}\right) - \frac{1}{2}\ln^2\left(\frac{1-\beta_i}{1+\beta_i}\right)\right], \\
\mathcal{I}_{ij} &= \ln\left(\frac{\hat{s}_{ij}^2}{m_i^2 m_j^2}\right)\ln\left(\frac{4(\Delta E)^2}{\lambda^2}\right) - \frac{1}{2}\ln^2\left(\frac{\hat{s}_{12}}{m_i^2}\right) - \frac{1}{2}\ln^2\left(\frac{1-\beta_i}{1+\beta_i}\right) - \frac{\pi^2}{3} \\
&\quad - 2\mathrm{Li}_2\left(1 - \frac{2p_i^0 p_j^0}{\hat{s}_{ij}}(1+\beta_j)\right) - 2\mathrm{Li}_2\left(1 - \frac{2p_i^0 p_j^0}{\hat{s}_{ij}}(1-\beta_j)\right), && \text{for } \begin{array}{l} i = \{1,2\}, \\ j = \{3,4\}, \end{array}
\end{aligned}
\tag{4.91}
$$

with $\hat{s}_{ij} = 2p_i \cdot p_j$, $\beta_i = |\vec{p}_i|/p_i^0$, $v_{ij} = \sqrt{1 - 4m_i m_j/\hat{s}_{ij}^2}$, and $\Delta E = \sqrt{\hat{s}_{12}}\delta_s/2$. The initial-state masses are used as a regulator in the singular region and set to a common value $m_1 = m_2 = m_\lambda$, and are neglected everywhere else. The dilogarithm $\mathrm{Li}_2(x)$ is defined as

$$\mathrm{Li}_2(x) = -\int_0^x \frac{\mathrm{d}t}{t} \ln(1-t) \,. \tag{4.92}$$
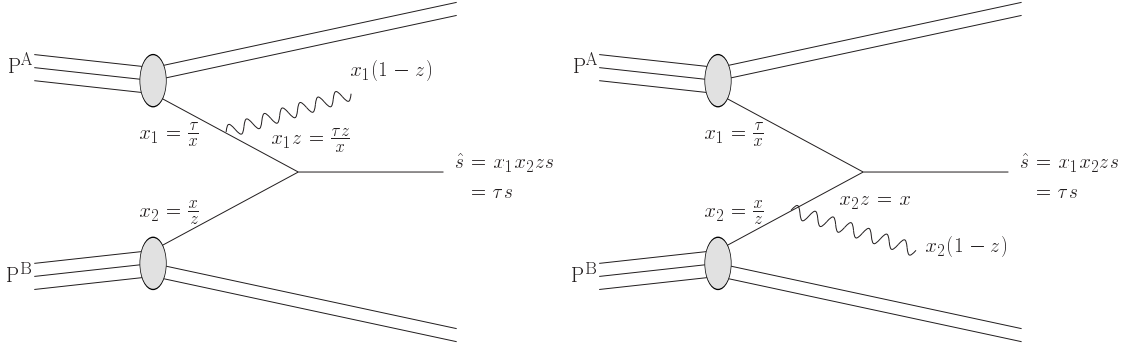
Figure 4.3: Definition of the momentum fractions in hadronic collisions for collinear splitting. Parton 1 from hadron A carries momentum fraction x_1 and parton 2 from hadron B momentum fraction x_2. The collinear photon carries away a momentum fraction $(1 - z)$. The remaining c.m. energy for the hard process is hence given by $\hat{s} = x_1 x_2 z s = \tau s$. Collinear splitting from both partons has to be taken into account.

The hadronic cross section in the soft regime is derived by inserting $\hat{\sigma}^{2,1}_{12 \to 34\gamma}(\hat{s}_{12})\big|_{\text{soft}}$ obtained from (4.88) into (4.22) for the convolution with the parton distribution functions.

Since the initial-state quarks are treated massless, one is also confronted with initial-state collinear singularities. In Figure 4.3 the momentum fractions carried by the partons and the collinear photon are defined. From this definition one has $\hat{s} = z\hat{s}_{12}$, i.e. $\hat{s}$ remains the c.m. energy of the hard process as defined in (4.21). Since the collinear photon takes away some of the initial partonic energy, the partonic cross section is not directly proportional to the tree-level cross section. However, it can be written in terms of the tree-level cross section, convoluted with a universal factor,

$$\mathrm{d}\hat{\sigma}^{2,1}_{12 \to 34\gamma}(\hat{s}_{12})\big|_{\text{coll}} = \frac{\alpha(e_i^2 + e_j^2)}{2\pi} \int_{z_0}^{1-\delta_s} \mathrm{d}z \; \kappa_{qq}(z, \hat{s}_{12}) \, \mathrm{d}\hat{\sigma}^{2,0}_{12 \to 34}(z\hat{s}_{12}) \,, \qquad (4.93)$$

The lower bound $z_0 = (m_3^2 + m_4^2)/\hat{s}$ corresponds to production at threshold. The universal factor κ_{qq} contains the quark–photon splitting function P_{qq} (compare also with (4.17) for the quark–gluon splitting),

$$\kappa_{qq}(z, \hat{s}) = \frac{1 + z^2}{1 - z} \ln\left(\frac{\hat{s}\delta_\theta}{2m_\lambda}\right) - \frac{2z}{1 - z} \,, \qquad\qquad P_{qq}(z) = \frac{1 + z^2}{1 - z} \,. \qquad (4.94)$$

The upper integration boundary in (4.93) is lowered by δ_s in order to avoid double counting of the soft regime, since the soft and collinear regime is already incorporated in (4.88). Care has to be taken when the partonic cross section is convoluted with the PDFs. With the definition of the momentum fractions in Figure 4.3, the hadronic cross section in the collinear region is given by

$$\sigma^{2,1}_{12 \to 34\gamma}(S)\big|_{\text{coll}} = \int_{\tau_0}^{1-\delta_s} \mathrm{d}\tau \int_{\tau}^{1-\delta_s} \mathrm{d}x \int_{x}^{1-\delta_s} \mathrm{d}z \, \frac{1}{xz} \, \hat{\sigma}^{2,1}_{12 \to 34\gamma}(\hat{s})\big|_{\text{coll}} \qquad (4.95)$$

$$\times \left\{ \frac{1}{1 + \delta_{q_1 q_2}} \left[f_{q_1}^A\left(\frac{\tau}{x}, \mu_F\right) f_{q_2}^B\left(\frac{x}{z}, \mu_F\right) + f_{q_2}^A\left(\frac{x}{z}, \mu_F\right) f_{q_1}^B\left(\frac{\tau}{x}, \mu_F\right) \right] \right\} \,,$$

$$= \int_{\tau_0}^{1-\delta_s} \mathrm{d}\tau \frac{\mathrm{d}L_{q_1 q_2}^{\mathrm{coll}}}{\mathrm{d}\tau} \,\hat{\sigma}_{12\to34\gamma}^{2,1}(\hat{s})\Big|_{\mathrm{coll}}. \tag{4.96}$$

The parton luminosity in the collinear region is given by

$$\frac{\mathrm{d}L_{\xi_i\xi_j}^{\mathrm{coll}}}{\mathrm{d}\tau} = \frac{1}{1+\delta_{q_1 q_2}} \int_{\tau}^{1-\delta_s} \frac{\mathrm{d}x}{x} \int_x^{1-\delta_s} \frac{\mathrm{d}z}{z} \left[f_{q_1}^A\!\left(\frac{\tau}{x},\mu_F\right) f_{q_2}^B\!\left(\frac{x}{z},\mu_F\right) + f_{q_2}^A\!\left(\frac{x}{z},\mu_F\right) f_{q_1}^B\!\left(\frac{\tau}{x},\mu_F\right) \right]. \tag{4.97}$$

When combining the cross section of the soft and collinear region with the virtual contributions $\sigma_{12\to34}^{2,1}(S)\big|_{\mathrm{virt}}$, the IR cutoff λ_γ cancels, and the remaining cross section is IR finite. However, the initial-state collinear singularities do not completely cancel. By taking the QED evolution of the partons into account, these are absorbed into the definition of the renormalized parton distribution functions, similar to the QCD case in (4.13). This is achieved by the following redefinition of the quark distribution function [155, 156],

$$\begin{aligned} f_q(x,\mu_F) &\to f_q(x,\mu_F) \left(1 - \frac{\alpha e_q^2}{\pi}\left\{\kappa_{v+s} + \frac{1}{4}f_{v+s}\right\}\right) \\ &\quad - \frac{\alpha e_q^2}{2\pi} \int_x^{1-\delta_s} \frac{\mathrm{d}z}{z} f_q\!\left(\frac{x}{z},\mu_F\right)\!\left(\kappa_c(z) - f_c(z)\right), \end{aligned} \tag{4.98}$$

where e_q denotes the electric charge of quark q and

$$\begin{aligned} \kappa_{v+s} &= 1 - \ln\delta_s - \ln^2\delta_s + \left(\ln\delta_s + \frac{3}{4}\right)\ln\!\left(\frac{\mu_F^2}{m_q^2}\right), \\ \kappa_c(z) &= P_{qq}(z)\ln\!\left(\frac{\mu_F^2}{m_q^2}\frac{1}{(1-z)^2} - 1\right), \end{aligned} \tag{4.99}$$

with the splitting function (4.94). In the DIS scheme, the factorization-scheme dependent functions are given by

$$\begin{aligned} f_{v+s} &= 9 + \frac{2\pi^2}{3} + 3\ln\delta_s - 2\ln^2\delta_s\,, \\ f_c(z) &= P_{qq}(z)\ln\!\left(\frac{1-z}{z}\right) - \frac{3}{2}\frac{1}{1-z} + 2z + 3\,. \end{aligned} \tag{4.100}$$

Making this replacement in the convolution of the $\mathcal{O}(\alpha_s^2)$ partonic cross section $\hat{\sigma}_{12\to34}^{2,0}$, one gets an extra contribution of $\mathcal{O}(\alpha_s^2\alpha)$ that cancels the remaining collinear singularities,

$$\begin{aligned} \sigma_{12\to34}^{2,0}(S) &= \frac{1}{1+\delta_{q_1 q_2}} \int_{\tau_0}^1 \mathrm{d}\tau \int_\tau^1 \frac{\mathrm{d}x}{x} \left[f_{q_1}^A\!\left(\frac{\tau}{x},\mu\right) f_{q_2}^B(x,\mu) + f_{q_2}^A(x,\mu)\, f_{q_1}^B\!\left(\frac{\tau}{x},\mu\right) \right] \hat{\sigma}_{12\to34}^{2,0}(\hat{s}) \\ &\to \int_{\tau_0}^1 \mathrm{d}\tau \frac{\mathrm{d}L_{q_1 q_2}}{\mathrm{d}\tau} \,\hat{\sigma}_{12\to34}^{2,0}(\hat{s}) \end{aligned} \tag{4.101a}$$

$$- \frac{\alpha}{\pi}\left(e_i^2 + e_j^2\right) \int_{\tau_0}^1 \mathrm{d}\tau \frac{\mathrm{d}L_{q_1 q_2}}{\mathrm{d}\tau}\left(\kappa_{v+s} + \frac{1}{4}f_{v+s}\right)\hat{\sigma}_{12\to34}^{2,0}(\hat{s}) \tag{4.101b}$$

$$- \frac{\alpha}{2\pi}\left(e_i^2 + e_j^2\right) \int_{\tau_0}^{1-\delta_s} \mathrm{d}\tau \frac{\mathrm{d}L_{q_1 q_2}^{\mathrm{coll}}}{\mathrm{d}\tau}\left(\kappa_c(z) - f_c(z)\right) \hat{\sigma}_{12\to34}^{2,0}(\hat{s}) \tag{4.101c}$$

$$= \sigma_{12\to34}^{2,0}(S) + \sigma_{12\to34}^{2,1}(S)\big|_{\mathrm{PDF}}^\gamma + \sigma_{12\to34\gamma}^{2,1}(S)\big|_{\mathrm{PDF}}^\gamma\,.$$
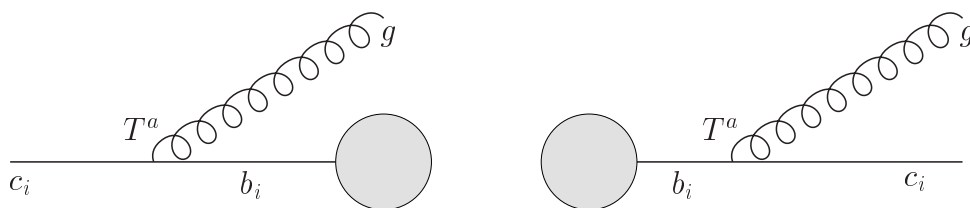
Figure 4.4: Conventions for color indices to keep track of the color correlation of the amplitudes. b_i and c_i are color indices belonging to the fundamental representation and a is the color index of the gluon belonging to the adjoint representation. The blob represents the tree-level amplitude. Left: Initial-state radiation. Right: Final-state radiation.

$\sigma^{2,1}_{12 \to 34}(S)\big|^\gamma_{\text{PDF}}$, given by (4.101b), cancels the remaining collinear singularities emerging from virtual contributions, while $\sigma^{2,1}_{12 \to 34\gamma}(S)\big|^\gamma_{\text{PDF}}$ given by (4.101c), cancels the remaining collinear singularities originating from real photon emission.

4.5.2 Soft and Collinear Gluon Emission

The real gluon radiation processes considered in this work are generally denoted by

$$a(p_1)\, b(p_2) \to c(p_3)\, d(p_4)\, g(k), \tag{4.102}$$

with a, b, c, and d as in (4.84). At $\mathcal{O}(\alpha_s^2 \alpha)$ they are given by the interference term of a tree-level QCD matrix element and a tree-level EW matrix element, both with an external gluon attached,

$$2\mathrm{Re}(\mathcal{M}^{\frac{3}{2},0}_{12 \to 34g}(\mathcal{M}^{\frac{1}{2},1}_{12 \to 34g})^\dagger)\,.$$

The real gluon can in principle be emitted from any colored particle. However, real gluon radiation from external gluons does not contribute at $\mathcal{O}(\alpha_s^2 \alpha)$ since in this case there is no matrix element $\mathcal{M}^{\frac{1}{2},1}_{12 \to 34g}$ which would be necessary to obtain the desired order in perturbation theory.

As in the case of real photon emission, one can divide real gluon emission into singular and non-singular regions using the phase-space slicing method. With help of the slicing parameters ΔE and $\Delta \theta$ or δ_s and δ_θ, respectively, the partonic cross section for real gluon emission can be decomposed into a soft, a collinear, and a finite part,

$$\mathrm{d}\hat{\sigma}^{2,1}_{12 \to 34g} = \mathrm{d}\hat{\sigma}^{2,1}_{12 \to 34g}\big|_{\text{soft}} + \mathrm{d}\hat{\sigma}^{2,1}_{12 \to 34g}\big|_{\text{coll}} + \mathrm{d}\hat{\sigma}^{2,1}_{12 \to 34g}\big|_{\text{finite}}\,. \tag{4.103}$$

Since the emitted gluon changes the color of the particle it is emitted off, one has to take into account the color correlation of the amplitudes, as depicted in Figure 4.4. The following notation will be used to keep track of the color factors.

Let $|c_1, \ldots, c_m\rangle$ denote a complete color basis. The color-stripped matrix element is obtained by projecting the colored matrix element $\mathcal{M}^{i,j}$ on the color basis. For m external particles carrying momenta p_i and color c_i the color-stripped matrix element is given by

$$\mathcal{M}^{i,j\ c_1 \ldots c_m}_{12 \to 3 \ldots m} = \left\langle c_1, \ldots, c_m \big| \mathcal{M}^{i,j}_{12 \to 3 \ldots m} \right\rangle. \tag{4.104}$$

For the color structure in the case of real gluon emission it is convenient to associate a color charge $\mathbf{T}_i$ with the emission of a gluon of color a from parton i. The action of this color charge onto the color space is given by

$$\left\langle c_1 \ldots c_i \ldots c_m \middle| \mathbf{T}_i \middle| b_1 \ldots b_i \ldots b_m \right\rangle = \delta_{c_1 b_1} \ldots \hat{T}^a_{c_i b_i} \ldots \delta_{c_m b_m}, \tag{4.105}$$

with

$$\hat{T}^a_{c_i b_i} = \begin{cases} -T^a_{b_i c_i}, & i: \text{ incoming particle, or outgoing anti-particle,} \\ T^a_{c_i b_i}, & i: \text{ outgoing particle, or incoming anti-particle.} \end{cases} \tag{4.106}$$

The color charge further obeys the following relations,

$$\mathbf{T}_i \mathbf{T}_j = \mathbf{T}_j \mathbf{T}_i, \quad \text{for } i \neq j; \qquad \mathbf{T}_i^2 = C_F = \frac{4}{3}. \tag{4.107}$$

In the soft region, the color-stripped matrix element of a gluon emitted off from particle i can be written as

$$\mathcal{M}^{i,j\, c_1 \ldots c_4}_{12 \to 34g} \Big|_{soft} = \sum_{i=1}^{4} \frac{2 g_s\, p_i \epsilon^*}{2 p_i k \pm i\epsilon} \hat{T}^a_{c_i b_i} \mathcal{M}^{i,j\, c_1 \ldots b_i \ldots c_4}_{12 \to 34g}. \tag{4.108}$$

The $i\epsilon$ prescription can be neglected for the same reason as in the real photon emission case. The cross section in the soft region is obtained by squaring the matrix element (4.108) and summing over color. After summing over the gluon polarizations and regularizing the integration over the soft gluon phase-space via a small gluon mass λ_g, the partonic differential cross section in the soft gluon approximation can be written as

$$d\hat{\sigma}^{2,1}_{12 \to 34g} \Big|_{soft} = -\frac{\alpha_s}{2\pi} \left\{ \sum_{i,j=1; i<j}^{4} \mathcal{I}_{ij} \mathcal{F}_{ij} \right\} \frac{dt}{16\pi \hat{s}^2}, \tag{4.109}$$

where the phase-space integrals $\mathcal{I}_{ij}$ are given in eq. (4.91)[7] and $\mathcal{F}_{ij}$ denote color correlated amplitudes. At $\mathcal{O}(\alpha_s^2 \alpha)$ the $\mathcal{F}_{ij}$ are given by

$$\begin{aligned}
\mathcal{F}_{ij} &= 2\,\mathrm{Re}\left\{ \left\langle \mathcal{M}^{0,1}_{12 \to 34} \middle| \mathbf{T}_i \mathbf{T}_j \middle| \mathcal{M}^{1,0}_{12 \to 34} \right\rangle \right\} \\
&= 2\,\mathrm{Re}\left\{ \left[\mathcal{M}^{0,1\, c_1 \ldots b_i \ldots b_j \ldots c_4}_{12 \to 34} \right]^* \hat{T}^a_{b_i c_i} \hat{T}^a_{b_j c_j} \mathcal{M}^{1,0\, c_1 \ldots c_i \ldots c_j \ldots c_4}_{12 \to 34} \right\}.
\end{aligned} \tag{4.110}$$

In the collinear region, the partonic cross section is again given by a convolution integral, similar to (4.93). Using the same definition of the momenta as shown in Figure 4.3, we have

$$d\hat{\sigma}^{2,1}_{12 \to 34g}(\hat{s}_{12}) \Big|_{coll} = \frac{\alpha_s C_F}{\pi} \int_{z_0}^{1-\delta_s} dz\, \kappa_{qq}(z, \hat{s}_{12})\, d\hat{\sigma}^{1,1}_{12 \to 34}(z \hat{s}_{12}), \tag{4.111}$$

with κ_{qq} as defined in (4.94). From this, one can see that collinear singularities due to gluon radiation are only present for processes that have non-vanishing QCD–EW interference

---

[7]In this case λ is the fictitious gluon mass.

contributions at tree level. The hadronic cross section in the collinear region can be expressed with help of (4.97) and is given by

$$
\sigma_{12\to34\gamma}^{2,1}(S)\big|_{\mathrm{coll}} = \int_{\tau_0}^{1-\delta_s} \mathrm{d}\tau \frac{\mathrm{d}L_{q_1q_2}^{\mathrm{coll}}}{\mathrm{d}\tau}\, \hat{\sigma}_{12\to34\gamma}^{2,1}(\hat{s})\big|_{\mathrm{coll}}. \tag{4.112}
$$

Combining the cross section of the soft and collinear region with the virtual contributions $\sigma_{12\to34}^{2,1}(S)\big|_{\mathrm{virt}}$ the IR cutoff λ_g cancels, similar to the cancellation of the photon regulator λ_γ. In the presence of initial-state collinear singularities, i.e. $\hat{\sigma}_{12\to34}^{1,1} \neq 0$, singular contributions remain that have to be absorbed into the definition of the renormalized PDFs,

$$
f_q(x,\mu_F) \to f_q(x,\mu_F)\Big(1 - \frac{\alpha_s C_F}{\pi}\kappa_{v+s}\Big) - \int_x^{1-\delta_s} \frac{\mathrm{d}z}{z}f_q\big(\frac{x}{z},\mu_F\big)\Big(\frac{\alpha_s C_F}{2\pi}\kappa_c(z)\Big), \tag{4.113}
$$

with κ_{v+s} and κ_c given in (4.99). Using this redefined PDFs in the convolution of the partonic cross section of the tree-level interference term $\hat{\sigma}_{12\to34}^{1,1}$, effectively generates contributions of $\mathcal{O}(\alpha_s^2\alpha)$,

$$
\sigma_{12\to34}^{1,1}(S) = \frac{1}{1+\delta_{q_1q_2}}\int_{\tau_0}^1 \mathrm{d}\tau \int_\tau^1 \frac{\mathrm{d}x}{x}\left[f_{q_1}^A\Big(\frac{\tau}{x},\mu\Big)f_{q_2}^B(x,\mu) + f_{q_2}^A(x,\mu)f_{q_1}^B\Big(\frac{\tau}{x},\mu\Big)\right]\hat{\sigma}_{12\to34}^{1,1}(\hat{s})
$$

$$
\to \int_{\tau_0}^1 \mathrm{d}\tau \frac{\mathrm{d}L_{q_1q_2}}{\mathrm{d}\tau}\hat{\sigma}_{12\to34}^{1,1}(\hat{s}) \tag{4.114a}
$$

$$
- \frac{\alpha_s C_F}{\pi}\int_{\tau_0}^1 \mathrm{d}\tau \frac{\mathrm{d}L_{q_1q_2}}{\mathrm{d}\tau}\kappa_{v+s}\hat{\sigma}_{12\to34}^{1,1}(\hat{s}) \tag{4.114b}
$$

$$
- \frac{\alpha_s C_F}{2\pi}\int_{\tau_0}^{1-\delta_s} \mathrm{d}\tau \frac{\mathrm{d}L_{q_1q_2}^{\mathrm{coll}}}{\mathrm{d}\tau}\kappa_c(z)\hat{\sigma}_{12\to34}^{1,1}(\hat{s}) \tag{4.114c}
$$

$$
= \sigma_{12\to34}^{1,1}(S) + \sigma_{12\to34}^{2,1}(S)\big|_{\mathrm{PDF}}^g + \sigma_{12\to34g}^{2,1}(S)\big|_{\mathrm{PDF}}^g.
$$

$\sigma_{12\to34}^{2,1}(S)\big|_{\mathrm{PDF}}^g$ cancels the remaining collinear gluon singularities emerging from virtual corrections, while $\sigma_{12\to34g}^{2,1}(S)\big|_{\mathrm{PDF}}^g$ cancels the remaining collinear gluon singularities originating from real gluon radiation.

4.5.3 Collinear Quark Emission

For a consistent treatment of all $\mathcal{O}(\alpha_s^2\alpha)$ contributions, also real quark radiation has to be considered. Real quark radiation processes are generally denoted by

$$
a(p_1)\,b(p_2) \to c(p_3)\,d(p_4)\,q(k), \tag{4.115}
$$

where q is either a quark or an anti-quark, depending on the specific process. In case of squark-pair production, exactly one of the initial-state particles has to be a fermion in order to get only one fermion in the final state. Hence, the possible initial states in hadronic collisions are gluon–(anti-)quark or photon–(anti-)quark. Due to the small photon PDF inside the proton, which is formally of $\mathcal{O}(\alpha)$, we will discard photon-induced processes of $\mathcal{O}(\alpha_s^2\alpha)$. The process of real quark radiation can be regarded as completely independent

to the virtual corrections, since it is IR finite by itself. However, as in the real gluon radiation case, collinear singularities are present for processes with non-vanishing tree-level interferences, $\hat{\sigma}_{12\to34}^{(1,1)} \neq 0$. These initial-state singularities have to be absorbed into the definition of the PDFs,

$$f_q(x, \mu_F) \to f_q(x, \mu_F) - \int_x^{1-\delta_s} \frac{dz}{z} f_g\left(\frac{x}{z}, \mu_F\right) \frac{\alpha_s C_F}{2\pi} P_{qg}(z) \ln\left(\frac{\mu_F^2}{m_q^2}\right), \tag{4.116}$$

with the gluon–quark splitting function

$$P_{qg}(z) = z^2 + (1 - z^2). \tag{4.117}$$

Performing this substitution in the definition of the hadronic cross section when convoluting the tree-level interference term,

$$\sigma_{12\to34}^{1,1}(S) = \frac{1}{1 + \delta_{q_1 q_2}} \int_{\tau_0}^1 d\tau \int_\tau^1 \frac{dx}{x} \left[f_{q_1}^A\left(\frac{\tau}{x}, \mu\right) f_{q_2}^B(x, \mu) + f_{q_2}^A(x, \mu) f_{q_1}^B\left(\frac{\tau}{x}, \mu\right) \right] \hat{\sigma}_{12\to34}^{1,1}(\hat{s})$$

$$\to \int_{\tau_0}^1 d\tau \frac{dL_{q_1 q_2}}{d\tau} \hat{\sigma}_{12\to34}^{1,1}(\hat{s}) \tag{4.118a}$$

$$- \frac{\alpha_s C_F}{2\pi} \int_{\tau_0}^{1-\delta_s} d\tau \left[\frac{dL_{q_1 g}^{\text{coll}}}{d\tau} + \frac{dL_{q_2 g}^{\text{coll}}}{d\tau} \right] P_{qg}(z) \ln\left(\frac{\mu_F^2}{m_q^2}\right) \frac{\hat{\sigma}_{12\to34}^{1,1}(\hat{s})}{1 + \delta_{q_1 q_2}} \tag{4.118b}$$

$$= \sigma_{12\to34}^{1,1}(S) + \sigma_{12\to34q}^{2,1}(S)|_{\text{PDF}}^q,$$

the initial-state collinear singularities originating from real quark radiation are canceled by $\sigma_{12\to34q}^{2,1}(S)|_{\text{PDF}}^q$.

4.6 Phase-Space Integration

In order to obtain the total cross section one has to integrate over the phase-space of the final-state particles and convolute the so obtained partonic cross section with the PDFs. In the case of hadronic cross sections with two final-state particles, one has to perform a three-dimensional integration, while for three particles in the final state the integral is six dimensional. It is tedious to perform these multi-dimensional integrations analytically. Even though the partonic cross section might be calculated, the convolution with the PDFs still remains to be done. Moreover, one is often interested in differential distributions with some kinematical cuts applied, which often are not available as analytic expressions. Hence, numerical integration methods have to be employed. In one dimension, the numerical integration can be performed by using Gaussian quadrature, or variants of this method [157]. To compute integrals in multi-dimensions, one approach would be to use repeated one-dimensional integration. However, in this approach the function evaluations grow exponentially as the number of dimensions increases. One method to overcome this "curse of dimensionality" [158] is to use Monte Carlo methods.

The multi-dimensional integration will be performed using Vegas [159, 160]. Vegas is a Monte Carlo algorithm that uses importance sampling as variance-reduction technique.

Since Vegas is integrating unit hypercubes, a suitable parametrization is needed to map the kinematic variables onto the interval $[0, 1]$. The momentum fractions needed to perform the convolution with the PDFs are trivially mapped. Since the cross section is a Lorentz-invariant quantity, the integration is performed in the c.m. frame. Care has to be taken when calculating differential distributions that are not Lorentz-invariant quantities, like e.g. pseudo-rapidity distributions. In this case, the single events have to be boosted into the lab-frame.

In the c.m. frame, the four-momenta of the incoming particles which are aligned along the z-axis at the hadronic c.m. energy $\sqrt{S}$, are simply given by

$$p_1 = \left(\sqrt{\tau S}, 0, 0, \sqrt{\tau S}\right), \qquad\qquad p_2 = \left(\sqrt{\tau S}, 0, 0, -\sqrt{\tau S}\right). \qquad (4.119)$$

$\tau = x_1 x_2$ with x_1 (x_2) being the momentum fractions carried by parton 1 (parton 2) in hadron 1 (hadron 2).

4.6.1 Final-State Kinematics

In the following the parametrizations of the two and three final-state particle phase-space used for the numerical integration are given. In order to take into account the singular behavior of the amplitude in the soft and collinear limit a suitable mapping of the integration variables is necessary. The differential cross section with two incoming particles moving along the z-axis with momenta p_1 and p_2 and $n - 2$ external particles with momenta p_n^f, can generally be written as

$$d\sigma = C \frac{dL_{p_1 p_2}}{d\tau} \frac{1}{\Phi} \left|\mathcal{M}(p_1 p_2 \to \{p_n^f\})\right|^2 d\tau \, d^n \text{Lips}, \qquad (4.120)$$

with the n-particle differential Lorentz-invariant phase-space d^nLips,

$$d^n \text{Lips} = (2\pi)^4 \delta^4 \left(p_1 + p_2 - \sum_{i=3}^{n} p_i\right) \prod_{i=3}^{n} \frac{d^3 p_i}{(2\pi)^3 2 p_i^0}, \qquad (4.121)$$

and the flux Φ of the incoming particles

$$\Phi \equiv \frac{1}{4 \left|p_1^0 p_2^3 - p_2^0 p_1^3\right|} \overset{\text{c.m.}}{=} 4 E_{CM} |p_z^3|. \qquad (4.122)$$

Since the calculation is usually performed in natural units with $\hbar = c = 1$ one has to multiply a conversion factor $C = \hbar c^2$ in order to retain the cross section in SI units.

Two-Particle Phase-Space

The two-particle differential Lorentz-invariant phase-space is given by

$$\begin{aligned}
d^2 \text{Lips} &= (2\pi)^4 \delta^4 (p_1 + p_2 - p_3 - p_4) \frac{dp_3}{(2\pi)^3 2 E_3} \frac{dp_4}{(2\pi)^3 2 E_4} \\
&\overset{\text{c.m.}}{=} \frac{1}{16\pi^2} \frac{|\vec{p}|}{E_{\text{CM}}} d\Omega,
\end{aligned} \qquad (4.123)$$

where p_1, p_2 (p_3, p_4) are the momenta of the incoming (outgoing) particles, and $\mathrm{d}\Omega = \sin\theta\mathrm{d}\theta\mathrm{d}\phi$. The absolute value of the three-momenta $\vec{p} = \vec{p}_1 = \vec{p}_2$ is given by

$$|\vec{p}| \equiv \frac{\sqrt{\lambda(\hat{s}, m_3^2, m_4^2)}}{2\sqrt{\hat{s}}} = \frac{\sqrt{E_{\mathrm{CM}}^4 - E_{\mathrm{CM}}^2(m_3^2 + m_4^2) + (m_3^2 - m_4^2)^2}}{2E_{\mathrm{CM}}}\,. \tag{4.124}$$

In the c.m. frame the momenta of the final-state particles can be parametrized according to

$$p_3 = \begin{pmatrix} \sqrt{m_3 + \vec{p}} \\ \vec{p}\cos\phi\sin\theta \\ \vec{p}\sin\phi\sin\theta \\ \vec{p}\cos\theta \end{pmatrix}, \qquad\qquad p_4 = \begin{pmatrix} \sqrt{m_4 + \vec{p}} \\ -\vec{p}\cos\phi\sin\theta \\ -\vec{p}\sin\phi\sin\theta \\ -\vec{p}\cos\theta \end{pmatrix}. \tag{4.125}$$

Due to azimuthal symmetry, no physical observable can depend on the azimuthal angle ϕ, and the integration over ϕ results in a factor 2π. In (4.125), ϕ can be set to any value, e.g. $\phi = 0$. The integration over $\cos\theta$ can be mapped linearly onto $x_3 = [0, 1]$ by defining

$$\cos\theta = 2x_3 - 1\,, \qquad\qquad \sin\theta = 2\sqrt{x_3 - x_3^2}\,. \tag{4.126}$$

The integration over the angles then becomes

$$\int \mathrm{d}\Omega = \int_0^{2\pi} \mathrm{d}\phi \int_{-1}^{1} \mathrm{d}\cos\theta = 4\pi \int_0^1 \mathrm{d}x_3\,. \tag{4.127}$$

In order to improve the convergence of the integration, it is often useful to parametrize the kinematic variables according to the kinematical structure of the amplitude. For example, for squark–squark production, only t-channel particle exchange occurs. Hence, one might think of parametrizing the integration by the Mandelstam variable t of (4.4) instead of parametrizing θ. This can be done with help of following considerations:
The components of t,

$$t = (p_1 - p_3)^2 = m_1^2 + m_3^2 - 2\left(p_1^0 p_3^0 - \vec{p}_1\vec{p}_3\right), \tag{4.128}$$

are given in the c.m. frame by

$$p_1^0 = \frac{\hat{s} - p_2^2 + p_1^2}{2\sqrt{\hat{s}}}\,, \qquad\qquad p_2^0 = \frac{\hat{s} - p_1^2 + p_2^2}{2\sqrt{\hat{s}}}\,, \tag{4.129a}$$

$$p_3^0 = \frac{\hat{s} - p_4^2 + p_3^2}{2\sqrt{\hat{s}}}\,, \qquad\qquad p_4^0 = \frac{\hat{s} - p_3^2 + p_4^2}{2\sqrt{\hat{s}}}\,, \tag{4.129b}$$

$$|\vec{p}|_1 = |\vec{p}|_2 = \frac{\sqrt{\lambda(\hat{s}, p_1^2, p_2^2)}}{2\sqrt{s}}\,, \qquad\qquad |\vec{p}|_3 = |\vec{p}|_4 = \frac{\sqrt{\lambda(\hat{s}, p_3^2, p_4^2)}}{2\sqrt{s}}\,. \tag{4.129c}$$

Since $|\cos\theta| \leq 1$ one gets for the integration boundaries of t,

$$t_{\mathrm{max,min}} = p_1^2 + p_3^2 - 2\left(p_1^0 p_3^0 - \vec{p}_1\vec{p}_3\cos\theta\right). \tag{4.130}$$

x_3 can be mapped onto t according to

$$t = -\left(\left[x_3(-t_{\max} + m^2)^{1-\nu} + (1 - x_3)(-t_{\min} + m^2)^{1-\nu}\right]^{\frac{1}{1-\nu}} - m^2\right), \quad \nu \neq 1, \quad (4.131)$$

with the two free parameters m and ν, which have to be chosen appropriately. With

$$\cos\theta = \frac{t - m_1^2 - m_3^2}{2\vec{p}_1\vec{p}_3} + \sqrt{\frac{m_1^2}{\vec{p}_1^2} + 1}\sqrt{\frac{m_3^2}{\vec{p}_3^2} + 1}, \quad (4.132)$$

$$\frac{\mathrm{d}\cos\theta}{\mathrm{d}t} = \frac{1}{2\vec{p}_1\vec{p}_3}, \quad (4.133)$$

$$\frac{\mathrm{d}t}{\mathrm{d}x_3} = -\frac{\left[(-t_{\max} + m^2)^{1-\nu} - (-t_{\min} + m^2)^{1-\nu}\right](-t + m^2)^{\nu}}{1 - \nu}, \quad (4.134)$$

one can write the integral over the angles as follows,

$$\int \mathrm{d}\Omega = \int_0^{2\pi} \mathrm{d}\phi \int_0^1 \frac{\mathrm{d}\cos\theta}{\mathrm{d}t} \frac{\mathrm{d}t}{\mathrm{d}x_3} \mathrm{d}x_3$$

$$= 2\pi \int_0^1 \mathrm{d}x_3 - \frac{\left[(-t_{\max} + m^2)^{1-\nu} - (-t_{\min} + m^2)^{1-\nu}\right](-t + m^2)^{\nu}}{(1 - \nu)(2\vec{p}_1\vec{p}_3)}. \quad (4.135)$$

The parameters m and ν introduced in (4.131) can be chosen such that the factor $(-t+m^2)^{\nu}$ flattens the integral in regions with large contributions appearing in the amplitude from $t-$channel particle exchange. Hence, m should equal the mass of the exchanged particle. The parameter ν can be used to further optimize the integration, a naive value is $\nu = 2$, since it should cancel the propagator structure of the squared amplitude.[8] However, for the processes considered in this work, no improvement was found by the use of t-channel mapping instead of a linear mapping of $\cos\theta$.

Three-Particle Phase-Space

The momenta of three final-state particles are given by a total of 3×4 components. However, not all of these parameters are independent. The on-shell requirement $p_i^2 = m_i^2$ gives three constraints, and momentum conservation, $p_1 + p_2 = p_3 + p_4 + p_5$, where $p_{1,2}$ are the momenta of the incoming particles, gives four additional constraints. Hence, one is left with a total of five independent parameters. A common parametrization of the three-particle phase-space is to use the energy of particle 3 and 5, and three angles,

$$p_3^0, \ p_5^0, \ \theta, \ \phi, \ \eta. \quad (4.136)$$

The variables θ and ϕ are the usual polar and azimuthal angles. Due to azimuthal symmetry the amplitudes are independent of ϕ. In this parametrization, $\vec{p}_3$ and $\vec{p}_5$ are given by

$$\vec{p}_5 = |\vec{p}_5| \begin{pmatrix} \sin\theta \\ 0 \\ \cos\theta \end{pmatrix}, \qquad \vec{p}_3 = |\vec{p}_3| \begin{pmatrix} \cos\theta & 0 & \sin\theta \\ 0 & 1 & 0 \\ -\sin\theta & 0 & \cos\theta \end{pmatrix} \begin{pmatrix} \sin\eta\sin\xi \\ \cos\eta\sin\xi \\ \cos\xi \end{pmatrix}. \quad (4.137)$$

---

[8] For many processes one finds that the propagator structure is partially canceled by other effects, hence a smaller value for ν might lead to faster convergence of the integral.

If one of the external particles is massless, it will be identified with particle 5. In this way one can easily apply the cuts introduced by the phase-space slicing method. ξ is the angle between $\vec{p}_3$ and $\vec{p}_5$ and is determined via the constraint $p_4^2 = m_4^2$,

$$
\begin{aligned}
m_4^2 &= \left(\hat{s} - p_3^0 - p_5^0\right)^2 - (\vec{p}_3 + \vec{p}_5)^2 \\
&= \left(\hat{s} - p_3^0 - p_5^0\right)^2 - 2|\vec{p}_3||\vec{p}_5|\cos\xi - |\vec{p}_3|^2 - |\vec{p}_5|^2 \\
\Rightarrow \cos\xi = c_\xi &\equiv \frac{(\hat{s} - p_3^0 - p_5^0)^2 - (p_3^0)^2 - (p_5^0)^2 + m_3^2 + m_5^2 - m_4^2}{2\sqrt{(p_3^0)^2 - m_3^2}\sqrt{(p_5^0)^2 - m_5^2}}\,.
\end{aligned}
\tag{4.138}
$$

The three-particle differential Lorentz-invariant phase-space is given by

$$
\begin{aligned}
\mathrm{d}^3\mathrm{Lips} &= (2\pi)^4\delta^4(p_1 + p_2 - p_3 - p_4 - p_5)\frac{\mathrm{d}^3p_3}{(2\pi)^3 2p_3^0}\frac{\mathrm{d}^3p_4}{(2\pi)^3 2p_4^0}\frac{\mathrm{d}^3p_5}{(2\pi)^3 2p_5^0} \tag{4.139} \\
&= \frac{1}{8(2\pi)^5}\delta(\sqrt{\hat{s}} - p_3^0 - p_4^0 - p_5^0)\frac{1}{p_3^0 p_4^0 p_5^0}\mathrm{d}^3p_3\mathrm{d}^3p_5\Big|_{-\vec{p}_4=\vec{p}_3+\vec{p}_5} \\
&= \frac{1}{8(2\pi)^5}\delta(\sqrt{\hat{s}} - p_3^0 - p_4^0 - p_5^0)\frac{p_3^2 p_5^2}{p_3^0 p_4^0 p_5^0}\mathrm{d}\Omega_3\mathrm{d}\Omega_5\mathrm{d}p_3\mathrm{d}p_5\Big|_{-\vec{p}_4=\vec{p}_3+\vec{p}_5} \\
&= \frac{1}{8(2\pi)^5}\frac{p_3 p_5}{p_3^0 p_4^0 p_5^0}\mathrm{d}\Omega_3\,\mathrm{d}\eta\,\mathrm{d}\cos\xi\,\mathrm{d}p_3^0\,\mathrm{d}p_5^0 \\
&\quad\times\delta\left(\sqrt{\hat{s}} - p_3^0 - p_5^0 - \sqrt{m_4^2 - 2|\vec{p}_3||\vec{p}_5|\cos\xi - |\vec{p}_3|^2 - |\vec{p}_5|^2}\right)\Big|_{-\vec{p}_4=\vec{p}_3+\vec{p}_5} \\
&= \frac{1}{8(2\pi)^5}\mathrm{d}p_3^0\,\mathrm{d}p_5^0\,\mathrm{d}\Omega_5\,\mathrm{d}\eta\Big|_{\substack{-\vec{p}_4=\vec{p}_3+\vec{p}_5 \\ \cos\xi=c_\xi}}\,. \tag{4.140}
\end{aligned}
$$

The integration boundaries for the angular integration $\mathrm{d}\Omega_5 = \mathrm{d}\phi\,\mathrm{d}\cos\theta$ and $\mathrm{d}\eta$ are simply given by

$$
(\phi,\,\eta,\,\cos\theta) \in [0, 2\pi] \times [0, 2\pi] \times [-1 + \delta_\theta, 1 - \delta_\theta]\,. \tag{4.141}
$$

The integration boundaries of the polar angle are lowered by δ_θ in order to exclude the collinear region defined by the phase-space slicing method. The ϕ integration is trivial due to azimuthal symmetry and yields a factor 2π. Taking p_5^0 as the outer integration, the integration bounds for p_3^0 can be obtained by exploiting the fact that $|\cos\xi| \leq 1$. The upper and lower integration boundaries are given by

$$
p_{3\,\mathrm{min,max}}^0 = \frac{1}{2b}\left(a\,(b + m_+ m_-) \mp |\vec{p}_5|\sqrt{(b - m_+^2)(b - m_-^2)}\right)\,, \tag{4.142}
$$

with

$$
a \equiv \sqrt{\hat{s}} - p_5^0\,, \qquad b \equiv a^2 - |\vec{p}_3|^2\,, \qquad m_\pm \equiv m_3 \pm m_4\,.
$$

The lower bound of p_5^0 is given by requiring $p_5^0 \geq m_5$, while the upper bound is obtained by the condition that p_3^0 is a real quantity, i.e. the discriminant in (4.142) must not be negative,

$(b - m_+^2)(b - m_-^2) \geq 0,$

$$p_{5\,\text{min}}^0 = m_5 + \lambda, \qquad (4.143\text{a})$$

$$p_{5\,\text{max}}^0 = \frac{\hat{s} - (m_3 + m_4)^2 + m_3^2}{2\sqrt{\hat{s}}}. \qquad (4.143\text{b})$$

The regulator λ has to be introduced in case of soft-photon or soft-gluon emission in order to regularize the IR singularity. The explicit form of the four-vectors p_3, p_4, and p_5 in terms of the independent parameters is given by

$$p_3 = \begin{pmatrix} p_3^0 \\ |\vec{p}_3|(\cos\theta\sin\eta\sin\xi + \sin\theta\cos\xi) \\ |\vec{p}_3|(\cos\eta\sin\xi) \\ |\vec{p}_3|(-\sin\theta\sin\eta\sin\xi + \cos\theta\cos\xi) \end{pmatrix}, \qquad p_5 = \begin{pmatrix} p_5^0 \\ |\vec{p}_5|\sin\theta \\ 0 \\ |\vec{p}_5|\cos\theta \end{pmatrix}, \qquad (4.144\text{a})$$

$$\Rightarrow p_4 = \begin{pmatrix} \sqrt{s} - p_3^0 - p_5^0 \\ -p_3^1 - p_5^1 \\ -p_3^2 - p_5^2 \\ -p_3^3 - p_5^3 \end{pmatrix}. \qquad (4.144\text{b})$$

In order to integrate the phase-space numerically, the remaining four independent parameters have to be mapped onto the interval $[0, 1]$. A linear mapping is given by

$$p_3^0 = (p_{3\,\text{max}}^0 - p_{3\,\text{min}}^0)x_3 + p_{3\,\text{min}}^0 \qquad \Rightarrow \qquad \mathrm{d}p_3^0 = (p_{3\,\text{max}}^0 - p_{3\,\text{min}}^0)\mathrm{d}x_3, \qquad (4.145\text{a})$$

$$p_5^0 = (p_{5\,\text{max}}^0 - p_{5\,\text{min}}^0)x_5 + p_{5\,\text{min}}^0 \qquad \Rightarrow \qquad \mathrm{d}p_5^0 = (p_{5\,\text{max}}^0 - p_{5\,\text{min}}^0)\mathrm{d}x_5, \qquad (4.145\text{b})$$

$$\eta = 2\pi x_4 \qquad \Rightarrow \qquad \mathrm{d}\eta = 2\pi\mathrm{d}x_4, \qquad (4.145\text{c})$$

$$\cos\theta = 2(1 - \delta_\theta)x_6 - (1 - \delta_\theta) \qquad \Rightarrow \qquad \mathrm{d}\cos\theta = 2(1 - \delta_\theta)\mathrm{d}x_6. \qquad (4.145\text{d})$$

The integration over the Lorentz-invariant three-particle phase-space (4.140) is then given by

$$\int \mathrm{d}^3\text{Lips} = \frac{1}{8(2\pi)^5} \int_{p_{5\,\text{min}}^0}^{p_{5\,\text{max}}^0} \mathrm{d}p_5^0 \int_{p_{3\,\text{min}}^0}^{p_{3\,\text{max}}^0} \mathrm{d}p_3^0 \int_0^{2\pi} \mathrm{d}\phi \int_0^{2\pi} \mathrm{d}\eta \int_{-(1-\delta_\theta)}^{1-\delta_\theta} \mathrm{d}\cos\theta \qquad (4.146)$$

$$= \frac{1}{4(2\pi)^3} \int_0^1 \mathrm{d}x_3\mathrm{d}x_4\mathrm{d}x_5\mathrm{d}x_6\, 2\,(1 - \delta_\theta)\left(p_{3\,\text{max}}^0 - p_{3\,\text{min}}^0\right)\left(p_{5\,\text{max}}^0 - p_{5\,\text{min}}^0\right). \qquad (4.147)$$

However, a linear mapping might not be adequate in the presence of soft and/or collinear singularities. In the case of soft singularities the integrand is logarithmically divergent in p_5, i.e. it has a singularity proportional to $1/p_5^0$. Hence, a mapping that takes this pole structure into account would be adequate. It should satisfy

$$\mathrm{d}p_5^0 \propto p_5^0\mathrm{d}x_5, \qquad (4.148)$$

which is the differential equation of an exponential function. Taking the boundary conditions into account, the mapping reads

$$p_5^0 = p_{5\,\text{min}}^0 \exp\left[\ln\left(\frac{p_{5\,\text{max}}^0}{p_{5\,\text{min}}^0}\right)x_5\right] \qquad \Rightarrow \qquad \mathrm{d}p_5^0 = p_5^0 \ln\left(\frac{p_{5\,\text{max}}^0}{p_{5\,\text{min}}^0}\right)\mathrm{d}x_5\,. \tag{4.149}$$

In the case of collinear singularities the poles are proportional to $1/(1 \pm \cos\theta)$. To flatten the integration, one needs a mapping that fulfills

$$\mathrm{dcos}\,\theta \propto (1 + \cos\theta)(1 - \cos\theta)\mathrm{d}x_6 = (1 - \cos^2\theta)\mathrm{d}x_6\,. \tag{4.150}$$

This is the differential equation of the hyperbolic tangent. Taking the boundary conditions into account, the mapping reads

$$\cos\theta = \tanh\left[\frac{1 - 2x_6}{2}\ln\left(\frac{\delta_\theta}{2 - \delta_\theta}\right)\right] \quad \Rightarrow \quad \mathrm{dcos}\,\theta = \ln\left(\frac{\delta_\theta}{2 - \delta_\theta}\right)\left(\cos^2\theta - 1\right)\mathrm{d}x_6\,. \tag{4.151}$$

For the processes considered in this work, one finds that the integration of the real emission amplitudes gets considerably improved by performing these mappings. The integrals converge much faster and for the same integration error much smaller χ^2 values are obtained.

4.6.2 Differential Distributions

Differential distributions of Lorentz-invariant observables are simply obtained by binning the weighted differential cross section for each phase-space point. For n_p equally distributed phase-space points, the weight factor is $1/n_p$. Since Vegas uses importance sampling for variance reduction, the phase-space points are not equally distributed anymore and the weight factor is in general $\neq 1/n_p$.

Since the differential cross section is calculated in the c.m. frame, the kinematic variables have to be boosted into the lab frame in order to generate non-Lorentz invariant observables that depend on the z-direction, i.e. the direction of the incoming particles. The affected observables considered in the following are rapidity distributions $\mathrm{d}\sigma/\mathrm{d}y$ and pseudo-rapidity distributions $\mathrm{d}\sigma/\mathrm{d}\eta$, respectively. The rapidity y and pseudo-rapidity η are defined as

$$y = \frac{1}{2}\ln\left(\frac{E + p_z}{E - p_z}\right), \qquad \eta = -\ln\left[\tan\left(\frac{\theta}{2}\right)\right] = \frac{1}{2}\ln\left(\frac{|\vec{p}| + p_z}{|\vec{p}| - p_z}\right), \tag{4.152}$$

where θ is the angle between $\vec{p}$ and the z-axis. The boost factor is obtained by comparing the momenta p_1' and p_2' of the incoming particles in the c.m.-frame (primed quantities) with the momenta p_1 and p_2 if the lab-frame (unprimed quantities),

$$\text{c.m.-frame:} \quad p_1' = \frac{\sqrt{x_1 x_2 S}}{2}(1, 0, 0, 1)^\mathrm{T}, \qquad p_2' = \frac{\sqrt{x_1 x_2 S}}{2}(1, 0, 0, 1)^\mathrm{T}, \tag{4.153a}$$

$$\text{Lab-frame:} \quad p_1 = x_1\frac{\sqrt{S}}{2}(1, 0, 0, 1)^\mathrm{T}, \qquad p_2 = x_2\frac{\sqrt{S}}{2}(1, 0, 0, 1)^\mathrm{T}\,. \tag{4.153b}$$
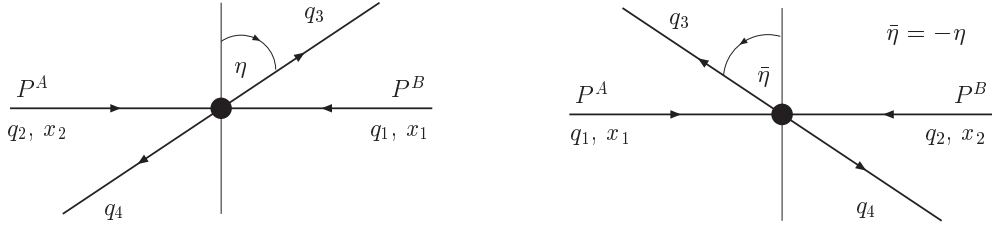
Figure 4.5: Pseudo-rapidity η of the third particle q_3 in the c.m. frame. The incoming particles q_1 and q_2 carry momentum fraction x_1 and x_2. They can emerge from proton A or proton B, yielding the same partonic cross section. However, the pseudo-rapidity distribution is different since $\bar{\eta} = -\eta$.

Both frames are connected by a Lorentz transformation $\Lambda^{\mu}_{\ \nu}$ defined via $p^{\mu} = \Lambda^{\mu}_{\ \nu} p'^{\nu}$,

$$
\Lambda^{\mu}_{\ \nu} = \begin{pmatrix} \gamma & 0 & 0 & -\gamma\beta \\ 0 & 1 & 0 & 0 \\ 0 & 0 & 1 & 0 \\ -\gamma\beta & 0 & 0 & \gamma \end{pmatrix}, \qquad \text{with} \qquad \begin{aligned} \gamma &= \frac{1}{2}\left(\sqrt{\frac{x_1}{x_2}} + \sqrt{\frac{x_2}{x_1}}\right), \\ \beta &= \frac{x_2 - x_1}{x_2 + x_1}. \end{aligned} \tag{4.154}
$$

The differential partonic cross section is a Lorentz-invariant quantity, however η is not. When calculating the differential hadronic cross section, one has an integrand of the form

$$
\begin{aligned}
& f^A_{q_1}(x_1) f^B_{q_2}(x_2) \frac{\mathrm{d}\hat{\sigma}(\hat{s})}{\mathrm{d}\bar{\eta}} + f^A_{q_2}(x_2) f^B_{q_1}(x_1) \frac{\mathrm{d}\hat{\sigma}(\hat{s})}{\mathrm{d}\eta} \\
& \overset{A=B}{=} f^A_{q_1}(x_1) f^A_{q_2}(x_2) \left(\frac{\mathrm{d}\hat{\sigma}(\hat{s})}{\mathrm{d}\bar{\eta}} + \frac{\mathrm{d}\hat{\sigma}(\hat{s})}{\mathrm{d}\eta} \right) \\
& = 2\, f^A_{q_1}(x_1) f^A_{q_2}(x_2) \frac{\mathrm{d}\hat{\sigma}(\hat{s})}{\mathrm{d}\eta},
\end{aligned} \tag{4.155}
$$

with η and $\bar{\eta}$ as defined in Figure 4.5. The last equation holds, since

$$
\frac{\mathrm{d}\hat{\sigma}(\hat{s})}{\mathrm{d}\bar{\eta}} = \frac{\mathrm{d}\hat{\sigma}(\hat{s})}{\mathrm{d}\eta}.
$$

In practice, (4.155) is used to calculate the hadronic cross section. In order to obtain the correct η-distribution, one has to boost the kinematic variables and then bin the differential cross section at η and $-\eta$, weighted by a factor $1/2$. Special care has to be taken, when calculating the η-distribution in the collinear region. Since the collinear particle carries away some momentum fraction z, the boost factor (4.154) is altered. It further depends on whether the collinear particle that takes away the momentum fraction $(1 - z)$ is emitted from the parton q_1 carrying momentum fraction x_1 or from parton q_2 carrying momentum fraction x_2, cf. Figure 4.3. For real photon emission from q_1 with charge e_1 one finds, after redefining the PDFs, that the integrand becomes

$$
\begin{aligned}
& -\frac{\alpha}{2\pi} e_1^2 f^A_{q_1}(x_1) f^A_{q_2}(x_2) \left(\frac{\mathrm{d}\hat{\sigma}(\hat{s})}{\mathrm{d}\bar{\eta}_1} + \frac{\mathrm{d}\hat{\sigma}(\hat{s})}{\mathrm{d}\eta_1} \right) \\
& = -2\frac{\alpha}{2\pi} e_1^2 f^A_{q_1}(x_1) f^A_{q_2}(x_2) \frac{\mathrm{d}\hat{\sigma}(\hat{s})}{\mathrm{d}\eta_1},
\end{aligned} \tag{4.156}
$$

where η_1 is given in the lab-frame by performing the boost (4.154) with $x_1 \to \tau z/x$ and $x_2 \to x/z$, i.e. using

$$\gamma_1 = \frac{1}{2}\left(\frac{z\sqrt{\tau}}{x} + \frac{x}{z\sqrt{\tau}}\right), \qquad\qquad \beta_1 = \frac{x^2 - z^2\tau}{x^2 + z^2\tau}. \qquad (4.157)$$

In the same way, for a photon emitted from q_2 with charge e_2 one has

$$-\frac{\alpha}{2\pi}e_2^2 f_{q_1}^A(x_1)f_{q_2}^A(x_2)\left(\frac{\mathrm{d}\hat{\sigma}(\hat{s})}{\mathrm{d}\bar{\eta}_2} + \frac{\mathrm{d}\hat{\sigma}(\hat{s})}{\mathrm{d}\eta_2}\right)$$
$$= -2\frac{\alpha}{2\pi}e_2^2 f_{q_1}^A(x_1)f_{q_2}^A(x_2)\frac{\mathrm{d}\hat{\sigma}(\hat{s})}{\mathrm{d}\eta_2}, \qquad (4.158)$$

where in the lab-frame η_2 is obtained by boosting with $x_1 \to \tau/x$ and $x_2 \to x$, i.e. using

$$\gamma_2 = \frac{1}{2}\left(\frac{\sqrt{\tau}}{x} + \frac{x}{\sqrt{\tau}}\right), \qquad\qquad \beta_2 = \frac{x^2 - \tau}{x^2 + \tau}. \qquad (4.159)$$

Hence by comparison with (4.101c) one finds that in order to obtain the correct η-distribution in the collinear photon region, the following steps have to be performed:

- Boost the kinematical variables using γ_1 (γ_2) and β_1 (β_2) to obtain η_1 (η_2) and bin the differential cross section at η_1 (η_2) and $-\eta_1$ ($-\eta_2$), weighted with the factor ω_1 (ω_2) given by

$$\omega_1 = \frac{1}{2}\frac{e_1^2}{e_1^2 + e_2^2}, \qquad\qquad \omega_2 = \frac{1}{2}\frac{e_2^2}{e_1^2 + e_2^2}. \qquad (4.160)$$

The factor $1/2$ emerges in the same way as in the non-collinear region. Since in (4.101c) the sum of the charges enters, the extra factor in (4.160) is needed to correct this for $e_1 \neq e_2$. In the collinear gluon region the coupling is independent of whether the collinear particle is emitted from parton 1 or parton 2, since for the considered processes the collinear gluon is always emitted from a quark line. The same is true for collinear quark emission, since the collinear quark always emerges from a gluon. In these cases, the weight factor is simply given by $\omega_1 = \omega_2 = 1/4$.

5 Electroweak Contributions to Squark–Squark Production

In this Chapter we study the hadronic production of two squarks and two anti-squarks,

$$PP \to \tilde{q}_\alpha \tilde{q}'_\beta, \quad PP \to \tilde{q}^*_\alpha \tilde{q}'^*_\beta, \qquad q, q' = \{u, d, c, s\}; \qquad (5.1)$$

where $\alpha, \beta = \{L, R\}$ label the chirality of the squarks, neglecting left-right mixing.

In the context of all squark and gluino production processes, squark–squark production is of particular interest at the proton–proton collider LHC. The partonic process proceeds at leading order (LO) from qq-induced diagrams only while squark–anti-squark and gluino–gluino production require $q\bar{q}$ or gg initial states instead. Since the final-state SUSY particles are very massive, an important contribution to the hadronic cross sections arises from the high-x region where valence-quark densities dominate, see also Figure 4.2, right plot. As a result, squark–squark production has generally a higher tree-level yield than squark–anti-squark production and can be comparable to gluino–gluino production depending on the precise squark–gluino mass configuration, cf. Figure 3.5.

First theoretical cross section predictions for squark-pair production processes based on LO calculations were made already many years ago [17]. Later calculations of next-to-leading order (NLO) in perturbative QCD [18, 19] could reduce theoretical uncertainties considerably. For renormaization and factorization scales of the order of the produced squark, the corrections due to NLO QCD are around $5 - 20\%$, and hence typically much smaller than for the other squark and gluino production processes, cf. Figure 3.6. Also results beyond the one-loop level in QCD have become available via soft gluon resummation at NLL accuracy [20–22], however changing the cross section less than 1% for sparticle masses below 1 TeV, cf. Figure 3.7. The scale uncertainty is slightly reduced.

For a reliable cross section prediction, also electroweak (EW) contributions up to $\mathcal{O}(\alpha_s^2 \alpha)$ have to be taken into account which are formally of the same order as NNLO QCD contributions. The contributing processes are manifold and their interplay is non-trivial, in particular since for squark–squark not only QCD-mediated but also EW-mediated production channels exist at tree-level. These tree-level EW contributions which are of $\mathcal{O}(\alpha_s \alpha + \alpha^2)$ can rise the cross section by up to 20% [25]. The main contribution is due to the QCD–EW interference of $\mathcal{O}(\alpha_s \alpha)$ and suffers from scale uncertainties which can be considerably reduced when taking the NLO EW contributions into account.

Squark–squark production consists of 36 processes and the same amount for anti-squark–anti-squark production which differ in flavor and chirality, respectively. In Section 5.1 we classify these processes and group them corresponding to their tree-level structure. The tree-level QCD and tree-level EW hadronic cross sections including the analytic formula are

given in Section 5.2. Section 5.3 shows the strategy and details for performing the NLO EW calculation at $\mathcal{O}(\alpha_s^2\alpha)$. In Section 5.4 we list the input parameters used in our numerical analysis and show hadronic cross sections and distributions for squark–squark production in proton–proton collisions at the LHC with $\sqrt{S} = 14$ TeV and $\sqrt{S} = 7$ TeV. Different scenarios are considered, and we study the dependence of the EW contribution on the final-state squark and gluino masses. Finally, we investigate the implications of an additional jet in the final state originating from real bremsstrahlung.

5.1 Classification of Processes

At lowest order in QCD there is only one partonic channel for each process,

$$
\begin{aligned}
q(p_1)\ q'(p_2) &\rightarrow \tilde{q}_\alpha(p_3)\ \tilde{q}'_\beta(p_4), \\
\bar{q}(p_1)\ \bar{q}'(p_2) &\rightarrow \tilde{q}^*_\alpha(p_3)\ \tilde{q}'^*_\beta(p_4),
\end{aligned}
\tag{5.2}
$$

where the initial-state quarks and the final-state squarks have to have the same flavor. We thus do not consider the production of top (bottom) squarks due to the vanishing (small) density of the corresponding quarks inside the proton. Moreover, b-squark production has special features and will be discussed separately in Chapter 6. The unpolarized cross sections for squark–squark and anti-squark–anti-squark production are related by charge-conjugation. In the following we will refer to squark–squark production only, while the charge-conjugated processes are properly taken into account in the numerical results.

Since the electroweak interaction is sensitive to flavor and chirality, one has to treat processes with final-state squarks of different chiralities or of different isospin separately, even in the limit of degenerate squark masses. CKM mixing effects are neglected in our discussion.

In total we distinguish 36 processes, resulting from the various combinations of squarks of different flavor or chirality in the final state. They can be classified as follows:

$-$Production of two squarks of the same flavor,
$$
PP \rightarrow\ \tilde{u}_\alpha\tilde{u}_\beta,\ \tilde{d}_\alpha\tilde{d}_\beta,\ \tilde{c}_\alpha\tilde{c}_\beta,\ \tilde{s}_\alpha\tilde{s}_\beta, \qquad \{\alpha\beta\} = \{LL,\ RR,\ LR\}.
\tag{5.3a}
$$
$-$Production of two squarks belonging to the same SU(2) doublet,
$$
PP \rightarrow\ \tilde{u}_\alpha\tilde{d}_\beta,\ \tilde{c}_\alpha\tilde{s}_\beta, \qquad \{\alpha\beta\} = \{LL,\ RR,\ LR,\ RL\}.
\tag{5.3b}
$$
$-$Production of two squarks in different SU(2) doublets,
$$
PP \rightarrow\ \tilde{u}_\alpha\tilde{c}_\beta,\ \tilde{u}_\alpha\tilde{s}_\beta,\ \tilde{d}_\alpha\tilde{c}_\beta,\ \tilde{d}_\alpha\tilde{s}_\beta, \qquad \{\alpha\beta\} = \{LL,\ RR,\ LR,\ RL\}.
\tag{5.3c}
$$

The corresponding tree-level diagrams of both QCD and EW origin are listed in Figure 5.1. QCD diagrams are of $\mathcal{O}(\alpha_s)$, mediated by gluino exchange. EW diagrams are of $\mathcal{O}(\alpha)$ and mediated by neutralino or chargino exchange. Quarks and squarks are of the same flavor, also in the EW diagrams. The only exception is given by the two pure-EW chargino-mediated subprocesses $ud \rightarrow \tilde{d}_L\tilde{c}_L$ and $cd \rightarrow \tilde{u}_L\tilde{s}_L$ belonging to the third class, which contribute to $\tilde{d}_L\tilde{c}_L$ and $\tilde{u}_L\tilde{s}_L$ final states, respectively. Hence we have to take 38 partonic processes into account. Note that only t- and u-channel diagrams are present, but no s-channel diagrams.

Class	QCD diagram(s)	EW diagram(s)
$PP \to \tilde{q}_\alpha \tilde{q}_\beta$ same flavor		
$PP \to \tilde{q}_\alpha \tilde{q}'_\beta$ different flavor, same doublet		
$PP \to \tilde{q}_\alpha \tilde{q}'_\beta$ different flavor, different doublet		

Figure 5.1: Parton-level Feynman diagrams for the three classes of squark-squark production at tree-level, where $\alpha, \beta = \{L, R\}$. The first class describes the production of two squarks of the same flavor, the second class that of two squarks of the same isospin doublet (but different flavor) and the third class refers to the production of two squarks belonging to different isospin doublets. In the third class, the subprocess in brackets cannot interfere with other diagrams due to different initial-state particles. In all three classes, the final-state squarks are of the same generation as the initial-state quarks.

For chirality-diagonal $\tilde{q}_\alpha \tilde{q}'_\alpha$ production the appearance of both t- and u-channel diagrams gives rise to nonzero interferences between QCD and EW diagrams already at tree-level.[1] In particular this are the eight processes of (5.3a) for $\alpha = \beta$ and the two processes of (5.3b) for $\alpha = \beta = L$. The full tree-level contributions to the cross section are thus given by the $\mathcal{O}(\alpha_s^2)$ Born contribution and the $\mathcal{O}(\alpha_s \alpha + \alpha^2)$ EW contributions. Photon-induced squark–squark production is not possible at lowest order from charge and color conservation.

5.2 Tree-Level Cross Sections

To keep track of the corresponding order in perturbation theory of the various contributions, we use the notation $d\hat{\sigma}^{a,b}$ $[\mathcal{M}^{a,b}]$ introduced last chapter, in order to refer to the cross section [matrix element] at a given order $\mathcal{O}(\alpha_s^a \alpha^b)$ in the strong and electroweak couplings. Results are given in terms of the Mandelstam variables, defined as usual,

$$\hat{s} = (p_1 + p_2)^2, \quad \hat{t} = (p_1 - p_3)^2, \quad \hat{u} = (p_1 - p_4)^2. \tag{5.4}$$

As described in Section 4.2, the hadronic cross sections are obtained from the partonic cross sections by convolution with the respective parton luminosity function. At $\mathcal{O}(\alpha_s^a \alpha^b)$,

---

[1]In the non-diagonal case, $\tilde{q}_L \tilde{q}'_R$ production, the interference contributions vanish as a consequence of the trivial squark mixing matrices in the limit of no L–R mixing, see also the discussion in Section 5.2.

it is given by

$$\mathrm{d}\sigma^{a,b}(S) = \int_{\tau_0}^1 \mathrm{d}\tau\, \frac{\mathrm{d}L_{qq'}}{\mathrm{d}\tau} \mathrm{d}\hat{\sigma}^{a,b}(\hat{s}), \tag{5.5}$$

with $\quad \dfrac{\mathrm{d}L_{qq'}}{\mathrm{d}\tau} = \dfrac{1}{1+\delta_{qq'}} \int_\tau^1 \dfrac{\mathrm{d}x}{x} \left[f_q^A\left(\dfrac{\tau}{x},\mu_F\right) f_{q'}^B(x,\mu_F) + f_{q'}^A(x,\mu_F) f_q^B\left(\dfrac{\tau}{x},\mu_F\right) \right].$

Here $\tau_0 = (m_{\tilde{q}_\alpha} + m_{\tilde{q}'_\beta})^2/S$ is the production threshold, determined by the masses of the two squarks $m_{\tilde{q}_\alpha}$ and $m_{\tilde{q}'_\beta}$. The parton distribution functions (PDFs) $f_q^A(x,\mu_F)$ give the probability to find a parton q with momentum fraction x inside hadron A at a factorization scale μ_F. At the LHC, both hadrons A,B are protons P. S and $\hat{s} = \tau S$ are the squared center-of-mass (c.m.) energies of the hadronic and partonic processes, respectively.

The differential partonic cross section for a given subprocess $qq' \to \tilde{q}_\alpha \tilde{q}'_\beta$ at LO can thus be written as

$$\mathrm{d}\hat{\sigma}^{2,0}(\hat{s}) = \overline{\sum} \left| \mathcal{M}^{1,0} \right|^2 \frac{\mathrm{d}\hat{t}}{16\pi\hat{s}^2}, \tag{5.6}$$

in terms of the squared lowest-order matrix element, $\mathcal{M}^{1,0}$, averaged (summed) over initial (final) state spin and color. Similarly, the pure EW differential cross section of $\mathcal{O}(\alpha^2)$ and the QCD–EW $\mathcal{O}(\alpha_s\alpha)$ interference contribution are given by

$$\mathrm{d}\hat{\sigma}^{0,2}(\hat{s}) = \overline{\sum} \left| \mathcal{M}^{0,1} \right|^2 \frac{\mathrm{d}\hat{t}}{16\pi\hat{s}^2}, \tag{5.7a}$$

$$\mathrm{d}\hat{\sigma}^{1,1}(\hat{s}) = \overline{\sum} 2\,\mathrm{Re}\Big\{ \left(\mathcal{M}^{0,1}\right)^* \mathcal{M}^{1,0} \Big\} \frac{\mathrm{d}\hat{t}}{16\pi\hat{s}^2}, \tag{5.7b}$$

where $\mathcal{M}^{0,1}$ denotes the EW tree-level amplitude. In the following we give explicit expressions for the tree-level differential cross sections (5.6)–(5.7) for all squark–squark production subprocesses.[2]

We closely follow [25] and express the over initial (final) state color- and spin-averaged (summed) squared t- and u-channel matrix elements and their interference in terms of the following functions,

$$\Phi(\tilde{\xi}_1,\tilde{\xi}_2,\tilde{q}_\alpha,\tilde{q}'_\beta) = \frac{1}{4} c_\Phi(\tilde{\xi}_1,\tilde{\xi}_2) \frac{1}{\hat{t}-m_{\tilde{\xi}_1}^2} \frac{1}{\hat{t}-m_{\tilde{\xi}_2}^2} \Big[A(\tilde{\xi}_1,\tilde{\xi}_2,\tilde{q}_\alpha,\tilde{q}'_\beta) \tag{5.8a}$$
$$\times \left(\hat{t}\hat{u} - m_{\tilde{q}_\alpha}^2 m_{\tilde{q}'_\beta}^2 \right) + B(\tilde{\xi}_1,\tilde{\xi}_2,\tilde{q}_\alpha,\tilde{q}'_\beta) m_{\tilde{\xi}_1} m_{\tilde{\xi}_2} \hat{s} \Big],$$

$$\Theta(\tilde{\xi}_1,\tilde{\xi}_2,\tilde{q}_\alpha,\tilde{q}'_\beta) = \frac{1}{4} c_\Theta(\tilde{\xi}_1,\tilde{\xi}_2) \frac{1}{\hat{u}-m_{\tilde{\xi}_1}^2} \frac{1}{\hat{u}-m_{\tilde{\xi}_2}^2} \Big[C(\tilde{\xi}_1,\tilde{\xi}_2,\tilde{q}_\alpha,\tilde{q}'_\beta) \tag{5.8b}$$
$$\times \left(\hat{t}\hat{u} - m_{\tilde{q}_\alpha}^2 m_{\tilde{q}'_\beta}^2 \right) + D(\tilde{\xi}_1,\tilde{\xi}_2,\tilde{q}_\alpha,\tilde{q}'_\beta) m_{\tilde{\xi}_1} m_{\tilde{\xi}_2} \hat{s} \Big],$$

---

[2]Explicit expressions for the squared matrix elements are also given in [18,25]. However, we correct a wrong color factor of [25], which affects the pure EW $\mathcal{O}(\alpha^2)$ contribution. The numerical impact is negligible for all squark–squark production processes but it can be sizable in squark–anti-squark production channels where the $\mathcal{O}(\alpha_s\alpha)$ interference contribution is suppressed.

$\tilde{\xi}_1, \tilde{\xi}_2$	$c_\Phi(\tilde{\xi}_1, \tilde{\xi}_2)$	$c_\Theta(\tilde{\xi}_1, \tilde{\xi}_2)$	$c_\Psi(\tilde{\xi}_1, \tilde{\xi}_2)$
$\tilde{g}, \tilde{g}$	$2/9$	$2/9$	$-2/27$
$\tilde{\chi}, \tilde{\chi}$	1	1	$1/3$
$\tilde{g}, \tilde{\chi}$	0	0	$4/9$

Table 5.1: Color factors in (5.8), with $\tilde{\chi}$ denoting any neutralino $\tilde{\chi}_k^0$ or chargino $\tilde{\chi}_k^\pm$.
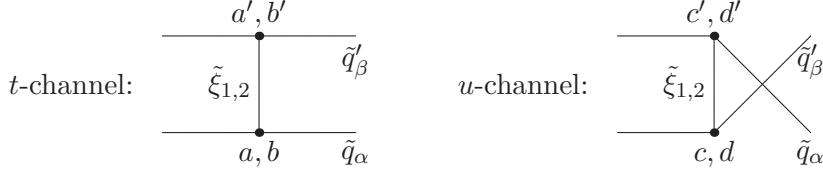
Figure 5.2: Notations for the couplings in the tree-level formulas in Section 5.2. Labels a,c refer to the couplings to left-handed squarks, b and d to that of right-handed squarks. Couplings at the upper and lower vertex, respectively, are denoted by distinct labels for convenience.

$$\Psi(\tilde{\xi}_1, \tilde{\xi}_2, \tilde{q}_\alpha, \tilde{q}'_\beta) = \frac{1}{4} c_\Psi(\tilde{\xi}_1, \tilde{\xi}_2) \frac{1}{\hat{t} - m_{\tilde{\xi}_1}^2} \frac{1}{\hat{u} - m_{\tilde{\xi}_2}^2} F(\tilde{\xi}_1, \tilde{\xi}_2, \tilde{q}_\alpha, \tilde{q}'_\beta) m_{\tilde{\xi}_1} m_{\tilde{\xi}_2} \hat{s}. \qquad (5.8c)$$

Here, $\tilde{\xi}_{1,2} \in \{\tilde{g}, \tilde{\chi}^0, \tilde{\chi}^\pm\}$ denote the exchanged particle in the t- or u-channel, respectively, and $c_{\{\Phi,\Theta,\Psi\}}$ are color matrices which are summarized in Table 5.1. Note that the color factors $c_\Psi(\tilde{\chi}, \tilde{\chi})$ differ from those in [25].

The coupling constants are collected in terms of the abbreviations A, B, C, D, F, as given by

$$A(\tilde{\xi}_1, \tilde{\xi}_2, \tilde{q}_\alpha, \tilde{q}'_\beta) = a_{\tilde{\xi}_1, \tilde{q}_\alpha} a^*_{\tilde{\xi}_2, \tilde{q}_\alpha} b'_{\tilde{\xi}_1, \tilde{q}'_\beta} b'^*_{\tilde{\xi}_2, \tilde{q}'_\beta} + a'_{\tilde{\xi}_1, \tilde{q}'_\beta} a'^*_{\tilde{\xi}_2, \tilde{q}'_\beta} b_{\tilde{\xi}_1, \tilde{q}_\alpha} b^*_{\tilde{\xi}_2, \tilde{q}_\alpha},$$

$$B(\tilde{\xi}_1, \tilde{\xi}_2, \tilde{q}_\alpha, \tilde{q}'_\beta) = a_{\tilde{\xi}_1, \tilde{q}_\alpha} a^*_{\tilde{\xi}_2, \tilde{q}_\alpha} a'_{\tilde{\xi}_1, \tilde{q}'_\beta} a'^*_{\tilde{\xi}_2, \tilde{q}'_\beta} + b_{\tilde{\xi}_1, \tilde{q}_\alpha} b^*_{\tilde{\xi}_2, \tilde{q}_\alpha} b'_{\tilde{\xi}_1, \tilde{q}'_\beta} b'^*_{\tilde{\xi}_2, \tilde{q}'_\beta},$$

$$C(\tilde{\xi}_1, \tilde{\xi}_2, \tilde{q}_\alpha, \tilde{q}'_\beta) = c_{\tilde{\xi}_1, \tilde{q}'_\beta} c^*_{\tilde{\xi}_2, \tilde{q}'_\beta} d'_{\tilde{\xi}_1, \tilde{q}_\alpha} d'^*_{\tilde{\xi}_2, \tilde{q}_\alpha} + c'_{\tilde{\xi}_1, \tilde{q}_\alpha} c'^*_{\tilde{\xi}_2, \tilde{q}_\alpha} d_{\tilde{\xi}_1, \tilde{q}'_\beta} d^*_{\tilde{\xi}_2, \tilde{q}'_\beta}, \qquad (5.9)$$

$$D(\tilde{\xi}_1, \tilde{\xi}_2, \tilde{q}_\alpha, \tilde{q}'_\beta) = c_{\tilde{\xi}_1, \tilde{q}'_\beta} c^*_{\tilde{\xi}_2, \tilde{q}'_\beta} c'_{\tilde{\xi}_1, \tilde{q}_\alpha} c'^*_{\tilde{\xi}_2, \tilde{q}_\alpha} + d_{\tilde{\xi}_1, \tilde{q}'_\beta} d^*_{\tilde{\xi}_2, \tilde{q}'_\beta} d'_{\tilde{\xi}_1, \tilde{q}_\alpha} d'^*_{\tilde{\xi}_2, \tilde{q}_\alpha},$$

$$F(\tilde{\xi}_1, \tilde{\xi}_2, \tilde{q}_\alpha, \tilde{q}'_\beta) = a_{\tilde{\xi}_1, \tilde{q}_\alpha} c^*_{\tilde{\xi}_2, \tilde{q}'_\beta} a'_{\tilde{\xi}_1, \tilde{q}'_\beta} c'^*_{\tilde{\xi}_2, \tilde{q}_\alpha} + b_{\tilde{\xi}_1, \tilde{q}_\alpha} d^*_{\tilde{\xi}_2, \tilde{q}'_\beta} b'_{\tilde{\xi}_1, \tilde{q}'_\beta} d'^*_{\tilde{\xi}_2, \tilde{q}_\alpha},$$

where the notation refers to the labels as listed in Figure 5.2. Finally the explicit coupling constants $a_{\tilde{\xi}_i, \tilde{q}_\alpha}$, $b_{\tilde{\xi}_i, \tilde{q}_\alpha}, \ldots$ are listed in Table 5.2.

For the differential cross sections, we refer to the three classes of subprocesses introduced in (5.3). $\alpha, \beta = \{L, R\}$ label the chirality of the squarks, k, l label the four (two) mass eigenstates of neutralinos (charginos).

$\tilde{\xi}_i, \tilde{q}_\alpha$	a, a', c, c'	b, b', d, d'
$\tilde{\chi}_k^0, \tilde{u}_\alpha$	$-\frac{ie}{\sqrt{2}s_{\mathrm{w}}}\left(\frac{1}{3}\frac{s_{\mathrm{w}}}{c_{\mathrm{w}}}N_{k1}^* + N_{k2}^*\right)\delta_{L\alpha}$	$\frac{4ie}{3\sqrt{2}c_{\mathrm{w}}}N_{k1}\,\delta_{R\alpha}$
$\tilde{\chi}_k^0, \tilde{d}_\alpha$	$-\frac{ie}{\sqrt{2}s_{\mathrm{w}}}\left(\frac{1}{3}\frac{s_{\mathrm{w}}}{c_{\mathrm{w}}}N_{k1}^* - N_{k2}^*\right)\delta_{L\alpha}$	$-\frac{2ie}{3\sqrt{2}c_{\mathrm{w}}}N_{k1}\,\delta_{R\alpha}$
$\tilde{\chi}_k^\pm, \tilde{u}_\alpha$	$-\frac{ie}{s_{\mathrm{w}}}V_{k1}^*\,\delta_{L\alpha}$	0
$\tilde{\chi}_k^\pm, \tilde{d}_\alpha$	$-\frac{ie}{s_{\mathrm{w}}}U_{k1}^*\,\delta_{L\alpha}$	0
$\tilde{g}, \tilde{u}_\alpha$	$-\sqrt{2}i\hat{g}_s\,\delta_{L\alpha}$	$\sqrt{2}i\hat{g}_s\,\delta_{R\alpha}$
$\tilde{g}, \tilde{d}_\alpha$	$-\sqrt{2}i\hat{g}_s\,\delta_{L\alpha}$	$\sqrt{2}i\hat{g}_s\,\delta_{R\alpha}$

Table 5.2: Coupling constants $a_{\tilde{\xi}_i,\tilde{q}_\alpha}, b_{\tilde{\xi}_i,\tilde{q}_\alpha}, \dots$ for exchange particle $\tilde{\xi}_i$ and produced light-flavor squark $\tilde{q}_\alpha$, following the conventions of [161]. L–R mixing of the squark mass eigenstates is neglected. N, U, V are the unitary matrices diagonalizing the neutralino and chargino mass matrix, respectively.

$PP \to \tilde{q}_\alpha\tilde{q}_\beta$ (two squarks of the same flavor)

The partonic process for this class of processes is $qq \to \tilde{q}_\alpha\tilde{q}_\beta$, i.e. all quarks and squarks are of the same flavor. The differential cross sections at $\mathcal{O}(\alpha_s^2)$, $\mathcal{O}(\alpha^2)$, $\mathcal{O}(\alpha_s\alpha)$ read, according to the notation of Section 5.2,

$$
\mathrm{d}\hat{\sigma}^{2,\,0} = \left\{ \Phi(\tilde{g}, \tilde{g}, \tilde{q}_\alpha, \tilde{q}_\beta) + \Theta(\tilde{g}, \tilde{g}, \tilde{q}_\alpha, \tilde{q}_\beta) + 2\,\mathrm{Re}\left\{\Psi(\tilde{g}, \tilde{g}, \tilde{q}_\alpha, \tilde{q}_\beta)\right\} \right\} \frac{\mathrm{d}\hat{t}}{16\pi\hat{s}^2},
$$

$$
\mathrm{d}\hat{\sigma}^{0,\,2} = \sum_{k,l=1}^{4} \left\{ \Phi(\tilde{\chi}_k^0, \tilde{\chi}_l^0, \tilde{q}_\alpha, \tilde{q}_\beta) + \Theta(\tilde{\chi}_k^0, \tilde{\chi}_l^0, \tilde{q}_\alpha, \tilde{q}_\beta) \right.
$$

$$
\left. + 2\,\mathrm{Re}\left\{\Psi(\tilde{\chi}_k^0, \tilde{\chi}_l^0, \tilde{q}_\alpha, \tilde{q}_\beta)\right\} \right\} \frac{\mathrm{d}\hat{t}}{16\pi\hat{s}^2},
$$

$$
\mathrm{d}\hat{\sigma}^{1,\,1} = \sum_{k=1}^{4} 2\,\mathrm{Re}\left\{\Psi(\tilde{g}, \tilde{\chi}_k^0, \tilde{q}_\alpha, \tilde{q}_\beta) + \Psi(\tilde{\chi}_k^0, \tilde{g}, \tilde{q}_\alpha, \tilde{q}_\beta)\right\} \frac{\mathrm{d}\hat{t}}{16\pi\hat{s}^2}.
$$

(5.10)

A factor $1/2$ for indistinguishable particles in the final state has correctly been taken into account. As can be seen from the couplings in Table 5.2, the interference terms Ψ and thus in particular the interference contribution $\mathrm{d}\hat{\sigma}^{1,\,1}$ are only present for diagonal squark–squark production (i.e. $\alpha = \beta$). This is a result from the absence of L–R mixing for the light-flavor squarks.

$PP \to \tilde{q}_\alpha \tilde{q}'_\beta$ (two squarks of different flavor in the same SU(2) doublet)

The only contributing partonic process is $qq' \to \tilde{q}_\alpha \tilde{q}'_\beta$, with q' being the SU(2) partner of q. The tree-level contributions to the cross section read:

$$
\begin{aligned}
\mathrm{d}\hat{\sigma}^{2,0} &= \Phi(\tilde{g}, \tilde{g}, \tilde{q}_\alpha, \tilde{q}'_\beta) \, \frac{\mathrm{d}\hat{t}}{16\pi \hat{s}^2}, \\
\mathrm{d}\hat{\sigma}^{0,2} &= \bigg\{ \sum_{k,l=1}^{4} \Phi(\tilde{\chi}^0_k, \tilde{\chi}^0_l, \tilde{q}_\alpha, \tilde{q}'_\beta) + \sum_{k,l=1}^{2} \Theta(\tilde{\chi}^\pm_k, \tilde{\chi}^\pm_l, \tilde{q}_\alpha, \tilde{q}'_\beta) \\
&\quad + \sum_{k=1}^{4}\sum_{l=1}^{2} 2\mathrm{Re}\{\Psi(\tilde{\chi}^0_l, \tilde{\chi}^\pm_k, \tilde{q}_\alpha, \tilde{q}'_\beta)\} \bigg\} \frac{\mathrm{d}\hat{t}}{16\pi \hat{s}^2}, \\
\mathrm{d}\hat{\sigma}^{1,1} &= \sum_{k=1}^{2} 2\,\mathrm{Re}\left\{ \Psi(\tilde{g}, \tilde{\chi}^\pm_k, \tilde{q}_\alpha, \tilde{q}'_\beta) \right\} \frac{\mathrm{d}\hat{t}}{16\pi \hat{s}^2}.
\end{aligned}
\tag{5.11}
$$

In this case, the interference terms are related to chargino-mediated diagrams and thus the interference contribution $\mathrm{d}\hat{\sigma}^{1,1}$ is only non-zero for the production of two left-handed squarks (i.e. $\alpha = \beta = L$).

$PP \to \tilde{q}_\alpha \tilde{q}'_\beta$ (two squarks in different doublets)

This class describes the production of two squarks of different flavor and of different generation, arising from the partonic process $qq' \to \tilde{q}_\alpha \tilde{q}'_\beta$, with $q \neq q'$. The tree-level cross sections read as follows,

$$
\begin{aligned}
\mathrm{d}\hat{\sigma}^{2,0} &= \Phi(\tilde{g}, \tilde{g}, \tilde{q}_\alpha, \tilde{q}'_\beta) \, \frac{\mathrm{d}\hat{t}}{16\pi \hat{s}^2}, \\
\mathrm{d}\hat{\sigma}^{0,2} &= \bigg\{ \sum_{k,l=1}^{4} \Phi(\tilde{\chi}^0_k, \tilde{\chi}^0_l, \tilde{q}_\alpha, \tilde{q}'_\beta) + \delta_{qu}\delta_{q's}\,\delta_{\tilde{q}\tilde{d}}\,\delta_{\tilde{q}'\tilde{c}} \sum_{k,l=1}^{2} \Phi(\tilde{\chi}^\pm_k, \tilde{\chi}^\pm_l, \tilde{q}_\alpha, \tilde{q}'_\beta) \\
&\quad + \delta_{qc}\delta_{q'd}\,\delta_{\tilde{q}\tilde{u}}\,\delta_{\tilde{q}'\tilde{s}} \sum_{k,l=1}^{2} \Phi(\tilde{\chi}^\pm_k, \tilde{\chi}^\pm_l, \tilde{q}_\alpha, \tilde{q}'_\beta) \bigg\} \frac{\mathrm{d}\hat{t}}{16\pi \hat{s}^2}, \\
\mathrm{d}\hat{\sigma}^{1,1} &= 0.
\end{aligned}
\tag{5.12}
$$

Here, two additional chargino-mediated partonic processes ($us \to \tilde{d}_L \tilde{c}_L$ and $cd \to \tilde{u}_L \tilde{s}_L$) can give an $\mathcal{O}(\alpha^2)$ contribution. The $\mathcal{O}(\alpha_s \alpha)$ interference contribution vanishes for this class of processes.

5.3 Next-to Leading Order EW Contributions

At $\mathcal{O}(\alpha_s^2 \alpha)$, squark–squark production gets contributions from virtual corrections, real photon and gluon emission, as well as real quark radiation. The calculation suffers of ultraviolet (UV) divergences as well as infrared (IR) and collinear singularities that are treated according to the procedure described in Chapter 4. These divergences and singularities arise in
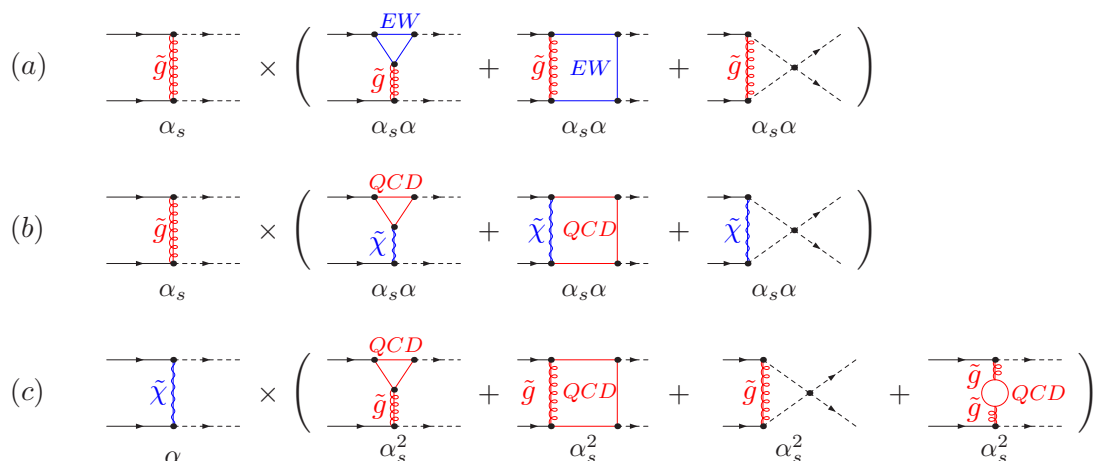
Figure 5.3: Sample of Feynman diagrams to illustrate the virtual contributions at $\mathcal{O}(\alpha_s^2 \alpha)$. Three gauge invariant subsets of interferences occur at this order. The label of perturbative order is attached to each diagram. *EW* refers to electroweakly interacting particles and *QCD* refers to strongly interacting particles in the loop insertions. The full sets of diagrams are shown in Figures 5.4, 5.5, and 5.6.

the one-loop diagrams, see Section 5.3.1. The IR singularities cancel in sufficiently inclusive observables once virtual and real photon- and gluon-bremsstrahlung corrections are added (see Section 5.3.2). Remaining collinear singularities are universal and can be absorbed by redefining the PDFs, explicit formulas are given in Section 5.3.3.

Diagrams and corresponding amplitudes are generated using `FeynArts` [162,163]. The algebraic simplifications and numerical evaluation is done with help of `FormCalc` and `LoopTools` [161, 163]. IR and collinear singularities are regularized by means of mass regularization, i.e. we introduce a fictitious mass for the photon and the gluon. Quarks are treated as massless, except where their masses are needed as regulators.

5.3.1 Virtual Corrections

The virtual contributions are given by the interference of tree-level and one-loop diagrams. In practice three types of interferences occur at $\mathcal{O}(\alpha_s^2 \alpha)$, as schematically depicted in Figure 5.3. All three interference terms yield non-vanishing contributions to the cross section. For each subprocess, the partonic cross section can be written as

$$
\begin{aligned}
d\hat{\sigma}_{\text{virt.}}^{2,1} =& \frac{d\hat{t}}{16\pi\hat{s}^2} \overline{\sum} 2\,\text{Re}\left\{ \left(\mathcal{M}^{1,0}\right)^* \mathcal{M}^{1,1}_{\text{(EW)}} + \left(\mathcal{M}^{1,0}\right)^* \mathcal{M}^{1,1}_{\text{(QCD)}} \right\} \\
&+ \frac{d\hat{t}}{16\pi\hat{s}^2} \overline{\sum} 2\,\text{Re}\left\{ \left(\mathcal{M}^{0,1}\right)^* \mathcal{M}^{2,0} \right\}.
\end{aligned}
\tag{5.13}
$$

The first line corresponds to (a) and (b) of Figure 5.3 and is given by the interference of $\mathcal{M}^{1,0}$ with $\mathcal{M}^{1,1}$. The amplitude $\mathcal{M}^{1,1}$ is split into two parts, $\mathcal{M}^{1,1}_{\text{(EW)}}$ and $\mathcal{M}^{1,1}_{\text{(QCD)}}$, the first arising from tree-level QCD diagrams with EW insertions (Figure 5.3a, right), and the

latter from tree-level EW diagrams with QCD insertions (Figure 5.3b, right). The second line in (5.13), corresponding to Figure 5.3c, is given by the interference of $\mathcal{M}^{0,1}$ with the pure-QCD one-loop amplitude $\mathcal{M}^{2,0}$. Care has to be taken with diagrams containing a four-squark vertex. This vertex includes the electroweak as well as the strong coupling and the appropriate part has to be selected in each interference contribution to match the right order, as indicated in Figure 5.3.

The full set of virtual corrections is UV finite after renormalization of the theory and the inclusion of the proper set of one-loop counterterms. The renormalization for squark–squark production involves the renormalization of the gluino mass and gluino field, the field renormalization of the light-flavor quarks and squarks, and the renormalization of the strong coupling constant. The renormalization procedure is described in detail in Section 4.4 and will not be repeated here. The relevant renormalization constants are given by eqs. (4.38), (4.48), (4.77), (4.81), and (4.83b), while the counterterms are listed in Table B.2 of Appendix B. Each of the three interference subsets of Figure 5.3 is gauge-independent by itself and can be renormalized separately. Further, the first set contains singularities originating from IR and collinear photons, while the second and third exhibit singularities due to IR and collinear gluons.

In the first group, shown in Figure 5.3a, gluino-mediated amplitudes with weak insertions ($\mathcal{M}^{1,1}_{(\text{EW})}$) are considered. The full set of Feynman diagrams entering at $\mathcal{O}(\alpha_s^2\alpha)$ consists of vertex and box corrections and is shown in Figure 5.4. We include the diagrams with counterterms for the $q\tilde{g}\tilde{q}_\alpha$ vertex (cf. Table B.2), and evaluate the renormalization constants at $\mathcal{O}(\alpha)$. The whole set of diagrams enters for all three classes, of (5.3) and hence for all 36 production processes. In the case of diagonal squark–squark production $\tilde{q}_\alpha\tilde{q}_\alpha$, corresponding to the first class, one in addition has to take crossed diagrams into account. At this order in the perturbative expansion we need to renormalize quark and squark fields, while the renormalization of gluino and strong coupling is not required. The regularization of the divergent amplitudes in this sector is done in dimensional reduction, and renormalization of quarks and squarks is performed in the on-shell scheme.

In the second case, Figure 5.3b, neutralino- or chargino-mediated amplitudes with strong insertions ($\mathcal{M}^{1,1}_{(\text{QCD})}$) are considered. As in the first case, is consists of vertex and box corrections. The full set of diagrams is shown in Figure 5.5. The diagrams are divided up into two sets, (a) and (b). The diagrams in the first set, Figure 5.5a, enter in all three process classes of (5.3). In the case of diagonal squark–squark production, $\tilde{q}_\alpha\tilde{q}_\alpha$, one again has to consider the crossed diagrams, which are not explicitly shown. The second set of diagrams, Figure 5.5b, is only present in the second class of processes, (5.3b). It is worth to notice, that due to color correlations, the vertex corrections are only present for the 10 processes of (5.3a) and (5.3b), with non-vanishing tree-level QCD–EW interference contributions. For these processes one in addition has to include diagrams containing counterterms for the $q\tilde{q}\tilde{\chi}^0$ vertex and, if arising, for the $q\tilde{q}'\tilde{\chi}^\pm$ vertex (cf. Table B.2) in order to obtain a UV-finite result. The renormalization constants have to be evaluated at $\mathcal{O}(\alpha_s)$ and no renormalization of the neutralino or chargino is required. Since the gluino does not enter this subset of one-loop amplitudes, it is thus sufficient to renormalize the quark and squark sector. As before,
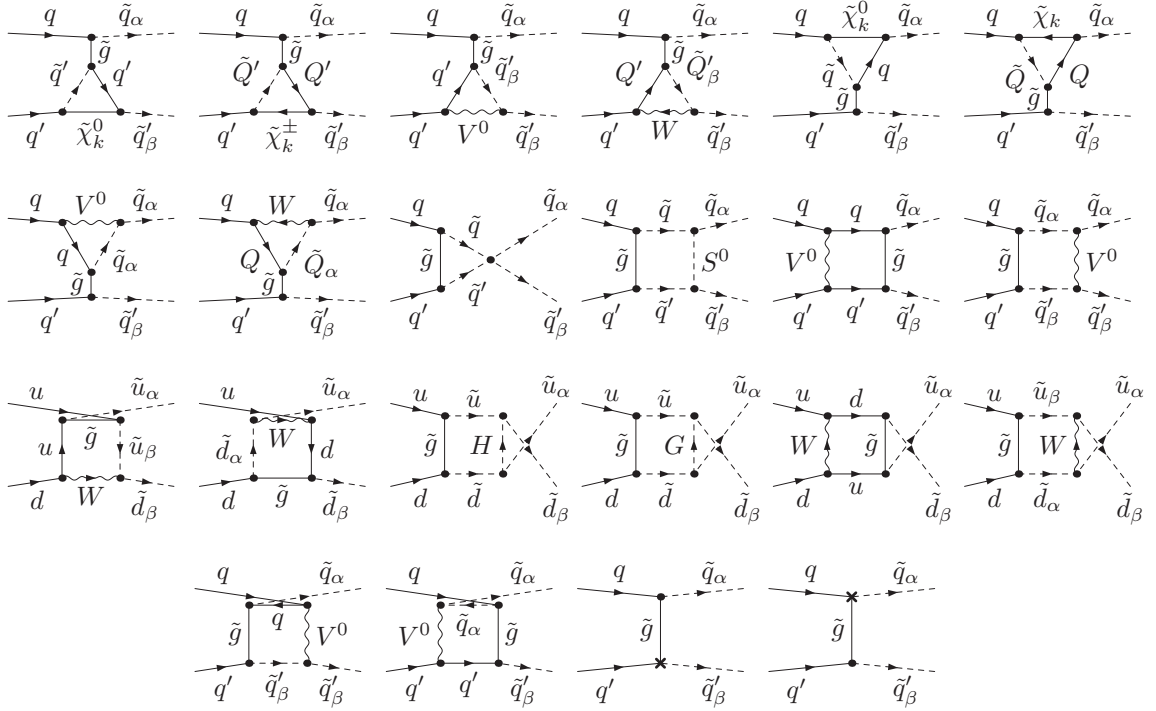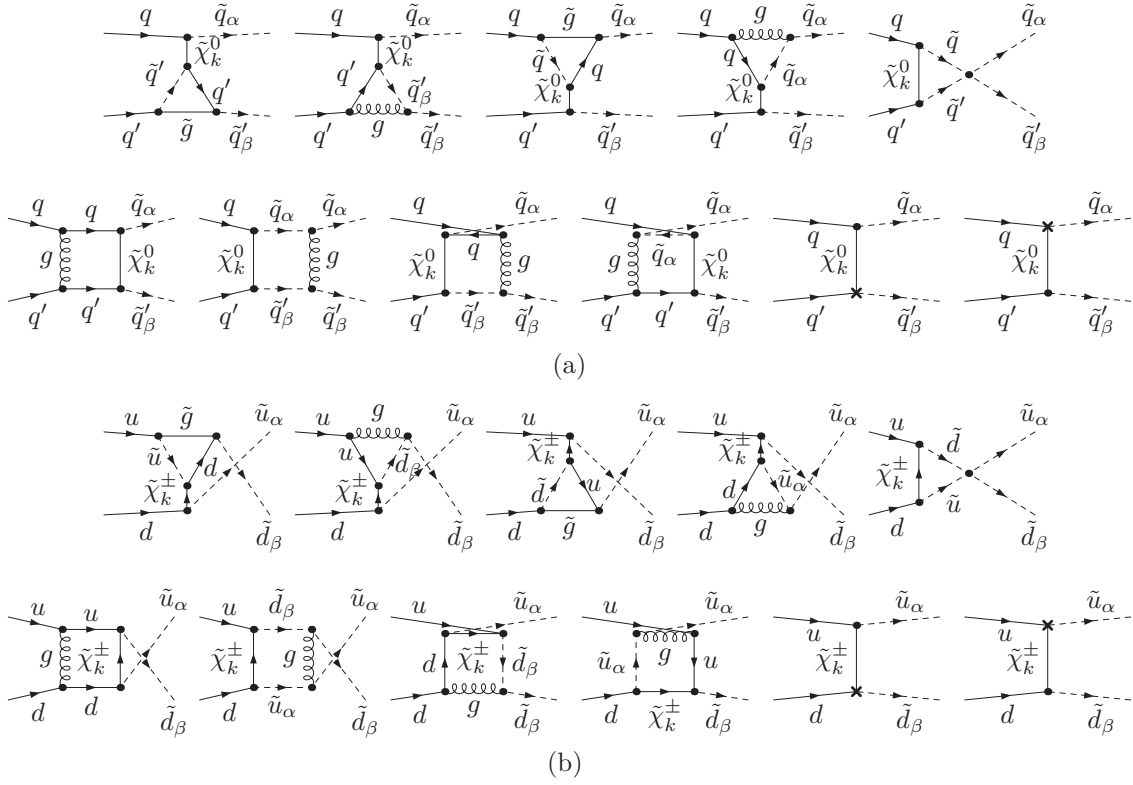
Figure 5.4: Virtual corrections (I): EW one-loop insertions into QCD Born diagrams. Q and Q' denote the SU(2) partner of quark q and q', respectively. We use generic labels $V^0 = \gamma, Z$ and $S^0 = h^0, H^0, G^0, A^0$. If the chirality of an internal squark is not specified, it can be any. The diagram containing the four-squark vertex has to be taken at $\mathcal{O}(\alpha_s \alpha)$. The diagrams in the third line contribute only for $u = \{u, c\}$, $d = \{d, s\}$. The last two diagrams contain the counterterms, whose renormalization constants have to be evaluated at $\mathcal{O}(\alpha)$. For $q = q'$ crossed diagrams have to be taken into account.

the divergent amplitudes are regularized in dimensional reduction and on-shell conditions are imposed to fix the (s)quark renormalization constants.

The third subset, Figure 5.3c, refers to pure-QCD one-loop amplitudes, i.e. gluino-mediated diagrams with strong insertions ($\mathcal{M}^{2,0}$). It consists of vertex and box corrections, and in addition self-energy corrections to the gluino have to be taken into account. The full set of diagrams is shown in Figure 5.6. However, due to color correlations, the self-energy and vertex corrections only contribute to the 10 processes with non-vanishing tree-level QCD–EW interferences. For those, one also has to take the counterterm diagrams into account (last three diagrams of Figure 5.6) and one has to renormalize the quark and squark sector as well as the gluino and the strong Yukawa coupling $\hat{g}_s$, which appears in the $q\tilde{q}\tilde{g}$ vertex. The renormalization constants have to be evaluated at $\mathcal{O}(\alpha_s)$. The strong scalar coupling $\hat{g}_s$ is related to the strong coupling g_s via supersymmetry. To match the definition of the strong coupling constant used in the extraction of the PDFs, g_s has to be given in the $\overline{\text{MS}}$ scheme with the contributions from heavy particles subtracted in the running of α_s, for further details on the definition of the PDFs, we refer to Section 4.2. We thus regularize
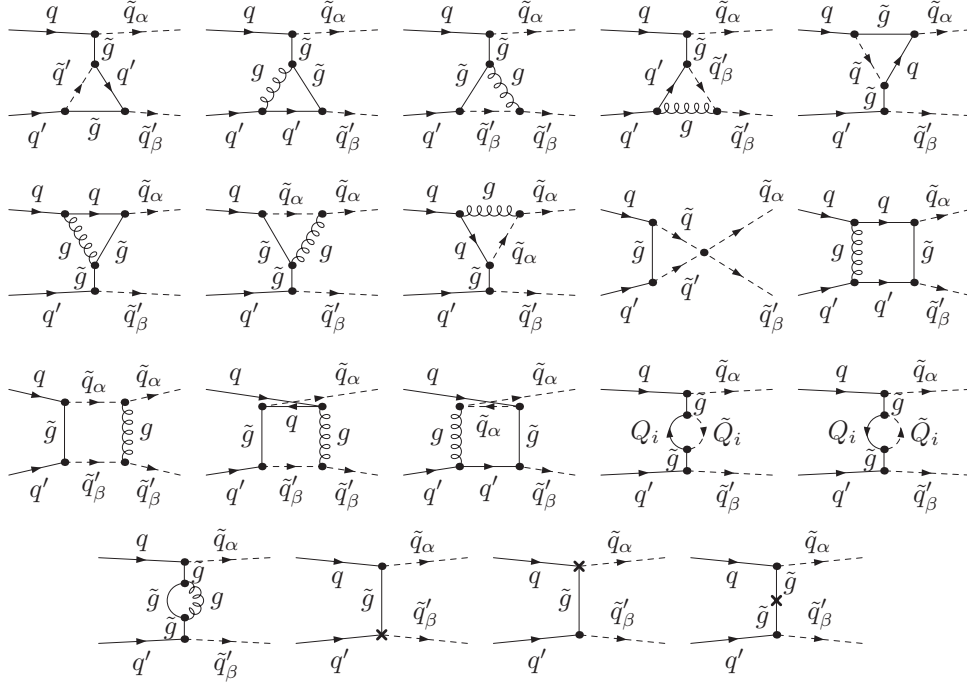
(a)

(b)

Figure 5.5: Virtual corrections (II): QCD one-loop insertions into EW Born diagrams. For $q = q'$ crossed diagrams have to be taken into account. The diagrams containing the four squark interaction vertex have to be evaluated at $\mathcal{O}(\alpha_s\alpha)$. The chargino-mediated diagrams only contribute for $u = \{u, c\}$, $d = \{d, s\}$. The renormalization constants appearing in the counterterm diagrams (last line) have to be evaluated at $\mathcal{O}(\alpha_s)$.

this part of the virtual corrections using dimensional regularization. Quarks and squarks are renormalized on-shell again, in the strong sector the $\overline{\text{MS}}$ scheme is applied. Dimensional regularization however induces a finite difference between g_s and $\hat{g}_s$ at the one-loop level and violates the supersymmetric relation between the two couplings [127]. We add the well-known finite shift in the definition of the renormalization constant for $\hat{g}_s$ in order to restore SUSY in the physical amplitudes [18]. The explicit counterterms for g_s and $\hat{g}_s$ are given by (4.81) and (4.83b).

The virtual corrections also exhibit photonic and gluonic mass singularities of infrared and collinear origin. In $\mathcal{M}^{1,1}_{(\text{EW})}$, mass singularities arise if two external particles exchange a low-energetic massless photon while collinear singularities appear if one of the massless initial-state quarks splits collinearly into a quark and a photon. In order to obtain an IR finite result, real photon radiation at $\mathcal{O}(\alpha_s^2\alpha)$ has to be added. In contrast in $\mathcal{M}^{1,1}_{(\text{QCD})}$, massless gluons running in the loops give rise to mass singularities in the soft and collinear limit. Similarly, the diagrams contributing to $\mathcal{M}^{2,0}$ suffer from gluonic IR and collinear singularities. Hence we have to include real gluon bremsstrahlung at $\mathcal{O}(\alpha_s^2\alpha)$ in order to

Figure 5.6: Virtual corrections (III): QCD one-loop insertions into QCD Born diagrams. For $q = q'$ crossed diagrams have to be taken into account. Here, Q_i can be any of the six quark flavors. The diagram containing the four squark vertex has to be evaluated at $\mathcal{O}(\alpha_s^2)$. The renormalization constants appearing in the counter term diagrams (last three diagrams) have to be evaluated at $\mathcal{O}(\alpha_s)$, i.e. the strong sector has to be renormalized.

cancel the IR singularities. We regularize the photonic singularities by means of mass regularization. Owing to the photon-like appearance of the gluon in the respective diagrams, it is also possible to regularize these IR singularities by a fictitious gluon mass. The treatment of soft and collinear photon and gluon emission is discussed in detail in Section 4.5.

5.3.2 Real Corrections

Three independent bremsstrahlung processes contribute at $\mathcal{O}(\alpha_s^2\alpha)$, as depicted in Figure 5.7. Real photon and real gluon radiation processes have to be combined with the corresponding subset of virtual corrections to obtain an IR finite result. We use the phase-space slicing method of Section 4.5.1 in order to divide the real photon and gluon emission into singular and non-singular regions. For real gluon emission, color correlations have to be taken into account, as described in Section 4.5.2. Remaining collinear singularities of photonic and gluonic origin have to be absorbed into the PDFs, see also Section 4.5.3. Also real quark radiation gives nonzero contributions from the interference of QCD and EW mediated diagrams and has to be included in the cross section at $\mathcal{O}(\alpha_s^2\alpha)$.

Photon bremsstrahlung:

Gluon bremsstrahlung:

Real quark radiation:
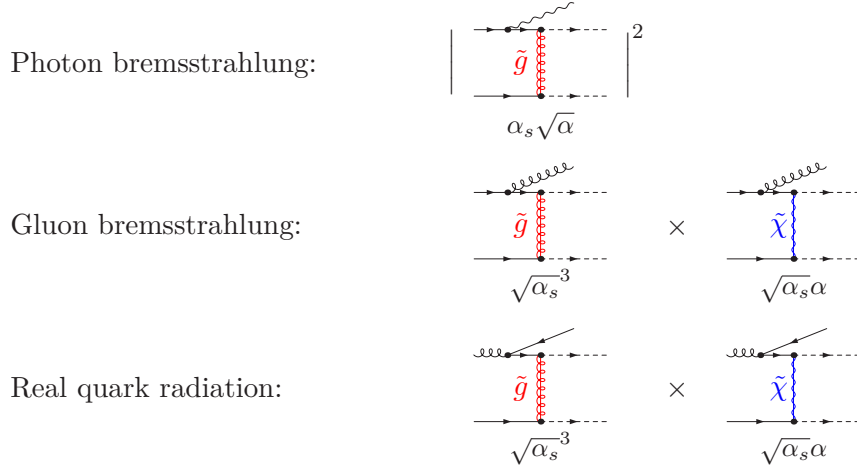
Figure 5.7: Sample of Feynman diagrams for the three subsets of real emission contributions at $\mathcal{O}(\alpha_s^2\alpha)$. The order in the perturbative expansion is specified for each diagram. The full sets of diagrams are given Figures 5.8, 5.9, and 5.10.

Real Photon Emission

The real photon emission at $\mathcal{O}(\alpha_s^2\alpha)$,

$$q(p_1)\, q'(p_2) \;\rightarrow\; \tilde{q}_\alpha(p_3)\, \tilde{q}'_\beta(p_4)\, \gamma(k), \tag{5.14}$$

is given by the squared matrix element of a QCD tree-level diagram with an external photon attached (see Figure 5.7, top and Figure 5.8 for the full set of diagrams). The integration over the photon phase-space is IR divergent in the soft-photon region, i.e. for $k^0 \to 0$. Further singularities arise in the collinear region if $p_i \cdot k \to 0$ for $i = \{1, 2\}$. We use phase-space slicing and apply a cut on the photon energy, $k^0 > \delta_s\sqrt{\hat{s}}/2$, and on the angle θ between the photon and incoming partons, $|\cos(\theta)| < 1-\delta_\theta$, to split off the singular regions. In the hard, non-collinear region the integration is convergent and is performed numerically. The cross sections in the soft- and collinear region can be approximated analytically and are given by, cf. Section 4.5.1,

$$\mathrm{d}\hat{\sigma}^{2,1}_{12\to34\gamma}\big|_{\mathrm{soft}} = -\frac{\alpha}{2\pi}\mathrm{d}\hat{\sigma}^{2,1}_{12\to34}\sum_{i,j=1;i<j}^{4} e_ie_j\sigma_i\sigma_j\mathcal{I}_{ij}\,, \tag{5.15}$$

$$\mathrm{d}\hat{\sigma}^{2,1}_{12\to34\gamma}(\hat{s})\Big|_{\mathrm{coll}} = \frac{\alpha(e_q^2+e_{q'}^2)}{2\pi}\int_{z_0}^{1-\delta_s}\mathrm{d}z\,\kappa_{qq}(z,\hat{s})\,\mathrm{d}\hat{\sigma}^{2,0}_{12\to34}(z\hat{s}), \tag{5.16}$$

e_i is the charge of the ith particle and $\sigma_i = \pm1$ depending on whether the particle is incoming or outgoing, respectively. The universal phase-space integrals $\mathcal{I}_{ij}$ are listed in (4.91), while z_0 and κ_{qq} are given by

$$z_0 = (m_{\tilde{q}}^2 + m_{\tilde{q}'}^2)/\hat{s}, \qquad \kappa_{qq}(z,\hat{s}) = \frac{1+z^2}{1-z}\ln\left(\frac{\hat{s}\delta_\theta}{2m_q}\right) - \frac{2z}{1-z}. \tag{5.17}$$
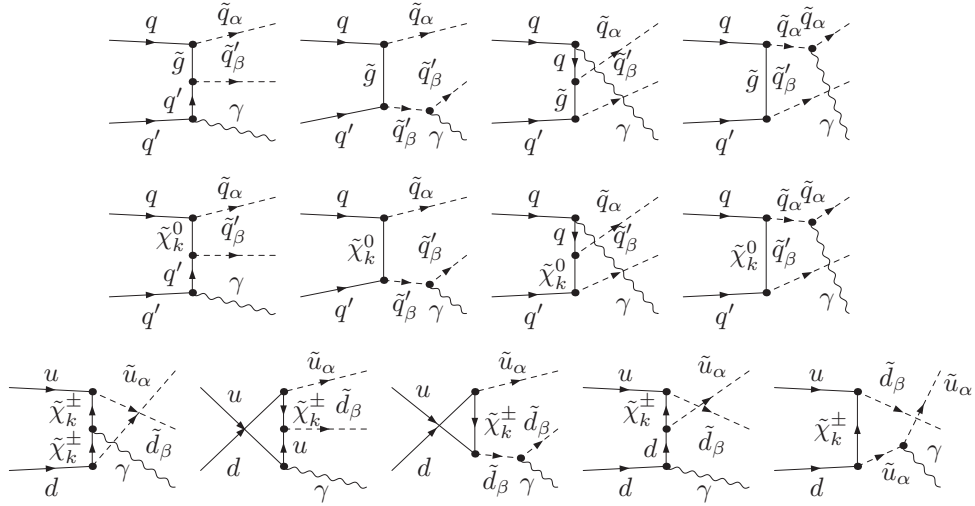
Figure 5.8: Feynman diagrams for real photon emission. For $q = q'$ crossed diagrams have to be taken into account. Diagrams in the last row only contribute for $u = \{u, c\}$, $d = \{d, s\}$.

As explained in Section 4.5.1, the upper integration bound in the collinear region is lowered by δ_s to avoid double counting of the soft regime.

By combining the real photon emission with the virtual EW-type corrections (Figure 5.3a), the soft singularities cancel. Remaining initial-state collinear singularities are universal and have to be absorbed via factorization in the PDFs, see Section 5.3.3. In the following, we will refer to this UV-, IR- and collinear-finite combination as the EW-type corrections.

Real Gluon Emission

Real gluon bremsstrahlung at $\mathcal{O}(\alpha_s^2 \alpha)$ proceeds via the partonic process

$$q(p_1)\, q'(p_2) \ \to \ \tilde{q}_\alpha(p_3)\, \tilde{q}'_\beta(p_3)\, g(k). \tag{5.18}$$

It is given by the interference term of a QCD and an EW tree-level diagram, both with an external gluon attached on (Figure 5.7, center and Figure 5.9). In the considered processes the gluon is Abelian like and we can treat soft and collinear singularities by mass regularization in close analogy to the photonic case. However the eikonal current has to be modified in order to take color correlations into account. Different to real photon emission, collinear singularities only arise for diagonal $\tilde{q}_\alpha \tilde{q}_\alpha$, $\tilde{u}_L \tilde{d}_L$, and $\tilde{c}_L \tilde{s}_L$ production. This can be seen by noticing that in the collinear cone the cross section becomes proportional to the corresponding $2 \to 2$ process, which in this case would be squark–squark production at $\mathcal{O}(\alpha_s \alpha)$; i.e. the interference of tree-level QCD and EW diagrams must be non-vanishing. In the notation of Section 4.5.2, the explicit expressions for the differential cross sections in the soft and

collinear limit are given by,

$$\mathrm{d}\hat{\sigma}^{2,1}_{12\to34g}\Big|_{\mathrm{soft}} = -\frac{\alpha_s}{2\pi}\Big\{ \sum_{i,j=1;i<j}^{4} \mathcal{I}_{ij}\mathcal{F}_{ij}\Big\}\frac{\mathrm{d}t}{16\pi\hat{s}^2},\tag{5.19}$$

$$\mathrm{d}\hat{\sigma}^{2,1}_{12\to34g}(\hat{s})\Big|_{\mathrm{coll}} = \frac{\alpha_s C_F}{\pi}\int_{z_0}^{1-\delta_s}\mathrm{d}z\,\kappa_{qq}(z,\hat{s})\,\mathrm{d}\hat{\sigma}^{1,1}_{12\to34}(z\hat{s}),\tag{5.20}$$

with the phase-space integrals $\mathcal{I}_{ij}$ and the color correlated amplitudes $\mathcal{F}_{ij}$ defined in (4.91) and (4.110), respectively. z_0 and κ_{qq} are the same as for collinear photon emission and given by eq. (5.17). In the case of squark–squark production the tree-level amplitude can be decomposed according to their color structure as

$$\mathcal{M}^{i,j\,c_1c_2c_3c_4}_{12\to34} = \delta_{c_1c_3}\delta_{c_2c_4}\mathcal{M}^{i,j}_1 + \delta_{c_1c_4}\delta_{c_2c_2}\mathcal{M}^{i,j}_2, \qquad (i,j)=(1,0),(0,1),$$
$$\mathcal{M}^{0,1}_1 = \mathcal{M}^{0,1}_T, \qquad \mathcal{M}^{1,0}_1 = \frac{1}{2}\left(\mathcal{M}^{1,0}_U - \frac{1}{3}\mathcal{M}^{1,0}_T\right),\tag{5.21}$$
$$\mathcal{M}^{0,1}_2 = \mathcal{M}^{0,1}_U, \qquad \mathcal{M}^{1,0}_2 = \frac{1}{2}\left(\mathcal{M}^{1,0}_T - \frac{1}{3}\mathcal{M}^{1,0}_U\right),$$

where $\mathcal{M}^{i,j}_{U,T}$ are the amplitudes corresponding to the u-channel and t-channel diagrams, respectively. In this case the color correlated amplitudes $\mathcal{F}_{ij}$ are given by

$$\mathcal{F}_{12} = \mathcal{F}_{34} = 4\left[\left(\mathcal{M}^{0,1}_1\right)^*\mathcal{M}^{1,0}_2 + \mathcal{M}^{0,1*}_2\mathcal{M}^{1,0}_1\right],$$
$$\mathcal{F}_{13} = \mathcal{F}_{24} = -12\left(\mathcal{M}^{0,1}_1\right)^*\mathcal{M}^{1,0}_1 - 4\left[\left(\mathcal{M}^{0,1}_1\right)^*\mathcal{M}^{1,0}_2 + \left(\mathcal{M}^{0,1}_2\right)^*\mathcal{M}^{1,0}_1\right],$$
$$\mathcal{F}_{14} = \mathcal{F}_{23} = -4\left[\left(\mathcal{M}^{0,1}_1\right)^*\mathcal{M}^{1,0}_2 + \left(\mathcal{M}^{0,1}_2\right)^*\mathcal{M}^{1,0}_1\right] - 12\left(\mathcal{M}^{0,1}_2\right)^*\mathcal{M}^{1,0}_2,\tag{5.22}$$
$$\mathcal{F}_{ii} = 12\left[\left(\mathcal{M}^{0,1}_1\right)^*\mathcal{M}^{1,0}_1 + \left(\mathcal{M}^{0,1}_2\right)^*\mathcal{M}^{1,0}_2\right] + 4\left[\left(\mathcal{M}^{0,1}_1\right)^*\mathcal{M}^{1,0}_2 + \left(\mathcal{M}^{0,1}_2\right)^*\mathcal{M}^{1,0}_1\right],$$

where in the last case $i=1,\dots,4$.

By combining real gluon emission and the two virtual QCD-type corrections (Figure 5.3b,c), the IR singularities cancel. Remaining collinear singularities are again absorbed into the PDFs, as described in Section 5.3.3. In the following we will refer to this UV-, IR- and collinear-finite combination as the QCD-type corrections.

Real Quark Emission

Finally, also real quark radiation contributes at $\mathcal{O}(\alpha_s^2\alpha)$,

$$g(p_1)\,q(p_2) \to \tilde{q}_\alpha(p_3)\,\tilde{q}'_\beta(p_4)\,\bar{q}'(k),$$
$$\text{and if } q\neq q' \qquad g(p_1)\,q'(p_2) \to \tilde{q}_\alpha(p_3)\,\tilde{q}'_\beta(p_4)\,\bar{q}(k),\tag{5.23}$$

via the interference of a QCD-type diagram with an EW-type diagram, as shown in Figure 5.7, bottom (see Figure 5.10 for the complete listing of diagrams). This process can be regarded as completely independent of the virtual corrections, since it is IR finite by itself. However it has to be taken into account in a consistent analysis of electroweak corrections up to

(a)

(b)
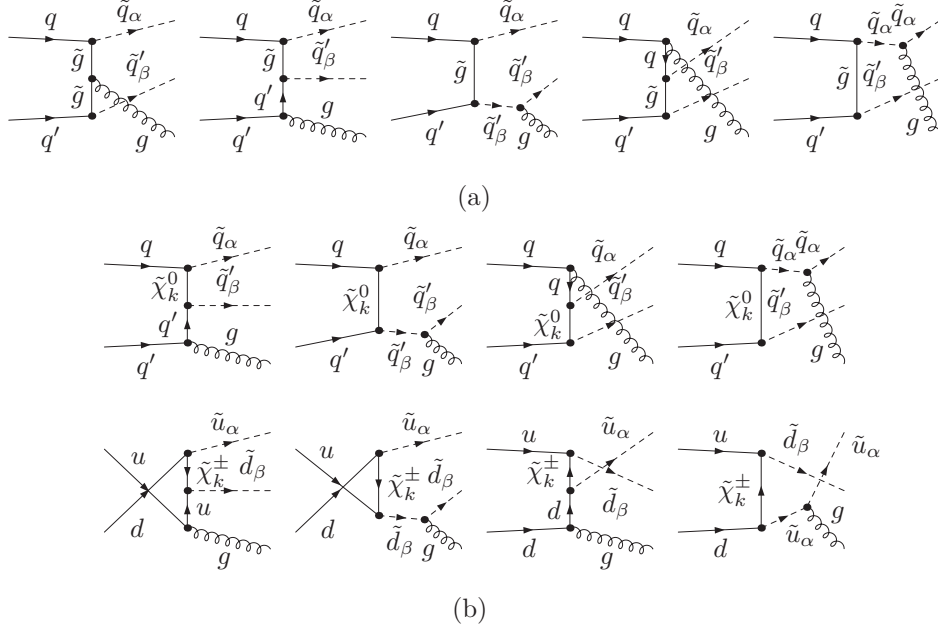
Figure 5.9: Feynman diagrams for real gluon emission. Only interferences of diagrams in (a) and (b) contribute at $\mathcal{O}(\alpha_s^2\alpha)$. For $q = q'$ crossed diagrams have to be taken into account. Diagrams in the last row only contribute for $u = \{u, c\}$, $d = \{d, s\}$.

$\mathcal{O}(\alpha_s^2\alpha)$. Initial-state collinear singularities are present for processes with non-vanishing tree-level interferences. The cross section in the collinear region is given by a convolution integral, cf. Section 4.5.3,

$$\mathrm{d}\hat{\sigma}^{2,1}_{12\to34\bar{q}}(\hat{s})\Big|_{\mathrm{coll}} = \frac{\alpha_s T_F}{2\pi}\int_{z_0}^{1}\mathrm{d}z\,\kappa_{qg}(z,\hat{s})\mathrm{d}\hat{\sigma}^{1,1}_{12\to34}(z\hat{s}), \tag{5.24}$$

with $T_F = 1/2$. κ_{qg} is given by

$$\kappa_{qg} = (z^2 + (1-z)^2)\ln\left(\frac{\hat{s}\delta_\theta(1-z)^2}{2m_q^2}\right) + 2z(1-z), \tag{5.25}$$

while z_0 is defined according to (5.17). As before, these singularities are absorbed via factorization into the PDFs, see Section 5.3.3.

Different to photon and gluon bremsstrahlung, the internal gluino, neutralino or chargino can go on-shell in specific SUSY scenarios, if heavier than one of the external squarks. In these cases, we include a Breit–Wigner width for the resonant particle in the corresponding propagators to regularize the poles. Note that physical resonances do not occur. This is different to the case of real quark radiation in e.g. gluino–squark production processes [28], where internal squarks can go on-shell in both the EW- and the QCD-mediated diagrams.

(a)

(b)
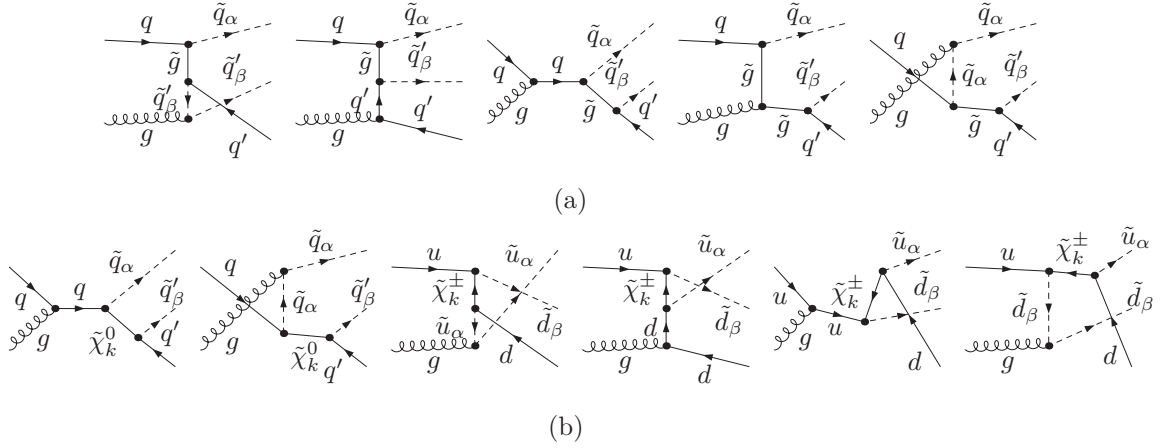
Figure 5.10: Feynman diagrams for real quark emission. Only interferences of diagrams in (a) and (b) contribute at $\mathcal{O}(\alpha_s^2\alpha)$. For $q \neq q'$ diagrams with q and q' exchanged have to be considered, too. For $q = q'$ crossed diagrams have to be taken into account. Diagrams in the last row only contribute for $u = \{u, c\}$, $d = \{d, s\}$.

5.3.3 Factorization of Initial-State Collinear Singularities

The remaining collinear singularities have to be absorbed by redefining the PDFs. At $\mathcal{O}(\alpha_s^2\alpha)$ this can be achieved by the replacement [155, 156], cf. Section 4.5,

$$
\begin{aligned}
f_q(x, \mu_F) \to\; & f_q(x, \mu_F) \left(1 - \frac{\alpha e_q^2 + \alpha_s C_F}{\pi} \kappa_{v+s} - \frac{1}{4} \frac{\alpha e_q^2}{\pi} f_{v+s} \right) \\
& - \int_x^{1-\delta_s} \frac{dz}{z} f_q\left(\frac{x}{z}, \mu_F\right) \left(\frac{\alpha e_q^2 + \alpha_s C_F}{2\pi} \kappa_c(z) - \frac{\alpha e_q^2}{2\pi} f_c(z) \right) \\
& - \int_x^1 \frac{dz}{z} f_g\left(\frac{x}{z}, \mu_F\right) \frac{\alpha_s C_F}{2\pi} P_{qg}(z) \ln\left(\frac{\mu_F^2}{m_q^2}\right),
\end{aligned}
\tag{5.26}
$$

where e_q denotes the electric charge of quark q, $C_F = 4/3$, and

$$
\begin{aligned}
\kappa_{v+s} &= 1 - \ln\delta_s - \ln^2\delta_s + \left(\ln\delta_s + \frac{3}{4}\right)\ln\left(\frac{\mu_F^2}{m_q^2}\right), \\
\kappa_c(z) &= P_{qq}(z)\ln\left(\frac{\mu_F^2}{m_q^2}\frac{1}{(1-z)^2} - 1\right).
\end{aligned}
\tag{5.27}
$$

The factorization-scheme dependent functions are

$$
\begin{aligned}
f_{v+s} &= 9 + \frac{2\pi^2}{3} + 3\ln\delta_s - 2\ln^2\delta_s, \\
f_c(z) &= P_{qq}(z)\ln\left(\frac{1-z}{z}\right) - \frac{3}{2}\frac{1}{1-z} + 2z + 3,
\end{aligned}
\tag{5.28}
$$

with the splitting functions

$$
P_{qq}(z) = \frac{1+z^2}{1-z}, \qquad\qquad P_{qg}(z) = z^2 + (1-z^2).
\tag{5.29}
$$

The factorization is done in the $\overline{\text{MS}}$ scheme at NLO QCD and in the physical DIS scheme at NLO EW. The replacement of the PDFs in (5.5) gives further contributions of $\mathcal{O}(\alpha_s^2\alpha)$ to the total cross section. The first and second line in (5.26) cancel the remaining singularities in the EW-type and QCD-type corrections. The third line in (5.26) cancels the collinear singularities in the real quark radiation.

5.4 Numerical Results

In the following we illustrate the impact of the EW contributions on the production cross section. Since we have 36 processes contributing to squark–squark production and the same amount for anti-squark–anti-squark production, we present (at least partly) inclusive results. We refer to four different combinations of (anti-)squarks in the final state, which differ with respect to the chirality of the produced particles:

- $\tilde{q}_L\tilde{q}'_L$ or "LL" refers to the inclusive production of two left-handed squarks and two left-handed anti-squarks.

- $\tilde{q}_L\tilde{q}'_R$ or "LR" refers to the inclusive production of one left-handed and one right-handed squark and the charge-conjugated process.

- $\tilde{q}_R\tilde{q}'_R$ or "RR" refers to the inclusive production of two right-handed squarks and two right-handed anti-squarks.

- $\tilde{q}\tilde{q}'$ or "incl." refers to the inclusive production of all (anti-)squarks. It is given by the sum of the three cases above, taking all 72 subprocesses of squark–squark and anti-squark–anti-squark final states into account.

We focus here on these chirality-based classes since squarks of different chiralities are, in principle, experimentally distinguishable by their decay chains, see e.g. Section 5.1.2 of [91].

In the discussion we refer to the following quantities, based on the cross section definitions in Section 5.2. The leading order cross section is denoted by $\sigma^{\text{Born}} = \sigma^{2,0}$. The tree-level EW and the NLO EW contributions to the cross section are labeled by

$$\Delta\sigma^{\text{tree EW}} = (\sigma^{1,1} + \sigma^{0,2}), \qquad \Delta\sigma^{\text{NLO EW}} = \sigma^{2,1}, \tag{5.30}$$

respectively, and $\Delta\sigma^{\text{EW}} = \Delta\sigma^{\text{tree EW}} + \Delta\sigma^{\text{NLO EW}}$ will be referred to as the EW contribution. The total sum of the LO cross section with the EW contributions is denoted by $\sigma^{\text{NLO}} = \sigma^{\text{Born}} + \Delta\sigma^{\text{EW}}$. Relative EW contributions are defined by

$$\delta^{\text{tree EW}} = \Delta\sigma^{\text{tree EW}}/\sigma^{\text{Born}}, \qquad \delta^{\text{NLO EW}} = \Delta\sigma^{\text{NLO EW}}/\sigma^{\text{Born}}, \qquad \delta^{\text{EW}} = \Delta\sigma^{\text{EW}}/\sigma^{\text{Born}}. \tag{5.31}$$

In distributions δ denotes the relative EW contribution defined as $\delta = (\mathcal{O}_{\text{NLO}} - \mathcal{O}_{\text{Born}})/\mathcal{O}_{\text{Born}}$, where $\mathcal{O}$ is a generic observable and $\mathcal{O}_{\text{NLO}}$ is the sum of the Born and the EW contribution.

	m_0	$m_{1/2}$	A_0	$\tan\beta$	$\text{sign}(\mu)$
SPS1a$'$	70 GeV	250 GeV	-300 GeV	10	$+$
SPS2	1450 GeV	300 GeV	0	9.66	$+$
SPS5	150 GeV	300 GeV	-1000 GeV	4.82	$+$

Table 5.3: High energy input parameters for the different SUSY scenarios considered. The mass parameters m_0, $m_{1/2}$ and A_0 are given at the GUT scale, $\tan\beta$ is evaluated at $M_{\text{SUSY}} = 1\,\text{TeV}$.

5.4.1 Input Parameters

The Standard Model input parameters are chosen in correspondence with [14, 140],

$$
\begin{aligned}
M_Z &= 91.1876 \text{ GeV}, & M_W &= 80.399 \text{ GeV}, \\
\alpha^{-1} &= 137.036, & \alpha_s(M_Z) &= 0.118, \\
m_t &= 170.9 \text{ GeV}, & m_b^{\overline{\text{MS}}}(M_Z) &= 2.94 \text{ GeV}.
\end{aligned}
\tag{5.32}
$$

The strong coupling constant α_s has been defined in the $\overline{\text{MS}}$ scheme using the two-loop renormalization group equation with five light flavors, cf. Section 4.4.2. The bottom-quark mass is taken from [164]. In particular, this value is consistent with the world average, usually quoted as $m_b^{\overline{\text{MS}}}(m_b) = 4.19^{+0.18}_{-0.06}$ and $m_b^{1S} = 4.67^{+0.18}_{-0.06}$, respectively [14].

For the SUSY parameters, we refer to three benchmark mSUGRA scenarios, the SPS1a$'$ scenario, the SPS2, and SPS5 scenario [90, 165]. The SPS1a$'$ scenario can be considered as a "typical" mSUGRA scenario. It has been proposed by the SPA convention and should be used for comparisons with other calculations. The SPS2 scenario features relatively heavy squarks with light charginos and neutralinos and a gluino lighter than the squarks. The SPS5 scenario leads to a very light $\tilde{t}_1$ with moderate light-flavor squark masses. In each scenario, the particle spectrum is determined by universal GUT scale parameters, cf. Table 5.3, which act as boundary conditions for the renormalization group running of the soft-breaking parameters. We use the program SOFTSUSY [166] to evolve the soft-breaking parameters down to the SUSY scale M_{SUSY}. We choose a common SUSY scale $M_{\text{SUSY}} = 1\,\text{TeV}$ for all scenarios, in reference to the SPA convention. At M_{SUSY} a consistent translation of the squark masses into the on-shell scheme is performed. The left-handed down-type squark is treated as a dependent mass parameter, fixed by SU(2) invariance. It is set to its corresponding on-shell value obtained at one-loop accuracy according to [143]. The on-shell mass parameters for the light-flavor squarks together with the masses of the gluino and the lightest neutralino/chargino are summarized in Table 5.4.

The technical cuts needed for the regularization of soft and collinear singularities are set to $\delta_s = 2{\cdot}10^{-3}$ and $\delta_\theta = 10^{-4}$. We checked numerically that these values are sufficiently small to justify the eikonal approximation. Figure 5.11 shows the dependence on the cut parameters δ_s (first line) and δ_θ (second line) for $\tilde{u}_L\tilde{u}_L$ production. This process is chosen exemplary, since it has a large tree-level contribution arising from QCD–EW interferences and hence

|	$\tilde{u}_L$	$\tilde{u}_R$	$\tilde{d}_L$	$\tilde{d}_R$	$\tilde{g}$	$\tilde{\chi}_1^0$	$\tilde{\chi}_1^\pm$
SPS1a$'$	561	543	566	539	609	101	180
SPS2	1559	1554	1561	1555	785	120	199
SPS5	677	655	681	654	724	123	225

Table 5.4: On-shell masses of the squarks, the gluino, and the lightest neutralino and chargino within the different SUSY scenarios considered. All masses are given in GeV.

exhibits a singular behavior for collinear gluon emission, cf. Section 5.3.2. The left panels show the contributions to $\Delta\sigma^{\mathrm{NLO\ EW}}$ from the virtual corrections combined with the soft singular region, from the collinear cone, and from the non-singular real radiation. For the δ_s dependence one gets large cancellations between the three plotted contributions for small cut parameters. The virtual and soft contributions are independent of the angular cut parameter δ_θ. On the right panels, the sum of all three contributions, including error-bars, is plotted separately. One can see that for small enough values of the cut parameters $\Delta\sigma^{\mathrm{NLO\ EW}}$ approaches an asymptotic value, i.e. the eikonal approximation becomes valid. However, for small values δ_s and δ_θ large cancellations occur which lead to higher uncertainties due to the numerical integration.

The results presented in this section are computed using the MRST2004QED parton distribution functions [126] and setting the hadronic center of mass energy to $\sqrt{S} = 14$ TeV. For comparison, we give results at $\sqrt{S} = 7$ TeV in Section 5.4.5.

5.4.2 Renormalization and Factorization Scale Dependence

Figure 5.12 shows the scale dependence for the SPS1a$'$ scenario. Here we are inclusive with respect to processes that contribute at $\mathcal{O}(\alpha_s\alpha)$. We compare the tree-level EW contribution with the cross section including the NLO EW contributions at $\mathcal{O}(\alpha_s^2\alpha)$, i.e. one order higher in the strong coupling. In the left panel, factorization and renormalization scales are identified, $\mu = \mu_R = \mu_F = \overline{m}_{\tilde{q}}$ with $\overline{m}_{\tilde{q}}$ being the average mass of the light-flavor squarks. The tree-level EW contribution $\Delta\sigma^{\mathrm{tree\ EW}}$ to the cross section is calculated using the MRST2001LO PDF set [167] which is the LO PDF set corresponding to the MRST2004QED set [168]. In the right panel the renormalization scale is fixed and only the factorization scale is varied. For the LO EW and NLO EW contributions given by the red and blue curves, the same PDF sets are used. The green curve, is obtained by using the MRST2004NNLO PDF set [169]. One finds that the scale dependence of the hadronic cross section is considerably reduced by taking the NLO EW contributions into account. The residual uncertainty arises mostly from the choice of the renormalization scale while the dependence on the factorization scale variation is mild at NLO as can be seen from Figure 5.12 (b). From Figure 5.12 (a) one finds that $\Delta\sigma^{\mathrm{tree\ EW}}$ and $\Delta\sigma^{\mathrm{EW}}$ coincide at the scale $\mu = 1.5\,\overline{m}_{\tilde{q}}$. This scale strongly differs from the scale proposed from NLO QCD corrections, where the LO and NLO cross section coincide at scales $\mu \approx 0.5\,\overline{m}_{\tilde{q}}$, cf. Section 3.2. It is interesting to note that the impact of QED effects

$$PP \to \tilde{u}_L \tilde{u}_L$$
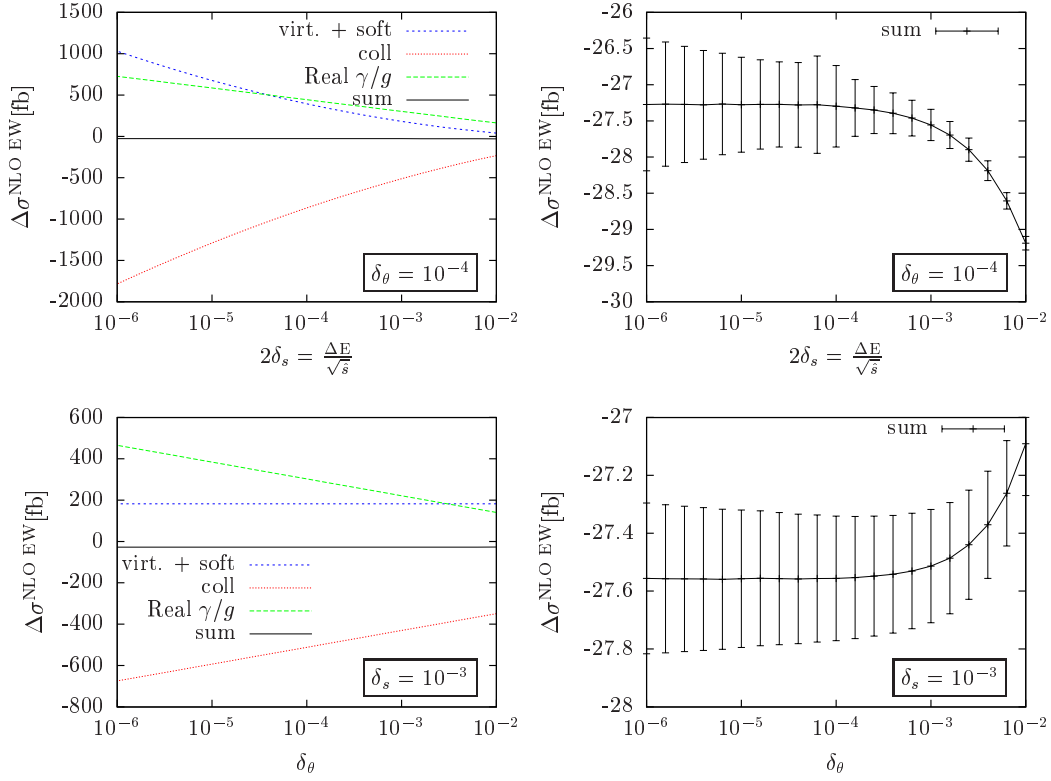
Figure 5.11: Dependence of $\Delta\sigma^{\text{NLO EW}}$ on the technical cut parameters δ_s (first line) and δ_θ (second line). The left panels show the contributions from the virtual corrections and the soft singular region (blue line), from the collinear cone (red line), and from the non-singular real radiation (green line). The sum of the contributions, given by the black line, is also shown separately on the right panels including error-bars.

in the evolution of the PDFs is small. This feature, already pointed out in [170], has been explicitly checked using the NLO QCD PDF provided by the MRST2004NNLO set, which does not include QED effects (green curve of Figure 5.12 (b)). In the following, the factorization and renormalization scales are set to the common value $\mu = \mu_R = \mu_F = \overline{m}_{\tilde{q}}$.

5.4.3 Total Hadronic Cross Sections

Tables 5.5–5.7 give the results for the hadronic cross sections for squark–squark production at the LHC at $\sqrt{S} = 14$ TeV within the SPS1a′, SPS2, and SPS5 scenario, respectively. We refer to the production of squarks of different chiralities separately and implicitly sum over flavor, cf. Section 5.4. Renormalization and factorization scales are set to $\mu = 560$ GeV (SPS1a′), $\mu = 1560$ GeV (SPS2), and $\mu = 666$ GeV (SPS5). We checked that the results for the tree-level EW contributions numerically agree with those quoted for the SPA1a scenario in [25]. Differences between [25] and Tables 5.5–5.7 are related to the choice of input parameters and to the strong scale dependence of the tree-level EW contributions, see Figure 5.12.

$$PP \to \{\tilde{q}_L\tilde{q}_L, \tilde{q}_R\tilde{q}_R, \tilde{u}_L\tilde{d}_L, \tilde{c}_L\tilde{s}_L\}$$

(a)   (b)
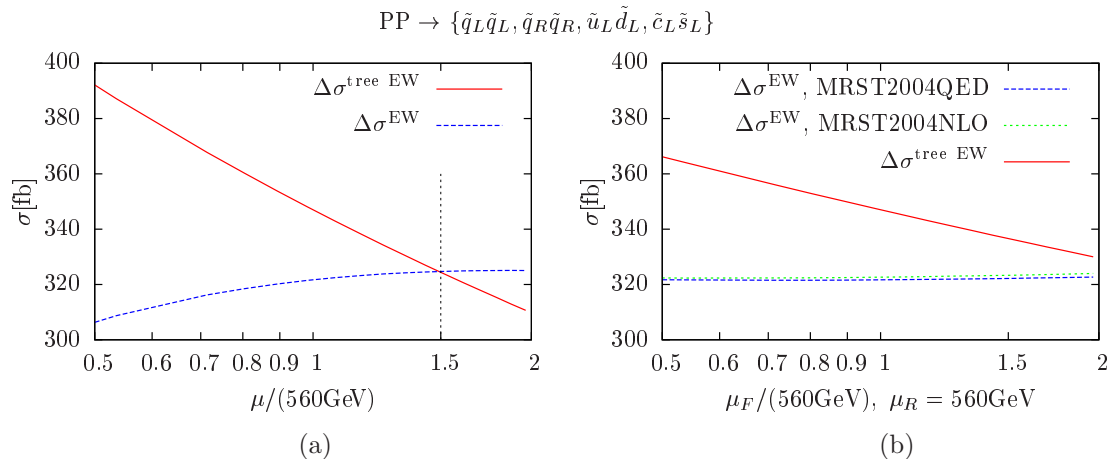
Figure 5.12: Dependence of the hadronic cross section σ on the renormalization and factorization scale μ_R and μ_F for the SPS1a' scenario: (a) both scales are set to a common value $\mu_R = \mu_F = \mu$ with μ varied by a factor two around $\overline{m}_{\tilde{q}} = 560$ GeV, (b) variation of μ_F, with fixed $\mu_R = \overline{m}_{\tilde{q}}$. Only processes that contribute at $\mathcal{O}(\alpha_s\alpha)$ are considered. The red line shows the tree-level EW contribution to the cross section using a LO PDF set, while the blue and green curve shows the EW contribution up to NLO EW using NLO QCD PDF sets with (blue) and without (green) QED evolution. Further details are given in the text.

The Born cross section is QCD mediated and does not depend on the chirality of the produced squarks. Indeed the cross sections for the diagonal production of two squarks, LL or RR, become equal for degenerate masses. The Born cross section for non-diagonal LR production, however, is different in general since the final-state particles are distinguishable. In the SPS1a' and SPS5 scenario it happens to be of similar size as the LL and RR production cross sections. In the SPS2 scenario, however, the LR cross section is enhanced and accounts for 50% of the total cross section for inclusive squark–squark production. As we will see below, cf. Figure 5.15 (b), the relative yield of the LR production cross section is determined by the ratio of squark and gluino masses, becoming more important if the exchanged gluino is lighter than the final-state squarks.

Due to the nature of the electroweak interaction, the EW cross section contributions depend strongly on the chirality of the produced squarks. The tree-level EW contributions have been studied extensively in [25]. Their impact is largest in case of the LL production of two SU(2) gauged left-handed squarks ($15 - 25\%$ in the considered scenarios). For RR production, where only U(1)$_Y$ couplings enter the EW-mediated diagrams, the tree-level EW contributions are around one order of magnitude smaller. They are even further suppressed for LR production, where the $\mathcal{O}(\alpha_s\alpha)$ tree-level interference contributions are completely absent. Also, LR production is induced by initial-state quarks of opposite helicities and thus suffers additionally from a p wave suppression. More details can be found in [25].

The situation is different for the NLO EW contributions. These are equally important in the case of LL and LR production (reducing the LO prediction by about $4 - 8\%$ in the considered scenarios), but negligible for RR production. In all three cases the NLO EW

SPS1a′	σ^{Born} $\mathcal{O}(\alpha_s^2)$	$\Delta\sigma^{\text{tree EW}}$ $\mathcal{O}(\alpha_s\alpha + \alpha^2)$	$\Delta\sigma^{\text{NLO EW}}$ $\mathcal{O}(\alpha_s^2\alpha)$	$\delta^{\text{tree EW}}$	$\delta^{\text{NLO EW}}$	δ^{EW}
$\tilde{q}_L\tilde{q}'_L$	1717.6(8)	378.9(1)	−74.8(6)	22.1 %	−4.4 %	17.7 %
$\tilde{q}_R\tilde{q}'_R$	1981.9(7)	31.81(2)	−1.60(9)	1.6 %	−0.1 %	1.5 %
$\tilde{q}_L\tilde{q}'_R$	1743.8(4)	2.538(1)	−70.71(4)	0.1 %	−4.1 %	−3.9%
$\tilde{q}\tilde{q}'$	5443(1)	413.3(1)	−147.1(6)	7.6 %	−2.7 %	4.9 %

Table 5.5: Hadronic cross sections in femtobarn (fb) for squark–squark production at the LHC within the SPS1a′ scenario for $\sqrt{S} = 14$ TeV. Shown are the LO cross section, the tree-level EW as well as NLO EW contributions and the relative corrections as defined in the text. Anti-particles are included. The numbers in brackets refer to the integration uncertainty in the last digit.

SPS2	σ^{Born} $\mathcal{O}(\alpha_s^2)$	$\Delta\sigma^{\text{tree EW}}$ $\mathcal{O}(\alpha_s\alpha + \alpha^2)$	$\Delta\sigma^{\text{NLO EW}}$ $\mathcal{O}(\alpha_s^2\alpha)$	$\delta^{\text{tree EW}}$	$\delta^{\text{NLO EW}}$	δ^{EW}
$\tilde{q}_L\tilde{q}'_L$	7.359(1)	1.0326(2)	−0.5776(7)	14.0 %	−7.8 %	6.2 %
$\tilde{q}_R\tilde{q}'_R$	7.529(1)	0.1005(1)	−0.0052(1)	1.3 %	−0.1 %	1.3 %
$\tilde{q}_L\tilde{q}'_R$	14.651(1)	0.0136(1)	−0.8676(2)	0.1 %	−5.9 %	−5.8 %
$\tilde{q}\tilde{q}'$	29.539(2)	1.1468(2)	−1.4506(7)	3.9 %	−4.9 %	−1.0 %

**Table 5.6:** Same as Table 5.5 but for the SPS2 scenario.

corrections are negative and partially compensate the EW tree-level contributions. Summing over all processes, the EW contributions to the total cross section for inclusive squark–squark production decrease from about 8% to about 5% in SPS1a′ and SPS5 after the inclusion of NLO EW corrections. In the SPS2 scenario, where LR production is the dominant production mechanism, the NLO EW corrections even overcompensate the EW tree-level contributions and the result turns negative.

In order to further investigate the dependence of the EW contributions on squark and gluino masses, we perform a parameter scan over those quantities. The independent squark masses are chosen equal to a common value $m_{\tilde{q}}$, with the dependent fourth squark mass set to its corresponding on-shell value. All other parameters are fixed to their SPS1a′ values. The renormalization and the factorization scale are set to $\mu_R = \mu_F = m_{\tilde{q}}$.

To start with, we show in Figure 5.13 the Born cross section (left panel) and the EW cross section contributions (right panel) for inclusive squark–squark production as a function of the common squark mass and for different values of the gluino mass. Both the Born and the EW contribution strongly decrease for growing squark masses. While the Born cross section is quite sensitive to the gluino mass for low squark masses, the EW contribution is almost independent in this regime. For high squark masses the behavior is vice versa.

| SPS5	σ^{Born} $\mathcal{O}(\alpha_s^2)$	$\Delta\sigma^{\text{tree EW}}$ $\mathcal{O}(\alpha_s\alpha + \alpha^2)$	$\Delta\sigma^{\text{NLO EW}}$ $\mathcal{O}(\alpha_s^2\alpha)$	$\delta^{\text{tree EW}}$	$\delta^{\text{NLO EW}}$	δ^{EW}
$\tilde{q}_L\tilde{q}'_L$	774.7(1)	185.71(4)	$-35.9(1)$	24.0 %	-4.6 %	19.3 %
$\tilde{q}_R\tilde{q}'_R$	888.0(1)	16.332(5)	$-0.69(2)$	1.8 %	-0.1 %	1.8 %
$\tilde{q}_L\tilde{q}'_R$	758.00(9)	1.1559(3)	$-33.68(1)$	0.2 %	-4.4 %	-4.3 %
$\tilde{q}\tilde{q}'$	2420.7(3)	203.20(4)	$-70.3(1)$	8.4 %	-2.9 %	5.5 %

Table 5.7: Same as Table 5.5 but for the SPS5 scenario.
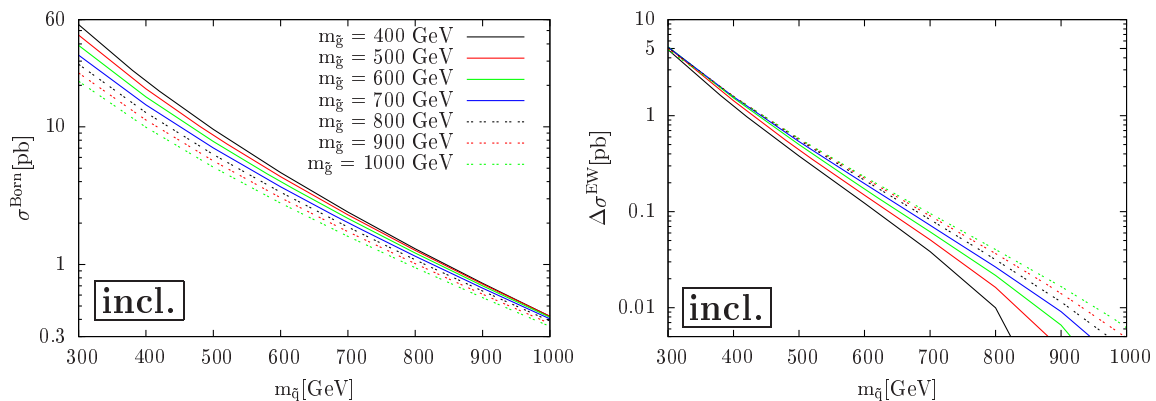
Figure 5.13: Hadronic Born cross section (left) and EW contributions (right) for inclusive squark–squark production as a function of a common squark mass $m_{\tilde{q}}$. Different gluino masses $m_{\tilde{g}}$ are considered, all other parameters are set to their SPS1a′ values.

Figure 5.14 shows the K-factor, defined as $K = \sigma^{\text{NLO}}/\sigma^{\text{Born}}$, for the same parameter range as considered in Figure 5.13. The three different combinations of chiralities of the final-state squarks, as well as the inclusive case are considered separately. The K-factor is largest for two left-handed squarks in the final state. Here, the EW contributions alter the LO cross section prediction between $10 - 50\%$, being most important in case of light squarks and a heavy gluino. The EW contribution is enhanced by the large tree-level EW contribution. In the case of RR production, the EW contributions are below 3% in most parts of the parameter space. For LR production the EW contributions are mainly given by the NLO EW corrections, leading to a K-factor smaller than unity. The LO cross section is reduced by -3% to -5%, most strongly in a scenario with heavy squarks and a heavy gluino. Altogether one finds for inclusive squark–squark production EW contributions that range from 9% for $m_{\tilde{g}} = 400$ GeV up to 22% for $m_{\tilde{g}} = 1000$ GeV for light squarks. For heavy squarks, the EW contributions are only at the percent level due to the interplay of positive EW corrections in the LL and RR case and negative EW corrections in the LR case, suppressing the EW contributions by one order in magnitude.

We can understand the smallness of the EW contribution for high squark and low gluino
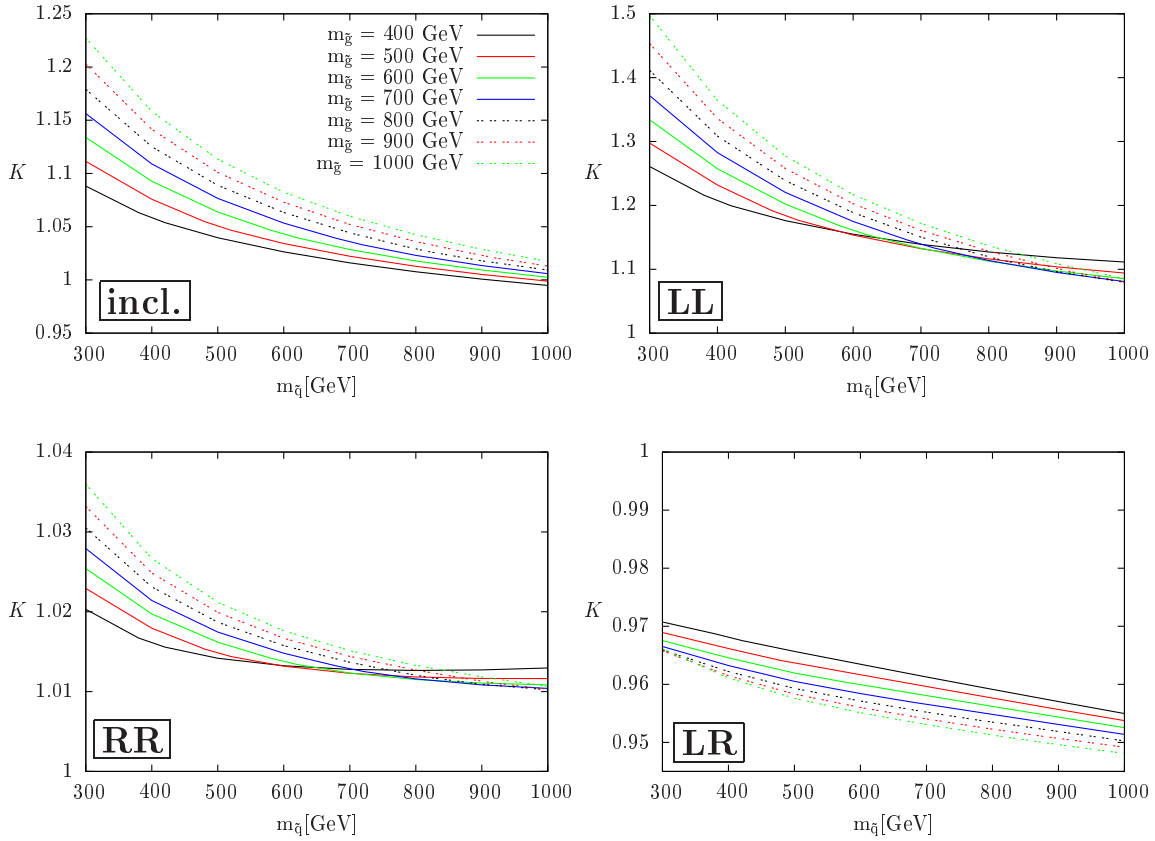
Figure 5.14: K-factor defined as $K = \sigma^{\mathrm{NLO}}/\sigma^{\mathrm{Born}}$, as a function of a common squark mass. Different gluino masses $m_{\tilde{g}}$ are considered, all other parameters are set to their SPS1a′ values. The labels "incl." and "LL", "RR", "LR" refer to inclusive squark–squark production and chirality-grouped subprocesses as explained in the text.

masses by having a closer look at the interplay of the tree-level EW and NLO EW contributions. The ratio $\Delta\sigma^{\mathrm{NLO\ EW}}/\Delta\sigma^{\mathrm{tree\ EW}}$ for inclusive squark–squark production is shown in Figure 5.15a. As one can see, the NLO EW corrections become more important for larger ratios $m_{\tilde{q}}/m_{\tilde{g}}$ and reach the same size as the tree-level EW contributions for about $m_{\tilde{q}}/m_{\tilde{g}} \gtrsim 1.5$, depending on the precise value of the gluino mass. This is due to the fact that the LR contribution becomes more relevant for increasing $m_{\tilde{q}}/m_{\tilde{g}}$, see Figure 5.15b. Owing to the suppressed tree-level contributions, the EW contributions to LR production are negative and partially compensate the positive yield from LL and RR production. Figure 5.15a also confirms our observation from the SPS2 scenario that the NLO EW corrections compensate the tree-level EW contributions in the inclusive cross section, cf. Table 5.6, which seems to be a generic feature in scenarios with the squark heavier than the gluino.
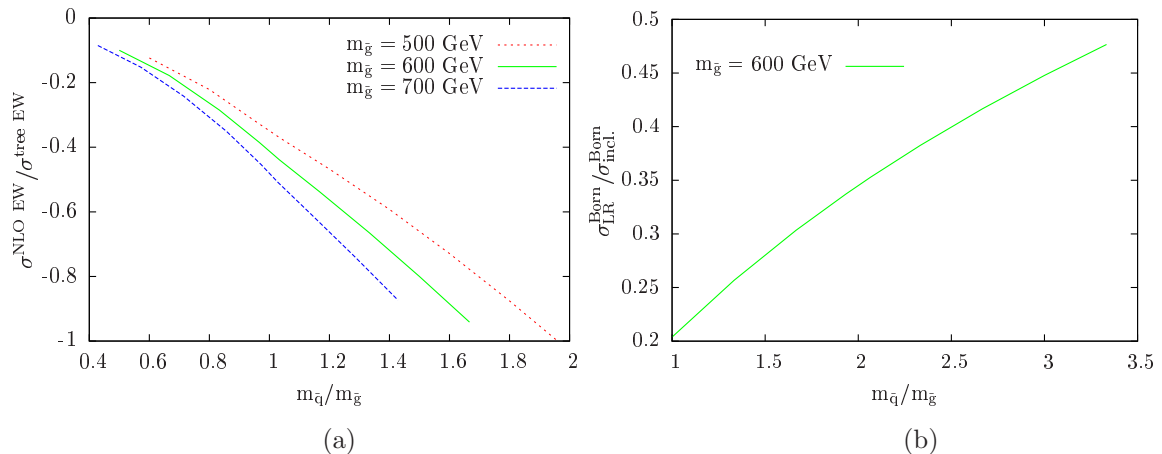
Figure 5.15: (a) Ratio of NLO EW to tree-level EW contributions for inclusive squark–squark production. (b) Relative contribution of LR final states to the inclusive Born cross section for a fixed gluino mass $m_{\tilde{g}} = 600$ GeV.

5.4.4 Differential Distributions

Here, we illustrate the results for the SPS1a′ scenario. In Figures 5.16, 5.17, and 5.18 we consider the differential distributions of the EW contributions with respect to various kinematical variables. In the left panels, the tree-level EW contributions and the three IR and collinear safe subsets of NLO EW contributions (EW-type corrections, QCD-type corrections, real quark radiation), as well as the summed EW contributions are shown. In the right panels, the impact of the EW contributions relative to the Born cross section, δ, is given.

Figure 5.16 refers to the distribution with respect to the transverse momentum p_T of the squark with highest p_T. The tree-level EW contributions are always positive with a maximum at about 250 GeV and dominate the sum over a wide range of the phase-space for LL, RR, and inclusive squark–squark production. Again, they are suppressed for LR production. The interplay of the NLO EW contributions is more complicated. For all processes, the real quark radiation is small and mostly negative. For LL production, large cancellations among the EW- and QCD-type corrections occur. As a result, the relative yield is dominated from the tree-level contributions in the small-p_T region where it is large and positive (up to 25%). For higher values of p_T, the relative corrections turn negative and grow up to -10%. In case of RR production the EW-type corrections are suppressed from the chirality and the QCD-type corrections are more important. However the relative EW contributions in total do not exceed a few percent. Finally in the LR case, the QCD-type corrections are negligible since they are related to QCD–EW interferences. The dominant contribution arises here from the EW-type corrections. The relative contributions are always negative, between -2% for small values of p_T and up to -10% in the high-p_T region. It is important to note that even though the relative NLO EW contributions to the integrated cross section are comparable for LL and LR production, cf. Table 5.5, they originate from
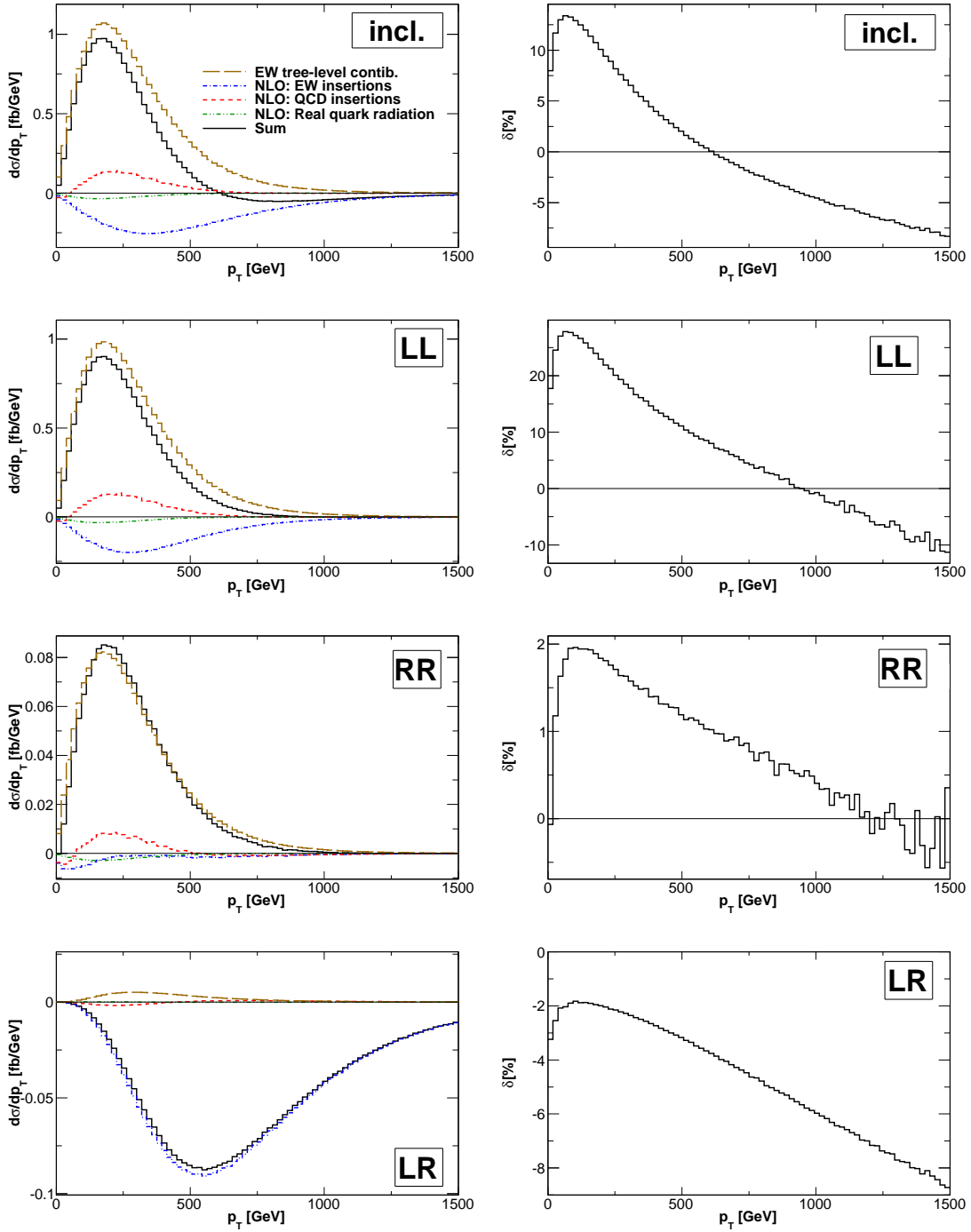
Figure 5.16: Transverse momentum distributions for squark–squark production at the LHC within the SPS1a′ scenario. Shown are the tree-level and NLO EW cross section contributions (left) and the impact of EW contributions relative to the QCD Born cross section (right) for inclusive $\tilde{q}\tilde{q}'$ production (top), production of two left-handed squarks $\tilde{q}_L\tilde{q}'_L$ (second), production of two right-handed squarks $\tilde{q}_R\tilde{q}'_R$ (third), and non-diagonal $\tilde{q}_L\tilde{q}'_R$ production (bottom). Charge-conjugated processes are included.
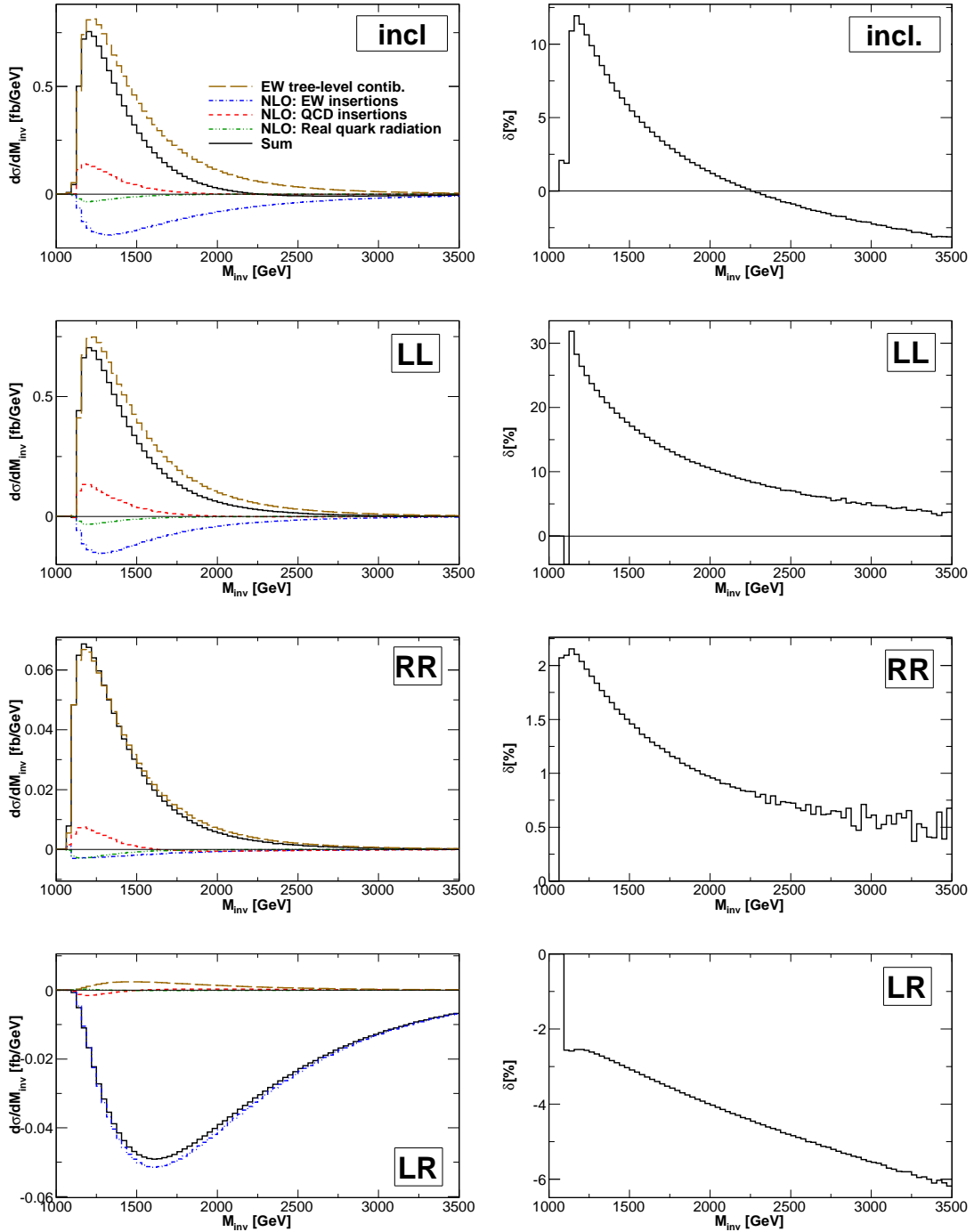
Figure 5.17: Invariant mass distributions for squark–squark production at the LHC within the SPS1a′ scenario. Shown are the tree-level and NLO EW cross section contributions (left) and the impact of EW contributions relative to the QCD Born cross section (right) for inclusive $\tilde{q}\tilde{q}'$ production (top), production of two left-handed squarks $\tilde{q}_L\tilde{q}'_L$ (second), production of two right-handed squarks $\tilde{q}_R\tilde{q}'_R$ (third), and non-diagonal $\tilde{q}_L\tilde{q}'_R$ production (bottom). Charge-conjugated processes are included.
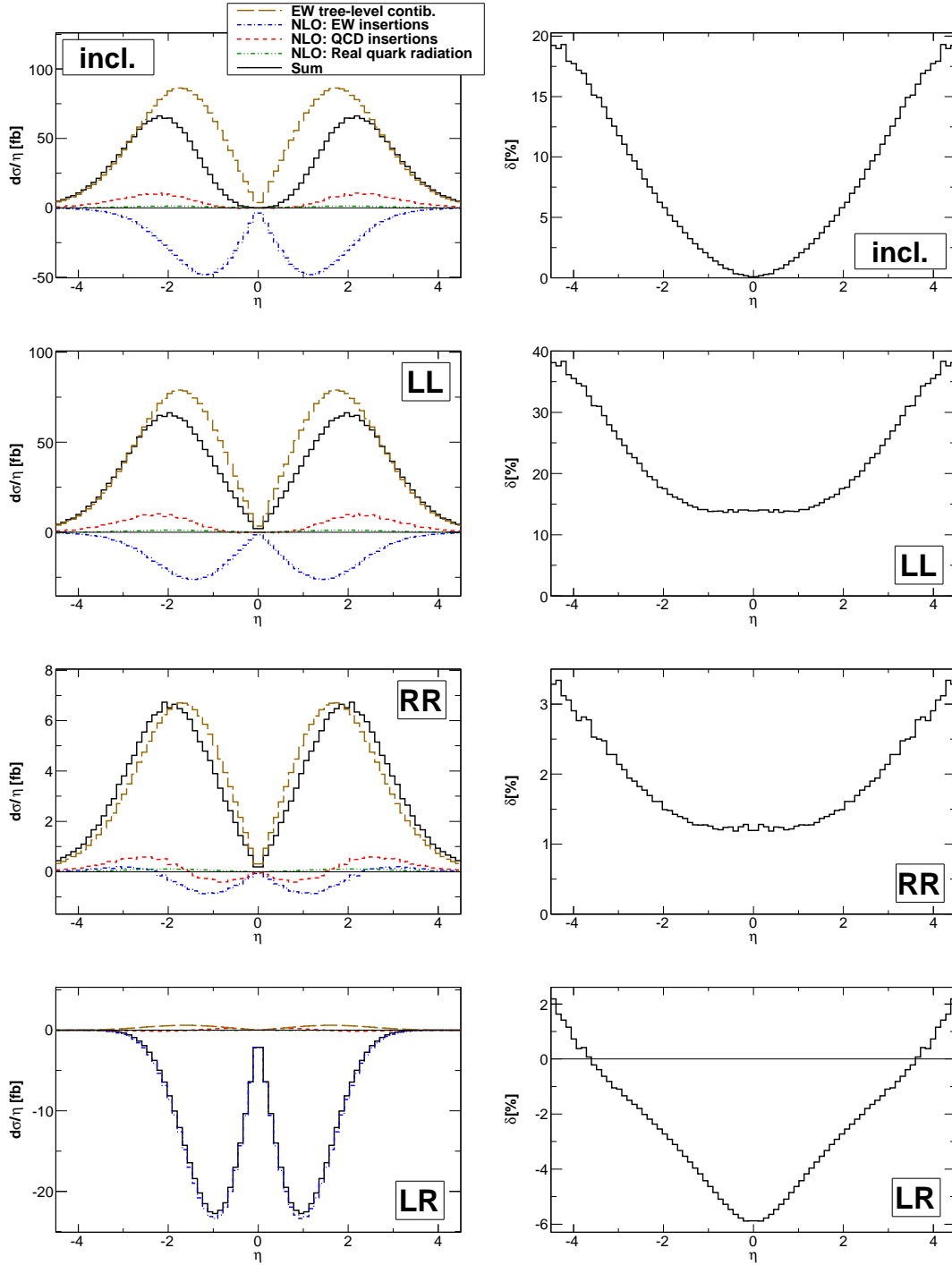
Figure 5.18: Pseudo-rapidity distributions for squark–squark production at the LHC within the SPS1a′ scenario. Shown are the tree-level and NLO EW cross section contributions (left) and the impact of EW contributions relative to the QCD Born cross section (right) for inclusive $\tilde{q}\tilde{q}'$ production (top), production of two left-handed squarks $\tilde{q}_L\tilde{q}'_L$ (second), production of two right-handed squarks $\tilde{q}_R\tilde{q}'_R$ (third), and non-diagonal $\tilde{q}_L\tilde{q}'_R$ production (bottom). Charge-conjugated processes are included.
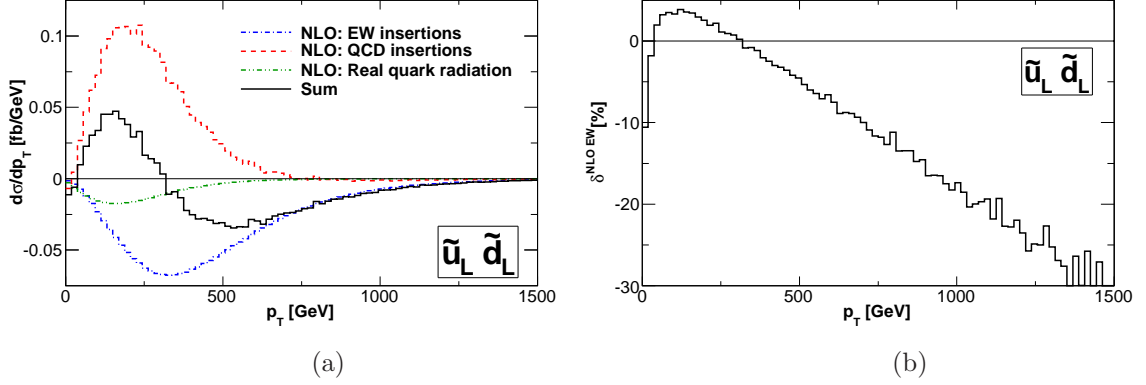
Figure 5.19: (a) Transverse momentum distribution of the hardest squark for $\tilde{u}_L \tilde{d}_L$ production within the SPS1a$'$ scenario. Strong cancellations occur between the different contributions at NLO EW. (b) Relative NLO EW contribution, defined as the ratio of $\mathrm{d}\Delta\sigma^{\mathrm{NLO\ EW}}/\mathrm{d}p_T$ and $\mathrm{d}\sigma^{\mathrm{Born}}/\mathrm{d}p_T$.

distinct sources and the differential distributions differ strongly.

In Figure 5.17 the distributions with respect to the invariant mass of the squark pair, $M_{\mathrm{inv}} = (p_3 + p_4)^2$, are shown. The interplay of the various subsets of EW contributions is similar as for the p_T distributions. For LL and RR production, the EW tree-level contributions are dominant and peak at around $M_{\mathrm{inv}} \approx 1200\,\mathrm{GeV}$. They shift the relative EW corrections to positive values, up to 30% in the low-M_{inv} region for LL production. In case of non-diagonal LR production, where the EW tree-level contributions are suppressed, the relative corrections are negative and grow up to -5% for the intermediate and high-energy region. Finally, in the inclusive case, we find a strong energy dependence of the relative EW corrections, ranging from $+10\%$ for $M_{\mathrm{inv}} \approx 1200\,\mathrm{GeV}$ to -5% for $M_{\mathrm{inv}} > 3500\,\mathrm{GeV}$.

In Figure 5.18 we present the pseudo-rapidity distributions, where always the squark with the higher absolute value of the pseudo-rapidity η (in the laboratory frame) is considered. All EW contributions are vanishing in the central $\eta \approx 0$ region. The characteristics of the rapidity gap in the distributions depend on the precise quantity considered and is enhanced by our choice of referring to the larger η. The tree-level contributions peak at around $|\eta| = 2$ and dominate the total result, if present. The distributions for EW-type and QCD-type NLO corrections differ in sign and shape from each other, leading to large cancellations over a wide phase-space range. In total, the EW contributions alter the LO distributions by up to $20-40\%$ for LL and up to $10-20\%$ for inclusive squark–squark production in the strong forward region for $|\eta| > 2$.

Up to now, our discussion has only been for inclusive combinations of final-state squarks for given chiralities. To get further insight on the cross section, we show in Table 5.8 the cross section divided up into the various subprocesses for squark–squark production within the SPS1a$'$ scenario. Again, anti-particles are included. Owing to the degenerate masses of first- and second-generation squarks, we do not distinguish between final states that

SPS1a′	$\sigma^{\mathbf{Born}}$ $\mathcal{O}(\alpha_s^2)$	$\boldsymbol{\Delta\sigma}^{\mathbf{tree\ EW}}$ $\mathcal{O}(\alpha_s\alpha + \alpha^2)$	$\boldsymbol{\Delta\sigma}^{\mathbf{NLO\ EW}}$ $\mathcal{O}(\alpha_s^2\alpha)$	$\delta^{\mathbf{tree\ EW}}$	$\delta^{\mathbf{NLO\ EW}}$	$\delta^{\mathbf{EW}}$
$\tilde{u}_L\tilde{u}_L$	486.8(3)	93.78(5)	−30.5(2)	19.27 %	−6.26 %	13.00 %
$\tilde{d}_L\tilde{d}_L$	143.83(8)	29.18(2)	−9.85(6)	20.29 %	−6.85 %	13.44 %
$\tilde{u}_L\tilde{d}_L$	692.6(7)	234.8(2)	−9.5(6)	33.90 %	−1.38 %	32.52 %
$\tilde{u}_L\tilde{s}_L$	211.3(2)	17.95(3)	−8.53(1)	8.50 %	−4.04 %	4.46 %
$\tilde{u}_L\tilde{c}_L$	102.96(8)	1.864(2)	−8.885(7)	1.81 %	−8.63 %	−6.82 %
$\tilde{d}_L\tilde{s}_L$	80.19(6)	1.390(2)	−7.526(4)	1.73 %	−9.39 %	−7.65 %
$\tilde{u}_R\tilde{u}_R$	537.1(4)	28.58(2)	−4.44(8)	5.32 %	−0.83 %	4.49 %
$\tilde{d}_R\tilde{d}_R$	173.1(1)	2.414(2)	−0.318(7)	1.39 %	−0.18 %	1.21 %
$\tilde{u}_R\tilde{d}_R$	799.1(6)	0.4458(8)	3.41(3)	0.06 %	0.43 %	0.48 %
$\tilde{u}_R\tilde{s}_R$	253.0(2)	0.1276(2)	1.36(1)	0.05 %	0.54 %	0.59 %
$\tilde{u}_R\tilde{c}_R$	118.95(9)	0.2365(4)	−1.337(8)	0.20 %	−1.12 %	−0.93 %
$\tilde{d}_R\tilde{s}_R$	100.65(8)	0.0126(1)	−0.281(2)	0.01 %	−0.28 %	−0.27 %
$\tilde{u}_L\tilde{u}_R$	629.7(4)	1.288(1)	−26.41(4)	0.20 %	−4.19 %	−3.99 %
$\tilde{d}_L\tilde{d}_R$	165.49(9)	0.0792(1)	−7.027(4)	0.05 %	−4.25 %	−4.20 %
$\tilde{u}_L\tilde{d}_R$	328.5(2)	0.1720(1)	−12.30(1)	0.05 %	−3.75 %	−3.69 %
$\tilde{u}_R\tilde{d}_L$	321.4(2)	0.6026(6)	−13.81(2)	0.19 %	−4.30 %	−4.11 %
$\tilde{u}_L\tilde{s}_R$	82.26(4)	0.0450(1)	−2.809(3)	0.05 %	−3.42 %	−3.36 %
$\tilde{u}_R\tilde{s}_L$	79.90(4)	0.1556(1)	−3.167(4)	0.19 %	−3.96 %	−3.77 %
$\tilde{u}_L\tilde{c}_R$	38.08(2)	0.0832(1)	−1.388(2)	0.22 %	−3.65 %	−3.43 %
$\tilde{u}_R\tilde{c}_L$	38.08(2)	0.0832(1)	−1.388(2)	0.22 %	−3.65 %	−3.44 %
$\tilde{d}_L\tilde{s}_R$	30.24(2)	0.0149(1)	−1.2015(9)	0.05 %	−3.97 %	−3.92 %
$\tilde{d}_R\tilde{s}_L$	30.24(2)	0.0149(1)	−1.2015(9)	0.05 %	−3.97 %	−3.92 %

Table 5.8: Hadronic cross section for squark–squark production at the LHC within the SPS1a′ scenario for $\sqrt{S} = 14$ TeV. Charge-conjugated processes are included. $\tilde{u}\tilde{u}$ final states include $\tilde{c}\tilde{c}$, $\tilde{d}\tilde{d}$ include $\tilde{s}\tilde{s}$, $\tilde{u}\tilde{d}$ include $\tilde{c}\tilde{s}$, and $\tilde{u}\tilde{s}$ includes $\tilde{c}\tilde{d}$. All cross sections are given in femtobarn (fb).

result from exchanging both squarks with their first or second generation counterpart, i.e. $\tilde{u}_L\tilde{u}_L$ production also includes $\tilde{c}_L\tilde{c}_L$ production, etc.. This reduces the number of distinct subprocesses from 36 down to 22. The contributions to $\Delta\sigma^{\text{tree EW}}$ are always positive and are largest for $\tilde{u}_L\tilde{d}_L$ production due to the interference of gluino and chargino exchange diagrams and constitute 57% of the inclusive tree-level EW contribution, see also Table 5.5. One even finds that the inclusive tree-level EW contribution is given to 98% by only five

| SPS1a′ | σ^{Born} | $\Delta\sigma^{\mathrm{tree\ EW}}$ | $\Delta\sigma^{\mathrm{NLO\ EW}}$ | $\delta^{\mathrm{tree\ EW}}$ | $\delta^{\mathrm{NLO\ EW}}$ | δ^{EW} |
	$\mathcal{O}(\alpha_s^2)$	$\mathcal{O}(\alpha_s\alpha + \alpha^2)$	$\mathcal{O}(\alpha_s^2\alpha)$			
$\tilde{q}_L\tilde{q}'_L$	342.0(1)	89.81(3)	−6.1(1)	26.3%	−1.8%	24.5%
$\tilde{q}_R\tilde{q}'_R$	408.7(1)	9.78(5)	0.40(2)	2.4%	0.1%	2.5%
$\tilde{q}_L\tilde{q}'_R$	274.79(7)	0.4571(2)	−9.661(7)	0.2%	−3.5%	−3.3%
$\tilde{q}\tilde{q}'$	1025.5(2)	100.05(3)	−15.3(1)	9.8%	−1.5%	8.3%

Table 5.9: Hadronic cross sections in femtobarn (fb) for squark–squark production at the LHC within the SPS1a′ scenario for $\sqrt{S} = 7$ TeV. Notation as in Table 5.5.

processes, namely $\tilde{u}_L\tilde{u}_L$, $\tilde{u}_R\tilde{u}_R$, $\tilde{d}_L\tilde{d}_L$, $\tilde{u}_L\tilde{d}_L$ and $\tilde{u}_L\tilde{s}_L$. The contributions to $\Delta\sigma^{\mathrm{NLO\ EW}}$ are mostly negative, reducing the importance of EW contributions. In contrast to the tree-level EW case, many processes contribute with a significant amount to the inclusive NLO EW contribution of the cross section. Especially for processes with squarks of different generations, $\Delta\sigma^{\mathrm{EW}}$ is mostly dominated by NLO EW contributions. The size of the NLO EW contributions is often reduced due to the interplay of QCD-type and EW-type corrections as shown in Figure 5.19 in the case of $\tilde{u}_L\tilde{d}_L$ production. The different types of NLO EW corrections partially cancel. Furthermore, the sum contains corrections of positive and negative sign, leading to an integrated result $\Delta\sigma^{\mathrm{NLO\ EW}}$ that is considerably smaller than the corrections affecting the LO result in various phase-space regions.

5.4.5 Hadronic Cross Section for $\sqrt{S} = 7$ TeV

In Table 5.9 we give the results for the hadronic cross sections for inclusive squark–squark production at the LHC for $\sqrt{S} = 7$ TeV within the SPS1a′ scenario. More exclusive results are shown in Table 5.10, similar to 5.8. All other inputs are chosen as in Table 5.5 and Section 5.4.

The integrated cross sections amount about $15 - 25\%$ of their values at $\sqrt{S} = 14$ TeV. The relative importance of tree-level EW contributions increases by a few percent points while the relative NLO EW corrections are less important. All subprocesses are quark–quark initiated and the corresponding luminosities are reduced to a similar extent. However the relative importance of each of the 36 subprocesses changes a little. At Born level the contribution of down-quark induced processes to the inclusive Born cross section is smaller than at 14 TeV, whereas their impact at NLO is increased. In particular the $\tilde{u}_\alpha\tilde{d}_\alpha$ channels give large and positive contributions at NLO EW. As a consequence, the NLO EW corrections for inclusive RR production are now positive and those for LL production are reduced to -2%. In summary, the full EW contributions alter the LO cross section for inclusive squark–squark production at the LHC for $\sqrt{S} = 7$ TeV by 8% within the SPS1a′ scenario.

SPS1a′	σ^{Born} $\mathcal{O}(\alpha_s^2)$	$\Delta\sigma^{\text{tree EW}}$ $\mathcal{O}(\alpha_s\alpha + \alpha^2)$	$\Delta\sigma^{\text{NLO EW}}$ $\mathcal{O}(\alpha_s^2\alpha)$	$\delta^{\text{tree EW}}$	$\delta^{\text{NLO EW}}$	δ^{EW}
$\tilde{u}_L\tilde{u}_L$	132.95(6)	29.01(1)	$-6.17(5)$	21.8%	-4.6%	17.2%
$\tilde{d}_L\tilde{d}_L$	22.52(1)	5.094(2)	$-1.107(8)$	22.6%	-4.9%	17.7%
$\tilde{u}_L\tilde{d}_L$	148.7(1)	53.73(3)	3.4(1)	36.1%	2.3%	38.4%
$\tilde{u}_L\tilde{s}_L$	21.30(1)	1.697(3)	$-0.737(1)$	8.0%	-3.5%	4.5%
$\tilde{u}_L\tilde{c}_L$	9.767(7)	0.1660(2)	$-0.8586(6)$	1.7%	-8.8%	-7.1%
$\tilde{d}_L\tilde{s}_L$	6.712(4)	0.1089(1)	$-0.6447(3)$	1.6%	-9.6%	-8.0%
$\tilde{u}_R\tilde{u}_R$	151.94(7)	9.209(5)	$-0.57(2)$	6.1%	-0.4%	5.7%
$\tilde{d}_R\tilde{d}_R$	28.86(1)	0.4534(2)	$-0.0110(9)$	1.6%	$<0.1\%$	1.5%
$\tilde{u}_R\tilde{d}_R$	179.9(1)	0.0870(1)	0.980(7)	0.1%	0.5%	0.6%
$\tilde{u}_R\tilde{s}_R$	27.05(1)	0.01212(1)	0.1792(9)	$<0.1\%$	0.7%	0.7%
$\tilde{u}_R\tilde{c}_R$	11.824(8)	0.02097(3)	$-0.1408(6)$	0.2%	-1.2%	-1.0%
$\tilde{d}_R\tilde{s}_R$	9.118(6)	0.001012(2)	$-0.0270(1)$	$<0.1\%$	-0.3%	-0.3%
$\tilde{u}_L\tilde{u}_R$	129.47(6)	0.2853(2)	$-4.588(6)$	0.2%	-3.5%	-3.3%
$\tilde{d}_L\tilde{d}_R$	20.108(8)	0.010171(7)	$-0.7536(4)$	0.1%	-3.8%	-3.7%
$\tilde{u}_L\tilde{d}_R$	52.61(2)	0.02953(2)	$-1.702(2)$	0.1%	-3.2%	-3.2%
$\tilde{u}_R\tilde{d}_L$	50.90(2)	0.10138(8)	$-1.903(2)$	0.2%	-3.7%	-3.5%
$\tilde{u}_L\tilde{s}_R$	6.318(3)	0.003663(3)	$-0.1897(2)$	0.1%	-3.0%	-3.0%
$\tilde{u}_R\tilde{s}_L$	6.055(2)	0.01240(1)	$-0.2135(2)$	0.2%	-3.5%	-3.3%
$\tilde{u}_L\tilde{c}_R$	2.739(1)	0.006325(6)	$-0.087(1)$	0.2%	-3.2%	-3.0%
$\tilde{u}_R\tilde{c}_L$	2.739(1)	0.006325(6)	$-0.087(1)$	0.2%	-3.2%	-3.0%
$\tilde{d}_L\tilde{s}_R$	1.9164(9)	0.000993(1)	$-0.0679(1)$	0.1%	-3.5%	-3.5%
$\tilde{d}_R\tilde{s}_L$	1.9164(9)	0.000993(1)	$-0.0678(1)$	0.1%	-3.5%	-3.5%

Table 5.10: Hadronic cross section for squark–squark production at the LHC within the SPS1a′ scenario for $\sqrt{S} = 7$ TeV. Charge-conjugated processes are included. $\tilde{u}\tilde{u}$ final states include $\tilde{c}\tilde{c}$, $\tilde{d}\tilde{d}$ include $\tilde{s}\tilde{s}$, $\tilde{u}\tilde{d}$ include $\tilde{c}\tilde{s}$, and $\tilde{u}\tilde{s}$ includes $\tilde{c}\tilde{d}$. All cross sections are given in femtobarn (fb).

SPS1a$'$	$\sigma^{\mathbf{Born}}$	$\mathbf{\Delta\sigma^{tree\ EW}}$	$\mathbf{\Delta\sigma^{NLO\ EW}}$	$\delta^{\mathbf{tree\ EW}}$	$\delta^{\mathbf{NLO\ EW}}$	$\delta^{\mathbf{EW}}$
	$\mathcal{O}(\alpha_s^2)$	$\mathcal{O}(\alpha_s\alpha + \alpha^2)$	$\mathcal{O}(\alpha_s^2\alpha)$			
$\tilde{q}_L\tilde{q}'_L$	1717.6(8)	378.9(1)	$-155.8(6)$	22.1 %	-9.1 %	13.0 %
$\tilde{q}_R\tilde{q}'_R$	1981.9(7)	31.81(2)	$-15.68(9)$	1.6 %	-0.8 %	0.8 %
$\tilde{q}_L\tilde{q}'_R$	1743.8(4)	2.538(1)	$-78.25(4)$	0.1 %	-4.5 %	-4.3 %
$\tilde{q}\tilde{q}'$	5443(1)	413.3(1)	$-249.7(6)$	7.6 %	-4.6 %	3.0 %

Table 5.11: Hadronic cross section in femtobarn (fb) for squark–squark production at the LHC within the SPS1a$'$ scenario for $\sqrt{S} = 14$ TeV. A kinetic cut is applied to quarks, photons, and gluons arising from real radiation processes since events with $p_T > 50$ GeV and $\eta < 2.5$ are rejected.

5.5 Phase-Space Cuts

In experiments the squarks cannot be measured directly and one is only sensitive to its decay products. Depending on the precise MSSM parameter space, one is left with a certain number of jets, leptons, and missing energy due to the undetectable neutralino which escapes the detector leading to missing transverse momenta $\not{p}_T$. In order to reconstruct the squark mass, specific observables are chosen for the experimental analysis which often rely on a fixed number of leptons and jets in the final state, cf. [91]. The experimental observations are then compared to theoretical (differential) cross section predictions. Care has to be taken when higher-order corrections are included into the analysis since real radiation processes of higher orders which lead to additional quarks, photons, and gluons in the final state can affect the analysis. In this section, we are going to investigate the impact of an additional massless particle in the final state arising due to NLO EW corrections on the cross section prediction.

Obviously, only processes with additional real particles that are neither soft nor collinear can be distinguished experimentally from the two-particle final state. Hence we require that this additional particle has high transverse momentum and is not collinear to the beam-axis. In the following we will define a hard non-collinear particle by the requirement that it has $p_T > 50$ GeV and $\eta < 2.5$. In order to investigate the impact of hard non-collinear particles arising due to NLO EW corrections, we apply the following cuts on the final state quark, photon and gluon phase-space,

$$p_T < 50 \text{ GeV}, \qquad\qquad \eta > 2.5, \qquad\qquad (5.33)$$

i.e. only those events are selected that are (almost) indistinguishable from two squarks in the final state. As we will see, this cut mainly affects processes with real hard gluons in the final state and hence it effectively corresponds on a cut on processes with an extra separable jet. Table 5.11 shows the resulting total cross section for the (partly) inclusive results defined at the beginning of Section 5.4. Obviously, such a cut does not alter the Born cross section and the tree-level EW contribution. However, it has a huge impact on
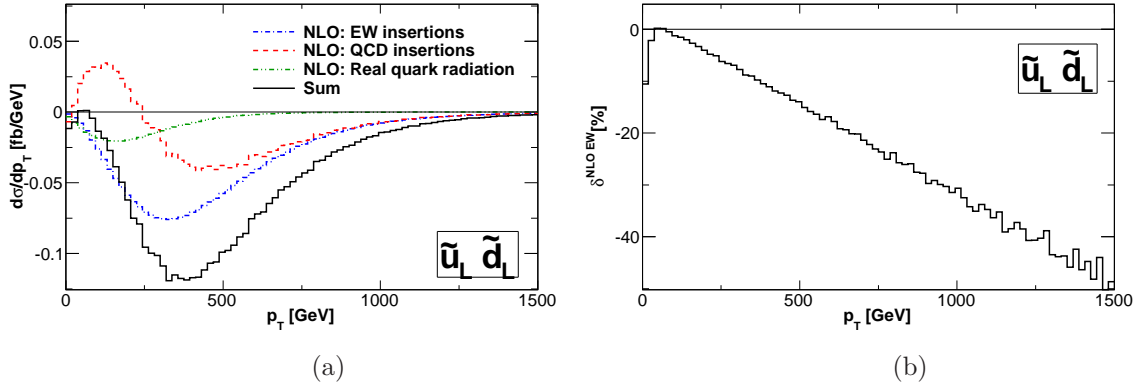
Figure 5.20: (a) Transverse momentum distribution of the hardest squark for $\tilde{u}_L \tilde{d}_L$ production within the SPS1a' scenario. Events with a real quark, gluon, or photon with $p_T > 50$ GeV and $\eta < 2.5$ are rejected. (b) Relative NLO EW contribution, defined as the ratio of $\mathrm{d}\Delta\sigma^{\mathrm{NLO\ EW}}/\mathrm{d}p_T$ and $\mathrm{d}\sigma^{\mathrm{Born}}/\mathrm{d}p_T$.

the NLO EW contribution to the cross section $\Delta\sigma^{\mathrm{NLO\ EW}}$. Comparing with Table 5.5, i.e. the case without any kinematical cuts, one finds that in the case of LL production, the EW contribution becomes more than twice as big as without cuts. The impact of the EW contribution is reduced from 22% down to 13% when taking the NLO EW contributions into account. In the case of RR production $\Delta\sigma^{\mathrm{NLO\ EW}}$ becomes even ten times larger, however its contribution still remains in the one-percent regime. Interestingly, for LR production the impact of the phase-space cut is rather small, i.e. it only changes the NLO EW contribution by roughly 10%. The small change in the NLO EW contribution for LR production will become clear further down, when looking at differential distributions. Considering inclusive $\tilde{q}\tilde{q}'$ production, the EW contribution to the total cross section gets reduced from about 8% to 3%, i.e. reducing the LO EW contribution by more than 50%. In order to see which subprocesses are most affected by this phase-space cut, Table 5.12 shows the cross section divided up into the various subprocesses in analogy to Table 5.8. Comparing these two tables, one finds that the phase-space cut has a big impact on those processes which exhibit a non-vanishing tree-level QCD–EW interference, while the change in $\Delta\sigma^{\mathrm{NLO\ EW}}$ for the other processes is quite moderate. For the former one finds large positive contributions due to QCD-type NLO EW corrections, which get enhanced by the radiation of hard gluons into the central region of the detector. Those events are excluded by applying the phase-space cut (5.33). This becomes clear by comparing e.g. the differential p_T distribution for $\tilde{u}_L\tilde{d}_L$ production without cut, Figure 5.19, with Figure 5.20 which shows the same distribution with the phase-space cut applied. One finds that EW-type corrections and the contribution from real quark radiation is hardly changed, while the QCD-type corrections are strongly reduced. The cancellations between the various contributions in Figure 5.19 is mild. In total, one is left with a vanishing NLO EW contribution for low p_T which becomes up to 40% of the differential Born cross section in the high p_T region.

SPS1a′	σ^{Born} $\mathcal{O}(\alpha_s^2)$	$\Delta\sigma^{\text{tree EW}}$ $\mathcal{O}(\alpha_s\alpha + \alpha^2)$	$\Delta\sigma^{\text{NLO EW}}$ $\mathcal{O}(\alpha_s^2\alpha)$	$\delta^{\text{tree EW}}$	$\delta^{\text{NLO EW}}$	δ^{EW}
$\tilde{u}_L\tilde{u}_L$	486.8(3)	93.78(5)	−52.7(2)	19.27	−10.83	8.43
$\tilde{d}_L\tilde{d}_L$	143.83(8)	29.18(1)	−15.48(6)	20.29	−10.77	9.52
$\tilde{u}_L\tilde{d}_L$	692.6(7)	234.8(1)	−61.5(5)	33.90	−8.88	25.02
$\tilde{u}_L\tilde{s}_L$	211.3(1)	17.95(3)	−10.13(1)	8.50	−4.80	3.70
$\tilde{u}_L\tilde{c}_L$	102.96(7)	1.864(2)	−8.674(7)	1.81	−8.42	−6.61
$\tilde{d}_L\tilde{s}_L$	80.19(5)	1.391(1)	−7.242(4)	1.73	−9.03	−7.30
$\tilde{u}_R\tilde{u}_R$	537.1(3)	28.58(2)	−13.15(8)	5.32	−2.45	2.87
$\tilde{d}_R\tilde{d}_R$	173.1(1)	2.41(1)	−0.955(6)	1.39	−0.55	0.84
$\tilde{u}_R\tilde{d}_R$	799.1(6)	0.4458(7)	−0.13(3)	0.06	−0.02	0.04
$\tilde{u}_R\tilde{s}_R$	253.0(2)	0.1276(2)	0.38(1)	0.05	0.15	0.20
$\tilde{u}_R\tilde{c}_R$	118.95(9)	0.2364(4)	−1.511(7)	0.20	−1.27	−1.07
$\tilde{d}_R\tilde{s}_R$	100.65(7)	0.01256(2)	−0.323(1)	0.01	−0.32	−0.31
$\tilde{u}_L\tilde{u}_R$	629.7(3)	1.288(1)	−29.16(3)	0.20	−4.63	−4.43
$\tilde{d}_L\tilde{d}_R$	165.49(8)	0.07916(6)	−7.382(4)	0.05	−4.46	−4.41
$\tilde{u}_L\tilde{d}_R$	328.5(2)	0.1720(1)	−14.48(1)	0.05	−4.41	−4.36
$\tilde{u}_R\tilde{d}_L$	321.4(1)	0.6026(5)	−15.09(1)	0.19	−4.70	−4.51
$\tilde{u}_L\tilde{s}_R$	82.26(4)	0.04502(4)	−3.258(3)	0.05	−3.96	−3.91
$\tilde{u}_R\tilde{s}_L$	79.90(4)	0.1556(1)	−3.398(3)	0.19	−4.25	−4.06
$\tilde{u}_L\tilde{c}_R$	38.08(2)	0.08323(8)	−1.479(2)	0.22	−3.88	−3.67
$\tilde{u}_R\tilde{c}_L$	38.08(2)	0.08323(8)	−1.481(2)	0.22	−3.89	−3.67
$\tilde{d}_L\tilde{s}_R$	30.24(1)	0.01490(1)	−1.2579(8)	0.05	−4.16	−4.11
$\tilde{d}_R\tilde{s}_L$	30.24(1)	0.01490(1)	−1.2572(8)	0.05	−4.166	−4.11

Table 5.12: Hadronic cross section for squark–squark production at the LHC within the SPS1a′ scenario for $\sqrt{S} = 14$ TeV. Charge-conjugated processes are included. Events with a real quark, gluon, or photon with $p_T > 50$ GeV and $\eta < 2.5$ are rejected. $\tilde{u}\tilde{u}$ final states include $\tilde{c}\tilde{c}$, $\tilde{d}\tilde{d}$ include $\tilde{s}\tilde{s}$, $\tilde{u}\tilde{d}$ include $\tilde{c}\tilde{s}$, and $\tilde{u}\tilde{s}$ includes $\tilde{c}\tilde{d}$. All cross sections are given in femtobarn (fb).

One might wonder, why events with additional hard gluons in the final state arise in NLO EW corrections. However, one has to remember that for processes that have a non-vanishing QCD–EW interference contribution of $\mathcal{O}(\alpha_s\alpha)$, the vertex and self-energy corrections of Figure 5.3c give a non-zero contribution at NLO EW. These corrections involve the renormalization of the strong sector, which explains the origin of the hard gluons.

Due to the strong impact of the phase-space cut (5.33) for left-handed squark-pair pro-
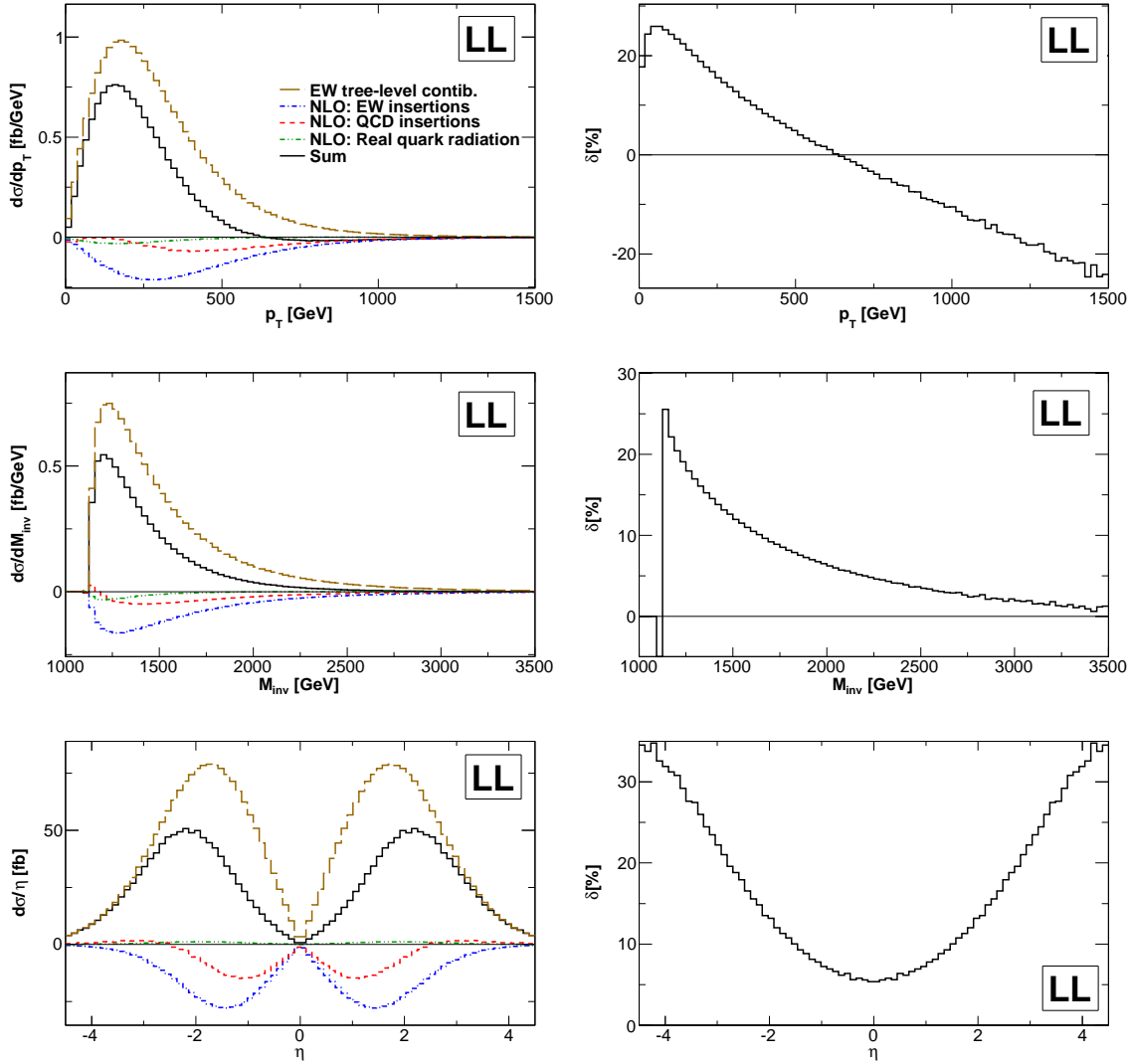
Figure 5.21: Differential distributions for left-handed squark–squark production at the LHC within the SPS1a′ scenario. Events with real quark, gluon, or photon with $p_T > 50$ GeV and $\eta < 2.5$ are rejected. Shown are the tree-level and NLO EW cross section contributions (left) and the impact of EW contributions relative to the QCD Born cross section (right) for the transverse mass distribution (top), the invariant mass distribution (middle), and the pseudo-rapidity distribution (bottom). Charge-conjugated processes are included.

duction, we show the differential transverse momentum, invariant mass, and pseudo-rapidity distributions for LL production in Figure 5.21. In all three cases the QCD-type corrections are significantly changed, while the other contributions are hardly affected by the cut, cf. Figures 5.16–5.18. While the QCD-type corrections without cut exhibit in all three cases a positive yield to the cross section it gives a negative yield when the cut is applied.

# 6 Electroweak Contributions to Sbottom–anti-Sbottom Production

In this chapter the electroweak contibutions to diagonal sbottom–anti-sbottom pair production in hadronic collisions,

$$PP \to \tilde{b}_\alpha \tilde{b}_\alpha^* \,, \tag{6.1}$$

are presented. The production of squarks of the third generation is peculiar and there are theoretical as well as experimental aspects that render a separate discussion of this process necessary. In contrast to squark-pair production, the mixing in the stop and sbottom sector cannot be neglected. This induces a splitting for the mass eigenstates and hence can lead to a relatively low mass for the lightest bottom and top squark, favoring their direct production at the LHC. Moreover, b-tagging makes bottom- and top- squark production experimentally distinguishable from the production of squarks of the first two generations [171–173]. A dedicated study looking at third generation stop production at the LHC is available [174].

From theoretical side, bottom-squark pair production has some aspects that are not present in the production of squark pairs of different flavor. Due to left- right-mixing of the bottom squarks, the renormalization scheme for the bottom-squark sector has to be chosen with special care, since especially the on-shell scheme can become unreliable for a wide range of the parameter space, cf. Section 4.4.1. Further, one of the bottom-squark masses remains a dependent quantity whose on-shell value gets radiative corrections. This requires a proper treatment of the IR- and collinear-singular regions at NLO EW. In addition, Higgs-boson exchange contributions can become significant due to enhanced Yukawa couplings for high values of $\tan\beta$, which do not decouple at low energies and hence have to be resummed. These features render the computation of the electroweak contributions to sbottom-pair production substantially different from the corresponding computations for squark–anti-squark and stop–anti-stop production.

The outline of this Chapter is as follows: In Section 6.1 we summarize the tree-level contributions which can be of QCD and EW origin. Section 6.2 shows how the $\tan\beta$ enhanced terms appearing in the bottom-quark sector can be resummed to all orders. The resummation alters the tree-level relation between the bottom-quark mass and its Yukawa coupling as well as the bottom–Higgs vertices. The details on the NLO EW calculation are given in Section 6.3. The numerical impact of the NLO EW contributions on the cross section and on differential distributions at the LHC with $\sqrt{S} = 14$ TeV and $\sqrt{S} = 7$ TeV is presented in Section 6.4. We consider different branchmark scenarios and investigate the dependence on the final-state sbottom mass and on $\tan\beta$.
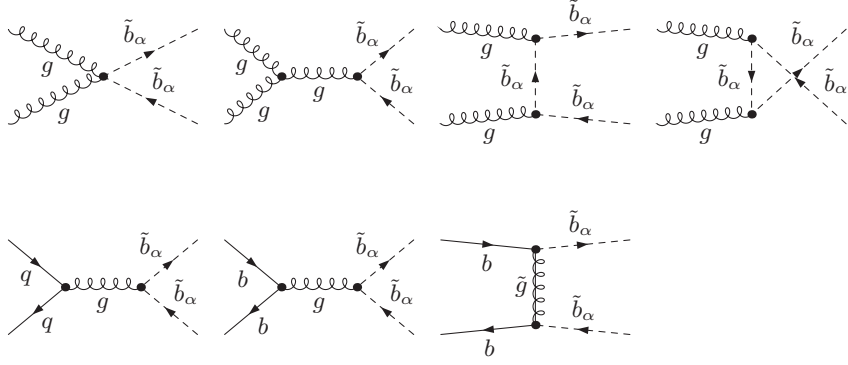
Figure 6.1: LO Feynman diagrams for sbottom-pair production. The first line corresponds to the gluon-induced channel (6.2a), while the second line corresponds to the $q\bar{q}$ channel (6.2b) (first diagram) and the $b\bar{b}$ channel (6.2c) (second and third diagram).

6.1 Tree-Level Cross Section

In this section we describe the tree-level contributions to $\tilde{b}_\alpha \tilde{b}_\alpha$ production, which are of order $\mathcal{O}(\alpha_s^2)$, $\mathcal{O}(\alpha_s\alpha)$, and $\mathcal{O}(\alpha^2)$. We will conventionally denote the cross section (amplitude) of a partonic process X at a given order $\mathcal{O}(\alpha_s^a \alpha^b)$ by $\mathrm{d}\hat{\sigma}_X^{a,b}$ ($\mathcal{M}_X^{a,b}$).

6.1.1 Tree-Level QCD Contributions

At LO three classes of partonic processes contribute,

$$g(p_1)\, g(p_2) \to \tilde{b}_\alpha(p_3)\, \tilde{b}_\alpha^*(p_4), \tag{6.2a}$$

$$q(p_1)\, \bar{q}(p_2) \to \tilde{b}_\alpha(p_3)\, \tilde{b}_\alpha^*(p_4), \tag{6.2b}$$

$$b(p_1)\, \bar{b}(p_2) \to \tilde{b}_\alpha(p_3)\, \tilde{b}_\alpha^*(p_4). \tag{6.2c}$$

The process with initial-state bottom quarks has to be treated different to light-flavor quarks due to t-channel gluino exchange, cf. Figure 6.1. The leading-order hadronic cross section, which is of the order $\mathcal{O}(\alpha_s^2)$, is given by the convolution of the partonic cross section with the corresponding luminosity, cf. (4.22) and (4.23),

$$\mathrm{d}\sigma_{PP\to\tilde{b}_a\tilde{b}_a^*}^{\mathrm{LO\ QCD}}(S) = \int_{\tau_0}^1 \mathrm{d}\tau\, \frac{\mathrm{d}L_{gg}}{\mathrm{d}\tau} \mathrm{d}\hat{\sigma}_{gg\to\tilde{b}_\alpha\tilde{b}_\alpha^*}^{2,0}(\hat{s}) + \sum_q \int_{\tau_0}^1 \mathrm{d}\tau\, \frac{\mathrm{d}L_{q\bar{q}}}{\mathrm{d}\tau} \mathrm{d}\hat{\sigma}_{q\bar{q}\to\tilde{b}_\alpha\tilde{b}_\alpha^*}^{2,0}(\hat{s}) \tag{6.3a}$$

$$+ \int_{\tau_0}^1 \mathrm{d}\tau\, \frac{\mathrm{d}L_{b\bar{b}}}{\mathrm{d}\tau} \mathrm{d}\hat{\sigma}_{b\bar{b}\to\tilde{b}_\alpha\tilde{b}_\alpha^*}^{2,0}(\hat{s}), \tag{6.3b}$$

where $\tau_0 = 4m_{\tilde{b}_\alpha}^2/S$ is the production threshold. S and $\hat{s} = \tau S$ are the squared center-of-mass (c.m.) energies of the hadronic and partonic processes, respectively. The sum runs over $q = u, d, c, s$. The corresponding partonic cross section can be obtained from the Feynman diagrams in Figure 6.1. In terms of the Mandelstam variables given in (4.4),

$$\hat{s} = (p_1 + p_2)^2, \quad \hat{t} = (p_1 - p_3)^2, \quad \hat{u} = (p_1 - p_4)^2, \tag{6.4}$$

the differential partonic cross section for a given subprocess $\xi\xi' \to \tilde{b}_\alpha \tilde{b}_\alpha^*$ can be written as

$$d\hat{\sigma}_{\xi\xi'\to\tilde{b}_\alpha\tilde{b}_\alpha^*}^{2,\,0}(\hat{s}) = \overline{\sum} \left| \mathcal{M}_{\xi\xi'\to\tilde{b}_\alpha\tilde{b}_\alpha^*}^{1,\,0} \right|^2 \frac{d\hat{t}}{16\pi\hat{s}^2}, \tag{6.5}$$

with the squared lowest order matrix element averaged (summed) over initial (final) state spin and color, cf. (4.6).

6.1.2 Tree-Level EW Contributions

The tree-level electroweak (EW) contributions are constituted out of pure EW contributions of the order $\mathcal{O}(\alpha^2)$ and QCD–EW interference contributions of $\mathcal{O}(\alpha_s\alpha)$. The differential hadronic cross section is given by

$$d\sigma_{PP\to\tilde{b}_\alpha\tilde{b}_\alpha^*}^{\text{LO EW}}(S) = \sum_q \int_{\tau_0}^1 d\tau \, \frac{dL_{q\bar{q}}}{d\tau} d\hat{\sigma}_{q\bar{q}\to\tilde{b}_\alpha\tilde{b}_\alpha^*}^{0,\,2}(\hat{s}) \tag{6.6a}$$

$$+ \int_{\tau_0}^1 d\tau \, \frac{dL_{b\bar{b}}}{d\tau} \left[d\hat{\sigma}_{b\bar{b}\to\tilde{b}_\alpha\tilde{b}_\alpha^*}^{0,\,2}(\hat{s}) + d\hat{\sigma}_{b\bar{b}\to\tilde{b}_\alpha\tilde{b}_\alpha^*}^{1,\,1}(\hat{s}) \right] \tag{6.6b}$$

$$+ \int_{\tau_0}^1 d\tau \, \frac{dL_{g\gamma}}{d\tau} d\hat{\sigma}_{g\gamma\to\tilde{b}_\alpha\tilde{b}_\alpha^*}^{1,\,1}(\hat{s}). \tag{6.6c}$$

The contributions of $\mathcal{O}(\alpha^2)$ arise from the processes (6.2b) and (6.2c), i.e. $q\bar{q}$ and $b\bar{b}$ annihilation. The partonic cross sections,

$$d\hat{\sigma}_{q\bar{q}\to\tilde{b}_\alpha\tilde{b}_\alpha^*}^{0,\,2}(\hat{s}) = \overline{\sum} \left| \mathcal{M}_{q\bar{q}\to\tilde{b}_\alpha\tilde{b}_\alpha^*}^{0,\,1} \right|^2 \frac{d\hat{t}}{16\pi\hat{s}^2}, \qquad d\hat{\sigma}_{b\bar{b}\to\tilde{b}_\alpha\tilde{b}_\alpha^*}^{0,\,2}(\hat{s}) = \overline{\sum} \left| \mathcal{M}_{b\bar{b}\to\tilde{b}_\alpha\tilde{b}_\alpha^*}^{0,\,1} \right|^2 \frac{d\hat{t}}{16\pi\hat{s}^2}, \tag{6.7}$$

are obtained from the diagrams in Figure 6.2a. Notice that for the $b\bar{b}$ channel also Higgs-boson exchange diagrams have to be taken into account. In the case of process (6.2c), the diagrams with t-channel gluino and neutralino exchange further allow for a non-vanishing QCD–EW interference term of $\mathcal{O}(\alpha_s\alpha)$,
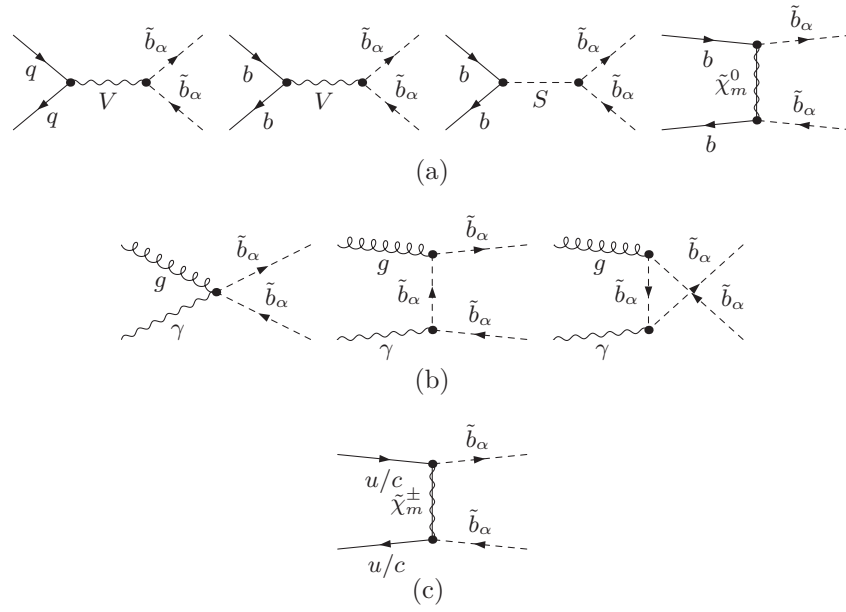
$$d\hat{\sigma}_{b\bar{b}\to\tilde{b}_\alpha\tilde{b}_\alpha^*}^{1,\,1}(\hat{s}) = 2\overline{\sum}\text{Re}\left\{ \mathcal{M}_{b\bar{b}\to\tilde{b}_\alpha\tilde{b}_\alpha^*}^{1,\,0} \left(\mathcal{M}_{b\bar{b}\to\tilde{b}_\alpha\tilde{b}_\alpha^*}^{0,\,1} \right)^* \right\} \frac{d\hat{t}}{16\pi\hat{s}^2}. \tag{6.8}$$

The non-vanishing photon density inside the proton, see also Section 4.2, allows for an EW contribution due to the photon-induced channel. This leads to the $\mathcal{O}(\alpha_s\alpha)$ contribution in (6.6c) which arises through the partonic process

$$g(p_1)\,\gamma(p_2) \to \tilde{b}_\alpha(p_3)\,\tilde{b}_\alpha^*(p_4). \tag{6.9}$$

The corresponding partonic cross section can be obtained from the diagrams in Figure 6.2b and reads as follows

$$d\hat{\sigma}_{g\gamma\to\tilde{b}_\alpha\tilde{b}_\alpha^*}^{1,\,1}(\hat{s}) = \overline{\sum} \left| \mathcal{M}_{g\gamma\to\tilde{b}_\alpha\tilde{b}_\alpha^*}^{1/2,\,1/2} \right|^2 \frac{d\hat{t}}{16\pi\hat{s}^2}. \tag{6.10}$$

Figure 6.2: Feynman diagrams for the EW contributions to $\tilde{b}_\alpha \tilde{b}_\alpha^*$ production. $V = \gamma, Z^0$, $S = h^0, H^0, G^0$. (a) $q\bar{q}$ and $b\bar{b}$ channel. (b) Photon-induced channel. (c) CKM-suppressed t-channel chargino exchange.

6.2 Radiative Corrections to the Bottom Yukawa Couplings

As mentioned in Section 2.2.3, when introducing the Higgs mechanism of the MSSM, the relation between the bottom-quark mass and its Yukawa coupling as well as the Higgs–bottom vertices gets altered by radiative corrections. These corrections have a contribution proportional to $\tan\beta$ that does not decouple at low energies. It was shown that these $\tan\beta$-enhanced contributions can be resummed to all orders in perturbation theory [79–84]. In this Section we recall how these corrections arise and give the resummed bottom-quark Yukawa coupling and the effective Higgs–bottom vertices used in this work for sbottom-pair production. The details of the calculation are collected in Appendix C.
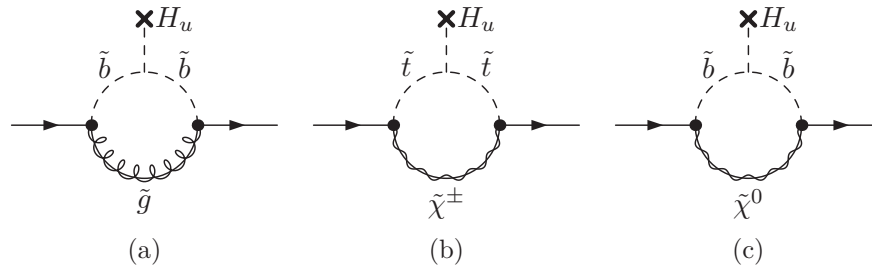
Figure 6.3: One loop SUSY diagram contributing to the effective Hbb coupling. (a) SUSY QCD contribution. (b) Higgsino/wino–stop contribution. (c) Bino–sbottom contribution.

The Higgs sector in the MSSM corresponds to a type-II two Higgs doublet model, i.e. the down-type quarks couple to H_d and the up-type quarks to H_u. After spontaneous symmetry breaking, the quarks get their mass by their coupling to the vacuum expectation value. At tree level, the down-type quark mass is therefore given by $m_{d_i} = \lambda_{d_i} v_1/\sqrt{2}$ and the up-type quark mass by $m_{u_i} = \lambda_{u_i} v_2/\sqrt{2}$, with the index i for the three quark generations. Here v_1 and v_2 denote the vacuum expectation values of the Higgs fields H_d and H_u, respectively. However, by taking radiative corrections into account, the down-type quarks get an effective coupling to H_u, and hence couple to v_2, see Figure 6.3. In particular, this can have a big impact on the relation between the bottom-quark mass and its Yukawa coupling since this higher-order contributions do not decouple at low energies and are enhanced by a factor $\tan\beta = v_2/v_1$. In [83] it was shown that the $\tan\beta$ enhanced terms can be resummed to all orders in perturbation theory. The relation between the physical bottom-quark mass m_b^{phys} and its bare Yukawa coupling λ_b then reads

$$m_b \equiv \frac{\lambda_b v_1}{\sqrt{2}} = \frac{m_b^{\text{phys}}}{1 + \Delta m_b},\qquad(6.11)$$

where Δm_b is given by

$$\Delta m_b = \Delta m_b^{\text{SQCD}} + \Delta m_b^{\text{Yukawa}} + \Delta m_b^{\text{SEW}},\qquad(6.12)$$

$$\Delta m_b^{\text{SQCD}} = \frac{2\alpha_s}{3\pi} \mu M_{\tilde{g}} \tan\beta\, I(m_{\tilde{b}_1}, m_{\tilde{b}_2}, m_{\tilde{g}}),\qquad(6.13)$$

$$\Delta m_b^{\text{Yukawa}} = \frac{\lambda_t^2}{16\pi^2} \mu A_t \tan\beta\, I(m_{\tilde{t}_1}, m_{\tilde{t}_2}, \mu),\qquad(6.14)$$

$$\Delta m_b^{\text{SEW}} = -\frac{g^2}{16\pi^2} \mu M_2 \tan\beta \left[\cos^2\theta_{\tilde{t}} I(m_{\tilde{t}_1}, M_2, \mu) + \sin^2\theta_{\tilde{t}_2} I(m_{\tilde{t}_2}, M_2, \mu)\right.$$
$$\left. + \frac{1}{2}\cos^2\theta_{\tilde{b}} I(m_{\tilde{b}_1}, M_2, \mu) + \frac{1}{2}\sin^2\theta_{\tilde{b}_2} I(m_{\tilde{b}_2}, M_2, \mu)\right],$$

and the vacuum integral function

$$I(a, b, c) = \frac{1}{(a^2 - b^2)(b^2 - c^2)(a^2 - c^2)}\left[a^2 b^2 \log\frac{a^2}{b^2} + b^2 c^2 \log\frac{b^2}{c^2} + c^2 a^2 \log\frac{c^2}{a^2}\right].\quad(6.15)$$

The contribution Δm_b^{SQCD} arises from SUSY QCD self-energy corrections to the bottom-quark propagator, Figure 6.3a, while the contribution Δm_b^{SEW} and $\Delta m_b^{\text{Yukawa}}$ arise from contributions due to higgsino/wino–stop exchange, Figure 6.3b,c. Bino effects in Figure 6.3c, were found to be numerical irrelevant.

Further $\tan\beta$ enhancement effects arise from three-point functions involving Higgs–bottom vertices, an example diagram is depicted in Figure 6.4. It is again possible to resum the $\tan\beta$ enhanced terms. One finds that all Higgs–bottom vertices except the ones with a charged Higgs get a modification. For $\tilde{b}_\alpha \tilde{b}_\alpha^*$ production the relevant Higgs–bottom vertices are the ones involving the neutral Higgs bosons h^0, H^0, and A^0. These appear at LO in the $b\bar{b}$ channel (6.2c) and at NLO EW in the gg channel (6.2a). The latter also involves $G^0 bb$ vertices. Performing a resummation in the Goldstone sector, and hence mixing perturbative
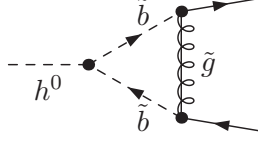
Figure 6.4: Example for SUSY vertex corrections to the h^0bb coupling that leads to an additional $\tan\beta$ enhanced contribution.

orders, is a dangerous task, since it may spoil gauge cancellations in the weak sector. For the neutral Goldstone boson G^0, we found by explicit calculating the resummed G^0bb vertex, that the contribution from the vertex corrections exactly compensates the contribution of the bottom-Yukawa coupling resummation, see (C.29) of Appendix C.2. Even though not relevant for this work, it is interesting to mention that we do not find such a cancellation for the charged Goldstone, i.e. the G^+bb vertex.

In our supersymmetric next-to leading order calculations, the bottom-quark mass is defined in the $\overline{\text{DR}}$ scheme, cf. (4.42) of Section 4.4.2. Combining this definition with the $\tan\beta$-improved bottom-quark Yukawa coupling (6.11), care has to be taken to not double-count the contribution Δm_b, i.e. one has to subtract it from (4.42). Therefore, the effective bottom-quark mass in the $\overline{\text{DR}}$ scheme is given by

$$m_b^{\overline{\text{DR}},\text{eff}} = \frac{m_b^{\overline{\text{DR}}}(\mu_R) + m_b\Delta m_b}{1 + \Delta m_b}. \tag{6.16}$$

In total, the above discussed effects are correctly taken into account by the following replacements:

1. Replace the bottom mass Yukawa coupling $\lambda_b = \sqrt{2}m_b/v_1$ by its resummed value everywhere but in the Goldstone sector,

$$\frac{\lambda_b}{\sqrt{2}} \to \frac{\bar{\lambda}_b}{\sqrt{2}} = \frac{m_b^{\overline{\text{DR}},\text{eff}}}{v_1}. \tag{6.17}$$

   In particular we use this coupling in the sbottom-mass matrix (2.50) in order to determine the mass eigenstates and mixing matrices.

2. Replace the $\mathcal{H}bb$ and $\mathcal{H}tb$[1] vertices by the following effective vertices:

$$g_{h^0bb} \to g_{h^0bb}\big|_{\lambda_b\to\bar{\lambda}_b}\left(1 - \frac{\Delta m_b}{\tan\beta\tan\alpha}\right), \qquad g_{H^\pm tb} \to g_{H^\pm tb}\big|_{\lambda_b\to\bar{\lambda}_b}, \tag{6.18a}$$

$$g_{H^0bb} \to g_{H^0bb}\big|_{\lambda_b\to\bar{\lambda}_b}\left(1 + \Delta m_b\frac{\tan\alpha}{\tan\beta}\right), \qquad g_{G^0bb} \to g_{G^0bb}, \tag{6.18b}$$

$$g_{Abb} \to g_{Abb}\big|_{\lambda_b\to\bar{\lambda}_b}\left(1 - \frac{\Delta m_b}{\tan\beta^2}\right). \tag{6.18c}$$

---

[1]Here $\mathcal{H}$ stands for any of the 5 physical Higgs bosons and the three Goldstone bosons.

The subscript $\lambda_b \to \bar{\lambda}_b$ denotes in accordance to (6.17), how the bottom mass in the coupling has to be treated. Couplings involving Goldstone bosons are not changed.

Considering $\tilde{b}_\alpha \tilde{b}_\alpha^*$ production, neutral-Higgs–bottom vertices are only present in the $b\bar{b}$-channel at tree level. For the gg channel, these couplings are present at NLO EW.

6.3 Next-to-Leading Order EW Contributions

In this section we list the NLO EW corrections to the process (6.1). These contributions are of order $\mathcal{O}(\alpha_s^2 \alpha)$ and arise from virtual corrections and bremsstrahlung processes. The corresponding contributions to the total cross section read as follows,

$$
\mathrm{d}\sigma^{\mathrm{NLO\ EW}}_{PP\to\tilde{b}_\alpha\tilde{b}_\alpha^*}(S) = \int_{\tau_0}^1 \mathrm{d}\tau\, \frac{\mathrm{d}L_{gg}}{\mathrm{d}\tau} \left[\mathrm{d}\hat{\sigma}^{2,1}_{gg\to\tilde{b}_\alpha\tilde{b}_\alpha^*}(\hat{s}) + \mathrm{d}\hat{\sigma}^{2,1}_{gg\to\tilde{b}_\alpha\tilde{b}_\alpha^*\gamma}(\hat{s}) \right]
$$
$$
+ \sum_q \int_{\tau_0}^1 \mathrm{d}\tau\, \frac{\mathrm{d}L_{q\bar{q}}}{\mathrm{d}\tau} \left[\mathrm{d}\hat{\sigma}^{2,1}_{q\bar{q}\to\tilde{b}_\alpha\tilde{b}_\alpha^*}(\hat{s}) + \mathrm{d}\hat{\sigma}^{2,1}_{q\bar{q}\to\tilde{b}_\alpha\tilde{b}_\alpha^*\gamma}(\hat{s}) + \mathrm{d}\hat{\sigma}^{2,1}_{q\bar{q}\to\tilde{b}_\alpha\tilde{b}_\alpha^*g}(\hat{s}) \right]
$$
$$
+ \sum_q \int_{\tau_0}^1 \mathrm{d}\tau \left[\frac{\mathrm{d}L_{qg}}{\mathrm{d}\tau} \mathrm{d}\hat{\sigma}^{2,1}_{gq\to\tilde{b}_\alpha\tilde{b}_\alpha^* q}(\hat{s}) + \frac{\mathrm{d}L_{\bar{q}g}}{\mathrm{d}\tau} \mathrm{d}\hat{\sigma}^{2,1}_{g\bar{q}\to\tilde{b}_\alpha\tilde{b}_\alpha^* \bar{q}}(\hat{s}) \right]. \tag{6.19}
$$

We do not consider the contributions arising from the bremsstrahlung processes

$$
\gamma(p_1)\, q(p_2) \to \tilde{b}_\alpha(p_3)\, \tilde{b}_\alpha^*(p_4)\, q(p_5), \qquad \gamma(p_1)\, \bar{q}(p_2) \to \tilde{b}_\alpha(p_3)\, \tilde{b}_\alpha^*(p_4)\, \bar{q}(p_5), \tag{6.20}
$$

since they are suppressed because of the $\mathcal{O}(\alpha)$ suppression of the photon PDF inside the proton, cf. Section 4.2. Moreover, these processes are further suppressed by an additional factor α_s with respect to the process (6.9) and thus negligible. The $\mathcal{O}(\alpha_s^2 \alpha)$ contributions of the partonic processes with a bottom quark in the initial state are neglected as well. The reason is twofold. First of all, these contributions are suppressed by the bottom PDF with respect to the contributions in eq. (6.19) and in addition they have an additional factor α_s with respect to the $\mathcal{O}(\alpha_s \alpha + \alpha^2)$ contributions of the process (6.2c), which turn out to be small (cf. Section 6.4.3).

CKM-mixing effects are neglected since mixing effects do not enter at tree-level and hence can be seen as a next-to-next-to leading order effect. There is one exception, the quark–anti-quark annihilation with t-channel chargino exchange for initial $u\bar{u}$ or $c\bar{c}$, see Figure 6.2c. These channels give contributions of $\mathcal{O}(\alpha_s \alpha)$ and $\mathcal{O}(\alpha^2)$. However, due to the small values of the CKM mixing elements $|V_{ub}| \approx 4.3 10^{-3}$ and $|V_{cb}| \approx 41.6 10^{-3}$ [175], which enter at least quadratically, their contributions are small and can be safely neglected. In the $u\bar{u}$ case, the CKM suppression yields a factor $\mathcal{O}(10^{-6})$ which cannot be compensated by the high sea quark contribution which in principle enhances the $u\bar{u}$ channel. In the $c\bar{c}$ channel the CKM suppression is around two orders of magnitude smaller, however the small c-quark PDF further reduces its importance. A numerical discussion is postponed to Section 6.4.3.

The amplitudes are generated and algebraically simplified with support of `FeynArts` [161, 162] and `FormCalc` [161, 163], while the numerical evaluation of the one-loop integrals has been performed using `LoopTools` [163]. Infrared (IR) singularities are regularized giving a

small mass to the photon, λ_γ, and to the gluon, λ_g. The mass of the light quarks is kept to regularize the collinear singularities, see also Section 4.3.

6.3.1 Virtual Corrections

The $\mathcal{O}(\alpha_s^2\alpha)$ virtual contributions to the gg channel, process (6.2a), are given in terms of the tree-level QCD matrix element $\mathcal{M}^{1,0}$ and the one-loop amplitude $\mathcal{M}^{1,1}$ resulting from EW insertions to the tree-level QCD diagrams,

$$\mathrm{d}\hat{\sigma}^{2,1}_{gg\to\tilde{b}_\alpha\tilde{b}^*_\alpha}(\hat{s}) = 2\,\overline{\sum}\mathrm{Re}\left\{\mathcal{M}^{1,0}_{gg\to\tilde{b}_\alpha\tilde{b}^*_\alpha}\left(\mathcal{M}^{1,1}_{gg\to\tilde{b}_\alpha\tilde{b}^*_\alpha}\right)^*\right\}\frac{\mathrm{d}\hat{t}}{16\pi\hat{s}^2}\,. \tag{6.21}$$

The one-loop amplitude $\mathcal{M}^{1,1}$ is obtained from the vertex, self-energy, and box corrections, given by the diagrams depicted in Figure 6.5.

The virtual corrections to $q\bar{q}$ channel, process (6.2b), are given by

$$\mathrm{d}\hat{\sigma}^{2,1}_{q\bar{q}\to\tilde{b}_\alpha\tilde{b}^*_\alpha}(\hat{s}) = 2\,\overline{\sum}\mathrm{Re}\left\{\mathcal{M}^{1,0}_{q\bar{q}\to\tilde{b}_\alpha\tilde{b}^*_\alpha}\left(\mathcal{M}^{1,1}_{q\bar{q}\to\tilde{b}_\alpha\tilde{b}^*_\alpha}\right)^* + \mathcal{M}^{0,1}_{q\bar{q}\to\tilde{b}_\alpha\tilde{b}^*_\alpha}\left(\mathcal{M}^{2,0}_{q\bar{q}\to\tilde{b}_\alpha\tilde{b}^*_\alpha}\right)^*\right\}\frac{\mathrm{d}\hat{t}}{16\pi\hat{s}^2}.$$
$$\tag{6.22}$$

$\mathcal{M}^{0,1}$ and $\mathcal{M}^{1,0}$ are the tree-level EW and the tree-level QCD amplitudes respectively. $\mathcal{M}^{1,1}$ is the one-loop amplitude obtained from the EW insertions to the leading-order diagrams and from the QCD corrections to the tree-level EW diagrams, collected in Figure 6.6. $\mathcal{M}^{2,0}$ is the amplitude corresponding to the QCD box diagrams depicted in Figure 6.7.

In order to cancel the UV divergences we need the $\mathcal{O}(\alpha)$ renormalization of the wavefunction of the light quarks and of the sbottom sector. This is done by including the diagrams with counterterms which are given in the last line of Figures 6.5 and 6.6, respectively. The expressions for the counterterms are listed in Table B.1 of Appendix B. The renormalization is performed as described in Section 4.4.2: The field renormalization constants are fixed in the on-shell scheme and the renormalization of the sbottom sector is performed together with the stop sector. In order to avoid numerical instabilities and artificially big contributions from the counterterms, the renormalization is performed in the "m_b $\overline{\mathrm{DR}}$ and A_b $\overline{\mathrm{DR}}$" scheme. Since in particular regions of the MSSM parameter space this scheme can give rise to numerical instabilities, we have explicitly checked its reliability in the SUSY scenarios considered in this paper (cf. Section 6.4). The explicit expression of the renormalization constants in the "m_b $\overline{\mathrm{DR}}$ and A_b $\overline{\mathrm{DR}}$" are given by (4.39) and (4.68)ff. Remind that the counterterm $\delta m_{\tilde{b}_1}$ has to be shifted according to (4.72) in order to compensate the induced one-loop contribution that arises by using the $\tilde{b}_1$ pole mass for the tree-level cross section.

Having a closer look at the Feynman diagrams contributing to the virtual corrections at $\mathcal{O}(\alpha_s^2\alpha)$, one finds that the gg channel (Figure 6.5) only contains gg-vertex corrections that couple to scalar particles (4th and 5th diagram of the second line). In principle there are also vertex corrections with internal vector bosons, however they vanish due to the Landau-Yang theorem [176], which states that two vector bosons cannot couple to a conserved current of spin 1. Those diagrams with s-channel scalar particle exchange are of special interest.
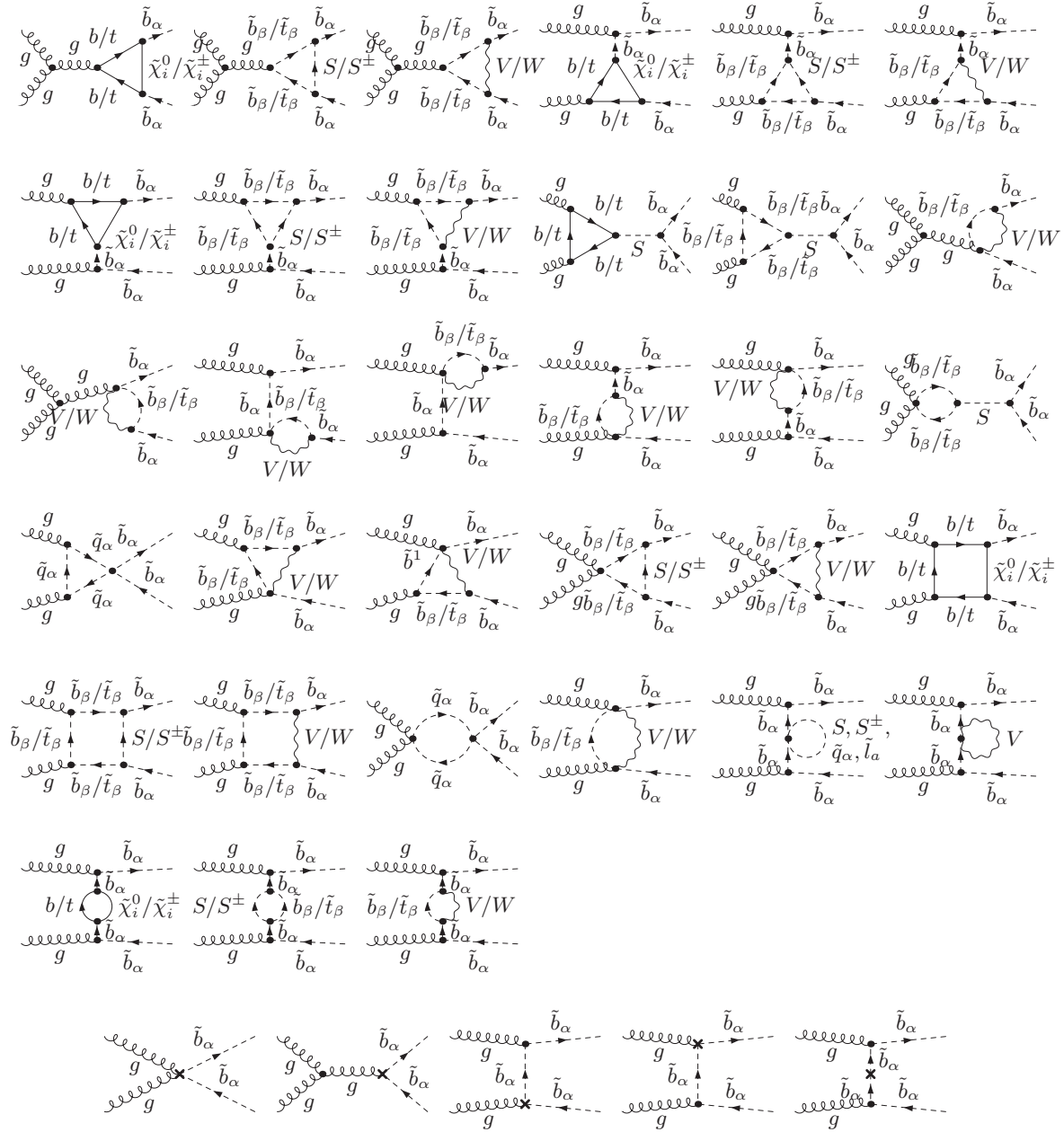
Figure 6.5: Virtual corrections to the process $gg \to \tilde{b}_\alpha \tilde{b}_\alpha^*$. A common label V is used for the neutral gauge bosons γ, Z^0, while S denotes any of the neutral Higgs or Goldstone bosons and $S^\pm$ denotes the charged ones. Crossed diagrams are not shown explicitly. The diagrams containing the counterterms are depicted in the last line. The counterterms have to be evaluated at $\mathcal{O}(\alpha)$.
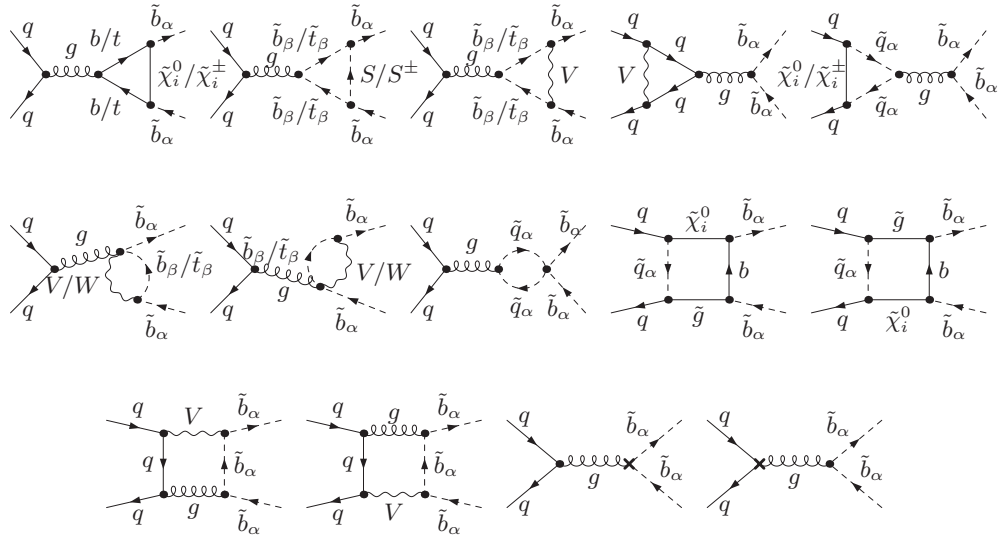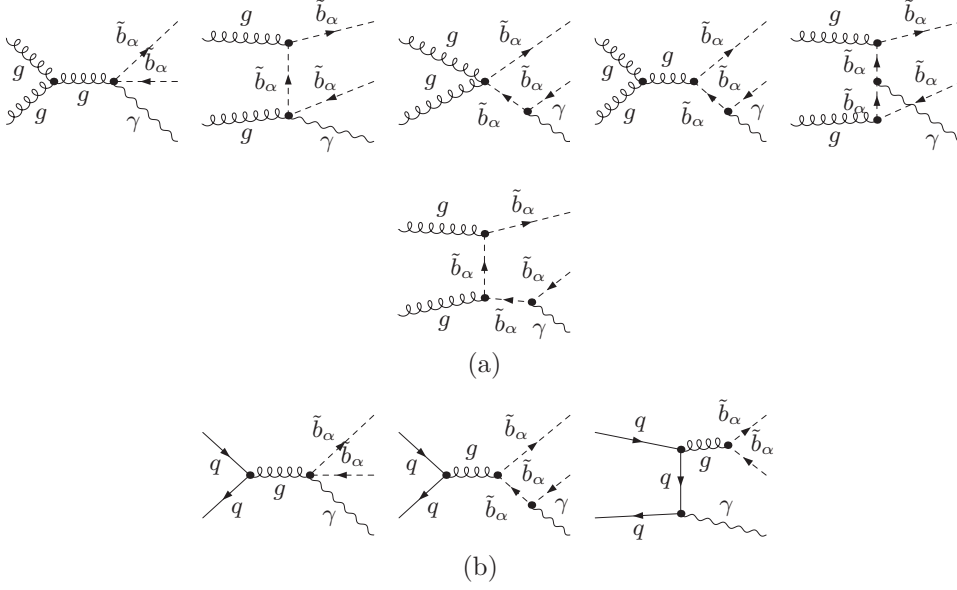
Figure 6.6: Virtual contributions to the process $q\bar{q} \to \tilde{b}_\alpha \tilde{b}_\alpha^*$. The diagrams result from EW insertions to tree-level QCD diagrams and from QCD insertions to tree-level EW diagrams. V, S and $S^\pm$ are defined as in Figure 6.5. Crossed diagrams are not shown. The counterterm diagrams in the last line have to be evaluated at $\mathcal{O}(\alpha)$.
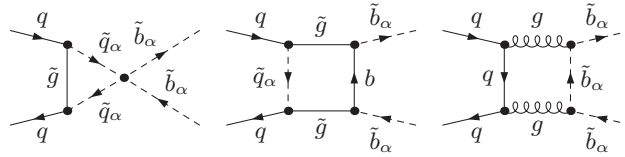
Figure 6.7: Virtual QCD box contributions to the process $q\bar{q} \to \tilde{b}_\alpha \tilde{b}_\alpha^*$. Crossed diagrams are not shown.

They are loop corrections to the ggH vertex which can be significantly enhanced due to $\tan\beta$-enhanced Hbb-couplings. However, this is the only diagram in the gg channel that involves $\tan\beta$-enhanced couplings at $\mathcal{O}(\alpha_s^2\alpha)$.

The UV divergences arising in the processes considered at $\mathcal{O}(\alpha_s^2\alpha)$ cancel when adding the counterterm diagrams with the counterterms evaluated at $\mathcal{O}(\alpha)$. As shown in Section 4.5, the soft-photon singularities arising from the diagrams in Figure 6.5 and 6.6 as well as the soft-gluon singularities from Figure 6.7 cancel in the sum of virtual and real corrections. Remaining initial-state photon singularities from the $q\bar{q}$ channel have to be absorbed into the definition of the PDFs.

(a)

(b)

Figure 6.8: Feynman diagrams contributing to real photon emission at $\mathcal{O}(\alpha_s^2\alpha)$. (a) Real photon emission for gg fusion. (b) Real photon emission for $q\bar{q}$ annihilation.

6.3.2 Real Corrections

The $\mathcal{O}(\alpha_s^2\alpha)$ contributions to the partonic processes (6.2a) and (6.2b) with a photon in the final state,

$$g(p_1)\, g(p_2) \rightarrow \tilde{b}_\alpha(p_3)\, \tilde{b}_\alpha^*(p_4)\, \gamma(p_5), \tag{6.23a}$$

$$q(p_1)\, \bar{q}(p_2) \rightarrow \tilde{b}_\alpha(p_3)\, \tilde{b}_\alpha^*(p_4)\, \gamma(p_5), \tag{6.23b}$$

are given by the squared matrix element of the tree-level QCD diagrams with an external photon attached, see Figure 6.8. The partonic cross section is hence given by

$$\hat{\sigma}^{2,\,1}_{gg\rightarrow\tilde{b}_\alpha\tilde{b}_\alpha\gamma} = \frac{1}{4\hat{s}} \int \mathrm{d}^3\mathrm{Lips} \left|\mathcal{M}^{1,\,\frac{1}{2}}_{gg\rightarrow\tilde{b}_\alpha\tilde{b}_\alpha\gamma}\right|, \tag{6.24a}$$

$$\hat{\sigma}^{2,\,1}_{q\bar{q}\rightarrow\tilde{b}_\alpha\tilde{b}_\alpha\gamma} = \frac{1}{4\hat{s}} \int \mathrm{d}^3\mathrm{Lips} \left|\mathcal{M}^{1,\,\frac{1}{2}}_{q\bar{q}\rightarrow\tilde{b}_\alpha\tilde{b}_\alpha\gamma}\right|. \tag{6.24b}$$

The phase-space integration is divergent in the soft-photon region, i.e. for $p_5^0 \rightarrow 0$. In the case of the process (6.23b), further singularities arise in the collinear region, i.e. for $p_{1,2} \cdot p_5 \rightarrow 0$. IR and collinear singularities are treated using the phase-space slicing method described in Section 4.5.1.

The gluon bremsstrahlung process,

$$q(p_1)\, \bar{q}(p_2) \rightarrow \tilde{b}_\alpha(p_3)\, \tilde{b}_\alpha^*(p_4)\, g(p_5), \tag{6.25}$$

contributes at $\mathcal{O}(\alpha_s^2\alpha)$ via the interference of QCD-based (Figure 6.9a) and EW-based (Figure 6.9b) Feynman diagrams. The partonic cross section is given by

(a)

(b)
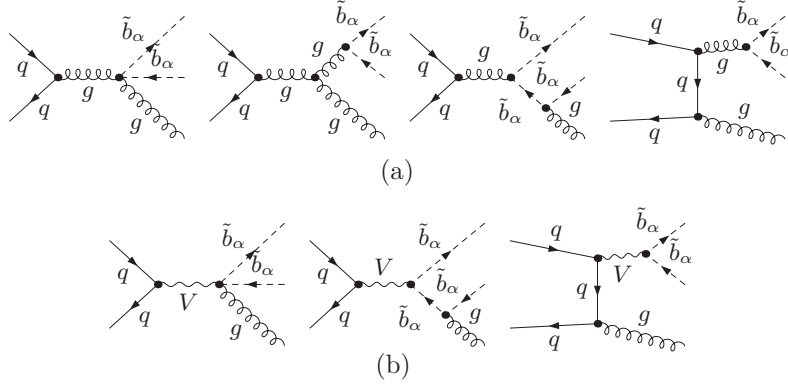
Figure 6.9: Real gluon emission for the $q\bar{q}$ channel. (a) QCD-based diagrams. (b) EW-based diagrams.

$$\hat{\sigma}^{2,1}_{q\bar{q}\to\tilde{b}_\alpha\tilde{b}_\alpha g} = \frac{1}{4\hat{s}} \int \mathrm{d}^3\mathrm{Lips}\, 2\,\mathrm{Re}\left[\left(\mathcal{M}^{\frac{3}{2},0}_{q\bar{q}\to\tilde{b}_\alpha\tilde{b}_\alpha\gamma}\right)^* \mathcal{M}^{\frac{1}{2},1}\right]. \tag{6.26}$$

The IR singularities of gluonic origin are in close analogy to the photonic case, however color correlations have to be taken into account, see Section 4.5.2. Decomposing the tree-level amplitudes according to their color structure as

$$\begin{aligned}
\mathcal{M}^{1,0\,c_1c_2c_3c_4}_{12\to34} &= \delta_{c_1c_2}\delta_{c_3c_4}\mathcal{M}^{1,0}_1 + \delta_{c_1c_3}\delta_{c_2c_4}\mathcal{M}^{1,0}_2, \\
\mathcal{M}^{0,1\,c_1c_2c_3c_4}_{12\to34} &= \delta_{c_1c_2}\delta_{c_3c_4}\mathcal{M}^{0,1}_1,
\end{aligned} \tag{6.27}$$

the $\mathcal{F}_{ij}$ of (4.108) are given by

$$\begin{aligned}
\mathcal{F}_{12} &= \mathcal{F}_{34} = 0, \\
\mathcal{F}_{14} &= \mathcal{F}_{23} = -\mathcal{F}_{13} = -\mathcal{F}_{24} = 4\left(\mathcal{M}^{1,0}_2\right)^* \mathcal{M}^{0,1}_1, \\
\mathcal{F}_{ii} &= 12\left(\mathcal{M}^{1,0}_1\right)^* \mathcal{M}^{0,1}_1 + 4\left(\mathcal{M}^{1,0}_2\right)^* \mathcal{M}^{0,1}_1.
\end{aligned} \tag{6.28}$$

Due to the color structure, the interference term of a QCD-based and an EW-based diagram in Figure 6.9 vanishes if both gluons are emitted from an initial-state or an final-state particle. The resulting squared matrix element is parity-odd and hence does neither contribute to the total cross section nor for any parity-symmetric observable.

Real quark radiation contributes at $\mathcal{O}(\alpha_s^2\alpha)$ as well,

$$g(p_1)\,q(p_2) \to \tilde{b}_\alpha(p_3)\,\tilde{b}^*_\alpha(p_4)\,q(p_5), \tag{6.29a}$$

$$g(p_1)\,\bar{q}(p_2) \to \tilde{b}_\alpha(p_3)\,\tilde{b}^*_\alpha(p_4)\,\bar{q}(p_5). \tag{6.29b}$$

This IR- and collinear-finite set is given by the interference of QCD-based and EW-based tree-level diagrams (Figure 6.10a and Figure 6.10b). Only the interference from initial-state and final-state radiation contributes. As in the real gluon emission case, the resulting squared matrix element is parity odd and hence does neither contribute to the total cross section nor for any parity-symmetric observable.
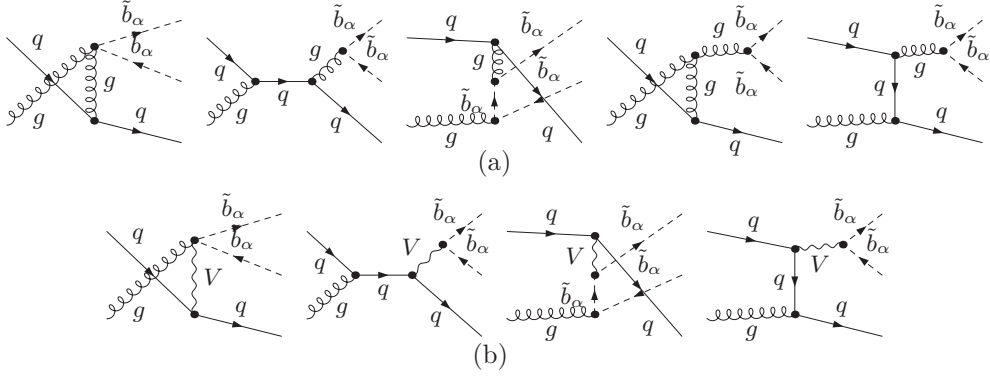
(a)

(b)

Figure 6.10: Feynman diagrams contributing to real quark radiation. (a) QCD-based diagrams. (b) EW-based diagrams.

The IR singularities arising in the gg channel cancel in the sum of virtual corrections, process (6.21), and real photon radiation, process (6.23a). In the $q\bar{q}$ channel the sum of virtual corrections (6.22), real photon radiation (6.23b), and real gluon radiation (6.25) is IR finite. This sum is affected by universal collinear singularities of photonic origin that can be absorbed in the PDFs. This can be achieved by means of the following substitution (cf. Section 4.5.1),

$$
f_q(x, \mu_F) \rightarrow f_q(x, \mu_F) \left(1 - \frac{\alpha e_q^2}{\pi} \kappa_{v+s} \right) - \frac{\alpha e_q^2}{2\pi} \int_x^{1-\delta_s} \frac{dz}{z} f_q\left(\frac{x}{z}, \mu_F \right) \kappa_c(z). \qquad (6.30)
$$

e_q is the electric charge of quark q expressed in units of the positron charge, while

$$
\kappa_{v+s} = 1 - \ln \delta_s - \ln^2 \delta_s + \left(\ln \delta_s + \frac{3}{4} \right) \ln \left(\frac{\mu_F^2}{m_q^2} \right) + \frac{1}{4} \left(9 + \frac{2\pi^2}{3} + 3 \ln \delta_s - 2 \ln^2 \delta_s \right),
$$

$$
\kappa_c(z) = P_{qq}(z) \ln \left(\frac{\mu_F^2}{m_q^2} \frac{1}{(1-z)^2} - 1 \right) - \left[P_{qq}(z) \ln \left(\frac{1-z}{z} \right) - \frac{3}{2} \frac{1}{1-z} + 2z + 3 \right],
$$

$$(6.31)$$

with the splitting function $P_{qq}(z) = (1 + z^2)/(1 - z)$. The factorization is performed in the DIS scheme. The replacement of the PDFs gives further contributions of $\mathcal{O}(\alpha_s^2 \alpha)$ to the total cross section, canceling the remaining collinear singularities. Using the notation of Section 4.5, the IR- and collinear-finite contributions to the partonic cross sections at $\mathcal{O}(\alpha_s^2 \alpha)$ are given by

$$
\begin{aligned}
\hat{\sigma}^{2,1}_{gg \to \tilde{b}_\alpha \tilde{b}_\alpha^* + X} &= \hat{\sigma}^{2,1}_{gg \to \tilde{b}_\alpha \tilde{b}_\alpha^*} \big|_{\text{virt}} + \hat{\sigma}^{2,1}_{gg \to \tilde{b}_\alpha \tilde{b}_\alpha^* \gamma} \big|_{\text{soft}} + \hat{\sigma}^{2,1}_{gg \to \tilde{b}_\alpha \tilde{b}_\alpha^* \gamma} \big|_{\text{finite}}, \\
\hat{\sigma}^{2,1}_{q\bar{q} \to \tilde{b}_\alpha \tilde{b}_\alpha^* + X} &= \hat{\sigma}^{2,1}_{q\bar{q} \to \tilde{b}_\alpha \tilde{b}_\alpha^*} \big|_{\text{virt}} + \hat{\sigma}^{2,1}_{q\bar{q} \to \tilde{b}_\alpha \tilde{b}_\alpha^*} \big|_{\text{PDF}}^\gamma + \hat{\sigma}^{2,1}_{q\bar{q} \to \tilde{b}_\alpha \tilde{b}_\alpha^* \gamma} \big|_{\text{soft}} + \hat{\sigma}^{2,1}_{q\bar{q} \to \tilde{b}_\alpha \tilde{b}_\alpha^* \gamma} \big|_{\text{coll}} \\
&\quad + \hat{\sigma}^{2,1}_{q\bar{q} \to \tilde{b}_\alpha \tilde{b}_\alpha^* \gamma} \big|_{\text{PDf}}^\gamma + \hat{\sigma}^{2,1}_{q\bar{q} \to \tilde{b}_\alpha \tilde{b}_\alpha^* \gamma} \big|_{\text{finite}}, \\
\hat{\sigma}^{2,1}_{qg \to \tilde{b}_\alpha \tilde{b}_\alpha^* + X} &= \hat{\sigma}^{2,1}_{qg \to \tilde{b}_\alpha \tilde{b}_\alpha^* q} + \hat{\sigma}^{2,1}_{\bar{q}g \to \tilde{b}_\alpha \tilde{b}_\alpha^* \bar{q}}.
\end{aligned}
$$

6.4 Numerical Results

In this section we perform a detailed numerical analysis for diagonal sbottom-pair production at NLO EW. We stick to the notation introduced in Section 5.4.1. The leading order cross section, the tree-level EW and the NLO EW contributions to the cross section are labeled by

$$\sigma^{\text{Born}} = \sigma^{2,0}, \qquad \Delta\sigma^{\text{tree EW}} = (\sigma^{1,1} + \sigma^{0,2}), \qquad \Delta\sigma^{\text{NLO EW}} = \sigma^{2,1}, \tag{6.33}$$

respectively. $\Delta\sigma^{\text{EW}} = \Delta\sigma^{\text{tree EW}} + \Delta\sigma^{\text{NLO EW}}$ will be referred to as the EW contribution. The total sum of the LO cross section with the EW contributions is denoted by $\sigma^{\text{NLO}} = \sigma^{\text{Born}} + \Delta\sigma^{\text{EW}}$. Relative EW contributions are defined by

$$\delta^{\text{tree EW}} = \Delta\sigma^{\text{tree EW}}/\sigma^{\text{Born}}, \qquad \delta^{\text{NLO EW}} = \Delta\sigma^{\text{NLO EW}}/\sigma^{\text{Born}}, \qquad \delta^{\text{EW}} = \Delta\sigma^{\text{EW}}/\sigma^{\text{Born}}.$$
$$\tag{6.34}$$

In distributions δ denotes the relative EW contribution defined as $\delta = (\mathcal{O}_{\text{NLO}} - \mathcal{O}_{\text{Born}})/\mathcal{O}_{\text{Born}}$, where $\mathcal{O}$ is a generic observable and $\mathcal{O}_{\text{NLO}}$ is the sum of the Born and the EW contributions.

6.4.1 Input Parameters

The Standard Model input parameters are given in (5.32).

For the numerical analysis we consider the mSUGRA scenarios SPS1a$'$ and SPS4. The first one is a "typical" SUSY scenario proposed by the SPA convention for comparison with other calculations [165]. The scenario SPS4 is characterized by a large value of $\tan\beta$. Within this scenario we study the dependence of the total cross section on the squark masses and on $\tan\beta$. The third scenario considered is the GMSB scenario SPS8.

The particle spectrum is determined following the procedure described in Section 5.4.1. Starting from GUT-scale parameters, cf. Table 6.1, we use the program SOFTSUSY [166] to evolve the soft-breaking parameters down to the SUSY scale $M_{\text{SUSY}} = 1\,\text{TeV}$. To get the right mixing in the sbottom sector, we first translate the sbottom masses into the OS-masses and use those to calculate the effective bottom-quark mass $m_b^{\overline{\text{DR}},\text{eff}}$, eq. (6.16). This mass is then used in the bottom-squark mass matrix to calculate the sbottom mass-eigenstates. The lighter of the two bottom squarks is taken as the dependent squark. Its mass is therefore fixed by $SU(2)$ invariance. The shift Δm_b, cf. (6.12), the effective bottom-quark mass together with the on-shell mass of the bottom squarks, the gluino and the lightest neutralino/chargino are summarized in Table 6.2.

Unless otherwise stated, the results presented in this section are computed setting the hadronic center of mass energy to $\sqrt{S} = 14$ TeV and using the MRST2004QED parton distribution functions [126]. The factorization and renormalization scales are set to a common value, $\mu = \mu_R = \mu_F = m_{\tilde{b}_\alpha}$, i.e. to the mass of the produced bottom squark.

6.4.2 Total Hadronic Cross Section

Table 6.3 shows the hadronic cross section for diagonal bottom-squark production within the three considered scenarios for the $\sqrt{S} = 14$ TeV LHC. As expected, the total cross

	m_0	$m_{1/2}$	A_0	$\tan\beta$	$\text{sign}(\mu)$
SPS1a′	70 GeV	250 GeV	−300 GeV	10	+
SPS4	400 GeV	300 GeV	0	49.4	+

	Λ	M_{mess}	N_{mess}	$\tan\beta$	$\text{sign}(\mu)$
SPS8	100 TeV	200 TeV	1	15	+

Table 6.1: High energy input parameters for the different SUSY scenarios considered. The mass parameters m_0, $m_{1/2}$ and A_0 are given at the GUT scale, $\tan\beta$ is evaluated at $M_{\text{SUSY}} = 1\,\text{TeV}$.

	$\Delta m_{\tilde b}$	$m_b^{\overline{\text{DR}},\text{eff}}$	$\tilde b_1$	$\tilde b_2$	$\tilde g$	$\tilde\chi_1^0$	$\tilde\chi_1^\pm$
SPS1a′	0.037	2.38	495	538	609	101	180
SPS4	0.22	2.08	433	633	736	123	217
SPS8	0.003	2.39	1070	1085	141	253	

Table 6.2: The shift $\Delta m_{\tilde b}$ and the resulting effective bottom-quark mass as well as the on-shell masses of the bottom squarks, the gluino, and the lightest neutralino and chargino within the different SUSY scenarios considered. All masses are given in GeV.

section is dominated by the LO QCD contribution of $\mathcal{O}(\alpha_s^2)$. The tree-level EW contributions are dominated by the photon-induced channel which is independent of the mixing angle. In each scenario, its yield relative to the leading-order cross section is similar for the two processes considered. Although formally suppressed by a factor α_s, the NLO EW corrections are typically bigger than the tree-level EW contributions. In the SPS1a′ (SPS4) scenario the tree-level and NLO EW contributions are more important in case of $\tilde b_1\tilde b_1^*$ ($\tilde b_2\tilde b_2^*$) production. This can be explained by the chirality dependence of the SU(2) coupling and by the fact that in the SPS1a′ (SPS4) scenario $\tilde b_1$ ($\tilde b_2$) is mostly left-handed.

In the SPS8 scenario the bottom-squark masses are in the TeV range and hence twice as heavy as in the aforementioned scenarios (cf. Table 6.2), thus the Born cross section is about two orders of magnitude smaller. Further, the mixing between left- and right- handed squarks is more important and the sbottom masses are nearly degenerate. These features partially soften the differences among the tree-level EW contributions to $\tilde b_1\tilde b_1^*$ production and the ones to $\tilde b_2\tilde b_2^*$ production.[2] Huge cancellations between the $q\bar q$ and the gg channel amplify the dependence of the NLO EW contribution on the production process considered. As a result the NLO EW contributions to $b_1 b_1^*$ production and the ones to $b_2 b_2^*$ production have opposite sign, the latter being three times bigger than the former. Summing up the various contributions, the relative yield in the scenarios considered is below 2%.

Table 6.4 collects the hadronic cross section for $\sqrt S = 7$ TeV. The leading-order total

---

[2]We checked that in the no-mixing limit the tree-level EW contributions to $\tilde b_L$ production is one order of magnitude higher than the one contributing to $\tilde b_R$ production

14 TeV	$\sigma^{\mathbf{Born}}$ $\mathcal{O}(\alpha_s^2)$	$\mathbf{\Delta\sigma^{tree\ EW}}$ $\mathcal{O}(\alpha_s\alpha + \alpha^2)$	$\mathbf{\Delta\sigma^{g\gamma}}$ $\mathcal{O}(\alpha_s\alpha)$	$\mathbf{\Delta\sigma^{NLO\ EW}}$ $\mathcal{O}(\alpha_s^2\alpha)$	$\mathbf{\Delta\sigma^{EW}}$ $\mathcal{O}(\alpha_s\alpha + \alpha^2 + \alpha_s^2\alpha)$
SPS1a$'$					
$\tilde{b}_1\tilde{b}_1^*$	444.3(3)	0.7933(4)	2.0106(5)	$-6.041(9)$	$-3.237(9)$
		0.18 %	0.45 %	-1.36 %	-0.73 %
$\tilde{b}_2\tilde{b}_2^*$	310.3(1)	0.00346(3)	1.4710(4)	$-2.892(4)$	$-1.418(4)$
		0.00 %	0.47 %	-0.93 %	-0.46 %
SPS4					
$\tilde{b}_1\tilde{b}_1^*$	1050.9(3)	$-0.3879(4)$	4.255(1)	$-19.35(1)$	$-15.48(1)$
		-0.04 %	0.40 %	-1.84 %	-1.47 %
$\tilde{b}_2\tilde{b}_2^*$	112.36(6)	0.2734(1)	0.6090(1)	$-2.852(2)$	$-1.969(2)$
		0.24 %	0.54 %	-2.54 %	-1.75 %
SPS8					
$\tilde{b}_1\tilde{b}_1^*$	3.405(1)	0.002296(1)	0.029004(7)	$-0.00307(9)$	0.02823(9)
		0.07 %	0.85 %	-0.09 %	0.83 %
$\tilde{b}_2\tilde{b}_2^*$	3.042(1)	0.007054(3)	0.026286(7)	0.00835(9)	0.04169(9)
		0.23 %	0.86 %	0.27 %	1.37 %

Table 6.3: Hadronic cross section for diagonal $\tilde{b}_\alpha\tilde{b}_\alpha^*$ production at the 14 TeV LHC within three different scenarios. Shown are the LO cross section, the tree-level EW as well as NLO EW contributions and the relative corrections as defined in the text. The numbers in brackets refer to the integration uncertainty in the last digit. All cross sections are given in femtobarn (fb).

cross sections are reduced proportionally to the mass of the produced squark. They amount to $1 - 10\%$ of their value at $\sqrt{S} = 14$ TeV. In all the scenarios considered, the contribution of the photon induced channel is enhanced with respect to the 14 TeV case. In the SPS1a$'$ (SPS4) scenario the importance of the NLO EW contributions to the mostly left-handed sbottom production, $\tilde{b}_1\tilde{b}_1^*$ ($\tilde{b}_2\tilde{b}_2^*$), is reduced. In contrast, the NLO EW contributions become more important in case of the production of the mostly right-handed sbottom. In the SPS8 scenario the EW contributions of the various channels are enhanced. In particular the NLO EW contributions are positive for both production processes. This is a consequence of the enhancement of the NLO EW contributions to the gg channel at $\sqrt{S} = 7$ TeV cf. Section 6.4.4).

7 TeV	σ^{Born} $\mathcal{O}(\alpha_s^2)$	$\Delta\sigma^{\text{tree EW}}$ $\mathcal{O}(\alpha_s\alpha + \alpha^2)$	$\Delta\sigma^{g\gamma}$ $\mathcal{O}(\alpha_s\alpha)$	$\Delta\sigma^{\text{NLO EW}}$ $\mathcal{O}(\alpha_s^2\alpha)$	$\Delta\sigma^{\text{EW}}$ $\mathcal{O}(\alpha_s\alpha + \alpha^2 + \alpha_s^2\alpha)$
SPS1a′					
$\tilde{b}_1\tilde{b}_1^*$	30.42(2)	0.09993(4)	0.20183(5)	$-0.3480(7)$	$-0.0462(7)$
		0.33 %	0.66 %	-1.14 %	-0.15 %
$\tilde{b}_2\tilde{b}_2^*$	19.286(6)	0.003521(2)	0.13565(3)	$-0.2027(3)$	$-0.0636(3)$
		0.02 %	0.70 %	-1.05 %	-0.33 %
SPS4					
$\tilde{b}_1\tilde{b}_1^*$	89.10(2)	$-0.00725(2)$	0.5153(1)	$-1.689(1)$	$-1.181(1)$
		-0.01 %	0.58 %	-1.90 %	-1.33 %
$\tilde{b}_2\tilde{b}_2^*$	5.175(2)	0.023176(9)	0.04325(1)	$-0.1251(1)$	$-0.0587(1)$
		0.45 %	0.84 %	-2.42 %	-1.13 %
SPS8					
$\tilde{b}_1\tilde{b}_1^*$	0.03706(1)	0.000044(1)	0.000588(1)	0.000097(1)	0.000730(1)
		0.12 %	1.59 %	0.26 %	1.97 %
$\tilde{b}_2\tilde{b}_2^*$	0.03118(1)	0.000111(1)	0.000506(1)	0.000301(1)	0.000918(1)
		0.36 %	1.62 %	0.97 %	2.95 %

Table 6.4: Same as Table 6.3 but considering diagonal $\tilde{b}_\alpha\tilde{b}_\alpha^*$ production at the 7 TeV LHC.

6.4.3 Parameter Scan

The impact of $\tan\beta$ and of the sbottom masses on the total cross section have been studied performing a parameter scan on these parameters. In this scan, the soft breaking parameters M_L and $M_{\tilde{b}_R}$ appearing the squared mass matrix, eq. (2.50), are set to a common value m_{squark}. All other parameters are set to their SPS4 values. The scans presented in this section are obtained for three different values of $m_{\text{squark}} = \{300, 600, 900\}$ GeV. $\tan\beta$ is varied from 10 to 50.

In all scenarios considered, we have verified the smallness of the bottom-initiated tree-level contributions, justifying our procedure of neglecting the $\mathcal{O}(\alpha_s^2\alpha)$ contributions to this channel. In Figure 6.11 we show the relevance of the various production channels at tree-level. For $\tilde{b}_1\tilde{b}_1$ and $\tilde{b}_2\tilde{b}_2$ production the total cross section is dominated by the gluon induced channel having a relative yield of $70-90\%$. The remaining $10-30\%$ of the total cross section are given by the $q\bar{q}$ channel, with the relative yield increasing with $\tan\beta$. As expected, the $b\bar{b}$ channel is strongly suppressed due to the small value of the bottom-quark density inside the proton. This can be seen from the right plot in Figure 4.2 where the sea quark PDFs including the bottom quark, given by the gray lines, are at least two orders of magnitude
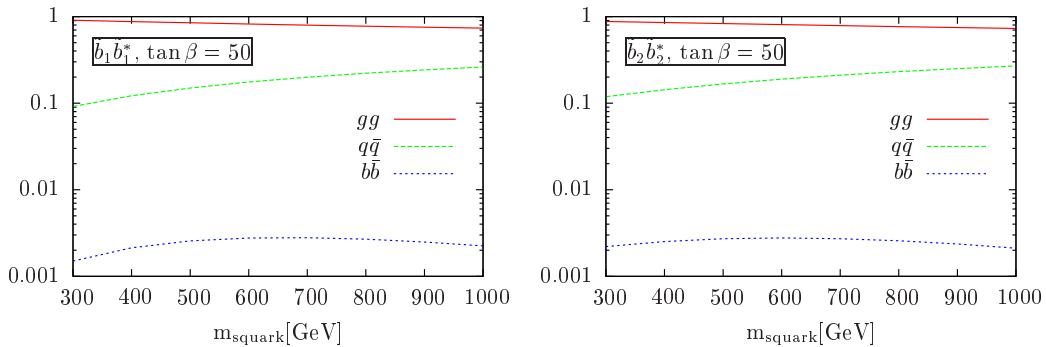
Figure 6.11: The relative yield of the various production channels at tree-level scanned over the common squark mass as defined in the text. The left (right) plot shows $\tilde{b}_1\tilde{b}_1$ ($\tilde{b}_2\tilde{b}_2$) production. In both cases the tree-level cross section is dominated by the gluon-induced channel, while $q\bar{q}$ annihilation contributes to $10-30\%$. The bottom-induced channel has a relative yield which lies at the per-mill level.

smaller in the relevant x-region. Its contribution to the tree-level cross section lies at the per-mill level, in accordance with the analysis in Ref. [23].[3] Due to the small yield of the $b\bar{b}$ channel at tree-level, we will safely neglect the NLO EW contributions to this channel.

The second approximation made in our calculation was to neglect CKM mixing effects. Figure 6.12 shows the ratio between the tree-level EW contributions to the cross section that arise for non-trivial CKM matrix only, and the Born cross section. The red lines show the relative yield for the $c\bar{c}$ channel while the blue lines are for the $u\bar{u}$ channel. Both channels exhibit contributions of similar size, depending on precise value of m_{SUSY} and $\tan\beta$. However, its contribution to the cross section is of $\mathcal{O}(10^{-6})$ of the Born cross section, which justifies our procedure of neglecting CKM effects.

The reliability of the renormalization scheme in the scenarios considered has been verified as well. In particular we have checked that the finite part of the renormalization constant of the dependent parameters is smaller than the parameter itself. Figure 6.13 shows the ratios

$$r_1 = \frac{\delta m_{\tilde{b}_1}^{2\,\mathrm{fin}}}{m_{\tilde{b}_1}^2}, \qquad r_2 = \frac{\delta A_t^{\mathrm{fin}}}{A_t}, \qquad r_3 = \frac{\delta\theta_b^{\mathrm{fin}}}{\theta_b}, \tag{6.35}$$

as a function of $\tan\beta$ for the various values of m_{squark}. r_1 and r_2 are below 0.2 while r_3 is at most of $\mathcal{O}(0.5)$ in the low $\tan\beta$ region. From the counterterms given in Table B.2 one can see that $\delta m_{\tilde{b}_1}^2$ is the only dependent renormalization constant entering our NLO EW calculation. The relative size of the finite part of this counterterm is moderate, rendering this scheme appropriate for our calculation. Care has to be taken when using this scheme for the calculation of observables that require the renormalization of the sbottom mixing

---

[3]The big contributions from the $b\bar{b}$ channel quoted in Ref. [108] are a consequence of two enhancement factors. First of all, resonant Higgs-boson exchange is considered. Moreover, the Hbb Yukawa coupling is enhanced by the choice of a negative value for the parameter μ such that $\Delta m_b \approx -0.76$. In our analysis the Higgs-masses are not tuned to be resonant and we do not consider negative values of μ since it is disfavored by the value of the anomalous magnetic moment of the muon $(g-2)_\mu$ [58].
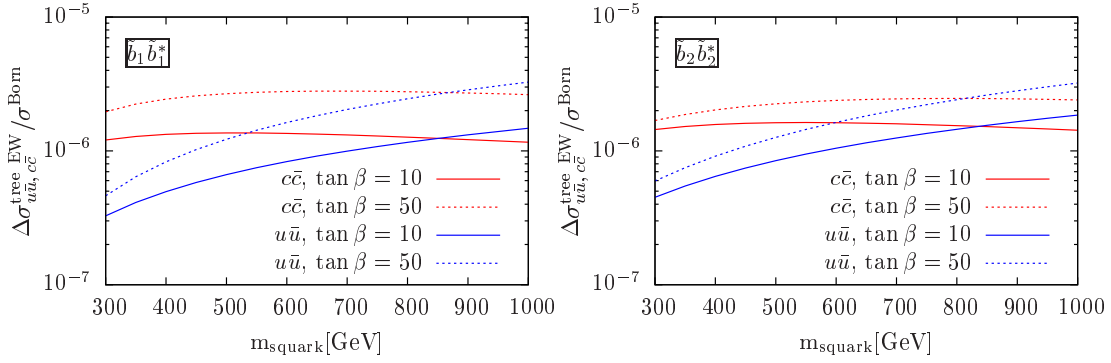
Figure 6.12: Relative yield of the tree-level EW contributions which are only present for non-trivial CKM mixing. The common squark mass m_{SUSY} is defined in the text. The left (right) plot shows $\tilde{b}_1 \tilde{b}_1^*$ ($\tilde{b}_2 \tilde{b}_2^*$) production for two different values of $\tan\beta$. The red lines show the $c\bar{c}$ initiated contribution which are suppressed via V_{cb}, while the blue lines show the $u\bar{u}$ initiated contribution which are suppressed via V_{ub}.
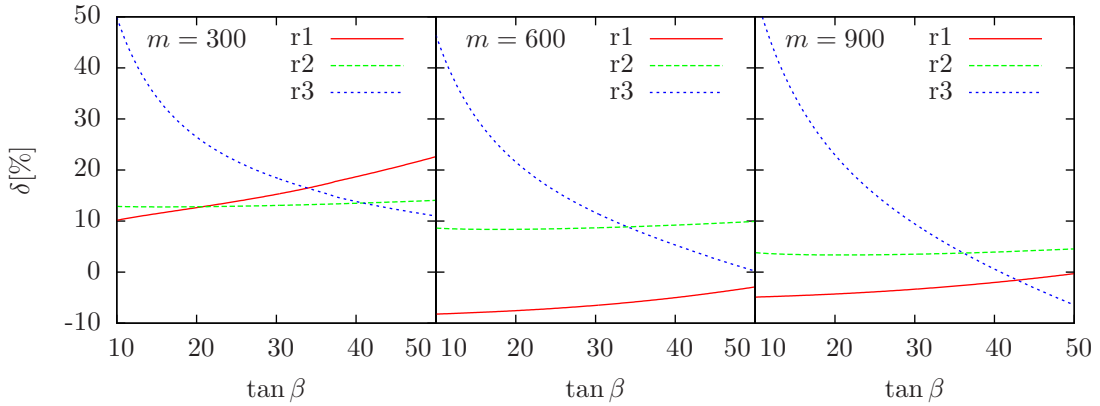
Figure 6.13: Reliability of the renormalization scheme for the $\tan\beta$ range considered and for different squark masses. The ratios $r_1, r_2,$ and r_3 are defined in (6.35).

angle θ_b since the large relative contribution to $\delta\theta_b$ for small values of $\tan\beta$ might spoil the reliability of the prediction. However, not the mixing angle itself but rather the sine or cosine of the angle enters the calculation, and it is questionable whether the large shift in the mixing angle propagates to the observable under consideration. For example, we have explicitly checked that the ratios $(\delta\sin\theta/\sin\theta)$ and $(\delta\cos\theta/\cos\theta)$ are between $30-40\%$ in the low $\tan\beta$ region.

The results of the scan are collected in Figures 6.14 and 6.15. $q\bar{q}$ refers to the sum of the tree-level EW and of the NLO EW contributions from the $q\bar{q}$ annihilation channel. The peaks in the corrections correspond to neutralino, chargino, or sfermion thresholds. These unphysical singularities affect the self-energy of the produced sbottom and can be regularized by taking into account the finite widths of the unstable particle [177]. The right panels of Figures 6.14 and 6.15 keep track of the particles responsible for the threshold behavior. These plots show the mass of the produced squark as a function of $\tan\beta$ as
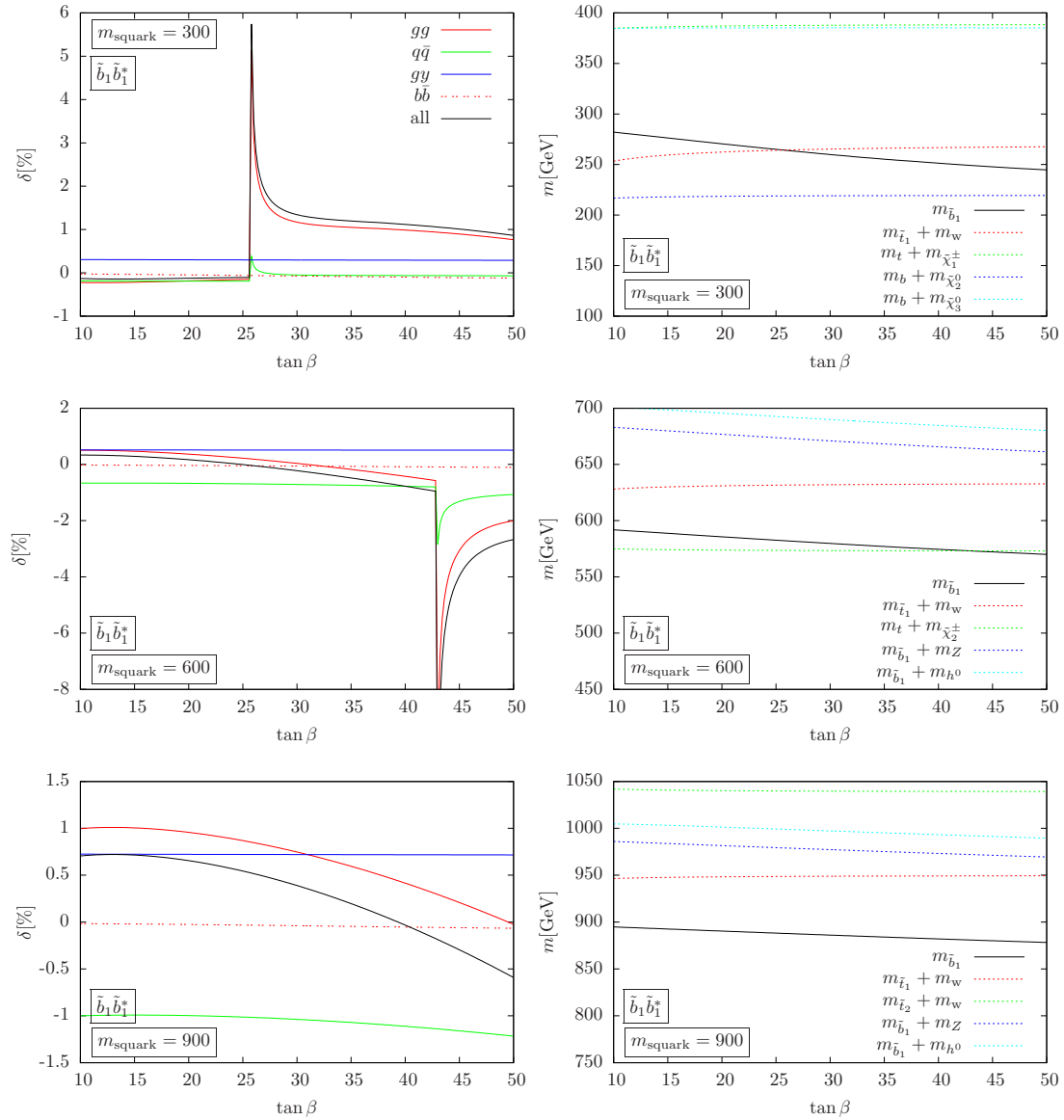
Figure 6.14: The relative yield of the EW contribution for $\tilde{b}_1 \tilde{b}_1^*$ production for the various production channels as well as the combinded effect are shown on the left. The $\tan \beta$ dependence of the produced bottom-squark mass, as well as the sum of the masses of particles close to it are shown on the right. $\tan \beta$ is varied from 10 to 50.

well as the threshold for the production of (some of) the particle pairs entering the loops of the sbottom self-energy. The curves in Figures 6.14 and 6.15 exhibit a step-function-like behavior in the region where the mass of the produced sbottom is above threshold. Since $\tan \beta$ affects the mixing of the bottom squarks, also their mass slightly changes by varying $\tan \beta$. $m_{\tilde{b}_1}$ slowly decreases while $m_{\tilde{b}_2}$ increases. Hence, the region above threshold corresponds to low $\tan \beta$ for $\tilde{b}_1$ and to high $\tan \beta$ for $\tilde{b}_2$. Both, in the $\tilde{b}_1 \tilde{b}_1^*$ and in the $\tilde{b}_2 \tilde{b}_2^*$ production case the behavior of the various contributions strongly depends on the size of
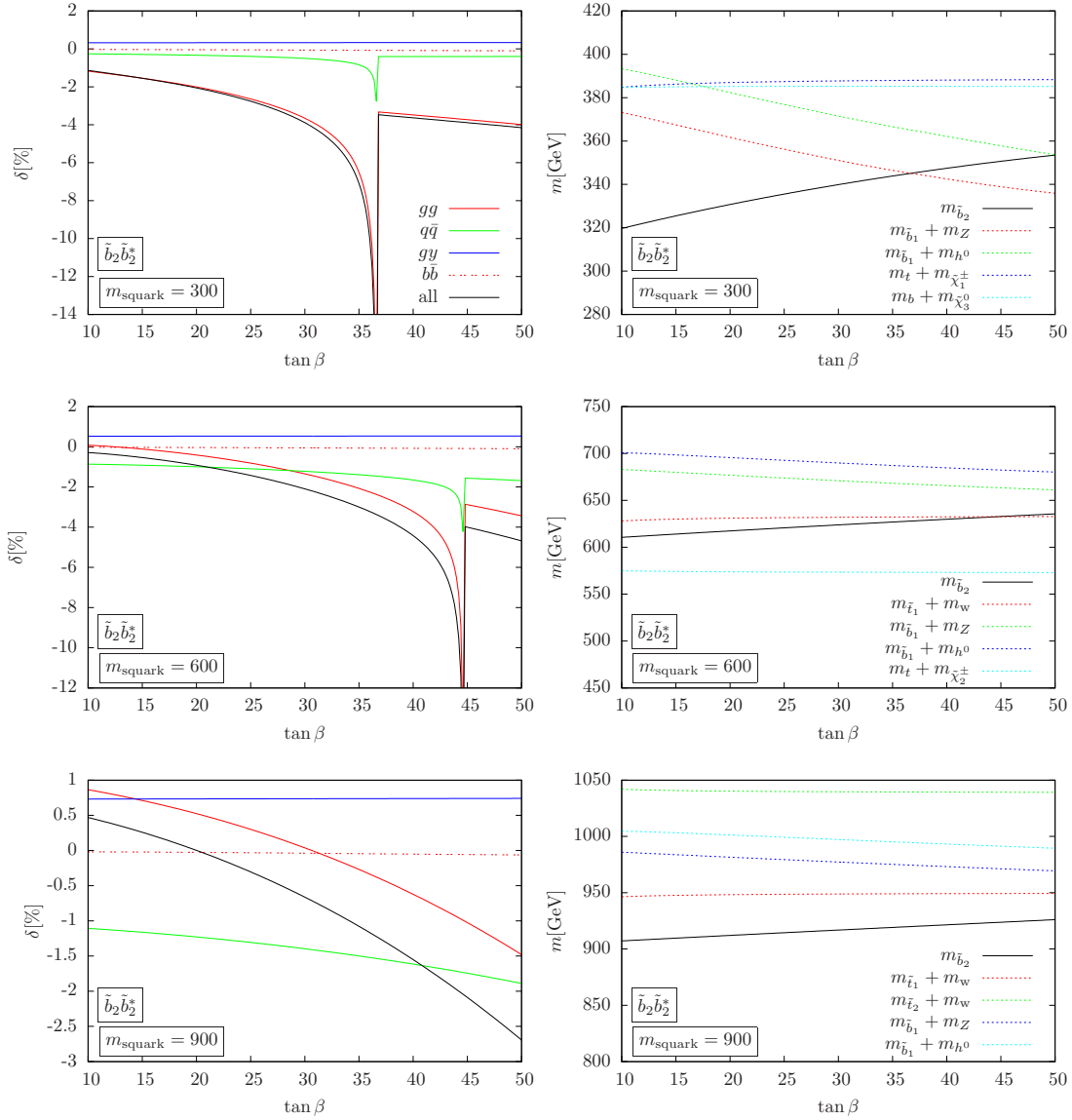
Figure 6.15: The relative yield of the EW contribution for $\tilde{b}_2\tilde{b}_2^*$ production for the various production channels as well as the combinded effect are shown on the left. The $\tan\beta$ dependence of the produced bottom-squark mass, as well as the sum of the masses of particles close to it are shown on the right. $\tan\beta$ is varied from 10 to 50.

$\tan\beta$. In the following we will distinguish between the low and the high $\tan\beta$ region, which are separated by the threshold.

The case of $\tilde{b}_1\tilde{b}_1^*$ production is shown in Figure 6.14. The EW contributions of the $q\bar{q}$ and the gg channel have substantially the same $\tan\beta$ dependence close to threshold. For $m_{\text{squark}} = 300, 600$ GeV one runs through threshold for $\tan\beta = 25.6$ and $\tan\beta = 43.0$, respectively. In the low $\tan\beta$ region the contributions from the $g\gamma$ channel cancel against the one from the $q\bar{q}$ annihilation. The overall effect of the EW contribution is below 1%
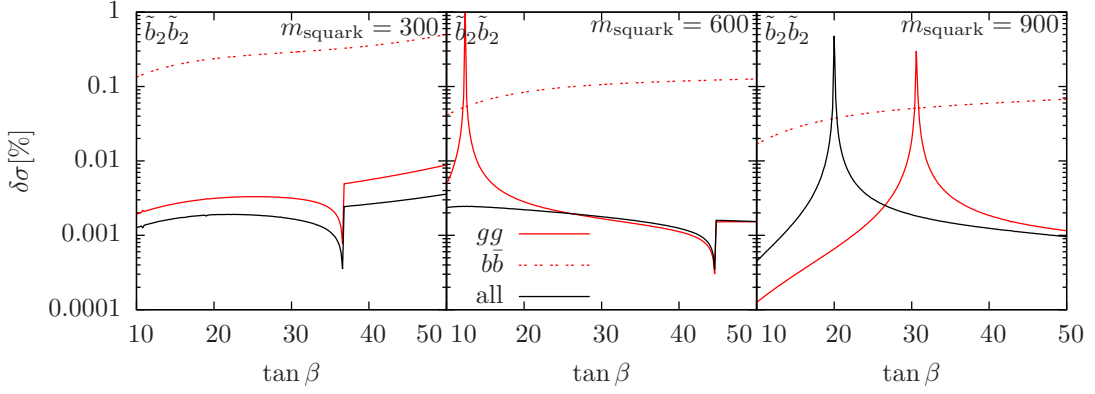
Figure 6.16: Relative difference between the EW contribution to the cross section for $\tilde{b}_2\tilde{b}_2$ production with and without enhanced Hbb couplings (black lines). The individual effect on the gg ($b\bar{b}$) channel is depicted by the red(-dotted) lines. The $q\bar{q}$ channel is not affected by the resummation and hence not shown.

of the Born cross section, with the precise value depending on the squark mass. In the high $\tan\beta$ region, the leading contributions comes from the gg channel and are only partly canceled by the other channels. The EW contributions are of the order of a few percents. However for $m_{\mathrm{squark}} = 900$ GeV and due to partial cancellations of the $g\gamma$ and $q\bar{q}$ channel one is left with EW contributions below 1%. $\tilde{b}_2\tilde{b}_2^*$ production exhibits similar features. In this case the NLO EW contributions are higher since the corrections from the gg channel are more important. They are of the order of several percents, e.g. 5% for $m_{\mathrm{squark}} = 600$ GeV and $\tan\beta \geq 45$.

It is worth to notice that the only practical effect of the resummation in the $b/\tilde{b}$ sector is to change the values of the bottom-squark masses. Indeed, we have explicitly checked that the impact of the effective Hbb couplings on the total cross section is negligible. This can be seen from Figure 6.16 where the relative difference between the electroweak contribution to the cross section, defined as

$$\delta\sigma := \frac{\Delta\sigma_{\mathrm{eff}}^{\mathrm{EW}} - \Delta\sigma_{\mathrm{no\text{-}eff}}^{\mathrm{EW}}}{\Delta\sigma_{\mathrm{eff}}^{\mathrm{EW}}}, \tag{6.36}$$

is given for $\tilde{b}_2\tilde{b}_2^*$ production. $\Delta\sigma_{\mathrm{eff}}^{\mathrm{EW}}$ and $\Delta\sigma_{\mathrm{no\text{-}eff}}^{\mathrm{EW}}$ denote the cross section with and without the effective Hbb couplings, respectively. The overall effect of the effective Yukawa coupling, given by the black line, is in most regions far below the per mille level. The positive peaks for $m_{\mathrm{squark}} = 600$ GeV and $m_{\mathrm{squark}} = 900$ GeV are due to a vanishing denominator, i.e. they correspond to zero-line transitions of $\Delta\sigma_{\mathrm{eff}}^{\mathrm{EW}}$, cf. Figure 6.15.

6.4.4 Differential Distributions

Even though the EW contributions have a small impact on the total cross section, they can become important in specific phase-space regions. In Figures 6.19 and 6.20 we consider differential distributions with respect to three different kinematical variables within the

SPS1a′ scenario for the 14 TeV LHC. The left panels show to total EW contributions to the differential cross section. The tree-level EW contribution and the NLO EW contribution of the various production channels are depicted as well. The right panels show the impact of the EW contributions relative to the tree-level QCD cross section for each production channel. In contrast to the left panels, in the right panels the $q\bar{q}$ contribution is given by the sum of the tree-level and NLO EW contributions.

Figure 6.19a refers to the transverse momentum distribution of the sbottom with highest p_T.[4] Close to threshold, i.e. in the region $p_T < 300$ GeV, the contribution of the gg channel is positive. Far from threshold, this contribution becomes negative and relatively more important. In the low p_T region the two contributions from the $q\bar{q}$ channel are different in sign, and their partial cancellation reduces the overall effect of this channel. In the high p_T region the $q\bar{q}$ channel increases its importance. The photon induced channel peaks at low p_T and it is almost proportional to the LO QCD cross section, i.e. its relative yield is constant in p_T. As expected, the $b\bar{b}$ channel is irrelevant in the whole region. The total EW contributions have a small positive yield of the order of $1 - 2\%$ in the low p_T region, while for $p_T > 500$ GeV the cross section is altered by $5 - 10\%$. It is interesting to note that a lower cut $p_{T\min}$ on the transverse momentum can significantly rise the impact of the EW contributions. For instance the cut $p_{T\min} = 320$ GeV would discard the positive yield of the gg channel in the low p_T region. As a consequence the relative yield of the EW contribution to the total cross section would become of the order of -3.2%. However, this feature is quite academic, since only the decay product of the sbottom is measured and hence it would be a quite difficult task from experimental side to perform such a cut on the p_T distribution.

The invariant mass distribution is displayed in Figure 6.19b. The EW contributions exhibit the same high energy behavior as in the case of the p_T distribution. In this energy region they alter the leading-order prediction up to 10%. The peaks in the gg channel are due to particle threshold. They correspond to resonant squarks in the vertex and box diagrams of Figure 6.5. The invariant mass corresponding to a threshold peak is directly related to the mass of the responsible squarks, namely $\tilde{b}_2$ and $\tilde{t}_2$. Since $\tilde{b}_2$ is only slightly heavier than $\tilde{b}_1$ the first peak appears directly after production threshold. Even though the threshold drives the EW contribution of the gg channel to positive values which combine with the other channels to give an overall positive contribution, the relative yield remains small in the low invariant mass region, approx. 2%. In order to study how the EW contributions to the total cross section are altered by a lower cut $M_{\text{inv,min}}$ on the invariant mass, we consider $\sigma(M_{\text{inv,min}})$ defined as the total cross section integrated from the value $M_{\text{inv,min}}$. The upper-left plot of Figure 6.17 shows the $\sigma(M_{\text{inv,min}})$ dependence on the relative yield of the EW contributions δ^{EW} defined in (6.34) together with the breakdown into the individual channels. The lower cut $M_{\text{inv,min}}$ excludes the region where the EW contributions are positive. Therefore the EW contributions decrease as $M_{\text{inv,min}}$ increases, while their relative impact increases. For instance, for $M_{\text{inv,min}} \geq 1500$ GeV the relative yield of the EW contributions δ^{EW} exceeds

---

[4]Although only sbottom-pair production is considered, different transverse momenta arise due to real radiation processes.
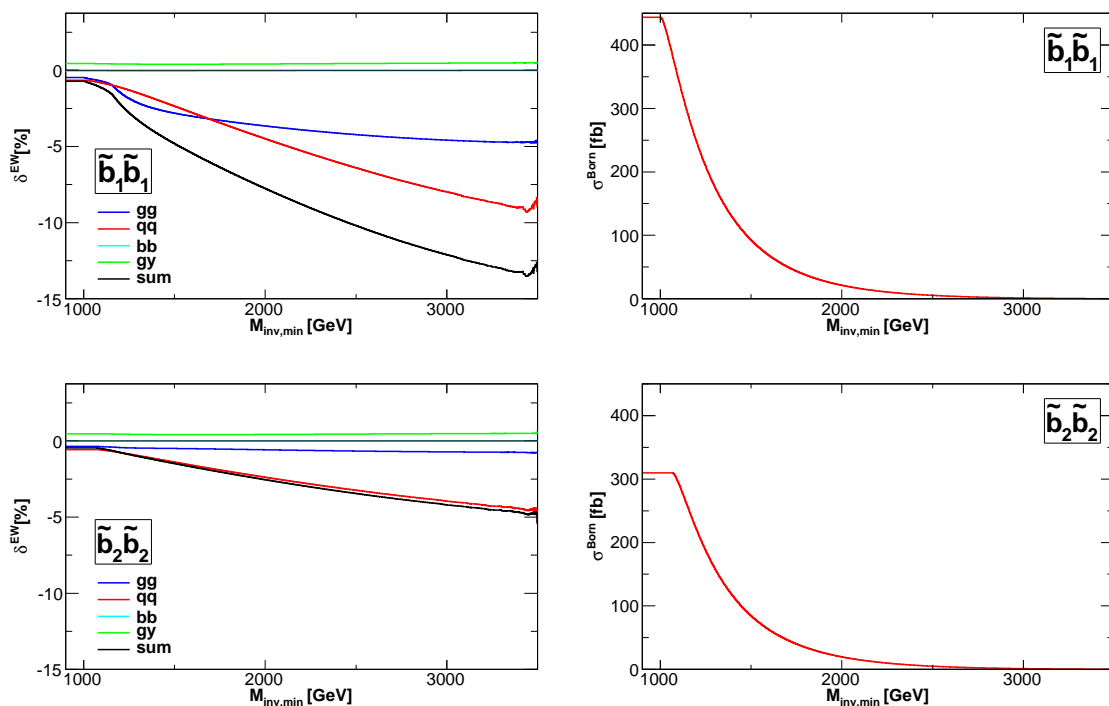
Figure 6.17: Left: Relative yield of the EW contributions for the different production channels in $\sigma(M_{\mathrm{inv,min}})$. Right: LO prediction for the same observable.

-5%. δ^{EW} is amplified by a factor of seven with respect to its value in the case of the fully inclusive cross section given by $\delta^{\mathrm{EW}} = -0.73$, cf. Table 6.3, which corresponds to the left edge of the plot. The LO cross section is reduced by a factor of five for $M_{\mathrm{inv,min}} = 1500$ GeV. This can be seen from the upper-right panel of Figure 6.17, which shows $\sigma^{\mathrm{Born}}(M_{\mathrm{inv,min}})$.

Figure 6.19c shows the pseudo-rapidity distribution, where always the squark with the higher absolute value of the pseudo-rapidity η (in the laboratory frame) is considered. The gap for zero rapidity is an artefact of this definition. The NLO EW contributions peak at $|\eta| = 1$ and dominate the EW contribution at this region. The contribution is negative for small values of η as expected from the p_T distribution, since intuitively small values of η correspond to high p_T.[5] The total effect on the LO QCD cross section is up to 2%.

Figure 6.20 shows the differential distributions for $\tilde{b}_2\tilde{b}_2^*$ production in the transverse momentum (a), in the invariant mass (b), and in the pseudo-rapidity (c). In contrast to $\tilde{b}_1\tilde{b}_1^*$ production, the threshold behavior, initiated by $\tilde{t}_2$ only, is mild and hardly visible in the transverse momentum as well as in the invariant mass distributions. The EW contribution is small, and its relative yield stays below 5%, even in the high energy region. This is expected since in the SPS1a′ scenario $\tilde{b}_2$ is mostly right handed. Interestingly, the contributions from the gg channel and the $g\gamma$ channel almost cancel in most parts of the phase-space. Therefore

---

[5]This statement gets further motivated by noticing that (in the c.m. frame) one has the relation $p_T = \frac{1}{2}\hat{s}\sin\theta$, with the scattering angle θ, cf. (4.152).
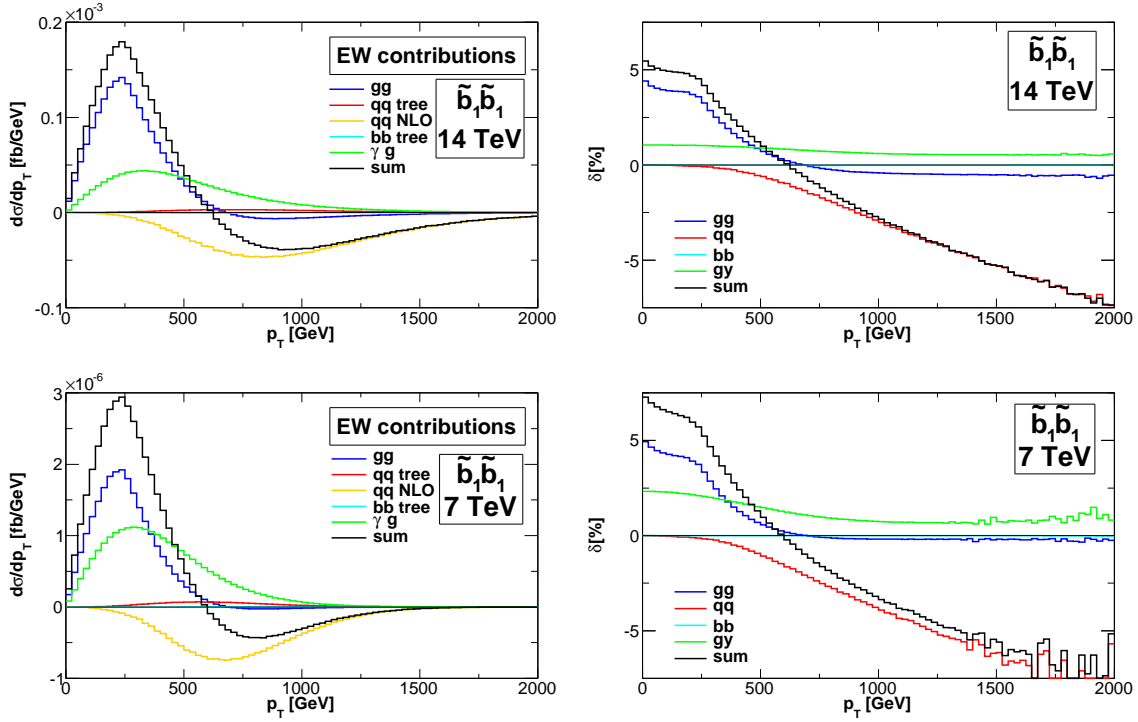
Figure 6.18: Differential transverse momentum distribution for $\tilde{b}_1\tilde{b}_1^*$ production within the SPS8 scenario for the 14 TeV (upper plots) and 7 TeV (lower plots) LHC.

the EW contributions are well approximated by the $q\bar{q}$ channel corrections especially in the hight p_T region and high M_{inv} region. The lower panels of Figure 6.17 show $\sigma(M_{\text{inv,min}})$ in the case of $\tilde{b}_2\tilde{b}_2^*$ production. In this scenario the EW contributions to $\tilde{b}_2\tilde{b}_2^*$ production can be safely neglected for each value of $M_{\text{inv,min}}$. Even in the case $M_{\text{inv,min}} = 2$ TeV the EW contributions change the Born cross section only by an amount of the order of 2%.

In Figure 6.18 we consider differential transverse mass distributions for $\tilde{b}_1\tilde{b}_1^*$ production within the SPS8 scenario for 14 TeV (upper panels) and 7 TeV (lower panels). It is worth analyzing the EW corrections to the gg channel in this scenario. The sbottom mass is heavier in the SPS8 scenario than in the SPS1a′ scenario. Therefore, the typical momentum fraction x of the initial-state gluons needed in order to be above production threshold is bigger in the SPS8 scenario than in the SPS1a′ scenario. Since the gluon PDF falls off rapidly at high x, the negative EW contributions of the gg channel in the high p_T region are strongly suppressed in the SPS8 scenario. For $\sqrt{S} = 7$ TeV the relevant x-values relevant for $\tilde{b}\tilde{b}^*$ production are even bigger and this phenomenon is enhanced. The cancellation between the positive low p_T corrections and the negative high p_T corrections is less effective. Therefore, as mentioned in Section 6.4.2, the overall (positive) gg channel contributions get relatively enhanced for $\sqrt{S} = 7$ TeV.
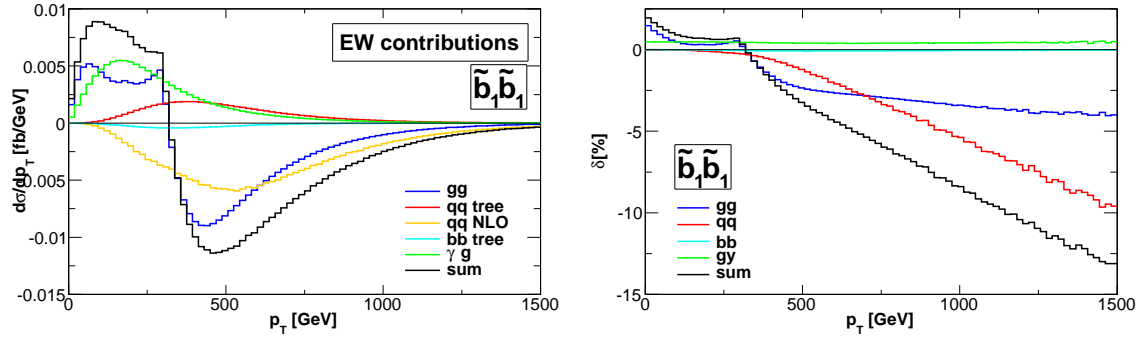
(a) p_T distribution
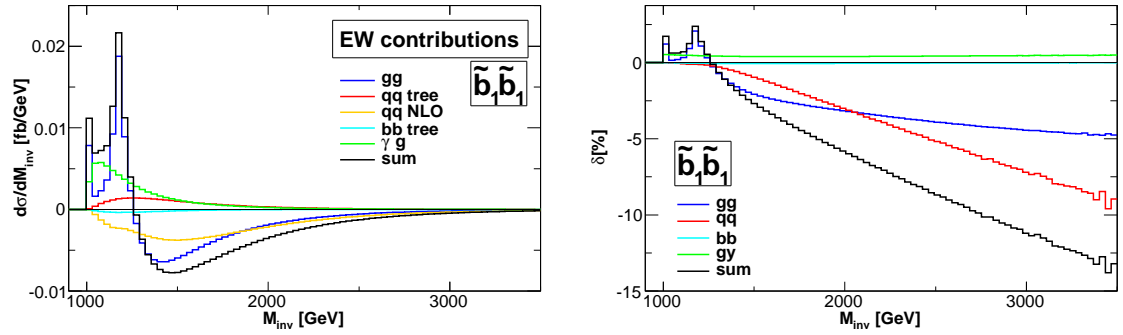
(b) M_{inv} distribution
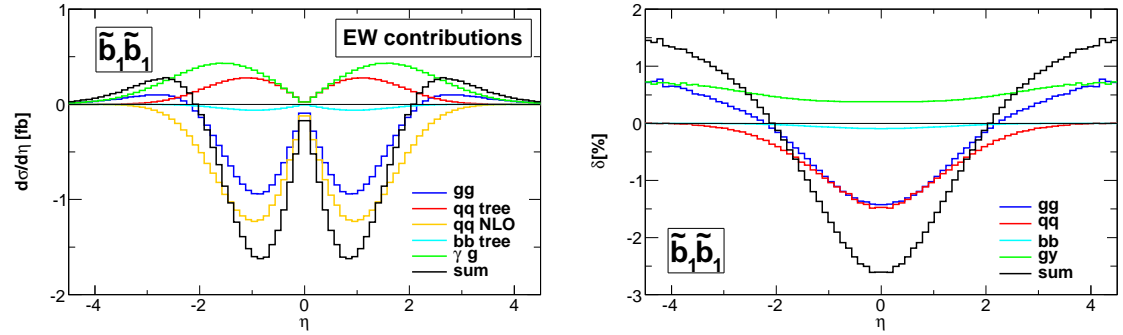
(c) η distribution

Figure 6.19: Differential distributions for the transverse momentum p_T, the in variant mass M_{inv} and the pseudo-rapidity η for $\tilde{b}_1 \tilde{b}_1^*$ production at the 14 TeV LHC within the SPS1a′ scenario. Shown are the tree-level and NLO EW cross section contributions for the various production channels (left) and the impact of the NLO EW contributions relative to the LO QCD cross section (right). In the left panels the tree-level and NLO EW contributions for the $q\bar{q}$ channel are plotted separately. In the right panels they are treated inclusively.
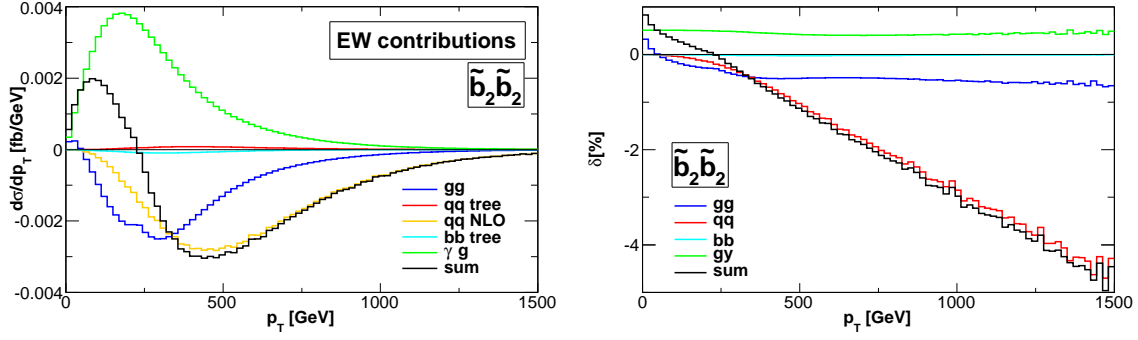
(a) p_T distribution
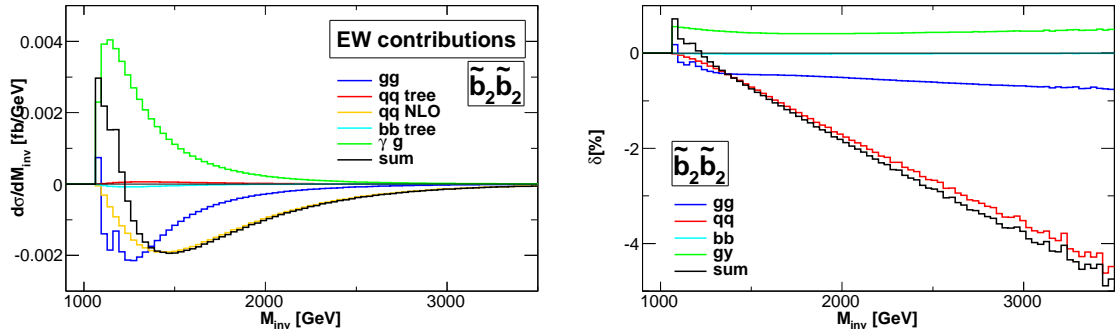
(b) M_{inv} distribution
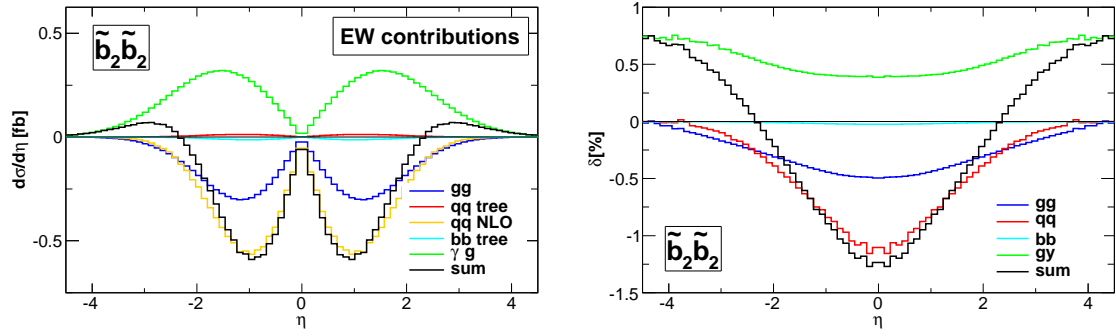
(c) η distribution

Figure 6.20: Same as Figure 6.19 but considering $\tilde{b}_2 \tilde{b}_2^*$ production.

7 Summary and Conclusions

In this thesis we have calculated the electroweak contributions up to $\mathcal{O}(\alpha_s^2\alpha)$ to squark–squark and sbottom–anti-sbottom production processes at the LHC.

With the LHC taking data the electroweak scale will be probed in detail and reveal the origin of electroweak symmetry breaking. A numerous amount of models beyond the standard model will be probed and eventually be validated or falsified.

As argued at the beginning of this thesis, supersymmetry and especially the realization via the MSSM with TeV scale SUSY particle content is an attractive extension of the SM, which has the potential to explain some of its open questions. If SUSY is realized at the TeV scale, colored SUSY particles will be produced at a high rate since their dominant production mechanism proceeds via the strong interaction. For $\mathcal{R}$-parity conserving theories as considered in this work, events involving SUSY particle production are characterized via large missing transverse energy since SUSY particles almost instantly decay into SM particles and the LSP which escapes the detector without leaving a signal. The identification of such events with the production of SUSY particles is done by comparing the experimental signatures with theoretical predictions. Contrariwise, the non-observation of such signatures can be used to derive lower SUSY mass bounds. In any case, precise theoretical predictions are needed in order to perform a reliable analysis. Hence, in addition to the NLO QCD corrections also corrections beyond one-loop have been calculated, reducing the remaining uncertainties of QCD origin down to the percent region.

Besides higher-order QCD corrections also EW contributions can give significant contributions to the cross section and are essential for a reliable prediction. In order to accomplish the same accuracy as in the QCD case, NLO EW contributions of $\mathcal{O}(\alpha_s^2\alpha)$ have been considered. These are formally of the same order than the NNLO QCD corrections. While the NLO EW corrections to stop–anti-stop, diagonal squark–anti-squark, gluino–squark and gluino–gluino production processes have been investigated in former work, we provided within this thesis the yet missing NLO EW corrections to squark–squark and sbottom–anti-sbottom production processes.

Since the EW interaction distinguishes flavor and chirality of the initial-state quarks and final-state squarks, the contributing processes are manifold and their interplay is non-trivial. In this work we have given all the technical issues needed in order to calculate the NLO EW corrections to squark–squark and sbottom–anti-sbottom production processes. Appropriate regularization procedures were presented and the renormalization constants for the relevant sectors were given in order to obtain an UV finite result. This included the renormalization of the quark, squark and gluino sector, as well as the renormalization of the strong coupling constant α_s. The complex structure of the NLO EW corrections required the renormalization constants to be evaluated at $\mathcal{O}(\alpha)$ and $\mathcal{O}(\alpha_s)$, respectively. The strong coupling constant was

defined carefully. We used its $\overline{\text{MS}}$ definition with five active flavors in order to be consistent with its definition used for the extraction of the PDFs. However, this explicitly breaks SUSY and proper symmetry restoring counterterms were taken into account. Mass singularities of photonic and gluonic origin had to be handled. They were regularized by means of mass regularization and we used the phase-space-slicing method for the cancellation of IR and collinear singularities originating from the virtual and real contribution. Remaining gluonic as well as photonic initial-state collinear singularities had to be absorbed into the definition of the PDFs.

We first applied these techniques to calculate the electroweak contributions to squark–squark and anti-squark–anti-squark production processes up to $\mathcal{O}(\alpha_s^2\alpha)$. Due to the large amount of possible final states that differ in flavor and chirality, respectively, squark–squark production consists of 36 processes and the same amount for anti-squark–anti-squark production. This and the fact that the LO process proceeds via two initial-state valence quarks, leads to a production yield that is generally higher than squark–anti-squark and can be comparable to gluino-pair production. The electroweak contributions are special for this process, since EW-mediated production channels exist already at tree-level and allow for non-trivial QCD–EW interferences which can rise the LO cross section by up to 20%. These LO QCD–EW interferences suffer from scale uncertainties and we have shown that they are considerably reduced by taking the NLO EW contributions into account. The residual scale uncertainties arise mostly from the choice of renormalization scale while the factorization scale dependence is mild at NLO EW. We performed a detailed numerical analysis for two left-handed squarks ($\tilde{q}_L\tilde{q}_L$), two right-handed squarks ($\tilde{q}_R\tilde{q}_R$), and one left-handed and one right-handed squark ($\tilde{q}_L\tilde{q}_R$), as well as for inclusive squark–squark ($\tilde{q}\tilde{q}$) production at the LHC for $\sqrt{S} = 14$ TeV. The tree-level EW contributions are largest for $\tilde{q}_L\tilde{q}_L$ production, where they are enhanced by $\mathcal{O}(\alpha_s\alpha)$ interference terms and can easily reach the 20% level. The interference contributions are suppressed for $\tilde{q}_R\tilde{q}_R$ production from the chiral couplings and vanish for $\tilde{q}_L\tilde{q}_R$ production in the limit of no L–R mixing. At NLO, partial cancellations occur among the various EW contributions. As a result, the integrated cross section is reduced by the NLO EW contributions by a few percent for most subprocesses. The interplay of tree-level and NLO EW contributions is not universal and depends sensitively on the ratio of squark and gluino masses as well as on their absolute values. The full EW contributions affect the integrated cross section for inclusive squark–squark production at the percent level (about 5% in SPS1a′ and SPS5, −1% in SPS2). In the distributions, however, the EW contributions range from −10% to +20% and even larger values for exclusive $\tilde{q}_L\tilde{q}_L$ production. Results for squark–squark production at the LHC for $\sqrt{S} = 7$ TeV were given within the SPS1a′ scenario. We found that the relative importance of the tree-level EW contributions increases by a few percent, while the relative NLO EW contributions are less important. We investigated the effect of hard real radiation processes, with the photon, gluon or quark being radiated into the central region of the detector. Such events are experimentally distinguishable from pure squark–squark production and might therefore modify the analysis if considered inclusively. We found that by excluding those event with hard non-collinear additional quarks, photons and gluons, the NLO EW corrections to the cross sections are

strongly affected and become more than twice as large as for exclusive $\tilde{q}_L\tilde{q}_L$ production.

In a next step we studied the NLO EW contributions to sbottom–anti-sbottom production processes. We recomputed the already known tree-level EW contributions from the $q\bar{q}$-annihilation and the gluon fusion channels and included the previously unknown contribution from the photon-induced channel. We presented the first complete computation of the NLO EW contributions, which together with the QCD corrections have completed the NLO analysis of the sbottom–anti-sbottom pair production process. We verified that CKM effects can be safely neglected. The production of sbottom–anti-sbottom pairs is quite involved due to the mixing between the left- and right-handed b-squarks, the renormalization of the sbottom sector, and the enhanced Yukawa couplings for large values of $\tan\beta$, with the related need of resummation. We specified the precise relation between the bottom-quark mass defined in the $\overline{\text{DR}}$ scheme and its Yukawa coupling, as well as the effective Higgs–bottom vertices with the $\tan\beta$ enhanced contributions correctly resummed to all orders. In the appendix it is shown how these resummed contributions arise in SQCD. Since the renormalization constants of the sbottom sector can obtain large finite shifts, we checked explicitly the reliability of our renormalization scheme for the scenarios considered. We performed an extensive numerical discussion for the diagonal production of two bottom-squark pairs at the LHC for $\sqrt{S} = 14$ TeV and $\sqrt{S} = 7$ TeV. The EW contributions to the total cross section were found to be strongly scenario dependent. Nevertheless, in all scenarios considered they are of the order of a few percent of the LO contribution since strong cancellations among different channels partly reduce their size. However, the EW contributions peak in different regions of phase space and hence become enhanced for reasonable kinematical cuts. For the same reason, the impact of the EW contributions is more important in differential distributions, in particular in the high energy region. Considering the invariant mass and the transverse momentum distributions for $\tilde{b}_1\tilde{b}_1$ production in the SPS1a$'$ scenario, they can even exceed the LO contribution by 10%.

This work provides an important step to the knowledge of all relevant EW contributions to squark and gluino production processes. The remaining class of processes consists of non-diagonal squark–anti-squark production, i.e. $\tilde{q}_\alpha\tilde{q}_\beta^*$ production for $\alpha \neq \beta$ and $\tilde{q}_\alpha\tilde{q}_\beta'^*$ production for $q \neq q'$. These processes can be classified in the same way as for squark–squark production. Using the methods elaborated in this work, it is a straightforward task to calculate the corresponding NLO EW corrections.

A Notation and Conventions

A.1 Metric Conventions

Elements of the four-dimensional Minkowski space are labeled by greek indices.[1] A contravariant vector has upper indices while the covanriant vector carries lower indices. They are related via the metric tensor g,

$$g^{\mu\nu} = g_{\mu\nu} = \text{diag}(1, -1, -1, -1), \tag{A.1}$$

$$x^{\mu} = g^{\mu\nu}x_{\nu}. \tag{A.2}$$

Repeated indices are understood to be implicitly summed.

A.2 Pauli and Dirac Matrices

The Pauli matrices σ^i, $i \in \{1, 2, 3\}$ are defined as

$$\sigma^1 = \begin{pmatrix} 0 & 1 \\ 1 & 0 \end{pmatrix}, \qquad \sigma^2 = \begin{pmatrix} 0 & -i \\ i & 0 \end{pmatrix}, \qquad \sigma^3 = \begin{pmatrix} 1 & 0 \\ 0 & -1 \end{pmatrix}, \tag{A.3}$$

and obey the Clifford algebra

$$\{\sigma^i, \sigma^j\} = 2\delta^{ij} \;, \tag{A.4}$$

and the Lie algebra

$$[\sigma^i, \sigma^j] = 2i\epsilon^{ijk}\sigma^k, \tag{A.5}$$

where ϵ is the total antisymmetric third rank tensor with $\epsilon^{123} = 1$. It has the following properties,

$$\begin{aligned} \epsilon^{ijk}\epsilon^{ilm} &= \delta^{jl}\delta^{km} - \delta^{jm}\delta^{kl}, \\ \epsilon^{ijk}\epsilon^{ijm} &= 2\delta^{km}, \\ \epsilon^{ijk}\epsilon^{ijk} &= 3!. \end{aligned} \tag{A.6}$$

The extended Pauli matrices σ^{μ} and $\bar{\sigma}^{\mu}$ which are defined as

$$\sigma^{\mu} = (\ , \sigma^i), \qquad\qquad \bar{\sigma}^{\mu} = (\ , -\sigma^i), \tag{A.7}$$

---

[1]As long as not stated otherwise, greek indeces run from 0 to 4 while roman indeces run from 1 to 3.

have the following properties:

$$\sigma^\mu \bar{\sigma}^\nu + \sigma^\nu \bar{\sigma}^\mu = 2g^{\mu\nu}\,,$$
$$\bar{\sigma}^\mu \sigma^\nu + \bar{\sigma}^\nu \sigma^\mu = 2g^{\mu\nu}\,,$$
$$\mathrm{Tr}(\sigma^\mu \bar{\sigma}^\nu) = 2g^{\mu\nu}, \tag{A.8}$$
$$\sigma^2 \sigma^\mu \sigma^2 = \bar{\sigma}^{\mu T},$$
$$\sigma^2 \bar{\sigma}^\mu \sigma^2 = \sigma^{\mu T}.$$

The two-dimensional spin tensors are defined as

$$\sigma^{\mu\nu} = \frac{i}{4}\left(\sigma^\mu \bar{\sigma}^\nu - \sigma^\nu \bar{\sigma}^\mu\right),$$
$$\bar{\sigma}^{\mu\nu} = \frac{i}{4}\left(\bar{\sigma}^\mu \sigma^\nu - \bar{\sigma}^\nu \sigma^\mu\right). \tag{A.9}$$

The four-dimensional Dirac matrices form a Clifford algebra,

$$\{\gamma^\mu, \gamma^\nu\} = 2g^{\mu\nu}\,. \tag{A.10}$$

γ^5 is defined as $\gamma^5 = i\gamma^0\gamma^1\gamma^2\gamma^3$ and has the properties,

$$\{\gamma^5, \gamma^\mu\} = 0, \qquad (\gamma^5)^2 = 1. \tag{A.11}$$

In the Weyl representation the Dirac matrices are given by

$$\gamma^\mu = \begin{pmatrix} 0 & \sigma^\mu \\ \bar{\sigma}^\mu & 0 \end{pmatrix}, \qquad \gamma^5 = \begin{pmatrix} & 0 \\ 0 & - \end{pmatrix}. \tag{A.12}$$

The projection operators $P_{L,R}$ are defined as

$$P_{L,R} = \frac{1}{2}(\ \pm \gamma^5). \tag{A.13}$$

A.3 Polarization Vectors

The polarization vectors $\epsilon^\mu(k, \lambda)$ for massless gauge bosons depend on the on-shell momentum k and polarization λ. They are transverse,

$$k^\mu \epsilon_\mu(k, \lambda) = 0\,, \tag{A.14}$$

and normalized according to

$$\epsilon_\mu^*(k, \lambda)\epsilon^\mu(k, \lambda') = -\delta_{\lambda\lambda'}\,. \tag{A.15}$$

There are only two physical (transverse) polarizations and the polarization sum is gauge-dependent. In the gauge $n_\mu \epsilon^\mu(k, \lambda) = 0$ with an external four vector n_μ it is given by

$$\sum_{\lambda=1}^{2} \epsilon_\mu^*(k, \lambda)\epsilon_\nu(k, \lambda) = -g_{\mu\nu} - \frac{k_\mu k_\nu}{(kn)^2}n^2 + \frac{n_\mu k_\nu + n_\nu k_\mu}{kn}\,. \tag{A.16}$$

A.4 Self-Energies

The unrenormalized self-energy is defined diagrammatically via

$$\Psi_i \quad\text{——(1 PI)——}\quad \Psi_j \quad =: \mathrm{i}\Sigma_{ij}(p).\tag{A.17}$$

In the case of Ψ being a spinor or a vector particle, it is convenient to decompose the self-energy according to its Lorentz structure:

Spinor:

$$\Sigma_{ij}(p) = \slashed{p}P_L\Sigma_{ij}^L(p^2) + \slashed{p}P_R\Sigma_{ij}^R(p^2) + P_L\Sigma_{ij}^{SL}(p^2) + P_R\Sigma_{ij}^{SR}(p^2)\,.\tag{A.18}$$

Vector:

$$\Sigma_{ij}^{\mu\nu}(p) = \Sigma_{ij}^T(p^2)\left(g^{\mu\nu} - p^\mu p^\nu\right) + \Sigma_{ij}^L(p^2)p^\mu p^\nu\,.\tag{A.19}$$

A.5 Grassmann Numbers

A Grassmann algebra $\mathcal{G}_N$ is an associative algebra that contains the unity element and N elements ξ^i that obey the following anticommutation relation:

$$\{\xi^i, \xi^j\} = 0\,.\tag{A.20}$$

From (A.20) it follows that $(\xi^I)^2 = 0$. Complex conjugation of the generators is defined via

$$(\xi^a\xi^b\ldots\xi^c)^* = \xi^c\ldots\xi^b\xi^a.\tag{A.21}$$

It follows that the generators are real since $(\xi^i)^* = \xi^i$. Elements of $\mathcal{G}_N$ are called super-numbers. They can be written with help of the basis as

$$z = c_0 + c_a\xi^a + \frac{1}{2!}c_{ab}\xi^a\xi^b + \ldots + \frac{1}{N!}c_{a_1,\ldots,a_N}\xi^{a_1}\ldots\xi^{a_N},\tag{A.22}$$

where the factors c are complex numbers, antisymmetric in their indices. Each super-number can be divided into an even and an odd part,

$$z = x + \theta.\tag{A.23}$$

x contains only terms with an even number of generators, while θ has only terms with an odd number of generators. The odd super-numbers are called Grassmann numbers and have the following properties,

$$\{\theta^A, \theta^B\} = 0, \qquad\qquad\qquad \theta\theta = 0.\tag{A.24}$$

The complex-conjugated of a Grassmann number is defined via

$$(\theta^A \theta^B \ldots \theta^C)^* = \theta^{C*} \ldots \theta^{B*} \theta^{C*}, \tag{A.25}$$

i.e. complex-conjugation equals Hermitian conjugation.

An analytic function f over the complex numbers can be continued to a function over Grassmann variables. It is defined via its Taylor series in the Grassmann numbers

$$f(q, \theta) = f_0(q) + f_A \theta^A + \frac{1}{2!} f_{AB}(q) \theta^A \theta^B + \ldots . \tag{A.26}$$

The sum breaks off for a finite number of Grassmann variables.

The differentiation with respect to a Grassmann number is defined as

$$\frac{\partial}{\partial \theta^A} \theta^B \equiv \delta_A^B, \qquad\qquad \frac{\partial}{\partial \theta^A} 1 \equiv 0 . \tag{A.27}$$

For each commutation of a Grassmann differential operator with an anti-commuting object one gets an extra factor of (-1). For the integration with respect to Grassmann variables one requires the integral to be translation invariant. One defines

$$\int \theta^B \mathrm{d}\theta^A = \delta_A^B, \qquad\qquad \int 1 \mathrm{d}\theta = 0. \tag{A.28}$$

Comparing (A.27) and (A.28) one finds that integration and differentiation with respect to Grassmann variables is the same. The differentiation with respect to Weyl spinors, whose components are Grassmann variables, cf. Section D.4, is defined as

$$\partial_A := \frac{\partial}{\partial \theta^A}, \qquad\qquad \partial^A := \frac{\partial}{\partial \theta_A}, \tag{A.29}$$

$$\bar{\partial}_{\dot{A}} := \frac{\partial}{\partial \bar{\theta}^{\dot{A}}}, \qquad\qquad \bar{\partial}^{\dot{A}} := \frac{\partial}{\partial \bar{\theta}_{\dot{A}}}. \tag{A.30}$$

With the definitions (A.27) one gets

$$\partial_A \theta^B = \delta_A^B, \qquad\qquad \partial^A \partial_B = \delta_B^A \tag{A.31}$$

$$\bar{\partial}_{\dot{A}} \bar{\theta}^{\dot{B}} = \delta_{\dot{A}}^{\dot{B}}, \qquad\qquad \bar{\partial}^{\dot{A}} \bar{\theta}_{\dot{B}} = \delta_{\dot{B}}^{\dot{A}} \tag{A.32}$$

To be consistent with the raising and lowering of indices as defined for Weyl spinors, one defines

$$\epsilon^{AB} \partial_B = -\partial^A, \qquad\qquad \partial^B \epsilon_{BA} = -\partial_A. \tag{A.33}$$

With this definitions one gets

$$\partial_A(\theta\theta) = 2\theta_A, \qquad\qquad \bar{\partial}_{\dot{A}}(\bar{\theta}\bar{\theta}) = -2\bar{\theta}_{\dot{A}}, \tag{A.34}$$

$$\partial^A \partial_A(\theta\theta) = 4, \qquad\qquad \bar{\partial}_{\dot{A}} \bar{\partial}^{\dot{A}} = 4. \tag{A.35}$$

Integration with respect to Weyl spinors is defined in the same way,

$$\int \mathrm{d}\theta_A = \frac{\partial}{\partial\theta_A} = \partial^A, \qquad\qquad \int \mathrm{d}\theta^A = \frac{\partial}{\partial\theta^A} = \partial_A, \qquad (A.36)$$

$$\int \mathrm{d}\bar\theta_{\dot A} = \frac{\partial}{\partial\bar\theta_{\dot A}} = \bar\partial^{\dot A}, \qquad\qquad \int \mathrm{d}\bar\theta^{\dot A} = \frac{\partial}{\partial\bar\theta^{\dot A}} = \bar\partial_{\dot A}. \qquad (A.37)$$

Further one defines

$$\mathrm{d}\theta^2 := \frac{1}{4}\mathrm{d}\theta^A \mathrm{d}\theta_A, \qquad\qquad \mathrm{d}\bar\theta^2 := \frac{1}{4}\mathrm{d}\bar\theta_{\dot A}\bar\theta^{\dot A}, \qquad (A.38)$$

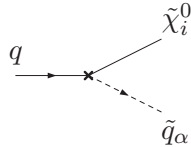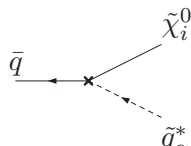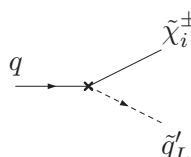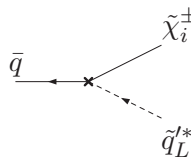$$\mathrm{d}^4\theta := \mathrm{d}\theta^2 \mathrm{d}\bar\theta^2.$$
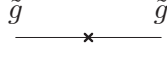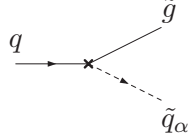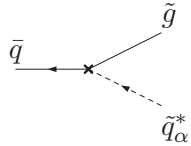
B Counterterms

In this appendix, we give the explicit expressions for the counterterm (CT) diagrams entering the NLO EW calculation to squark–squark and sbottom–anti-sbottom production processes.

$$\tilde{b}_\alpha\text{---}\times\text{---}\tilde{b}_\alpha \qquad = \qquad \mathrm{i}\left[\left(p^2 - m_{\tilde{b}_\alpha}^2\right)\delta Z_{\alpha\alpha}^{\tilde{b}} - \delta m_{\tilde{b}_\alpha}^2\right]$$

$$\begin{array}{c} g \\ g \end{array}\!\!\times\!\!\begin{array}{c}\tilde{b}_\alpha \\ \tilde{b}_\alpha\end{array} \qquad = \qquad \mathrm{i}g_s^2\left(T^{c_1}T^{c_2} + T^{c_2}T^{c_1}\right)\delta Z_{\alpha\alpha}^{\tilde{b}}g_{\mu\nu}$$

$$g\text{---}\times\!\!<\!\!\begin{array}{c}\tilde{b}_\alpha \\ \tilde{b}_\alpha\end{array} \qquad = \qquad -\mathrm{i}g_s\, T^c\, \delta Z_{\alpha\alpha}^{\tilde{b}}\left(k + k'\right)_\mu$$

$$g\text{---}\times\!\!<\!\!\begin{array}{c}q \\ \bar{q}\end{array} \qquad = \qquad -\mathrm{i}g_s\, T^c\left(\delta Z_L^q \gamma_\mu P_L + \delta Z_R^q \gamma_\mu P_R\right)$$

Table B.1: Feynman rules for the counterterms needed for sbottom–anti-sbottom production following the conventions of [161, 163]. Arrows indicate charge and fermion number flow, respectively. For Majorana particles the fermion number flow has to be considered in accordance to [178]. The counterterms enter the calculation of the NLO EW contributions via Figures 6.6 and 6.7 and the renormalization constants have to be evaluated at $\mathcal{O}(\alpha)$.

$$\tilde{g} \quad\longcross\quad \tilde{g} \qquad = \qquad \mathrm{i}\left[\left(\not{p} - m_{\tilde{g}}\right)\delta Z^{\tilde{g}} - \delta m_{\tilde{g}}\right]$$

$$q \quad\tilde{g}\;/\;\tilde{q}_\alpha \qquad = \qquad -\mathrm{i}\frac{g_s}{\sqrt{2}}T^c\left[\left(\delta Z^{\tilde{q}}_{LL} + 2\delta Z_{\hat{g}} + \delta Z_{\tilde{g}} + \delta Z^q_L\right)\delta_{aL}P_L - (L \leftrightarrow R)\right]$$

$$\bar{q} \quad\tilde{g}\;/\;\tilde{q}^*_\alpha \qquad = \qquad \mathrm{i}\frac{g_s}{\sqrt{2}}T^c\left[\left(\delta Z^{\tilde{q}}_{RR} + 2\delta Z_{\hat{g}} + \delta Z_{\tilde{g}} + \delta Z^q_R\right)\delta_{aR}P_L - (L \leftrightarrow R)\right]$$

$$q \quad\tilde{\chi}^0_i\;/\;\tilde{q}_\alpha \qquad = \qquad \mathrm{i}e\frac{1}{\sqrt{2}}\left[-\left(\frac{N^*_{i1}}{6c_{\mathrm{w}}} + I^3_q\frac{N^*_{i2}}{s_{\mathrm{w}}}\right)\left(\delta Z^{\tilde{q}}_{LL} + \delta Z^q_L\right)\delta_{\alpha L}P_L \right.$$
$$\left. + \frac{e_q N_{i1}}{c_{\mathrm{w}}}\left(\delta Z^{\tilde{q}}_{RR} + \delta Z^q_R\right)\delta_{\alpha R}P_R\right]$$

$$\bar{q} \quad\tilde{\chi}^0_i\;/\;\tilde{q}^*_\alpha \qquad = \qquad \mathrm{i}e\frac{1}{\sqrt{2}}\left[\frac{e_q N^*_{i1}}{c_{\mathrm{w}}}\left(\delta Z^{\tilde{q}}_{RR} + \delta Z^q_R\right)\delta_{\alpha R}P_L \right.$$
$$\left. - \left(\frac{N_{i1}}{6c_{\mathrm{w}}} + I^3_q\frac{N_{i2}}{s_{\mathrm{w}}}\right)\left(\delta Z^{\tilde{q}}_{LL} + \delta Z^q_L\right)\delta_{\alpha L}P_R\right]$$

$$q \quad\tilde{\chi}^\pm_i\;/\;\tilde{q}'_L \qquad = \qquad -\mathrm{i}e\frac{U^*_{i1}\delta_{qu} + V^*_{i1}\delta_{qd}}{2s_{\mathrm{w}}}\left(\delta Z^{\tilde{q}'}_{LL} + \delta Z^q_L\right)P_L$$

$$\bar{q} \quad\tilde{\chi}^\pm_i\;/\;\tilde{q}'^*_L \qquad = \qquad -\mathrm{i}e\frac{U_{i1}\delta_{qu} + V_{i1}\delta_{qd}}{2s_{\mathrm{w}}}\left(\delta Z^{\tilde{q}'}_{LL} + \delta Z^q_L\right)P_R$$

Table B.2: Feynman rules for the counterterms (CTs) needed for squark–squark production following the conventions of [161, 163]. Arrows indicate charge and fermion number flow, respectively. For Majorana particles the fermion number flow has to be considered in accordance to [178]. The counterterms appear in Figures 5.4, 5.5 and 5.6. The first three CTs enter the calculation of the NLO EW corrections via Figures 5.4 and 5.6 and the renormalization constants have to be evaluated at $\mathcal{O}(\alpha)$ and $\mathcal{O}(\alpha_s)$, respectively. The remaining CTs enter the calculation via Figure 5.5 and the renormalization constants have to be evaluated at $\mathcal{O}(\alpha)$.

C Resummation in the Bottom-Quark Sector

In this appendix, the $\tan\beta$-enhanced contributions that spoil the relation between the bottom-quark mass and its Yukawa coupling are calculated in perturbative SQCD. Further, the $\tan\beta$-enhanced loop effects to the Higgs-bottom vertices are calculated. According to [83], these corrections are correctly resummed to all orders.

C.1 Effective Bottom-Quark Propagator

All diagrams that give a contribution to the bottom self-energy at $\mathcal{O}(\alpha_s\mu\tan\beta/M_{\mathrm{SUSY}})$ are shown in Figure C.1. Higher order loop diagrams are either not enhanced by $\tan\beta$ or further suppressed by $1/M_{\mathrm{SUSY}}$.

The physical mass of the bottom quark is related to the pole of the inverse two-point vertex function Γ_{ij}. It is obtained via the Dyson summation of the diagrams in Figure C.1,

$$\frac{\mathrm{i}}{\slashed{p}-m} + \frac{\mathrm{i}}{\slashed{p}-m}\left(\mathrm{i}\Sigma(\slashed{p})\right)\frac{\mathrm{i}}{\slashed{p}-m} + \ldots = \frac{\mathrm{i}}{\slashed{p}-m}\sum\left(-\Sigma(\slashed{p})\right)\frac{1}{\slashed{p}-m} \qquad (\mathrm{C}.1)$$

$$= \frac{\mathrm{i}}{\slashed{p}-(m-\Sigma(\slashed{p}))}.$$

In the limit of vanishing external momenta, the physical mass is given by $m^{\mathrm{phys}} = m - \Sigma(0)$, with $\Sigma = -\delta m_b + \Sigma_{SE} + \Sigma_{CT}$ corresponding to diagrams (b), (c), and (d) of Figure C.1. Starting with calculating diagram (c) one finds in the limit of vanishing external momenta,

$$\begin{aligned}
\Sigma_{SE}(k) = -\frac{2}{3\pi}\alpha_s C_F \Big[& m_{\tilde{g}}\sin(\theta_{\tilde{b}})\cos(\theta_{\tilde{b}})\left(B_0(k^2, m_{\tilde{g}}^2, m_{\tilde{b}_1}^2) - B_0(k^2, m_{\tilde{g}}^2, m_{\tilde{b}_2}^2)\right) \\
& + \left(\sin^2(\theta_{\tilde{b}})P_L\slashed{k} + \cos^2(\theta_{\tilde{b}})P_R\slashed{k}\right)B_1(k^2, m_{\tilde{g}}^2, m_{\tilde{b}_2}^2) \\
& + \left(\sin^2(\theta_{\tilde{b}})P_R\slashed{k} + \cos^2(\theta_{\tilde{b}})P_L\slashed{k}\right)B_1(k^2, m_{\tilde{g}}^2, m_{\tilde{b}_1}^2)\Big]
\end{aligned} \qquad (\mathrm{C}.2)$$
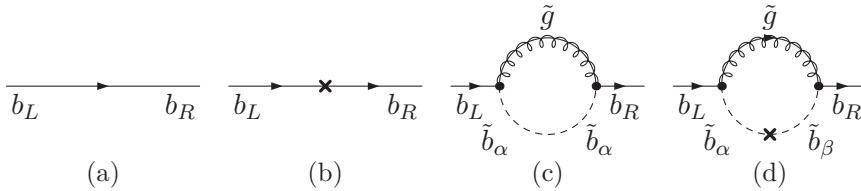
Figure C.1: One-loop bottom propagator in SQCD. The "×" in (b) and (d) denote mass counterterm insertions.

$$\overset{k \to 0}{\to} -\frac{1}{3\pi}\alpha_s C_F m_{\tilde{g}} \sin(2\theta_{\tilde{b}}) \left(B_0(0, m_{\tilde{g}}^2, m_{\tilde{b}_1}^2) - B_0(0, m_{\tilde{g}}^2, m_{\tilde{b}_2}^2) \right).$$

The loop integrals are given in the notation of [135]. Using

$$B_0(0, m_{\tilde{g}}^2, m_{\tilde{b}_1}^2) - B_0(0, m_{\tilde{g}}^2, m_{\tilde{b}_2}^2) = (m_{\tilde{b}_1}^2 - m_{\tilde{b}_2}^2)\, C_0(0,0,0, m_{\tilde{g}}^2, m_{\tilde{b}_1}^2, m_{\tilde{b}_2}^2), \tag{C.3}$$

and

$$\sin(2\theta_{\tilde{b}}) = \frac{2m_b(A_b - \mu \tan\beta)}{m_{\tilde{b}_1}^2 - m_{\tilde{b}_2}^2}, \tag{C.4}$$

one finds in the limit of large $\tan\beta$

$$\Sigma_{SE}(0) = \frac{2}{3\pi}\alpha_s\, C_F\, m_b\, m_{\tilde{g}}\, \mu\, \tan\beta\, C_0(0,0,0, m_{\tilde{g}}^2, m_{\tilde{b}_1}^2, m_{\tilde{b}_2}^2). \tag{C.5}$$

With help of the recursion relations for vacuum integrals

$$T_0^N(0,\ldots,0, m_0^2,\ldots,m_{N-1}^2) = \sum_{i=0}^{N-1} \left[\left(m_i^2 - m_{i+1}^2\right)\left(m_i^2 - m_{i+2}^2\right) \right]^{-1} A_0(m_i^2), \tag{C.6}$$

$$A_0(m^2) = m^2 \left(\Delta - \log(\frac{m^2}{\mu^2}) + 1 \right),$$

where $m_N = m_0$, $m_{N+1} = m_1$, $\ldots$, one finds

$$C_0(0,0,0, m_{\tilde{g}}^2, m_{\tilde{b}_1}^2, m_{\tilde{b}_2}^2) = -I(m_{\tilde{g}}^2, m_{\tilde{b}_1}^2, m_{\tilde{b}_2}^2), \tag{C.7}$$

leading to

$$\Sigma_{SE}(0) = -\frac{2}{3\pi}\alpha_s\, C_F\, m_b\, m_{\tilde{g}}\, \mu\, \tan\beta\, I(m_{\tilde{g}}^2, m_{\tilde{b}_1}^2, m_{\tilde{b}_2}^2) \tag{C.8}$$

$$= -m_b\, \Delta m_b\,.$$

The next step is to calculate diagram (d) of Figure C.1 which contains the mass counterterm insertion. Since the strong interaction is chirality conserving, only diagrams with $\tilde{b}_\alpha \neq \tilde{b}_\beta$ have to be taken into account. Inserting the squark-mass counterterm eq. (4.55a), one finds for vanishing external momenta

$$\Sigma_{CT}(0) = -\frac{2}{3\pi}\alpha_s\, m_{\tilde{g}}\, C_F\, (\delta\mathcal{D}_{\tilde{b}})_{12}\, \cos(2\theta)\frac{B_0(0, m_{\tilde{g}}^2, m_{\tilde{b}_1}) - B_0(0, m_{\tilde{g}}^2, m_{\tilde{b}_2})}{(m_{\tilde{b}_1} - m_{\tilde{b}_2})} \tag{C.9}$$

$$= \frac{2}{3\pi}\alpha_s\, m_{\tilde{g}}\, C_F\, (\delta\mathcal{D}_{\tilde{b}})_{12}\, \cos(2\theta)\, I(m_{\tilde{g}}^2, m_{\tilde{b}_1}^2, m_{\tilde{b}_2}^2)$$

$$= -\frac{2}{3\pi}\alpha_s\, m_{\tilde{g}}\, C_F\, \delta m_b\, \mu\, \tan\beta\, \cos^2(2\theta)\, I(m_{\tilde{g}}^2, m_{\tilde{b}_1}^2, m_{\tilde{b}_2}^2)$$

$$= -\frac{2}{3\pi}\alpha_s\, m_{\tilde{g}}\, C_F\, \delta m_b\, \mu\, \tan\beta\, I(m_{\tilde{g}}^2, m_{\tilde{b}_1}^2, m_{\tilde{b}_2}^2)\,(1 - \sin^2(2\theta))$$

$$= -\delta m_b \Delta m_b + \mathcal{O}\left(\frac{m_b}{M_{\text{SUSY}}} \right).$$
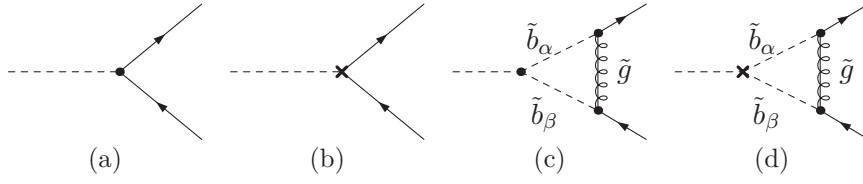
Figure C.2: $\tan\beta$ enhanced Higgs-bottom vertex diagrams.

In the third line the explicit representation of the mixing angle $U_{\tilde{b}}$ with $\det U_{\tilde{b}} = 1$ is inserted, cf.(2.54). The off-diagonal sbottom mass counterterm $(\delta\mathcal{D}_{\tilde{b}})_{12}$ is given by (cf.(4.55a))

$$(\delta\mathcal{D}_{\tilde{b}})_{12} = \delta\left(\cos(2\theta)(A_b - m_b\,\mu\,\tan\beta) + \frac{1}{2}\left((\mathcal{M}_{\tilde{b}})_{22} - (\mathcal{M}_{\tilde{b}})_{11}\right)\sin(2\theta)\right) \tag{C.10}$$
$$\to -\delta m_b\,\mu\,\tan\beta\,\cos(2\theta),$$

where only the part proportional to $(\mu\,\tan\beta)$ is taken and only δm_b has SQCD contributions.

Altogether, one gets for the physical bottom-quark mass

$$m_b^{\text{phys}} = m_b + \delta m_b + m_b\Delta m_b + \delta m_b\Delta m_b \tag{C.11}$$
$$= (m_b + \delta m_b)\left(1 + \Delta m_b\right)$$

It follows that the proper relation between the Yukawa coupling and the mass parameter can be taken into account by replacing the bare Yukawa coupling $h_b^0\,v/\sqrt{2} = m_b^0 = m_b + \delta m_b$ in the Lagrangian by an effective coupling:

$$\frac{h_b^0\,v}{\sqrt{2}} = \frac{h_b\,v + \delta h_b\,v}{\sqrt{2}} = m_b + \delta m_b \tag{C.12}$$
$$= \frac{m_b^{\text{phys}}}{1 + \Delta m_b} \tag{C.13}$$

C.2 Effective Hbb Vertices

In addition to the $\tan\beta$-enhanced corrections to the effective bottom-quark mass, one also has $\tan\beta$-enhanced corrections to the Higgs–bottom vertices which arise due to the diagrams depicted in Figure C.2. Taking these diagrams into account all $\tan\beta$-enhanced contributions are correctly resummed to all orders in perturbation theory. In the following we calculate these couplings for the neutral Higgs sector and especially show the cancellation of the resummed terms in the neutral Goldstone sector.

$h^0 b\bar{b}$-Vertex

We denote the tree-level coupling by $\Gamma_{\text{tree}}^{h^0 bb}$. It is given by

$$\Gamma_{\text{tree}}^{h^0 bb} = -i\frac{e\,m_b\sin\alpha}{2\,m_W\cos\beta\sin\theta_{\text{w}}}, \tag{C.14}$$

while the tree-level diagram containing the counterterm is given by

$$\Gamma^{h^0bb}_{\text{tree,CT}} = \frac{\delta m_b}{m_b}\Gamma^{h^0bb}_{\text{tree}}. \tag{C.15}$$

For the one-loop contribution, Figure C.2c only diagrams with $\tilde{b}_\alpha \neq \tilde{b}_\beta$ have to be taken into account, since the gluino coupling is chirality conserving. For vanishing external momenta one finds

$$\begin{aligned}
\Gamma^{h^0b\bar{b}}_{1-\text{loop}} &= -i\frac{\alpha_s\, e\, m_{\tilde{g}} C_0(0,0,0,m_{\tilde{g}}^2,m_{\tilde{b}_1}^2,m_{\tilde{b}_2}^2)}{18\pi c_{\text{w}} s_{\text{w}} M_W \cos\beta}\cos^2(2\theta_{\text{w}}) \times \\
&\quad (6c_{\text{w}}m_b(A_b\sin\alpha + \mu\cos\alpha) + \cos\beta\, M_W M_Z \sin(\alpha+\beta)(3 - 4\sin^2\theta_{\text{w}})\tan(2\theta_{\text{w}})) \\
&= \Gamma^{h^0b\bar{b}}_{\text{tree}}\frac{\alpha_s m_{\tilde{g}} I(,m_{\tilde{g}}^2,m_{\tilde{b}_1}^2,m_{\tilde{b}_2}^2)}{18\pi c_{\text{w}} m_b \sin\alpha}(12c_{\text{w}}m_b(\sin^2(2\theta_{\text{w}}) - 1)(\sin\alpha A_b + \mu\cos\alpha) \\
&\quad\quad + \cos\beta M_W M_Z \sin(\alpha+\beta)(4\sin^2\theta_{\text{w}} - 3)\sin(4\theta_{\text{w}})) \\
&= -\Gamma^{h^0b\bar{b}}_{\text{tree}}\frac{\Delta m_b(A_b\sin\alpha + \mu\cos\alpha)}{\mu\sin\alpha\tan\beta} \\
&= -\Gamma^{h^0b\bar{b}}_{\text{tree}}\frac{\Delta m_b}{\tan\alpha\tan\beta}, \tag{C.16}
\end{aligned}$$

where we neglect terms that are either suppressed via m_b or $1/M_{\text{SUSY}}$, or are not $\tan\beta$ enhanced. For the one-loop diagram containing the counterterm, Figure C.2d, one finds

$$\Gamma^{h^0b\bar{b}}_{1-\text{loop,CT}} = \frac{\delta m_b}{m_b}\Gamma^{h^0b\bar{b}}_{1-\text{loop}}. \tag{C.17}$$

Altogether, the effective $h^0b\bar{b}$ coupling is given by

$$\begin{aligned}
\Gamma^{h^0b\bar{b}}_{\text{eff}} &= \Gamma^{h^0b\bar{b}}_{\text{tree}} + \frac{\delta m_b}{m_b}\Gamma^{h^0b\bar{b}}_{\text{tree,CT}} + \Gamma^{h^0b\bar{b}}_{1-\text{loop}} + \frac{\delta m_b}{m_b}\Gamma^{h^0b\bar{b}}_{1-\text{loop,CT}} \\
&= \left(1 + \frac{\delta m_b}{m_b}\right)\left(1 - \frac{\Delta m_b}{\tan\alpha\tan\beta}\right)\Gamma^{h^0b\bar{b}}_{\text{tree}} \\
&= \frac{\Gamma^{h^0b\bar{b}}_{\text{tree}}}{1 + \delta m_b}\left(1 - \frac{\Delta m_b}{\tan\alpha\tan\beta}\right). \tag{C.18}
\end{aligned}$$

$H^0b\bar{b}$-Vertex

The tree-level coupling $\Gamma^{H^0b\bar{b}}_{\text{tree}}$ is given by

$$\Gamma^{H^0b\bar{b}}_{\text{tree}} = i\frac{e\, m_b \cos\alpha}{2\, M_W \cos\beta\sin\theta_{\text{w}}}. \tag{C.19}$$

Again the tree-level counterterm diagram is related to the tree-level coupling via a factor $\delta m_b/m_b$

$$\Gamma^{H^0b\bar{b}}_{\text{tree,CT}} = \frac{\delta m_b}{m_b}\Gamma^{H^0b\bar{b}}_{\text{tree}}. \tag{C.20}$$

Calculating the one-loop diagram, Figure C.2c, for $\tilde{b}_\alpha \neq \tilde{b}_\beta$ and vanishing external momenta, one gets

$$
\begin{aligned}
\Gamma^{H^0 b\bar{b}}_{1-\text{loop}} &= -i \frac{\alpha_s e m_{\tilde{g}} \cos^2(2\theta_{\text{w}}) C_0(0,0,0,m_{\tilde{g}}^2, m_{\tilde{b}_1}^2, m_{\tilde{b}_2}^2)}{18\pi s_{\text{w}} c_{\text{w}} M_W \cos\beta} \times \Big(6c_{\text{w}} m_b(\mu\sin\alpha - A_b\cos\alpha) \\
&\quad + \cos(\alpha+\beta) M_W M_Z \cos\beta(4\sin^2\theta_{\text{w}} - 3)\tan(2\theta_{\text{w}}) \Big) \\
&= \Gamma^{H^0 b\bar{b}}_{\text{tree}} \Delta m_b \left(1 - \sin(2\theta_{\text{w}}) \right) \left(\frac{\tan\alpha}{\tan\beta} - \frac{A_b}{\mu\tan\beta} \right) \\
&\quad + \Gamma^{H^0 b\bar{b}}_{\text{tree}} \Delta m_b \frac{\cos(\alpha+\beta) M_W M_Z \cos\beta(4\sin^2\theta_{\text{w}} - 3)\sin(4\theta_{\text{w}})}{12\cos\alpha c_{\text{w}} m_b \mu\tan\beta} \\
&= \Gamma^{H^0 b\bar{b}}_{\text{tree}} \Delta m_b \frac{\tan\alpha}{\tan\beta} + \mathcal{O}\left(\frac{1}{\tan\beta} \right) + \mathcal{O}\left(\frac{m_b}{M_{\text{SUSY}}} \right).
\end{aligned}
\tag{C.21}
$$

The one-loop counterterm diagram is again related via

$$
\Gamma^{H^0 b\bar{b}}_{1-\text{loop},\text{CT}} = \frac{\delta m_b}{m_b} \Gamma^{H^0 b\bar{b}}_{1-\text{loop}},
\tag{C.22}
$$

so that altogether one finds

$$
\begin{aligned}
\Gamma^{H^0 b\bar{b}}_{\text{eff}} &= \Gamma^{H^0 b\bar{b}}_{\text{tree}} + \frac{\delta m_b}{m_b} \Gamma^{H^0 b\bar{b}}_{\text{tree},\text{CT}} + \Gamma^{H^0 b\bar{b}}_{1-\text{loop}} + \frac{\delta m_b}{m_b} \Gamma^{H^0 b\bar{b}}_{1-\text{loop},\text{CT}} \\
&= \frac{\Gamma^{H^0 b\bar{b}}_{\text{tree}}}{1 + \Delta m_b} \left(1 + \Delta m_b \frac{\tan\alpha}{\tan\beta} \right).
\end{aligned}
\tag{C.23}
$$

$Ab\bar{b}$-Vertex

The tree-level $Ab\bar{b}$ coupling is given by

$$
\Gamma^{Ab\bar{b}}_{\text{tree}} = \frac{e\, m_b \tan\beta}{2\, M_W s_{\text{w}}}(P_L - P_R),
\tag{C.24}
$$

with the projectors P_L and P_R for left- and right-handed particles, respectively. At one-loop one finds with $\tilde{b}_\alpha \neq \tilde{b}_\beta$ and vanishing external momenta

$$
\begin{aligned}
\Gamma^{Ab\bar{b}}_{1-\text{loop}} &= \frac{\alpha_s e\, m_b\, m_{\tilde{g}}(A_b \tan\beta + \mu)}{3\,\pi\, M_W s_{\text{w}}} C_0(0,0,0,m_{\tilde{g}}^2, m_{\tilde{b}_1}^2, m_{\tilde{b}_2}^2)(P_L - P_R) \\
&= -\Delta m_b \Gamma^{Ab\bar{b}}_{\text{tree}} \left(\frac{A_b}{\mu\tan\beta} + \frac{1}{\tan^2\beta} \right) \\
&= 0 + \mathcal{O}\left(\frac{1}{\tan\beta} \right),
\end{aligned}
\tag{C.25}
$$

i.e. there is no extra enhancement factor of $\mathcal{O}(1)$ owing to the one-loop vertex corrections. Hence, adding the contributions of the diagrams (a)$-$(d) of Figure C.2, one gets

$$
\begin{aligned}
\Gamma^{Ab\bar{b}}_{\text{eff}} &= \Gamma^{Ab\bar{b}}_{\text{tree}} + \frac{\delta m_b}{m_b} \Gamma^{Ab\bar{b}}_{\text{tree},\text{CT}} + \Gamma^{Ab\bar{b}}_{1-\text{loop}} + \frac{\delta m_b}{m_b} \Gamma^{Ab\bar{b}}_{1-\text{loop},\text{CT}} \\
&= \frac{\Gamma^{Ab\bar{b}}_{\text{tree}}}{1 + \Delta m_b}.
\end{aligned}
\tag{C.26}
$$

$G^0 b\bar{b}$-Vertex

The coupling of the neutral Golstone boson to fermions is closely related to the Z-boson coupling to fermions and specific tree-level relations have to be fulfilled. Changing the $G^0 b\bar{b}$-coupling can give rise to gauge-symmetry violation. Fortunately, by taking consistently all $\tan\beta$ enhanced corrections into account, the enhancement factors cancel and one is left with the tree-level coupling $\Gamma_{\text{tree}}^{G^0 b\bar{b}}$,

$$\Gamma_{\text{tree}}^{G^0 b\bar{b}} = -\frac{e\, m_b}{2\, M_W s_{\text{w}}}(P_L - P_R). \tag{C.27}$$

The one-loop correction yields for $\tilde{b}_\alpha \neq \tilde{b}_\beta$ and vanishing external momenta

$$
\begin{aligned}
\Gamma_{1-\text{loop}}^{G^0 b\bar{b}} &= -\frac{\alpha_s\, e\, m_b\, m_{\tilde{g}}(A_b - \mu \tan\beta)}{3\,\pi\, M_W s_{\text{w}}} C_0(0,0,0,m_{\tilde{g}}, m_{\tilde{b}_1}^2, m_{\tilde{b}_2}^2)(P_L - P_R) \\
&= \Delta m_b \Gamma_{\text{tree}}^{G^0 b\bar{b}} \left(1 - \frac{A_b}{\mu \tan\beta}\right) \\
&= \Delta m_b \Gamma_{\text{tree}}^{G^0 b\bar{b}} + \mathcal{O}\left(\frac{1}{\tan\beta}\right),
\end{aligned}
\tag{C.28}
$$

so that adding all contributions yields

$$
\begin{aligned}
\Gamma_{\text{eff}}^{G^0 b\bar{b}} &= \Gamma_{\text{tree}}^{G^0 b\bar{b}} + \frac{\delta m_b}{m_b}\Gamma_{\text{tree,CT}}^{G^0 b\bar{b}} + \Gamma_{1-\text{loop}}^{G^0 b\bar{b}} + \frac{\delta m_b}{m_b}\Gamma_{1-\text{loop,CT}}^{G^0 b\bar{b}} \\
&= \frac{\Gamma_{\text{tree}}^{G^0 b\bar{b}}}{1 + \Delta m_b}(1 + \Delta m_b) \\
&= \Gamma_{\text{tree}}^{G^0 b\bar{b}}.
\end{aligned}
\tag{C.29}
$$

D Supersymmetry

In this appendix the technical issues needed in order to construct supersymmetric theories are given. First of all, we give an overview over general symmetry transformations and representations of symmetry generators. Afterwards, in Section D.2 the generators of the Poincaré group are derived. From this we construct the irreducible representations of the homogeneous Lorentz group using the Weyl formalism. It is shown how these objects can be used in order to construct Lorentz-invariant quantities. After introducing the concept of graded Lie algebras at the beginning of Section D.5, the supersymmetry algebra is written down in the general case. With help of the superfield formalism, introduced in Section D.6, it is shown how one can construct supersymmetric gauge theories for $N = 1$ supersymmetry.

D.1 Symmetry Transformations

D.1.1 Noether's Theorem

Noether's theorem (due to Noether (1918) in the classical field case) claims that if a Lagrangian is invariant under a continuous transformation, then there will be an associated symmetry current. The volume integral of the $\mu = 0$ component of the symmetry current is a symmetry operator, i.e. it is constant in time.

Consider a Lagrangian $\mathcal{L}$ depending on the fields ϕ_i. $\mathcal{L}(\phi_i)$ shall be invariant under a continuous symmetry transformations $\phi_i \to \phi_i'$,

$$\mathcal{L}(\phi_i') = \mathcal{L}(\phi_i). \tag{D.1}$$

An infinitesimal transformation can be written as,

$$\phi_i' = \phi_i + \delta\phi_i \,. \tag{D.2}$$

Since $\mathcal{L}$ is invariant under this transformation, one finds for the variation $\delta\mathcal{L}$,

$$0 = \delta\mathcal{L} = \frac{\partial\mathcal{L}}{\partial(\partial_\mu\phi_i)}\delta(\partial_\mu\phi_i) + \frac{\partial\mathcal{L}}{\partial\phi_i}\delta\phi_i \,. \tag{D.3}$$

Using the Euler–Lagrange equations,

$$0 = \frac{\partial\mathcal{L}}{\partial\phi_i} - \partial_\mu\left(\frac{\partial\mathcal{L}}{\partial(\partial_\mu\phi_i)}\right), \tag{D.4}$$

and the fact that $\delta(\partial_\mu\phi_i) = \partial_\mu\delta\phi_i$ one finds

$$0 = \partial_\mu\left[\frac{\partial\mathcal{L}}{\partial(\partial_\mu\phi_i)}\delta\phi_i\right] \equiv \epsilon\partial_\mu j^\mu, \tag{D.5}$$

where ϵ is some expansion parameter for the symmetry transformation. This defines a conserved symmetry current j^μ,

$$j^\mu = \frac{dj^0}{dt} + \vec{\nabla}\vec{j} = 0. \tag{D.6}$$

Performing an integration over the whole space yields

$$\frac{d}{dt}\int_V d^3x j^0 + \int_V d^3x \vec{\nabla} \cdot \vec{j} = 0 \tag{D.7}$$

$$\frac{d}{dt}\int_V d^3x j^0 + \int_{S\to\infty} d\vec{S} \cdot \vec{j} = 0 \tag{D.8}$$

$$\Rightarrow \frac{d}{dt}\underbrace{\int_V d^3x j^0}_{\equiv \mathcal{J}} = 0, \tag{D.9}$$

i.e. the volume integral of the $\mu = 0$ component of a symmetry current $\mathcal{J}$, is a symmetry operator.

D.1.2 Relation Between Symmetry Generators and Symmetry Operators

In the following, we show the relation between the generators of a symmetry group $\hat{T}$ and the corresponding symmetry operators T which are a field theoretical representation, i.e. they are themselves quantum operators. The continuous symmetry transformation on the fields that leaves the theory invariant, can be written in the form

$$\phi' = S(\alpha)\phi = \exp[-i\alpha\hat{T}]\phi. \tag{D.10}$$

Since ϕ and ϕ' obey the same (anti)commutation relations, they have to be related by a unitary transformation

$$\phi^\dagger = U(\alpha)\,\phi\,U^\dagger(\alpha), \tag{D.11}$$

with

$$U = \exp[i\alpha T]. \tag{D.12}$$

It is important to notice that the Ts are quantum field operators (and therefore different to $\hat{T}$, which are the generators of a symmetry group). For an infinitesimal transformation one gets,

$$\begin{aligned}
\phi' &= \phi + \delta_\epsilon \phi \\
&\overset{(D.11)}{=} (1 + i\epsilon T)\phi(1 - i\epsilon T) \\
&= \phi + i\epsilon[T, \phi] \tag{D.13} \\
&\overset{(D.10)}{=} (1 - i\epsilon\hat{T})\phi \\
&= \phi + i\epsilon(-\hat{T}\phi). \tag{D.14}
\end{aligned}$$

Comparing (D.13) and (D.14), one finds

$$[T, \phi] = -\hat{T}\phi. \tag{D.15}$$

For quantum mechanical fields that obey the canonical equal-time (anti)commutation relations

$$\left[\phi(\vec{x}, t), \frac{\partial \mathcal{L}}{\partial(\partial_0 \phi)}(\vec{y}, t)\right] = \mathrm{i}\delta^3(\vec{x} - \vec{y}), \tag{D.16}$$

one can easily show that the symmetry operator T in (D.15) is given by the conserved Noether charge $\mathcal{J}$ introduced in (D.9). The symmetry generators of a continuous group, especially Lie groups, are specified by their algebra, the Lie algebra. The Ts are a field-theoretical representation of the symmetry generators if they obey the same commutation relations than the $\hat{T}$,

$$[\hat{T}_i, \hat{T}_j] = \mathrm{i}f_{ijk}\hat{T}_k. \tag{D.17}$$

To find the commutation relations of the T_i, consider the difference of two infinitesimal transformations, $(\delta_{\epsilon_i}\delta_{\epsilon_j} - \delta_{\epsilon_j}\delta_{\epsilon_i})\phi$, with

$$\delta_{\epsilon_i}\phi = -\mathrm{i}\epsilon\hat{T}_i\phi \tag{D.18}$$

$$= \mathrm{i}\epsilon_i[T_i, \phi]. \tag{D.19}$$

Using the identity (D.18) one finds,

$$\begin{aligned}
\delta_{\epsilon_i}\delta_{\epsilon_j}\phi &= \delta_{\epsilon_i}(-\mathrm{i}\epsilon_j\hat{T}_j)\phi = (-\mathrm{i}\epsilon_j\hat{T}_j)(-\mathrm{i}\epsilon_i\hat{T}_i)\phi \\
&= -\epsilon_i\epsilon_j\hat{T}_j\hat{T}_i\phi \\
\Rightarrow (\delta_{\epsilon_i}\delta_{\epsilon_j} - \delta_{\epsilon_j}\delta_{\epsilon_i})\phi &= \epsilon_i\epsilon_j[\hat{T}_i, \hat{T}_j]\phi \\
&= \epsilon_i\epsilon_j\,\mathrm{i}\sum_k f_{ijk}\hat{T}_k \\
&\stackrel{(D.15)}{=} -\mathrm{i}\epsilon_i\epsilon_j\sum_k f_{ijk}[T_k, \phi] \\
&= -\mathrm{i}\epsilon_i\epsilon_j\sum_k [f_{ijk}T_k, \phi].
\end{aligned} \tag{D.20}$$

In the same way, by using the identity (D.19), one gets

$$\begin{aligned}
\delta_{\epsilon_i}\delta_{\epsilon_j}\phi &= \delta_{\epsilon_i}\,\mathrm{i}\epsilon_j[T_j, \phi] = \mathrm{i}\epsilon_j\,\mathrm{i}\epsilon_i[T_i, [T_j, \phi]] \\
&= -\epsilon_i\epsilon_j[T_i, [T_j, \phi]] \\
\Rightarrow (\delta_{\epsilon_i}\delta_{\epsilon_j} - \delta_{\epsilon_j}\delta_{\epsilon_i})\phi &= -\epsilon_i\epsilon_j\left([T_i, [T_j, \phi]] - [T_j, [T_i, \phi]]\right) \\
&= -\epsilon_i\epsilon_j[[T_i, T_j], \phi],
\end{aligned} \tag{D.21}$$

where in the last line the Jacobi identity was exploited. Comparing (D.20) and (D.21) one finally finds that

$$[T_i, T_j] = \mathrm{i}f_{ijk}T_j, \tag{D.22}$$

which proves that the T_is are a field theoretical representation of the symmetry generators.

D.2 Poincaré Group

D.2.1 Lorentz Group

A point in spacetime is characterized by a four-vector in Minkowski space

$$x^\mu = \left(x^0, x^1, x^2, x^3\right) = (ct, \vec{x}). \tag{D.23}$$

The scalar product of two vectors is defined via the metric tensor g

$$x \cdot y = x^\mu g_{\mu\nu} y^\nu, \qquad\qquad g_{\mu\nu} = g^{\mu\nu} = \mathrm{diag}(1, -1, -1, -1). \tag{D.24}$$

If not stated differently, repeated indices are always understood to be summed over (Einsteins sum convention). Four-vectors with upper indices are called contravariant. Contracting them with the metric tensor one gets the covariant components,

$$x_\mu = g_{\mu\nu} x^\nu. \tag{D.25}$$

Lorentz transformations are linear transformations on the Minkowski space that leave the scalar product invariant, i.e. rotations on the Minkowski space,

$$x^\mu g_{\mu\nu} x^\nu = x'^\mu g_{\mu\nu} x'^\nu. \tag{D.26}$$

Writing the Lorentz transformation on contravariant vectors as

$$x^\mu \to x'^\mu = \Lambda^\mu{}_\nu x^\nu, \tag{D.27}$$

with a constant matrix Λ and inserting this expression in (D.26), one finds that Λ leaves the metric invariant,

$$g_{\mu\nu} = \Lambda^\rho{}_\mu \Lambda^\sigma{}_\nu g_{\rho\sigma}. \tag{D.28}$$

The Lorentz transformation for covariant vectors is given through $\Lambda_\mu{}^\nu = (\Lambda^{-1})^\mu{}_\nu$

$$x_\mu \to \Lambda_\mu{}^\nu x_\nu. \tag{D.29}$$

The contra- and covariant differentiation operators are given by

$$\partial_\mu \equiv \left(\frac{\partial}{\partial x^\mu}\right), \qquad \partial^\mu \equiv \left(\frac{\partial}{\partial x_\mu}\right). \tag{D.30}$$

The transformation properties for the differentiation operators are easily obtained by noticing that from (D.27) it follows that

$$\Lambda^\mu{}_\nu = \frac{\partial x'^\mu}{\partial x^\nu}, \tag{D.31}$$

and using the chain rule for partial differentiation.

The manifold of the Lorentz group has four components, which are not simply connected. They can be classified by the determinant of Λ, $\det|\Lambda| = \pm 1$, and the sign of $\Lambda^0{}_0$. The one with $\det \Lambda = 1$ and $\Lambda^0{}_0 > 0$ preserves orientation and the direction of time and is called proper, orthochronous Lorentz group, or restricted Lorentz group. It consists of all Lorentz transformations which can be connected to the identity by a continuous curve lying in the group.

D.2.2 Poincaré Group

Poincaré transformations are transformations in Minkowski space that are constituted by Lorentz transformations $\Lambda^\mu{}_\nu$ and translations a_μ,

$$x^\mu \to x'^\mu = \Lambda^\mu{}_\nu x^\nu + a^\mu. \tag{D.32}$$

While under Lorentz transformations the scalar product of four-vectors is invariant, only distances (i.e. $(x-y)^2$) are invariant under Poincaré transformations. Ordinary Lorentz transformations are often referred to as homogeneous Lorentz transformations, and Poincaré transformations are also called inhomogeneous Lorentz transformations. Performing two successive transformations,

$$x^\mu \overset{(\Lambda,a)}{\to} x'^\mu \overset{(\bar\Lambda,\bar a)}{\to} x''^\mu$$
$$x''^\mu = \bar\Lambda^\mu{}_\rho x'^\rho + \bar a^\mu = \bar\Lambda^\mu{}_\rho \Lambda^\rho{}_\nu x^\nu + \bar\Lambda^\mu{}_\rho a^\rho + \bar a^\mu,$$

one finds that Poincaré transformations have to satisfy

$$(\bar\Lambda, \bar a) \circ (\Lambda, a) = (\bar\Lambda\Lambda, \bar\Lambda a + \bar a). \tag{D.33}$$

From this, one can read off the inverse element and the one element,

$$(\Lambda, a)^{-1} = (\Lambda^{-1}, -\Lambda^{-1} a), \tag{D.34}$$
$$= (1, 0). \tag{D.35}$$

To get the Lie algebra of the proper, orthochronous Poincaré group, consider a representation $S(\Lambda, a)$ for an arbitrary but fixed representation space. For infinitesimal transformations,

$$\Lambda^\mu{}_\nu = g^\mu{}_\nu + \omega^\mu{}_\nu, \qquad a^\mu = \epsilon^\mu, \tag{D.36}$$

S can be expanded to first order in ϵ and ω,

$$S(1 + \omega, \epsilon) = 1 - \frac{1}{2}\mathrm{i}\,\omega_{\mu\nu}\hat{J}^{\mu\nu} - \mathrm{i}\,\epsilon_\mu\,\hat{P}^\mu. \tag{D.37}$$

By considering successive transformations and using the multiplication rule (D.33), one obtains the Lie algebra of the Poincaré group,

$$\begin{aligned}
&[\hat{P}^\mu, \hat{P}^\nu] = 0, \\
&[\hat{P}^\mu, \hat{J}^{\rho\sigma}] = \mathrm{i}(g^{\mu\rho}\hat{P}^\sigma - g^{\mu\sigma}\hat{P}^\rho), \\
&[\hat{J}^{\mu\nu}, \hat{J}^{\rho\sigma}] = -\mathrm{i}(g^{\mu\rho}\hat{J}^{\nu\sigma} - g^{\mu\sigma}\hat{J}^{\nu\rho} - g^{\nu\rho}\hat{J}^{\mu\sigma} + g^{\nu\sigma}\hat{J}^{\mu\rho}).
\end{aligned} \tag{D.38}$$

It is convenient to write these commutation relations in terms of the generators of three-dimensional rotations $\hat{J}^i$ and boosts $\hat{K}^i$, as well as the generators of time and space translation $\hat{H}$ and $\hat{P}$, by defining,

$$\begin{aligned}
\hat{J}^k &= \frac{1}{2}\epsilon^{ijk}\hat{J}^{ij} = \{\hat{J}^{23}, \hat{J}^{13}, \hat{J}^{21}\}, \\
\hat{K}^k &= \hat{J}^{0k} = \{\hat{J}^{01}, \hat{J}^{02}, \hat{J}^{03}\}, \\
\hat{H} &= \hat{P}^0, \\
\hat{P}^k &= \hat{P}^i = \{\hat{P}^1, \hat{P}^2, \hat{P}^3\},
\end{aligned} \tag{D.39}$$

with the indices $i, j, k \in \{1, 2, 3\}$. With this definitions, the commutation relations (D.38) can be rewritten as

$$
\begin{aligned}
[\hat{J}^i, \hat{J}^j] &= \mathrm{i}\epsilon^{ijk}\hat{J}^k, & [\hat{P}^i, \hat{J}^j] &= \mathrm{i}\epsilon^{ijk}\hat{P}^k, \\
[\hat{J}^i, \hat{K}^j] &= \mathrm{i}\epsilon^{ijk}\hat{K}^k, & [\hat{P}^i, \hat{K}^j] &= \mathrm{i}\delta^{ij}\hat{H}, \\
[\hat{K}^i, \hat{K}^j] &= -\mathrm{i}\epsilon^{ijk}\hat{J}^k, & [\hat{H}, \hat{K}^i] &= \mathrm{i}\hat{P}^i, \\
[\hat{H}, \hat{J}^i] &= [\hat{H}, \hat{P}^i], = [\hat{H}, \hat{H}] = 0.
\end{aligned}
\tag{D.40}
$$

The Poincaré group contains two Casimir operators, i.e. operators that commute with all generators of the group. To get these it is helpful to introduce the Pauli–Lubanski vector

$$
W^\mu = \frac{1}{2}\epsilon_{\mu\nu\rho\sigma}\hat{P}^\nu\hat{J}^{\rho\sigma}.
\tag{D.41}
$$

The Casimir operators are given by $\hat{P}^2 = \hat{P}_\mu\hat{P}^\mu$ and $\hat{W}^2 = \hat{W}_\mu\hat{W}^\mu$.

Decomposing the generators for rotations $\hat{J}^{\mu\nu}$ into angular momentum $\hat{L}^{\mu\nu}$ and spin $\hat{\Sigma}^{\mu\nu}$,

$$
\begin{aligned}
\hat{J}^{\mu\nu} &= \hat{L}^{\mu\nu} + \hat{\Sigma}^{\mu\nu}, \\
\hat{L}^{\mu\nu} &\equiv \hat{x}^\mu\hat{P}^\nu - \hat{x}^\nu\hat{P}^\mu, \\
[\hat{P}^\mu, \hat{x}^\nu] &= \mathrm{i}g^{\mu\nu},
\end{aligned}
\tag{D.42}
$$

one finds that only the generators $\hat{\Sigma}$ contribute to the Pauli–Lubanski vector. Physical states are irreducible representations of the Poincaré group and can be classified by the eigenvalues of the Casimir operators:

1. *Massive representation* with $\hat{P}^2 = m^2 > 0$ and $\hat{W}^2 = -m^2 s(s+1)$, $s = 0, \frac{1}{2}, 1, \dots$.
   This representation is characterized by the mass m and spin s.

2. *Massless representation* with $\hat{P}^2 = 0$ and $\hat{W}^2 = 0$.
   In this case also the helicity operator $h = \hat{W}^0/\hat{P}^0 = \hat{P} \cdot \hat{S}/|\hat{P}|$ is a Casimir operator with eigenvalues $h = \pm s$. Therefore the massless states are characterized by their helicity and spin, with $h = \pm s$ and $s = 0, \frac{1}{2}, 1, \dots$.

D.3 Irreducible Representation of the Homogeneous Lorentz Group

The generators of the homogeneous Lorentz group are given by (D.40) for vanishing $\hat{P}^i$ and $\hat{H}$. The irreducible representations of the homogeneous Lorentz group are obtained by defining

$$
\hat{A}^i \equiv (\hat{J}^i + \mathrm{i}\hat{K}^i), \qquad\qquad \hat{B}^i \equiv (\hat{J}^i - \mathrm{i}\hat{K}^i),
\tag{D.43}
$$

which obey the following commutation relations,

$$
[\hat{A}^i, \hat{A}^j] = \mathrm{i}\epsilon_{ijk}\hat{A}^k, \qquad\qquad [\hat{B}^i, \hat{B}^j] = \mathrm{i}\epsilon_{ijk}\hat{B}^k,
\tag{D.44}
$$

$$
[\hat{A}^i, \hat{B}^j] = 0.
\tag{D.45}
$$

The operators $\hat{A}$ and $\hat{B}$ fulfill the $SU(2)$ Lie algebra, respectively. Because of the complex combination (D.43) this is the complex group $SL(2,\mathbb{C})$ and not the product group $SU(2) \otimes SU(2)$. The finite-dimensional representations are classified by the eigenvalues of the Casimir operators $\hat{A}^2$ and $\hat{B}^2$, which take the values $m(m+1)$ and $n(n+1)$, respectively. The representations are labeled as

$$(m,n), \qquad\qquad \text{with} \quad m, n = 0, \frac{1}{2}, 1, \frac{3}{2}, \dots . \tag{D.46}$$

Since $\hat{J}^i = \hat{A}^i + \hat{B}^i$, the spin of the representation is given by $j = m + n$. By defining $\omega_{0i} = -\omega_{i0} = \nu_i$ and $\omega_{ij} = \epsilon_{ijk}\varphi_k$, the Lorentz transformation $S^{(m,n)}(\Lambda)$ corresponding to the (m,n) representation can be written as

$$
\begin{aligned}
S^{(m,n)}(\Lambda) &= \exp\left(-\frac{i}{2}\omega_{\mu\nu}\hat{J}^{\mu\nu}\right) \\
&= \exp\left(-\frac{i}{2}\omega_{ij}\hat{J}^{ij} - i\omega_{0i}\hat{J}^{0i}\right) \\
&= \exp\left[-i(\varphi_i\hat{J}^i + \nu_i\hat{K}^i)\right] \\
&= \exp\left[-i(\varphi_i - i\nu_i)\hat{A}^i\right] \cdot \exp\left[-i(\varphi_i + i\nu_i)\hat{B}^i\right].
\end{aligned}
\tag{D.47}
$$

There are two fundamental representations from which all other representations can be derived by either the direct product or the direct sum of these.

1. $(\frac{1}{2}, 0)$ or *left-handed* representation:
   A left-handed spinor Ψ_L belonging to this representation transforms as

   $$\Psi_L(x) \to \Psi_L'(x') = S_L(\Lambda)\Psi_L(x), \tag{D.48}$$

   which is the spinor representation of (D.47) with $\hat{A}^i = \frac{1}{2}\sigma^i$ and $\hat{B}^i = 0$,

   $$S_L(\Lambda) = S^{(\frac{1}{2},0)} = \exp\left[-\frac{i}{2}(\varphi_i - i\nu_i)\sigma^i\right]. \tag{D.49}$$

   The Pauli matrices σ^i are given by (A.5).

2. $(0, \frac{1}{2})$ or *right-handed* representation:
   A right-handed spinor belonging to this representation transforms as

   $$\Psi_R(x) \to \Psi_R'(x') = S_R(\Lambda)\Psi_R(x), \tag{D.50}$$

   which is the spinor representation of (D.47) with $\hat{A}^i = 0$ and $\hat{B}^i = \frac{1}{2}\sigma^i$,

   $$S_R(\Lambda) = S^{(0,\frac{1}{2})} = \exp\left[-\frac{i}{2}(\varphi_i + i\nu_i)\sigma^i\right]. \tag{D.51}$$

Notice that S_L and S_R are not unitary, since they are elements of $SL(2,\mathbb{C})$. They can be decomposed into (unitary) rotations and boosts,

$$S_{L,R}(\varphi, \nu) = U(\varphi)\, S_{L,R}(0, \nu). \tag{D.52}$$

With help of the spin tensors (A.9), the Lorentz transformations S_L and S_R can also be written as

$$S_L = \exp\left[-\frac{i}{2}\omega_{\mu\nu}\sigma^{\mu\nu}\right], \qquad\qquad S_R = \exp\left[-\frac{i}{2}\omega_{\mu\nu}\bar\sigma^{\mu\nu}\right]. \qquad (D.53)$$

This can be verified by inserting the definition of φ and ν, and using (A.5) and (A.6),

$$\omega_{\mu\nu}\sigma^{\mu\nu} = \omega_{ij}\sigma^{ij} + 2\omega_{0i}\sigma^{01} = \frac{i}{4}\epsilon_{ijk}\varphi_k \underbrace{[\sigma^j,\sigma^i]}_{=2i\epsilon_{ijl}\sigma^l} + 2\frac{i}{4}\nu_i(-2\sigma^i)$$

$$= \frac{1}{2}\epsilon_{ijk}\epsilon_{ijl}\varphi_k\sigma^l - i\nu_i\sigma^i = \varphi_i\sigma^i - i\nu_i\sigma^i. \qquad (D.54)$$

In the same way, one finds

$$\omega_{\mu\nu}\bar\sigma^{\mu\nu} = \varphi_i\sigma^i + i\nu_i\sigma^i. \qquad (D.55)$$

D.3.1 Lorentz Invariant Combinations of Weyl Spinors

The quantities $\Psi_{L,R}$ in (D.48) and (D.50) are called Weyl spinors. The transformation matrices that transform the left- and right-handed spinors, cf. (D.49) and (D.51), are related to each other by the following algebraic relations,

$$S_L^{-1} = S_R^\dagger, \qquad (D.56)$$

$$\sigma^2 S_L \sigma^2 = S_R^*, \qquad \overset{(\sigma^2)^T=-\sigma^2}{\Rightarrow} \qquad S_R^\dagger = \sigma^2 S_L^T \sigma^2 \qquad \overset{(\sigma^2)^2=1}{\Rightarrow} \qquad \sigma^2 = S_L^T \sigma^2 S_L. \qquad (D.57)$$

Using this properties, one can show that $\sigma^2\Psi_L^*$ has the transformation properties of a right-handed spinor,

$$\sigma^2\Psi_L^* \quad\rightarrow\quad \sigma^2 S_L^*\Psi_L^* = \sigma^2 A_L^*\sigma^2\sigma^2\Psi_L^* = S_R(\sigma^2\Psi_L^*), \qquad (D.58)$$

and analogue $\sigma^2\Psi_R^*$ transforms under the left-handed representation. Therefore, left- and right-handed spinors are related via

$$\Psi_R = -i\sigma^2\Psi_L^*, \qquad\qquad \Psi_L = i\sigma^2\Psi_R^*, \qquad (D.59)$$

with the proportionality constants chosen such that inserting the second equation in the first leads to the identity. There are two contractions of spinors that are invariant under Lorentz transformations,

$$\text{Lorentz scalars:} \qquad \Phi_R^\dagger\Psi_L, \quad \Phi_L^\dagger\Psi_R, \qquad (D.60)$$

since,

$$\Phi_R^\dagger\Psi_L = i\Phi_L^T\sigma^2\Psi_L \quad\rightarrow\quad i\Phi_L^T S_L^T\sigma^2 S_L\Psi_L \overset{(D.57)}{=} i\Phi_L^T\sigma^2\Psi_L = \Phi_R^\dagger\Psi_L, \qquad (D.61)$$

and analogous for $\Phi_L^\dagger\Psi_R$.

Four-Vectors

Each (real-valued) four-vector x^μ can be mapped to Hermitian (2×2)-matrices X and $\bar{\text{X}}$ with help of the extended Pauli matrices (A.7),

$$x^\mu \to \text{X} = \sigma_\mu x^\mu, \qquad\qquad x^\mu \to \bar{\text{X}} = \bar\sigma_\mu x^\mu, \qquad\qquad \text{(D.62)}$$

which can be inverted with help of (A.8) by multiplying with $\bar\sigma_\mu$ and σ_μ, respectively, and taking the trace,

$$\text{X} \to x^\mu = \frac{1}{2}\text{Tr}\,\text{X}\bar\sigma^\mu, \qquad\qquad \bar{\text{X}} \to x^\mu = \frac{1}{2}\text{Tr}\,\bar{\text{X}}\sigma^\mu. \qquad\qquad \text{(D.63)}$$

The determinant of X and $\bar{\text{X}}$ is a Lorentz invariant quantities, since

$$\det(\text{X}) = \det(\bar{\text{X}}) = x_\mu x^\mu. \qquad\qquad \text{(D.64)}$$

The transformations

$$\text{X}' \to \text{A}\,\text{X}\,\text{A}^\dagger, \qquad\qquad \bar{\text{X}}' \to \bar{\text{A}}\,\bar{\text{X}}\,\bar{\text{A}}^\dagger, \qquad\qquad \text{(D.65)}$$

with $SL(2,\mathbb{C})$ elements A and $\bar{\text{A}}$, define new Hermitian matrices X' and $\bar{\text{X}}'$. (D.65) describes a Lorentz transformation, since it leaves the determinant invariant,

$$\det(\text{X}') = \det(\text{A}\,\text{X}\,\text{A}^\dagger) = \det(\text{A})\det(\text{X})\det(\text{A}^\dagger) = \det(\text{X}) = x_\mu x^\mu, \qquad\qquad \text{(D.66)}$$

and the same for $\det(\bar{\text{X}}')$. Since σ_μ and $\bar\sigma_\mu$ form a basis of $U(2)$, there is a unique four-vector x'^μ for which

$$\text{X}' = \text{A}\,\sigma_\mu\text{A}^\dagger x^\mu = \sigma_\mu x'^\mu = \sigma_\mu \Lambda^\mu{}_\nu x^\nu. \qquad\qquad \text{(D.67)}$$

Since this is true for all x^μ one has

$$\sigma_\mu \Lambda^\mu{}_\nu = \text{A}\,\sigma_\nu\text{A}^\dagger, \qquad\qquad \text{(D.68)}$$

i.e. one can associate to each Lorentz transformation $\Lambda^\mu{}_\nu$ a matrix $\text{A}(\Lambda)$. More specific, this matrix is given by S_L. This can be seen by using the representation (D.53) and looking at infinitesimal transformations,

$$
\begin{aligned}
\sigma_\mu(g^{\mu\nu} + \omega^{\mu\nu}) &\overset{!}{=} \left(-\frac{\text{i}}{2}\omega_{\rho\sigma}\sigma^{\rho\sigma}\right)\sigma^\nu\left(+\frac{\text{i}}{2}\omega_{\alpha\beta}\bar\sigma^{\alpha\beta}\right) \\
&= \sigma_\nu - \frac{\text{i}}{2}\omega_{\rho\sigma}\sigma^{\rho\sigma}\sigma_\nu + \frac{\text{i}}{2}\omega_{\alpha\beta}\sigma^\nu\bar\sigma^{\alpha\beta} + \mathcal{O}(\omega^2) \\
&\overset{(A.8)}{=} \sigma^\nu - \frac{\text{i}}{2}\omega_{\rho\sigma}(\text{i}\sigma^\rho g^{\sigma\nu} - \text{i}\sigma^\sigma g^{\rho\nu} + \sigma^\nu\bar\sigma^{\rho\sigma}) + \frac{\text{i}}{2}\omega_{\alpha\beta}\sigma^\nu\bar\sigma^{\alpha\beta} \\
&= \sigma^\nu + \omega^{\mu\nu}\sigma_\mu.
\end{aligned}
\qquad\qquad \text{(D.69)}
$$

The transformation performed by $\bar{\text{A}}$ is given by S_R, which can also be seen by noticing that,

$$
\begin{aligned}
x'^\mu &= \frac{1}{2}\text{Tr}(\bar{\text{X}}'\sigma^\mu) = \frac{1}{2}\text{Tr}(S_R\bar\sigma_\nu S_R^\dagger\sigma^\mu)\,x^\nu \\
&= \frac{1}{2}\text{Tr}(\underbrace{\sigma^2 S_R\sigma^2}_{A_L^*}\,\underbrace{\sigma^2\bar\sigma_\nu\sigma^2}_{\sigma_\nu^T}\,\underbrace{\sigma^2 S_R^\dagger\sigma^2}_{S_L^T}\,\underbrace{\sigma^2\sigma^\mu\sigma^2}_{\bar\sigma^{\mu T}})\,x^\nu \\
&= \frac{1}{2}\text{Tr}(A_L^*\sigma_\nu^T S_L^T\bar\sigma^{\mu T})\,x^\nu = \frac{1}{2}\text{Tr}(\bar\sigma^\mu S_L\sigma_\nu S_L^\dagger)\,x^\nu = \Lambda^\mu{}_\nu x^\nu.
\end{aligned}
\qquad\qquad \text{(D.70)}
$$

Due to these transformation properties of X and $\bar{\text{X}}$ one can construct two new Lorentz scalars out of two spinors Φ and Ψ,

$$
\begin{aligned}
\Phi_L^\dagger \bar{\text{X}} \Psi_L &\to (S_L \Phi_L)^\dagger ((S_L^\dagger)^{-1} \bar{\text{X}} S_L^{-1})(S_L \Psi_L) = \Phi_L^\dagger \bar{\text{X}} \Psi_L, \\
\Phi_R^\dagger \text{X} \Psi_R &\to (S_R \Phi_R)^\dagger ((S_R^\dagger)^{-1} \text{X} S_R^{-1})(S_R \Psi_R) = \Phi_R^\dagger \text{X} \Psi_R.
\end{aligned}
\tag{D.71}
$$

Choosing explicitly ∂_μ as four-vector one gets the Lorentz invariant combinations usually referred to as the kinetic term.

$$
\text{Lorentz scalars:} \qquad \Phi_L^\dagger \bar{\sigma}^\mu \partial_\mu \Psi_L, \quad \Phi_R^\dagger \sigma^\mu \partial_\mu \Psi_R.
\tag{D.72}
$$

D.3.2 Dirac and Majorana Spinors

A Dirac spinor Ψ and its conjugate $\bar{\Psi}$ are bi-spinors which correspond to the direct sum $(\frac{1}{2}, 0) \oplus (0, \frac{1}{2})$,

$$
\Psi \equiv \begin{pmatrix} \Psi_L \\ \Phi_R \end{pmatrix}, \qquad \bar{\Psi} \equiv \Psi^\dagger \gamma_0 = (\Phi_R^\dagger, \Psi_L^\dagger),
\tag{D.73}
$$

with γ_0 given in (A.10). A Dirac spinor transforms under Lorentz transformations according to (D.48) and (D.50) as

$$
\Psi \to \Psi' = S^{(\frac{1}{2}, 0) \oplus (0, \frac{1}{2})} \Psi = \begin{pmatrix} S_L & 0 \\ 0 & S_R \end{pmatrix} \Psi.
\tag{D.74}
$$

The Lorentz scalars (D.60) and (D.72) can be written in terms of Dirac spinors,

$$
\bar{\Psi}\Psi = \Phi_R^\dagger \Psi_L + \Psi_L^\dagger \Phi_R,
\tag{D.75}
$$

$$
\bar{\Psi}\gamma^\mu \partial_\mu \Psi = \Phi_R^\dagger \sigma^\mu \partial_\mu \Phi_R + \Psi_L^\dagger \bar{\sigma}^\mu \partial_\mu \Psi_L.
\tag{D.76}
$$

In the following we will consider the transformation properties of Dirac spinors under parity transformation P and charge-conjugation C. A parity transformation $P : \vec{x} \to -\vec{x}$ transforms Weyl spinors according to

$$
\Psi_L \xrightarrow{P} \Psi_R, \qquad \Psi_R \xrightarrow{P} \Psi_L.
\tag{D.77}
$$

A Dirac spinor transforms under a parity transformation by construction as

$$
\Psi = \begin{pmatrix} \Psi_L \\ \Phi_R \end{pmatrix} \xrightarrow{P} \begin{pmatrix} \Phi_R \\ \Psi_L \end{pmatrix}.
\tag{D.78}
$$

There is a second discrete transformation defined on a bi-spinor, the charge-conjugation

$$
\begin{pmatrix} \Psi_L \\ \Phi_R \end{pmatrix} \xrightarrow{C} \begin{pmatrix} \Phi_L \\ \Psi_R \end{pmatrix} = \Psi^C \equiv C \bar{\Psi}^T,
\tag{D.79}
$$

where C is given by (according to (D.59))

$$
C = \begin{pmatrix} i\sigma^2 & 0 \\ 0 & -i\sigma^2 \end{pmatrix} = i\gamma^2 \gamma^0.
\tag{D.80}
$$

Performing the charge-conjugation twice leaves the state invariant, i.e. $\Psi^{CC} = \Psi$. A bi-spinor that is invariant under charge-conjugation is called Majorana spinor. In terms of Weyl spinors it has the form

$$\Psi_M = \begin{pmatrix} \Psi_L \\ \Psi_R \end{pmatrix} = \Psi_M^C. \tag{D.81}$$

D.4 Spinor Calculus

In this section a component notation for Weyl spinors is introduced. The components of a spinor are anti-commuting numbers (Grassmann numbers), since otherwise the invariant eq. (D.60) would vanish for $\Phi = \Psi$. Spinors corresponding to the $(\frac{1}{2}, 0)$ representation get undotted indices while spinors of the $(0, \frac{1}{2})$ representation get dotted indices,

$$\Psi_L = \begin{pmatrix} \psi_1 \\ \psi_2 \end{pmatrix}, \qquad\qquad \Psi_R^\dagger = (\psi^1, \psi^2), \tag{D.82}$$

$$\Psi_R = \begin{pmatrix} \bar{\psi}^{\dot{1}} \\ \bar{\psi}^{\dot{2}} \end{pmatrix}, \qquad\qquad \Psi_L^\dagger = (\bar{\psi}_{\dot{1}} \bar{\psi}_{\dot{2}}). \tag{D.83}$$

Spinor indices are labeled in the following with capital roman letters. Since for Grassmann numbers complex conjugation equals Hermitian conjugation, one has

$$(\psi_A)^\dagger = (\psi_A)^* = \bar{\psi}_{\dot{A}}, \qquad\qquad (\psi^A)^\dagger = (\psi^A)^* = \bar{\psi}^{\dot{A}}. \tag{D.84}$$

As standard summation rules one defines

$$\phi\psi \equiv \phi^A \psi_A, \qquad\qquad \bar{\phi}\bar{\psi} \equiv \bar{\phi}_{\dot{A}} \bar{\psi}^{\dot{A}}, \tag{D.85}$$

i.e. the summation of undotted indices goes always from upper-left to lower-right and for dotted indices from lower-left to upper-right. One can define metric tensors ϵ and $\bar{\epsilon}$ that rise and lower spinor indices. These are found by writing (D.59) in index notation,

$$\psi^A = (-i\sigma^2)^{AB}\psi_B = \epsilon^{AB}\psi_B, \qquad \bar{\psi}^{\dot{A}} = \bar{\psi}_{\dot{B}}(i\sigma^2)^{\dot{B}\dot{A}} = \bar{\psi}_{\dot{B}}\epsilon^{\dot{B}\dot{A}}. \tag{D.86}$$

In total one finds,

$$\left(\epsilon^{AB}\right) = (\epsilon_{AB}) = \begin{pmatrix} 0 & -1 \\ 1 & 0 \end{pmatrix}, \qquad \epsilon_A{}^B = \delta_A^B, \qquad \epsilon^A{}_B = -\delta_B^A \tag{D.87}$$

$$\left(\bar{\epsilon}^{\dot{A}\dot{B}}\right) = (\bar{\epsilon}_{\dot{A}\dot{B}}) = \begin{pmatrix} 0 & 1 \\ -1 & 0 \end{pmatrix}, \qquad \bar{\epsilon}^{\dot{A}}{}_{\dot{B}} = \delta_{\dot{B}}^{\dot{A}}, \qquad \bar{\epsilon}_{\dot{A}}{}^{\dot{B}} = -\delta_{\dot{A}}^{\dot{B}}. \tag{D.88}$$

By writing (D.48), (D.50), (D.53), and (D.72) in index notation, one finds the index structure of S_L, S_R, σ^μ, $\bar{\sigma}^\mu$, $\sigma^{\mu\nu}$ and $\bar{\sigma}^{\mu\nu}$,

$$\begin{array}{cccc} (S_L)_B{}^A, & (S_L^{-1})_A{}^B, & (S_R)^{\dot{B}}{}_{\dot{A}}, & (S_R^{-1})^{\dot{A}}{}_{\dot{B}}, \\[2mm] (\sigma^\mu)_{A\dot{B}}, & (\bar{\sigma}^\mu)^{\dot{A}B}, & (\sigma^{\mu\nu})_A{}^B, & (\bar{\sigma}^{\mu\nu})^{\dot{A}}{}_{\dot{B}}. \end{array} \tag{D.89}$$

For the extended Pauli matrices and the spin-tensors one further has the relations,

$$(\sigma^\mu)^{A\dot{B}} = (\bar{\sigma}^\mu)^{\dot{B}A}, \qquad (\sigma^{\mu\dagger})_{A\dot{B}} = (\sigma^\mu)_{B\dot{A}}, \qquad (\bar{\sigma}^{\mu\dagger})_{\dot{A}B} = (\bar{\sigma}^\mu)_{\dot{B}A}, \qquad \text{(D.90)}$$

$$(\sigma^{\mu\nu})_A{}^B = (\sigma^{\mu\nu})^B{}_A, \qquad (\bar{\sigma}^{\mu\nu})^{\dot{A}}{}_{\dot{B}} = (\bar{\sigma}^{\mu\nu})_{\dot{B}}{}^{\dot{A}}, \qquad (\sigma^{\mu\nu\dagger})_B^A = (\bar{\sigma}^{\mu\nu})_{\dot{B}}^{\dot{A}}. \qquad \text{(D.91)}$$

D.5 Supersymmetry Algebra

Coleman and Mandula showed in [51] that under reasonable assumptions the most general Lie algebra of symmetry operators that commute with the S matrix, consists of the generators P_μ and $J_{\mu\nu}$ of the Poincaré group, plus ordinary internal symmetry generators. The assumptions refer to the particle content, the existence of scattering at almost all energies, and the analyticity of the S matrix.

The generators of an internal symmetry group T_a, have the following commutation relations,

$$[T_a, P_\mu] = 0, \qquad [T_a, J_{\mu\nu}] = 0, \qquad [T_a, T_b] = \mathrm{i}f_{abc}T_c, \qquad \text{(D.92)}$$

with the so-called structure constants f_{abc} of the Lie algebra. By definition they have trivial commutation relations with the generators of the Poincaré group, i.e. they cannot relate particles of different spin.

The Coleman–Mandula theorem can be overcome by taking symmetry operators into account that obey a Clifford algebra instead of a Lie algebra, hence violating one of the conditions of the theorem. These operators can therefore have non-trivial commutation relations with the generators of the Poincaré algebra and can connect particles of different spin. Such a symmetry is called supersymmetry.

D.5.1 Graded Lie Algebras

Supersymmetry is expressed in terms of symmetry generators that form a $\mathbb{Z}_2$-graded Lie algebra [179]. In general, a $\mathbb{Z}_2$-graded algebra is defined in the following way:
Consider a vector space $\mathbb{V}$ that is a direct sum of $\mathbb{V}_0$ and $\mathbb{V}_1$, $\mathbb{V} = \mathbb{V}_0 \oplus \mathbb{V}_1$. A $\mathbb{Z}_2$ graded algebra is defined by

$$u_1 \circ u_2 \in \mathbb{V}_0 \qquad\qquad \text{for all } u_1, u_2 \in \mathbb{V}_0, \qquad \text{(D.93)}$$

$$u \circ v \in \mathbb{V}_1 \qquad\qquad \text{for all } u \in \mathbb{V}_0, \;\; v \in \mathbb{V}_1, \qquad \text{(D.94)}$$

$$v_1 \circ v_2 \in \mathbb{V}_0 \qquad\qquad \text{for all } v_1, v_2 \in \mathbb{V}_1. \qquad \text{(D.95)}$$

A $\mathbb{Z}_2$-graded Lie algebra is then defined by

$$\text{Grading:} \qquad x_i \circ x_j \in \mathbb{V}_{(i+j)\mathrm{mod}2}. \qquad \text{(D.96)}$$

$$\text{Supersymmetry:} \qquad x_i \circ x_j = (-1)^{i\cdot j} x_j \circ x_i. \qquad \text{(D.97)}$$

$$\text{Jacobi identity:} \qquad 0 = (-1)^{k\cdot m}\, x_k \circ (x_l \circ x_m) + (-1)^{l\cdot k}\, x_l \circ (x_m \circ x_k) \qquad \text{(D.98)}$$
$$+ (-1)^{m\cdot l}\, x_m \circ (x_k \circ x_l),$$

with $x_i \in \mathbb{V}_i$, $i = 0, 1$. The (anti-)commutation relations of symmetry generators T_a that form a $\mathbb{Z}_2$-graded Lie algebra are given by

$$T_a T_b - (-1)^{\eta_a \eta_b} T_b T_a = \mathrm{i} f_{abc} T_c \equiv [T_a, T_b]_\pm, \tag{D.99}$$

where η_a is either $+1$ or 0, depending on the grading of the generator T_a. Generators for which $\eta_a = 0$ are called bosonic, the ones with $\eta_a = 1$ are called fermionic. The Jacobi identity can be written as

$$(-1)^{\eta_c \eta_a}[[T_a, T_b]_\pm, T_c]_\pm + (-1)^{\eta_a \eta_b}[[T_b, T_c]_\pm, T_a]_\pm + (-1)^{\eta_b \eta_c}[[T_c, T_a]_\pm, T_b]_\pm = 0.$$

D.5.2 Poincaré Superalgebra

One can now start to construct a Poincaré superalgebra, which is a $\mathbb{Z}_2$-graded Poincaré algebra. The subspace $\mathbb{V}_0$ is spanned by the generators $\hat{P}^\mu$ and $\hat{J}^{\mu\nu}$ of the Poincaré algebra eq. (D.38). This vector space is extended by a vector space $\mathbb{V}_1$ which is spanned by N fermionic generators Q_A.

The variety of supersymmetries is strongly restricted by the fact, that the bosonic symmetry generators still have to obey the Coleman–Mandula theorem. Haag, Łopuszański, and Sohnius showed in [52] that the only fermionic symmetry generators that do not violate the Coleman–Mandula theorem must belong to the $(0, \frac{1}{2})$ or $(\frac{1}{2}, 0)$ representation of the Lorentz group. It further states that the most general graded Lie algebra must have the following form (see also [180]),

$$\begin{aligned}
[P^\mu, P^\nu] &= 0, \\
[P^\mu, J^{\rho\sigma}] &= \mathrm{i}(g^{\mu\rho}P^\sigma - g^{\mu\sigma}P^\rho), \\
[J^{\mu\nu}, J^{\rho\sigma}] &= -\mathrm{i}(g^{\mu\rho}J^{\nu\sigma} - g^{\mu\sigma}J^{\nu\rho} - g^{\nu\rho}J^{\mu\sigma} + g^{\nu\sigma}J^{\mu\rho}),
\end{aligned} \tag{D.100}$$

$$\begin{aligned}
[P_\mu, Q_{A,r}] &= [P_\mu, \bar{Q}_{\dot{A},r}] = 0, \\
[Q_{Ar}, J^{\mu\nu}] &= \frac{1}{2}(\sigma^{\mu\nu})_A{}^B Q_{Br}, \\
[\bar{Q}_{\dot{A}r}, J^{\mu\nu}] &= -\frac{1}{2}\bar{Q}_{\dot{B}r}(\bar{\sigma}^{\mu\nu})^{\dot{B}}{}_{\dot{A}},
\end{aligned} \tag{D.101}$$

$$\begin{aligned}
\{Q_{Ar}, \bar{Q}_{\dot{B}s}\} &= 2\delta_{r,s}(\sigma^\mu)_{A\dot{B}}P_\mu, \\
\{Q_{Ar}, Q_{Bs}\} &= -\epsilon_{AB}Z_{rs}, \qquad \text{with } Z_{rs} = (a^i)_{rs}T_i, \\
\{\bar{Q}_{\dot{A}r}, \bar{Q}_{\dot{B}s}\} &= -\epsilon_{\dot{A}\dot{B}}(Z^\dagger)_{rs},
\end{aligned} \tag{D.102}$$

$$\begin{aligned}
[T_i, T_j] &= \mathrm{i} f_{ijk} T_k, \\
[T_i, Q_{Ar}] &= -(t_i)_{rs} Q_{As}, \qquad t_i = t_i^\dagger, \qquad [t_i, t_j] = \mathrm{i} f_{ijk} t_k, \\
[T_i, \bar{Q}_{\dot{A}r}] &= \bar{Q}_{\dot{A}s}(t_i)_{sr}, \\
[Z_{rs}, \text{anything}] &= 0.
\end{aligned} \tag{D.103}$$

As usual, capital roman letters denote the spinor indices of fermionic symmetry generators. The lower case letters r, s, t, u are used to distinguish the N different two-component generators with the same Lorentz properties. The T_i are the generators of the internal symmetry. Objects corresponding to the internal symmetry are labeled with the lower case indices i, j, k. The commutator relation for the t_i follows from the Jacobi identity of two Ts and one Q. Since these are Hermitian ($N \times N$) matrices, the largest possible internal symmetry which can act non-trivially on Q is $U(N)$.

The Z_{rs} commute with all symmetry generators and are therefore called central charges. They are antisymmetric in interchanging their indices.

If there is only one supercharge Q, i.e. $N = 1$, one speaks of a simple or unextended supersymmetry. If $N > 1$ one speaks of extended supersymmetry.

$\mathcal{R}$-Symmetry

In the case of $N = 1$ supersymmetry, there is no central charge due to the fact that it is antisymmetric in its indices. The only non-trivially acting internal symmetry is a simple $U(1)$, generated by a charge which is called the $\mathcal{R}$ charge. By taking (D.103) and defining $R_i = T_i/t_i$ one finds (suppressing the index i)

$$[R, Q_A] = -Q_A, \qquad [R, \bar{Q}_{\dot{A}}] = \bar{Q}_{\dot{A}}. \tag{D.104}$$

From (D.15) together with (D.10) and (D.11) one gets the transformation of the supersymmetry generators under $\mathcal{R}$ charge,

$$e^{\mathrm{i}\varphi R} Q_A e^{-\mathrm{i}\varphi R} = e^{-\mathrm{i}\varphi} Q_A, \qquad e^{\mathrm{i}\varphi R} \bar{Q}_{\dot{A}} e^{-\mathrm{i}\varphi R} = e^{\mathrm{i}\varphi} \bar{Q}_{\dot{A}}. \tag{D.105}$$

D.6 Superfields

In the following we will restrict our discussion to $N = 1$ supersymmetry, since it leads to a supersymmetric field theory of phenomenological interest. The so-called superfield formalism is a technique in which supermultiplets are gathered into superfields. A superfields Φ depend on the four coordinates of spacetime as well as on the four fermionic coordinates θ_A and $\bar{\theta}^{\dot{A}}$. It can be Taylor expanded in its fermionic coordinates,

$$\begin{aligned} \Phi(x, \theta, \bar{\theta}) = &\, C(x) + \theta^A \psi_A(x) + \bar{\theta}_{\dot{A}} \bar{\xi}^{\dot{A}}(x) + (\theta\theta) M(x) + (\bar{\theta}\bar{\theta}) N(x) \\ &+ \theta\sigma_\mu \bar{\theta} A^\mu + (\theta\theta)\bar{\theta}_{\dot{A}} \bar{\lambda}^{\dot{A}} + (\bar{\theta}\bar{\theta})\theta^A \eta_A + (\theta\theta)(\bar{\theta}\bar{\theta}) D(x). \end{aligned} \tag{D.106}$$

Products of superfields are again superfields and therefore form a vector space. However, general superfields are reducible. Before looking at irreducible superfields we will first consider supersymmetry transformations on the space of superfields, since such a transformation must map a superfield belonging to an irreducible subspace into the same subspace. A supersymmetry transformation on the superfields is given by a unitary transformation $U(x, \theta, \bar{\theta})$ with a four-vector x and fermionic parameters θ and $\bar{\theta}^{\dot{A}}$,

$$U(x, \theta, \bar{\theta}) = \exp\left[\mathrm{i}\left(x_\mu P^\mu + \theta Q + \bar{\theta}\bar{Q}\right)\right], \tag{D.107}$$

where P, Q and $\bar{Q}$ are field theoretical representations of the supersymmetry generators. The transformed field is given by

$$
\begin{aligned}
\Phi(x', \theta', \bar{\theta}') &= U(\epsilon, \xi, \bar{\xi})\Phi(x, \theta, \bar{\theta})U^{-1}(\epsilon, \xi, \bar{\xi}) \\
&= U(\epsilon, \xi, \bar{\xi})U(x, \theta, \bar{\theta})\Phi(0, 0, 0)U^{-1}(x, \theta, \bar{\theta})U^{-1}(\epsilon, \xi, \bar{\xi}).
\end{aligned}
\tag{D.108}
$$

With help of the Baker–Campbell–Hausdorff formula one can show that the product of two transformations is given by

$$
\begin{aligned}
U(\epsilon, \xi, \bar{\xi})U(x, \theta, \bar{\theta}) &= \exp\Big[\mathrm{i}\left((x_\mu + \epsilon_\mu)P^\mu + (\theta + \xi)Q + (\bar{\theta} + \bar{\xi})\bar{Q}\right) \\
&\qquad + \frac{1}{2}\left[\mathrm{i}\left(\epsilon_\mu P^\mu + \xi Q + \bar{\xi}\bar{Q}\right), \mathrm{i}\left(x_\mu P^\mu + \theta Q + \bar{\theta}\bar{Q}\right)\right]\Big] \\
&= \exp\Big[\mathrm{i}\left((x_\mu + \epsilon_\mu + \mathrm{i}\xi\sigma_\mu\bar{Q} - \mathrm{i}\theta\sigma_\mu\bar{\xi})P^\mu + (\theta + \xi)Q + (\bar{\theta} + \bar{\xi})\bar{Q}\right)\Big] \\
&= U(x + \epsilon + \mathrm{i}\xi\sigma\bar{\theta} - \mathrm{i}\theta\sigma\bar{\xi}, \theta + \xi, \bar{\theta} + \bar{\xi}).
\end{aligned}
\tag{D.109}
$$

Inserting (D.109) in (D.108) one gets an explicit expression for the transformed field. By considering infinitesimal transformations ϵ, ξ, and $\bar{\xi}$ one finds

$$
\Phi(x', \theta', \bar{\theta}') = \Phi(x + \epsilon + \mathrm{i}\xi\sigma\bar{\theta} - \mathrm{i}\theta\sigma\bar{\xi}, \theta + \xi, \bar{\theta} + \bar{\xi})
\tag{D.110}
$$

$$
\approx \Phi(x, \theta, \bar{\theta}) + \left[(\epsilon^\mu + \mathrm{i}\xi\sigma\bar{\theta} - \mathrm{i}\theta\sigma\bar{\xi})\partial_\mu + \xi^A\partial_A + \bar{\xi}_{\dot{A}}\partial^{\dot{A}}\right]\Phi(x, \theta, \bar{\theta})
\tag{D.111}
$$

$$
\overset{!}{=} \left(1 + \mathrm{i}(\epsilon^\mu P_\mu + \xi Q + \bar{\xi}\bar{Q})\right)\Phi(x, \theta, \bar{\theta})\left(1 - \mathrm{i}(\epsilon^\mu P_\mu + \xi Q + \bar{\xi}\bar{Q})\right)
\tag{D.112}
$$

$$
= \Phi + \mathrm{i}\epsilon^\mu[P_\mu, \Phi] + \mathrm{i}[\xi Q, \Phi] + \mathrm{i}[\bar{\xi}\bar{Q}, \Phi].
\tag{D.113}
$$

In the second line the expression was Taylor expanded. The third line corresponds to (D.108) with the infinitesimal form of (D.107) inserted. The representation of the supersymmetry generators in the space of superfields,

$$
\Phi(x', \theta', \bar{\theta}') = S(\epsilon, \xi, \bar{\xi})\Phi(x, \theta, \bar{\theta}),
\tag{D.114}
$$

with

$$
S(x, \theta, \bar{\theta}) = \exp[-\mathrm{i}(x_\mu\hat{P}^\mu - \theta\hat{Q} - \bar{\theta}\hat{\bar{Q}})],
\tag{D.115}
$$

can be read off of (D.113) using the relation (D.15),

$$
\hat{P}_\mu = \mathrm{i}\partial_\mu,
\tag{D.116}
$$

$$
\hat{Q}_A = -\mathrm{i}\partial_A + (\sigma^\mu\bar{\theta})_A\partial_\mu, \qquad\qquad \hat{Q}^A = \mathrm{i}\partial^A + \epsilon^{AB}(\sigma^\mu\bar{\theta})_B\partial_\mu,
\tag{D.117}
$$

$$
\hat{\bar{Q}}_{\dot{A}} = \mathrm{i}\bar{\partial}_{\dot{A}} - (\theta\sigma^\mu)_{\dot{A}}\partial_\mu, \qquad\qquad \hat{\bar{Q}}^{\dot{A}} = -\mathrm{i}\bar{\partial}^{\dot{A}} + (\theta\sigma^\mu)_{\dot{B}}\epsilon^{\dot{A}\dot{B}}\partial_\mu.
\tag{D.118}
$$

By construction, his operators fulfill the super-algebra (D.102), cf. Section D.1.2. One can define covariant derivatives that anti-commute with the differential operators (D.118),

$$
D_A = \partial_A - \mathrm{i}(\sigma^\mu\bar{\theta})_A\partial_\mu, \qquad\qquad D^A = -\partial^A + \mathrm{i}(\bar{\theta}\bar{\sigma}^\mu)^A\partial_\mu,
\tag{D.119}
$$

$$
\bar{D}_{\dot{A}} = -\bar{\partial}_{\dot{A}} + \mathrm{i}(\theta\sigma^\mu)_{\dot{A}}\partial_\mu, \qquad\qquad \bar{D}^{\dot{A}} = \bar{\partial}^{\dot{A}} - \mathrm{i}(\bar{\sigma}^\mu\theta)^{\dot{A}}\partial_\mu.
\tag{D.120}
$$

The covariant derivatives have the following properties,

$$\{D, Q\} = \{\bar{D}, \bar{Q}\} = \{D, \bar{Q}\} = \{\bar{D}, Q\},$$
$$\{D, D\} = \{\bar{D}, \bar{D}\} = 0,$$
$$\{D_A, \bar{D}_{\dot{B}}\} = 2\mathrm{i}\sigma^\mu_{A\dot{B}}\partial_\mu,$$
$$\{D^A, \bar{D}^{\dot{B}}\} = 2\mathrm{i}\bar{\sigma}^{\mu\dot{B}A}\partial_\mu,$$
$$D^3 = \bar{D}^3 = 0.$$

(D.121)

An infinitesimal supersymmetry transformation in the spinorial space is given by

$$\delta_\epsilon = \mathrm{i}(\epsilon\hat{Q} + \bar{\epsilon}\hat{\bar{Q}}).$$

(D.122)

By performing an infinitesimal supersymmetry transformation on the superfield Φ given by (D.106), one gets the transformation properties of the component fields. Of special interest is the transformation of the $(\theta\theta)(\bar{\theta}\bar{\theta})$-component, since it transforms as a total derivative,

$$\delta_\epsilon D = \frac{\mathrm{i}}{2}\partial_\mu(\epsilon\sigma^\mu\bar{\lambda} - \eta\sigma^\mu\bar{\epsilon}).$$

(D.123)

D.6.1 Chiral Superfields

Chiral and anti-chiral superfields are defined via the following conditions.

Chiral superfield:	$\bar{D}_{\dot{A}}\Psi = 0,$	(D.124)
Anti-chiral superfield:	$D_A\Psi = 0.$	(D.125)

Since an infinitesimal supersymmetry transformation in the spinorial space (D.122), commutes with the covariant derivatives (D.119), chiral superfields are an irreducible representation of the superfields. One can construct them by noticing that for $y^\mu = x^\mu - \mathrm{i}\theta\sigma^\mu\bar{\theta}$ one finds

$$\bar{D}_{\dot{A}}y^\mu = (-\bar{\partial}_{\dot{A}} + \mathrm{i}(\theta\sigma^\nu)_{\dot{A}}\partial_\nu)(x^\mu - \mathrm{i}\theta\sigma^\mu\bar{\theta}) = \mathrm{i}(\theta\sigma^\mu)_{\dot{A}} - \mathrm{i}(\theta\sigma^\mu)_{\dot{A}} = 0.$$

(D.126)

By expressing the covariant derivatives (D.119) with respect to the complex coordinates $(y^\mu, \theta, \bar{\theta})$, i.e.

$$\frac{\partial}{\partial x^\mu} = \frac{\partial}{\partial y^\mu}, \qquad \frac{\partial}{\partial\theta^A} = \frac{\partial}{\partial\theta^A} - \mathrm{i}(\sigma\bar{\theta})_A\frac{\partial}{\partial y^\mu}, \qquad \frac{\partial}{\partial\bar{\theta}^{\dot{A}}} = \frac{\partial}{\partial\bar{\theta}^{\dot{A}}} + \mathrm{i}(\theta\sigma)_{\dot{A}}\frac{\partial}{\partial y^\mu}, \qquad$$

(D.127)

one finds that $\bar{D}_{\dot{A}}$ is given by

$$\bar{D}_{\dot{A}}(y, \theta, \bar{\theta}) = -\frac{\partial}{\partial\bar{\theta}^{\dot{A}}} = \bar{\partial}_{\dot{A}}.$$

(D.128)

Expressing the condition for a chiral superfield (D.124) in terms of $(y^\mu, \theta, \bar{\theta})$ one gets

$$\frac{\partial}{\partial\bar{\theta}^{\dot{A}}}\Phi(y, \theta, \bar{\theta}) = 0,$$

(D.129)

i.e. $\Phi(y^\mu, \theta, \bar\theta)$ has to be independent of $\bar\theta$. Taylor expanding Φ with respect to the complex variables, it can be written as

$$\Phi(y, \theta) = \varphi(y) + \sqrt{2}\theta\psi(y) + (\theta\theta)F(y). \tag{D.130}$$

By performing the same steps eqs. (D.126)–(D.128) but for the complex variable $\bar y = x^\mu + i\theta\sigma\bar\theta = y^*$, one finds that the anti-chiral superfield (D.124) is given by the condition $\partial_\theta \Psi^\dagger(\bar y, \theta, \bar\theta) = 0$. It can therefore be Taylor expanded as

$$\Phi^\dagger(\bar y, \theta) = \varphi^*(\bar y) + \sqrt{2}\bar\psi(\bar y)\bar\theta + (\bar\theta\bar\theta)F^*(\bar y). \tag{D.131}$$

Reexpressing the fields Φ and $\Phi^\dagger$ in terms of the variables $(x, \theta, \bar\theta)$ one finally gets

$$\Phi(x, \theta, \bar\theta) = \varphi(x - i\theta\sigma\bar\theta) + \sqrt{2}\theta\psi(x - i\theta\sigma\bar\theta) + (\theta\theta)F(x - i\theta\sigma\bar\theta) \tag{D.132}$$

$$= \varphi(x) + \sqrt{2}\theta\psi + (\theta\theta)F - i(\theta\sigma\bar\theta)\partial_\mu\varphi$$
$$+ \frac{i}{\sqrt{2}}(\theta\theta)\partial_\mu(\psi\sigma^\mu\bar\theta) - \frac{1}{4}(\theta\theta)(\bar\theta\bar\theta)\partial_\mu\partial^\mu\varphi, \tag{D.133}$$

$$\Phi^\dagger(x, \theta, \bar\theta) = \varphi^*(x) + \sqrt{2}\bar\theta\bar\psi + (\bar\theta\bar\theta)F^* + i(\theta\sigma\bar\theta)\partial_\mu\varphi^*$$
$$- \frac{i}{\sqrt{2}}(\bar\theta\bar\theta)\partial_\mu(\theta\sigma^\mu\bar\psi) - \frac{1}{4}(\theta\theta)(\bar\theta\bar\theta)\partial_\mu\partial^\mu\varphi^*. \tag{D.134}$$

The $\theta\theta$ and $\bar\theta\bar\theta$ components, respectively, remain unchanged after the variable transformation. Therefore, for chiral superfields one has $F(y) = F(x)$.

An infinitesimal supersymmetry transformation, cf. (D.122), transforms the components of Ψ in the following way:

$$\delta_\epsilon\varphi = \sqrt{2}\epsilon\psi,$$
$$\delta_\epsilon\phi = -i\sqrt{2}\sigma^\mu\bar\epsilon\partial_\mu\varphi + \sqrt{2}\epsilon F, \tag{D.135}$$
$$\delta_\epsilon F = i\sqrt{2}\partial_\mu\left(\psi\sigma^\mu\bar\epsilon\right).$$

Like the D-term of the general superfield, eq. (D.123), the F-term of a chiral superfield transforms as a total derivative.

D.6.2 Vector Superfields and Supersymmetric Field Strength

The building block for the supersymmetric field strength are vector superfields.
A vector superfield $V(x, \theta, \bar\theta)$ is defined by the reality condition

$$V(x, \theta, \bar\theta) = V^\dagger(x, \theta, \bar\theta). \tag{D.136}$$

In components, it can be expressed as

$$V(x, \theta, \bar\theta) = C + \sqrt{2}\theta\chi + \sqrt{2}\bar\theta\bar\chi + (\theta\theta)M + (\bar\theta\bar\theta)M^* + (\theta\sigma^\mu\bar\theta)A_\mu$$
$$+ (\theta\theta)\bar\theta\left(\bar\lambda - \frac{i}{\sqrt{2}}\bar\sigma^\mu\partial_\mu\chi\right) + (\bar\theta\bar\theta)\theta\left(\lambda - \frac{i}{\sqrt{2}}\sigma^\mu\partial_\mu\bar\chi\right) \tag{D.137}$$
$$+ \frac{1}{2}(\theta\theta)(\bar\theta\bar\theta)\left(D - \frac{1}{2}\partial_\mu\partial^\mu C\right),$$

with real valued fields C, D, and A_μ. One defines a supersymmetric gauge transformation on V via

$$V \to V' = V + \mathrm{i}(\varLambda - \varLambda^\dagger). \tag{D.138}$$

$\varLambda$ is a chiral superfield and $\varLambda^\dagger$ is the corresponding anti-chiral superfield. Expanded in its fermionic components, $\mathrm{i}\varLambda$ is given by

$$\begin{aligned} \mathrm{i}\varLambda = &\, a + \sqrt{2}\theta\rho + (\theta\theta)b + \mathrm{i}(\theta\sigma\bar\theta)\partial_\mu a \\ &- \frac{\mathrm{i}}{\sqrt{2}}(\theta\theta)\partial_\mu(\rho\sigma^\mu\bar\theta) - \frac{1}{4}(\theta\theta)(\bar\theta\bar\theta)\partial_\mu\partial^\mu a. \end{aligned} \tag{D.139}$$

The components of V transform under a supersymmetric gauge transformation as

$$\begin{aligned} C &\to C + (a + a^*), & A_\mu &= A_\mu + \mathrm{i}\partial_\mu(a - a^*), \\ \chi &\to \chi + \rho, & \lambda &\to \lambda, \\ M &\to M + b, & D &\to D. \end{aligned} \tag{D.140}$$

In the Wess–Zumino gauge, the components b, ρ, and $\mathrm{Im}(a)$ of $\varLambda$ are fixed such that the components C, χ, and M of V vanish. The real part of a is not fixed by this gauge. Hence, $U(1)$ gauge transformations of the kind

$$A_\mu \to A'_\mu = A_\mu + \partial_\mu(a + a^*) \tag{D.141}$$

are still allowed. In the Wess–Zumino gauge, the vector superfield is given by

$$V_{WZ} = (\theta\sigma\bar\theta)A_\mu + (\theta\theta)\bar\theta\bar\lambda + (\bar\theta\bar\theta)\theta\lambda + \frac{1}{2}(\theta\theta)(\bar\theta\bar\theta)D. \tag{D.142}$$

One still has the freedom to perform a gauge transformation on the vector field with the yet unfixed real part of a, $A_\mu \to A_\mu - \partial_\mu(a - a^*)$.

The supersymmetric field strength on the super vectorfield is defined as

$$W_A \equiv -\frac{1}{4}(\bar D\bar D)D_A V(x, \theta, \bar\theta), \tag{D.143}$$

$$\bar W_{\dot A} \equiv -\frac{1}{4}(DD)\bar D_{\dot A} V(x, \theta, \bar\theta). \tag{D.144}$$

Since $D^3 = \bar D^3 = 0$, cf. (D.121), the supersymmetric field strength W_A $(\bar W_{\dot A})$ is a (anti-) chiral superfield. The supersymmetric field strength is invariant under the supersymmetric gauge transformation, (D.138). Hence, one can calculate its components in the Wess–Zumino gauge. In the variables $(y, \theta, \bar\theta)$ and $(\bar y, \theta, \bar\theta)$ they are given by

$$W_A = \lambda_A(y) + D(y)\theta_A - (\sigma^{\mu\nu}\theta)_A F_{\mu\nu}(y) + \mathrm{i}(\theta\theta)(\sigma^\mu\partial_\mu\bar\lambda(y))_A, \tag{D.145}$$

$$\bar W_{\dot A} = \mathrm{i}\bar\lambda_{\dot A}(\bar y) + D(\bar y)\bar\theta_{\dot A} - (\bar\sigma^{\mu\nu}\theta)_{\dot A} F_{\mu\nu}(\bar y) - \mathrm{i}(\theta\theta)(\sigma^\mu\partial_\mu\bar\lambda(\bar y))_{\dot A}, \tag{D.146}$$

with the usual $U(1)$ field-strength $F_{\mu\nu} = \partial_\mu A_\nu - \partial_\nu A_\mu$. Because of (D.140), each of this components is by itself gauge invariant.

D.7 Supersymmetric Lagrange Densities

With help of the in the previous section defined superfields, it is quite easy to write down supersymmetric Lagrange densities that leave the action invariant under global supersymmetry transformations,

$$S = \int \mathrm{d}^4 x\, \mathcal{L} \quad \rightarrow \quad \delta_\epsilon S = \int \mathrm{d}^4 x\, \delta_\epsilon \mathcal{L} = 0. \tag{D.147}$$

Because of Gauss's law, in order to fulfill (D.147), the Lagrangian density has to be invariant up to a total derrivative,

$$\delta_\epsilon \mathcal{L} = \partial_\mu V^\mu \quad \Rightarrow \quad \delta_\epsilon S = 0. \tag{D.148}$$

Eqs. (D.123) and (D.135) give suitable candidates for a supersymmetric Lagrange density, since the D-term of a general superfield and the F-term of a chiral superfield transform into a total derrivative. With help of the definition (A.38), a supersymmetric Lagrange density can therefore be written as

$$\mathcal{L} = \int \mathrm{d}\theta^4 (\text{general superfields}) + \int \mathrm{d}\theta^2 (\text{chiral superfields}) + \text{h.c.} \,. \tag{D.149}$$

For each chiral superfield Φ one can construct a kinematic term $\mathcal{L}_{\mathrm{kin}}$ by taking the D-term of the product of a chiral superfield with its conjugate, and a mass term $\mathcal{L}_{\mathrm{mass}}$ by taking the F-term of the squared of the superfields:

$$\mathcal{L}_{\mathrm{kin}} \equiv \int \mathrm{d}^4 \theta \left(\Phi^\dagger(x, \theta, \bar\theta) \Phi(x, \theta, \bar\theta) \right)$$

$$= (\partial_\mu \varphi^*)(\partial^\mu \varphi) + \frac{\mathrm{i}}{2} (\bar\psi \bar\sigma^\mu \partial_\mu \psi + \psi \sigma^\mu \partial_\mu \bar\psi) + F^* F, \tag{D.150}$$

$$\mathcal{L}_{\mathrm{mass}} \equiv \int \mathrm{d}^2 \theta \frac{m}{2} \Phi^2(y, \theta)\big|_{y \to x} + \text{h.c.}$$

$$= -\frac{m}{2} (\psi\psi + \bar\psi\bar\psi) + m(\varphi F + \varphi^* F^*). \tag{D.151}$$

As one can see, in this way one recovers the Lagrangian density for chiral fermions.

The mass term as well as other interactions between several chiral superfields Φ_i are usually given in terms of the superpotential $\mathcal{W}$ which is an analytic function of the fields. Renormalizability of the theory restrict the superpotential to be a Polynomial of power tree or less,

$$\mathcal{W} = c_i \Phi_i + \frac{1}{2} m_{ij} \Phi_i \Phi_j + \frac{1}{3!} g_{ijk} \Phi_i \Phi_j \Phi_k, \tag{D.152}$$

where the m_{ij} and g_{ijk} are symmetric in their indices. As a product of chiral superfields, the superpotential is itself a chiral superfield. Hence, the supersymmetric Lagrange density for the interaction Lagrangian $\mathcal{L}_{\mathrm{int}}$ is given by the F-term of the superpotential,

$$\mathcal{L}_{\mathrm{int}} = \int \mathrm{d}^2 \theta\, \mathcal{W} + \text{h.c.}$$

$$= c_i F_i + m_{ij} \left(\varphi_i F_j - \frac{1}{2} \psi_i \psi_j \right) + \frac{1}{2} g_{ijk} \left(\varphi_i \varphi_j F_k - \varphi_i(\psi_j \psi_k) \right) + \text{h.c.} \,. \tag{D.153}$$

The Lagrange density for the supersymmetric field strength $\mathcal{L}_{\text{gauge}}$ is defined in such a way that it incorporates the usual gauge kinetic terms,

$$\mathcal{L}_{\text{gauge}} \equiv \int \mathrm{d}^2\theta \left(\frac{1}{4} W^A(x,\theta,\bar{\theta}) W_A(x,\theta,\bar{\theta})\right) + h.c.$$

$$= \mathrm{i} \left(\lambda \sigma^\mu \partial_\mu \bar{\lambda} + \bar{\lambda} \bar{\sigma}^\mu \partial_\mu \lambda\right) - \frac{1}{4} F_{\mu\nu} F^{\mu\nu} + \frac{1}{2} D^2. \tag{D.154}$$

D.7.1 Supersymmetric Gauge Theories

The fundamental forces in nature are described in terms of local gauge-invariant field theories. Hence, in a realistic model one has to incorporate local gauge transformations into the supersymmetric Lagrangian. To construct a gauge- and supersymmetry-invariant Lagrangian density one makes use of the properties of the vector superfields, cf. Section D.6.2. For a $SU(N)$ gauge group with generators T_A in the fundamental representation that obey the Lie algebra

$$[T_a, T_b] = \mathrm{i} f_{abc} T_c \tag{D.155}$$

with the structure constants f_{abc}, one defines the chiral superfield $\Lambda(x,\theta,\bar{\theta})$ as

$$\Lambda = T_a \Lambda^a. \tag{D.156}$$

The supersymmetric gauge transformation on a $SU(N)$ vector-superfield multiplet in the adjoint representation $V(x,\theta,\bar{\theta})$ is defined as

$$e^{2gV} \to e^{-\mathrm{i}2g\Lambda^\dagger} e^{2gV} e^{\mathrm{i}2g\Lambda}. \tag{D.157}$$

In the case of a $U(1)$ symmetry eq. (D.138) is recovered.

A supersymmetric gauge transformation on a chiral superfield is defined as

$$\Phi' = e^{-\mathrm{i}2g\Lambda(x)} \Phi. \tag{D.158}$$

In order to be gauge invariant, the kinetic Lagrange density (D.149) has to be altered in the following way,

$$\mathcal{L}_{\text{kin}} = \int \mathrm{d}^4\theta \, \Phi^\dagger e^{2gV} \Phi \tag{D.159}$$

$$= (D_\mu \varphi)^\dagger (D^\mu \varphi) + \mathrm{i}\psi \sigma^\mu D_\mu^* \bar{\psi}$$

$$- \sqrt{2} g \left(\bar{\psi} \bar{\lambda} \varphi + \varphi^* \lambda \psi\right) + g T^a \varphi^* \varphi D + F^\dagger F, \tag{D.160}$$

with the gauge-covariant derivative $D_\mu = \partial_\mu + \mathrm{i} g A_\mu$. The non-Abelian supersymmetric field strength, is defined as

$$W_A := -\frac{1}{4} (\bar{D}\bar{D}) e^{-2gV} D_A e^{2gV}, \tag{D.161}$$

$$\bar{W}_{\dot{A}} := -\frac{1}{4} (DD) e^{-2gV} \bar{D}_{\dot{A}} e^{2gV}. \tag{D.162}$$

Since V is a bosonic function, (D.143) and (D.144) are recovered in the Abelian case. The supersymmetric field strength $\mathcal{L}_{\text{gauge}}$ is now given by

$$
\begin{aligned}
\mathcal{L}_{\text{gauge}} &= \frac{1}{16g^2} \int \mathrm{d}^2\theta \, \mathrm{Tr} \left(W^A W_A \right) + \text{h.c.} \\
&= -\frac{1}{4} F^a_{\mu\nu} F^{a\,\mu\nu} + \mathrm{i}\lambda^a \sigma^\mu D_\mu \bar{\lambda}^a + \frac{1}{2} D^a D^a.
\end{aligned}
\tag{D.163}
$$

For the superpotential (D.152) only gauge-invariant combinations of chiral fields are allowed. This strongly restricts the possible field combinations. Putting all together, the supersymmetric Lagrange density for n chiral fields can be written as

$$
\begin{aligned}
\mathcal{L} &= \sum_{i=1}^{n} \mathcal{L}_{\text{kin},i} + \mathcal{L}_{\text{gauge}} + \mathcal{L}_{\text{int}} \tag{D.164} \\
&= (D_\mu \varphi_i)^\dagger (D^\mu \varphi_i) + \mathrm{i}\,\psi_i \sigma^\mu D^*_\mu \bar{\psi}_i - \sqrt{2} g \left(\bar{\psi}_i \bar{\lambda}\varphi_i - \varphi^*_i \lambda\psi_i \right) + g T^a \varphi^*_i \varphi_i D + F^\dagger_i F_i \\
&\quad - \frac{1}{4} F^a_{\mu\nu} F^{a\,\mu\nu} + i\lambda^a \bar{\sigma}^\mu D_\mu \bar{\lambda}^a + \frac{1}{2} D^a D^a \\
&\quad + c_i F_i + m_{ij} \left(\varphi_i F_j - \psi_i \psi_j \right) + \frac{1}{2} g_{ijk} \left(\varphi_i \varphi_j F_k - \varphi_i (\psi_j \psi_k) \right) + \text{h.c.}. \tag{D.165}
\end{aligned}
$$

The two auxiliary fields F_i and D do not have a kinematic term and can hence be eliminated with help of the Euler–Lagrange equation of motion,

$$
\frac{\partial \mathcal{L}}{\partial F_i} = \frac{\partial \mathcal{L}}{\partial D} = 0.
\tag{D.166}
$$

Bibliography

[1] I. Newton, *Philosophiae naturalis principia mathematica*, *Royal Society* (1687).

[2] J. Maxwell, *A dynamical theory of the electromagnetic field*, *Philosophical Transactions of the Royal Society of London* **155** (1865) 459–512.

[3] A. Michelson and E. Morley, *On the relative motion of the earth and the luminiferous ether*, *American Journal of Science* **34** (1887) 333–345.

[4] A. Einstein, *Zur Elektrodynamik bewegter Körper*, *Annalen der Physik und Chemie* **17** (1905) 891–921.

[5] A. Einstein, *The foundation of the general theory of relativity*, *Annalen Phys.* **49** (1916) 769–822.

[6] W. Gerlach and O. Stern, *Das magnetische moment des silberatoms*, *Zeitschrift für Physik* **9** (1922) 353–355.

[7] W. Heisenberg, *Über den anschaulichen Inhalt der quantentheoretischen Kinematik und Mechanik*, *Zeitschrift für Physik* **43** (1927) 172–198.

[8] R. P. Feynman, *Mathematical formulation of the quantum theory of electromagnetic interaction*, *Phys. Rev.* **80** (1950) 440–457.

J. S. Schwinger, *Quantum electrodynamics. I: A covariant formulation*, *Phys. Rev.* **74** (1948) 1439.

S. Tomonaga, *On a relativistically invariant formulation of the quantum theory of wave fields*, *Prog. Theor. Phys.* **1** (1946) 27–42.

[9] S. Weinberg, *A Model of Leptons*, *Phys. Rev. Lett.* **19** (1967) 1264–1266.

S. L. Glashow, *Partial Symmetries of Weak Interactions*, *Nucl. Phys.* **22** (1961) 579–588.

A. Salam, *Weak and Electromagnetic Interactions*, . Originally printed in *Svartholm: Elementary Particle Theory, Proceedings Of The Nobel Symposium Held 1968 At Lerum, Sweden*, Stockholm 1968, 367-377.

[10] M. Gell-Mann, *Quarks*, *Acta Phys. Austriaca Suppl.* **9** (1972) 733–761.

H. Fritzsch, M. Gell-Mann, and H. Leutwyler, *Advantages of the Color Octet Gluon Picture*, *Phys. Lett.* **B47** (1973) 365–368.

D. J. Gross and F. Wilczek, *Asymptotically Free Gauge Theories. 1*, Phys. Rev. **D8** (1973) 3633–3652.

D. J. Gross and F. Wilczek, *Ultraviolet behavior of non-Abelian gauge theories*, Phys. Rev. Lett. **30** (1973) 1343–1346.

H. D. Politzer, *Reliable perturbative results for strong interactions?*, Phys. Rev. Lett. **30** (1973) 1346–1349.

[11] F. Englert and R. Brout, *Broken symmetry and the mass of the gauge vector mesons*, Phys. Rev. Lett. **13** (1964) 321–322.

P. W. Higgs, *Broken symmetries, massless particles and gauge fields*, Phys. Lett. **12** (1964) 132–133.

T. W. B. Kibble, *Symmetry breaking in non-Abelian gauge theories*, Phys. Rev. **155** (1967) 1554–1561.

[12] J. Wess and B. Zumino, *A Lagrangian Model Invariant Under Supergauge Transformations*, Phys. Lett. **B49** (1974) 52.

[13] A. Salam and J. A. Strathdee, *Supersymmetry and Fermion Number Conservation*, Nucl. Phys. **B87** (1975) 85.

P. Fayet, *Supergauge Invariant Extension of the Higgs Mechanism and a Model for the electron and Its Neutrino*, Nucl. Phys. **B90** (1975) 104–124.

G. R. Farrar and P. Fayet, *Phenomenology of the Production, Decay, and Detection of New Hadronic States Associated with Supersymmetry*, Phys. Lett. **B76** (1978) 575–579.

[14] **Particle Data Group** Collaboration, K. Nakamura *et. al.*, *Review of particle physics*, J. Phys. **G37** (2010) 075021.

[15] H. P. Nilles, *Supersymmetry, Supergravity and Particle Physics*, Phys. Rept. **110** (1984) 1–162.

[16] H. E. Haber and G. L. Kane, *The Search for Supersymmetry: Probing Physics Beyond the Standard Model*, Phys. Rept. **117** (1985) 75–263.

[17] P. R. Harrison and C. H. Llewellyn Smith, *Hadroproduction of Supersymmetric Particles*, Nucl. Phys. **B213** (1983) 223.

S. Dawson, E. Eichten, and C. Quigg, *Search for Supersymmetric Particles in Hadron - Hadron Collisions*, Phys. Rev. **D31** (1985) 1581.

E. Reya and D. P. Roy, *Supersymmetric particle production at p anti-p collider energies*, Phys. Rev. **D32** (1985) 645.

H. Baer and X. Tata, *Component formulae for hadroproduction of left-handed and right-handed squarks*, Phys. Lett. **B160** (1985) 159.

[18] W. Beenakker, R. Hopker, M. Spira, and P. M. Zerwas, *Squark and gluino production at hadron colliders*, *Nucl. Phys.* **B492** (1997) 51–103, [`hep-ph/9610490`].

[19] W. Beenakker, M. Kramer, T. Plehn, M. Spira, and P. M. Zerwas, *Stop production at hadron colliders*, *Nucl. Phys.* **B515** (1998) 3–14, [`hep-ph/9710451`].

[20] A. Kulesza and L. Motyka, *Threshold resummation for squark-antisquark and gluino-pair production at the LHC*, *Phys. Rev. Lett.* **102** (2009) 111802, [`arXiv:0807.2405`].

[21] A. Kulesza and L. Motyka, *Soft gluon resummation for the production of gluino-gluino and squark-antisquark pairs at the LHC*, *Phys. Rev.* **D80** (2009) 095004, [`arXiv:0905.4749`].

[22] W. Beenakker *et. al.*, *Soft-gluon resummation for squark and gluino hadroproduction*, *JHEP* **12** (2009) 041, [`arXiv:0909.4418`].

[23] W. Beenakker *et. al.*, *Supersymmetric top and bottom squark production at hadron colliders*, *JHEP* **08** (2010) 098, [`arXiv:1006.4771`].

[24] U. Langenfeld and S.-O. Moch, *Higher-order soft corrections to squark hadro-production*, *Phys. Lett.* **B675** (2009) 210–221, [`arXiv:0901.0802`].

[25] S. Bornhauser, M. Drees, H. K. Dreiner, and J. S. Kim, *Electroweak Contributions to Squark Pair Production at the LHC*, *Phys. Rev.* **D76** (2007) 095020, [`arXiv:0709.2544`].

[26] W. Hollik, M. Kollar, and M. K. Trenkel, *Hadronic production of top-squark pairs with electroweak NLO contributions*, *JHEP* **02** (2008) 018, [`arXiv:0712.0287`].

[27] W. Hollik and E. Mirabella, *Electroweak corrections to squark–anti-squark pair production at the LHC*, *Nuovo Cim.* **123B** (2008) 803–805, [`arXiv:0807.4124`].

[28] W. Hollik, E. Mirabella, and M. K. Trenkel, *Electroweak contributions to squark–gluino production at the LHC*, *JHEP* **02** (2009) 002, [`arXiv:0810.1044`].

[29] E. Mirabella, *NLO electroweak contributions to gluino pair production at hadron colliders*, *JHEP* **12** (2009) 012, [`arXiv:0908.3318`].

[30] J. Germer, W. Hollik, E. Mirabella, and M. K. Trenkel, *Hadronic production of squark-squark pairs: The electroweak contributions*, *JHEP* **08** (2010) 023, [`arXiv:1004.2621`].

[31] J. Germer, W. Hollik, E. Mirabella, and M. K. Trenkel, *NLO electroweak contributions to squark pair production at the LHC*, *AIP Conf. Proc.* **1200** (2010) 329–332, [`arXiv:0909.3046`].

[32] J. Germer, W. Hollik, and E. Mirabella, *Hadronic production of bottom-squark pairs with electroweak contributions*, `arXiv:1103.1258`.

[33] J. Goldstone, A. Salam, and S. Weinberg, *Broken Symmetries*, *Phys. Rev.* **127** (1962) 965–970.

[34] S. L. Glashow, J. Iliopoulos, and L. Maiani, *Weak Interactions with Lepton-Hadron Symmetry*, *Phys. Rev.* **D2** (1970) 1285–1292.

[35] G. 't Hooft and M. J. G. Veltman, *Regularization and Renormalization of Gauge Fields*, *Nucl. Phys.* **B44** (1972) 189–213.

[36] J. Goldstone, *Field Theories with Superconductor Solutions*, *Nuovo Cim.* **19** (1961) 154–164.

[37] N. Cabibbo, *Unitary Symmetry and Leptonic Decays*, *Phys. Rev. Lett.* **10** (1963) 531–533.

[38] M. Kobayashi and T. Maskawa, *CP Violation in the Renormalizable Theory of Weak Interaction*, *Prog. Theor. Phys.* **49** (1973) 652–657.

[39] U. Amaldi, W. de Boer, and H. Furstenau, *Comparison of grand unified theories with electroweak and strong coupling constants measured at LEP*, *Phys. Lett.* **B260** (1991) 447–455.

[40] A. D. Sakharov, *Violation of CP Invariance, c Asymmetry, and Baryon Asymmetry of the Universe*, *Pisma Zh. Eksp. Teor. Fiz.* **5** (1967) 32–35.

[41] F. R. Klinkhamer and N. S. Manton, *A Saddle Point Solution in the Weinberg-Salam Theory*, *Phys. Rev.* **D30** (1984) 2212.

[42] **LEP Working Group for Higgs boson searches** Collaboration, R. Barate *et. al.*, *Search for the standard model Higgs boson at LEP*, *Phys. Lett.* **B565** (2003) 61–75, [hep-ex/0306033].

[43] T. Hambye and K. Riesselmann, *Matching conditions and Higgs mass upper bounds revisited*, *Phys. Rev.* **D55** (1997) 7255–7262, [hep-ph/9610272].

[44] **Muon G-2** Collaboration, G. W. Bennett *et. al.*, *Final report of the muon E821 anomalous magnetic moment measurement at BNL*, *Phys. Rev.* **D73** (2006) 072003, [hep-ex/0602035].

[45] T. Moroi, *The Muon Anomalous Magnetic Dipole Moment in the Minimal Supersymmetric Standard Model*, *Phys. Rev.* **D53** (1996) 6565–6575, [hep-ph/9512396].

[46] A. Czarnecki and W. J. Marciano, *The muon anomalous magnetic moment: A harbinger for 'new physics'*, *Phys. Rev.* **D64** (2001) 013014, [hep-ph/0102122].

[47] M. Davier, *The hadronic contribution to (g-2)(mu)*, *Nucl. Phys. Proc. Suppl.* **169** (2007) 288–296, [hep-ph/0701163].

[48] J. P. Miller, E. de Rafael, and B. L. Roberts, *Muon g-2: Review of Theory and Experiment*, *Rept. Prog. Phys.* **70** (2007) 795, [`hep-ph/0703049`].

[49] F. Jegerlehner, *Essentials of the Muon g-2*, *Acta Phys. Polon.* **B38** (2007) 3021, [`hep-ph/0703125`].

[50] M. Passera, W. J. Marciano, and A. Sirlin, *The Muon g-2 and the bounds on the Higgs boson mass*, *Phys. Rev.* **D78** (2008) 013009, [`arXiv:0804.1142`].

[51] S. R. Coleman and J. Mandula, *All possible symmetries of the S matrix*, *Phys. Rev.* **159** (1967) 1251–1256.

[52] R. Haag, J. T. Lopuszanski, and M. Sohnius, *All Possible Generators of Supersymmetries of the s Matrix*, *Nucl. Phys.* **B88** (1975) 257.

[53] J. Iliopoulos and B. Zumino, *Broken Supergauge Symmetry and Renormalization*, *Nucl. Phys.* **B76** (1974) 310.

[54] S. Ferrara, J. Iliopoulos, and B. Zumino, *Supergauge Invariance and the Gell-Mann - Low Eigenvalue*, *Nucl. Phys.* **B77** (1974) 413.

[55] B. Zumino, *Supersymmetry and the Vacuum*, *Nucl. Phys.* **B89** (1975) 535.

[56] M. T. Grisaru, W. Siegel, and M. Rocek, *Improved Methods for Supergraphs*, *Nucl. Phys.* **B159** (1979) 429.

[57] S. Heinemeyer, W. Hollik, D. Stockinger, A. M. Weber, and G. Weiglein, *Precise prediction for M(W) in the MSSM*, *JHEP* **08** (2006) 052, [`hep-ph/0604147`].

[58] D. Stockinger, *The muon magnetic moment and supersymmetry*, *J. Phys.* **G34** (2007) R45–R92, [`hep-ph/0609168`].

[59] O. Buchmueller *et. al.*, *Prediction for the Lightest Higgs Boson Mass in the CMSSM using Indirect Experimental Constraints*, *Phys. Lett.* **B657** (2007) 87–94, [`arXiv:0707.3447`].

[60] S. L. Adler, *Axial vector vertex in spinor electrodynamics*, *Phys. Rev.* **177** (1969) 2426–2438.

[61] W. A. Bardeen, *Anomalous Ward identities in spinor field theories*, *Phys. Rev.* **184** (1969) 1848–1857.

[62] J. S. Bell and R. Jackiw, *A PCAC puzzle: pi0 → gamma gamma in the sigma model*, *Nuovo Cim.* **A60** (1969) 47–61.

[63] G. R. Farrar and S. Weinberg, *Supersymmetry at ordinary energies. 2. R-invariance, Goldstone bosons, and gauge fermion masses*, *Phys. Rev.* **D27** (1983) 2732.

[64] L. M. Krauss and F. Wilczek, *Discrete Gauge Symmetry in Continuum Theories*, *Phys. Rev. Lett.* **62** (1989) 1221.

[65] L. Girardello and M. T. Grisaru, *Soft Breaking of Supersymmetry*, *Nucl. Phys.* **B194** (1982) 65.

[66] T. Ibrahim and P. Nath, *The neutron and the lepton EDMs in MSSM, large CP violating phases, and the cancellation mechanism*, *Phys. Rev.* **D58** (1998) 111301, [`hep-ph/9807501`].

[67] M. Brhlik, G. J. Good, and G. L. Kane, *Electric dipole moments do not require the CP-violating phases of supersymmetry to be small*, *Phys. Rev.* **D59** (1999) 115004, [`hep-ph/9810457`].

[68] L. J. Hall, V. A. Kostelecky, and S. Raby, *New Flavor Violations in Supergravity Models*, *Nucl. Phys.* **B267** (1986) 415.

[69] H. E. Haber, *The status of the minimal supersymmetric standard model and beyond*, *Nucl. Phys. Proc. Suppl.* **62** (1998) 469–484, [`hep-ph/9709450`].

[70] A. H. Chamseddine, R. L. Arnowitt, and P. Nath, *Locally Supersymmetric Grand Unification*, *Phys. Rev. Lett.* **49** (1982) 970.

[71] R. Barbieri, S. Ferrara, and C. A. Savoy, *Gauge Models with Spontaneously Broken Local Supersymmetry*, *Phys. Lett.* **B119** (1982) 343.

[72] M. Dine and A. E. Nelson, *Dynamical supersymmetry breaking at low-energies*, *Phys. Rev.* **D48** (1993) 1277–1287, [`hep-ph/9303230`].

[73] M. Dine, A. E. Nelson, and Y. Shirman, *Low-energy dynamical supersymmetry breaking simplified*, *Phys. Rev.* **D51** (1995) 1362–1370, [`hep-ph/9408384`].

[74] M. Dine, A. E. Nelson, Y. Nir, and Y. Shirman, *New tools for low-energy dynamical supersymmetry breaking*, *Phys. Rev.* **D53** (1996) 2658–2669, [`hep-ph/9507378`].

[75] L. Randall and R. Sundrum, *Out of this world supersymmetry breaking*, *Nucl. Phys.* **B557** (1999) 79–118, [`hep-th/9810155`].

[76] G. F. Giudice, M. A. Luty, H. Murayama, and R. Rattazzi, *Gaugino Mass without Singlets*, *JHEP* **12** (1998) 027, [`hep-ph/9810442`].

[77] H. E. Haber and R. Hempfling, *The Renormalization group improved Higgs sector of the minimal supersymmetric model*, *Phys. Rev.* **D48** (1993) 4280–4309, [`hep-ph/9307201`].

[78] H. E. Haber, R. Hempfling, and A. H. Hoang, *Approximating the radiatively corrected Higgs mass in the minimal supersymmetric model*, *Z. Phys.* **C75** (1997) 539–554, [`hep-ph/9609331`].

[79] M. S. Carena, M. Olechowski, S. Pokorski, and C. E. M. Wagner, *Electroweak symmetry breaking and bottom - top Yukawa unification*, *Nucl. Phys.* **B426** (1994) 269–300, [`hep-ph/9402253`].

[80] L. J. Hall, R. Rattazzi, and U. Sarid, *The Top quark mass in supersymmetric SO(10) unification*, *Phys. Rev.* **D50** (1994) 7048–7065, [`hep-ph/9306309`].

[81] R. Hempfling, *Yukawa coupling unification with supersymmetric threshold corrections*, *Phys. Rev.* **D49** (1994) 6168–6172.

[82] D. M. Pierce, J. A. Bagger, K. T. Matchev, and R.-j. Zhang, *Precision corrections in the minimal supersymmetric standard model*, *Nucl. Phys.* **B491** (1997) 3–67, [`hep-ph/9606211`].

[83] M. S. Carena, D. Garcia, U. Nierste, and C. E. M. Wagner, *Effective Lagrangian for the $\bar{t}bH^+$ interaction in the MSSM and charged Higgs phenomenology*, *Nucl. Phys.* **B577** (2000) 88–120, [`hep-ph/9912516`].

[84] M. S. Carena and H. E. Haber, *Higgs boson theory and phenomenology. ((V))*, *Prog. Part. Nucl. Phys.* **50** (2003) 63–152, [`hep-ph/0208209`].

[85] **ATLAS** Collaboration, W. W. Armstrong *et. al.*, *ATLAS: Technical proposal for a general-purpose p p experiment at the Large Hadron Collider at CERN*, . CERN-LHCC-94-43.

[86] *CMS, the Compact Muon Solenoid: Technical proposal*, . CERN-LHCC-94-38.

[87] R. H. Hierck, *Physics performance study of the B/s0 –> D/s pi and B/s0 –> D/s K decay channels for the technical proposal of the LHCb detector*, . CERN-THESIS-2000-045.

[88] *ALICE: Technical proposal for a large ion collider experiment at the CERN LHC*, . CERN-LHCC-95-71.

[89] P. de Jong, *Prospects for SUSY searches in CMS and ATLAS*, *AIP Conf. Proc.* **1078** (2009) 21–29, [`arXiv:0809.3708`].

[90] B. C. Allanach *et. al.*, *The Snowmass points and slopes: Benchmarks for SUSY searches*, *Eur. Phys. J.* **C25** (2002) 113–123, [`hep-ph/0202233`].

[91] **LHC/LC Study Group** Collaboration, G. Weiglein *et. al.*, *Physics interplay of the LHC and the ILC*, *Phys. Rept.* **426** (2006) 47–358, [`hep-ph/0410364`].

[92] B. C. Allanach, C. G. Lester, M. A. Parker, and B. R. Webber, *Measuring sparticle masses in non-universal string inspired models at the LHC*, *JHEP* **09** (2000) 004, [`hep-ph/0007009`].

[93] **D0** Collaboration, V. M. Abazov *et. al.*, *Search for squarks and gluinos in events with jets and missing transverse energy using 2.1 fb^{-1} of p$\bar{p}$ collision data at $\sqrt{s} = 1.96$- TeV*, *Phys. Lett.* **B660** (2008) 449–457, [`arXiv:0712.3805`].

[94] **CDF** Collaboration, T. Aaltonen *et. al.*, *Inclusive Search for Squark and Gluino Production in p$\bar{p}$ Collisions at $\sqrt{s} = 1.96$-TeV*, *Phys. Rev. Lett.* **102** (2009) 121801, [`arXiv:0811.2512`].

[95] J. Hisano, K. Kawagoe, R. Kitano, and M. M. Nojiri, *Scenery from the top: Study of the third generation squarks at CERN LHC*, *Phys. Rev.* **D66** (2002) 115004, [`hep-ph/0204078`].

[96] J. Hisano, K. Kawagoe, and M. M. Nojiri, *A detailed study of the gluino decay into the third generation squarks at the CERN LHC*, *Phys. Rev.* **D68** (2003) 035007, [`hep-ph/0304214`].

[97] **D0** Collaboration, V. M. Abazov *et. al.*, *Search for scalar bottom quarks and third-generation leptoquarks in ppbar collisions at sqrt(s) = 1.96 TeV*, `arXiv:1005.2222`.

[98] **CDF** Collaboration, T. Aaltonen *et. al.*, *Search for the Production of Scalar Bottom Quarks in ppbar collisions at sqrt(s) = 1.96 TeV*, *Phys. Rev. Lett.* **105** (2010) 081802, [`arXiv:1005.3600`].

[99] **D0** Collaboration, V. M. Abazov *et. al.*, *Search for pair production of scalar bottom quarks in p$\bar{p}$ collisions at $\sqrt{s} = 1.96$-TeV*, *Phys. Rev. Lett.* **97** (2006) 171806, [`hep-ex/0608013`].

[100] O. Buchmueller *et. al.*, *Predictions for Supersymmetric Particle Masses in the CMSSM using Indirect Experimental and Cosmological Constraints*, *JHEP* **09** (2008) 117, [`arXiv:0808.4128`].

[101] **WMAP** Collaboration, J. Dunkley *et. al.*, *Five-Year Wilkinson Microwave Anisotropy Probe (WMAP) Observations: Likelihoods and Parameters from the WMAP data*, *Astrophys. J. Suppl.* **180** (2009) 306–329, [`arXiv:0803.0586`].

[102] **CMS** Collaboration, G. L. Bayatian *et. al.*, *CMS technical design report, volume II: Physics performance*, *J. Phys.* **G34** (2007) 995–1579.

[103] *ATLAS detector and physics performance. Technical design report. Vol. 2*, . CERN-LHCC-99-15.

[104] H. Baer, A. Mustafayev, S. Profumo, A. Belyaev, and X. Tata, *Neutralino cold dark matter in a one parameter extension of the minimal supergravity model*, *Phys. Rev.* **D71** (2005) 095008, [`hep-ph/0412059`].

[105] J. C. Collins, D. E. Soper, and G. F. Sterman, *Factorization of Hard Processes in QCD*, *Adv. Ser. Direct. High Energy Phys.* **5** (1988) 1–91, [`hep-ph/0409313`].

[106] W. Beenakker, R. Hopker, and M. Spira, *PROSPINO: A program for the PROduction of Supersymmetric Particles In Next-to-leading Order QCD*, `hep-ph/9611232`.

[107] G. Bozzi, B. Fuks, and M. Klasen, *Non-diagonal and mixed squark production at hadron colliders*, *Phys. Rev.* **D72** (2005) 035016, [`hep-ph/0507073`].

[108] A. Arhrib, R. Benbrik, K. Cheung, and T.-C. Yuan, *Higgs boson enhancement effects on squark-pair production at the LHC*, *JHEP* **02** (2010) 048, [`arXiv:0911.1820`].

[109] L. H. Ryder, *Quantum Field Theory*, . Cambridge, Uk: Univ. Pr. (1985) 443p.

[110] M. E. Peskin and D. V. Schroeder, *An Introduction to quantum field theory*, . Reading, USA: Addison-Wesley (1995) 842 p.

[111] R. K. Ellis, W. J. Stirling, and B. R. Webber, *QCD and collider physics*, *Camb. Monogr. Part. Phys. Nucl. Phys. Cosmol.* **8** (1996) 1–435.

[112] M. Bohm, A. Denner, and H. Joos, *Gauge theories of the strong and electroweak interaction*, . Stuttgart, Germany: Teubner (2001) 784 p.

[113] J. D. Bjorken, *Asymptotic Sum Rules at Infinite Momentum*, *Phys. Rev.* **179** (1969) 1547–1553.

[114] R. P. Feynman, *Photon-hadron interactions*, . Reading 1972, 282p.

[115] V. N. Gribov and L. N. Lipatov, *e+ e- pair annihilation and deep inelastic e p scattering in perturbation theory*, *Sov. J. Nucl. Phys.* **15** (1972) 675–684.

[116] L. N. Lipatov, *The parton model and perturbation theory*, *Sov. J. Nucl. Phys.* **20** (1975) 94–102.

[117] Y. L. Dokshitzer, *Calculation of the Structure Functions for Deep Inelastic Scattering and e+ e- Annihilation by Perturbation Theory in Quantum Chromodynamics*, *Sov. Phys. JETP* **46** (1977) 641–653.

[118] G. Altarelli and G. Parisi, *Asymptotic Freedom in Parton Language*, *Nucl. Phys.* **B126** (1977) 298.

[119] G. Curci, W. Furmanski, and R. Petronzio, *Evolution of Parton Densities Beyond Leading Order: The Nonsinglet Case*, *Nucl. Phys.* **B175** (1980) 27.

[120] W. Furmanski and R. Petronzio, *Singlet Parton Densities Beyond Leading Order*, *Phys. Lett.* **B97** (1980) 437.

[121] E. G. Floratos, D. A. Ross, and C. T. Sachrajda, *Higher Order Effects in Asymptotically Free Gauge Theories: The Anomalous Dimensions of Wilson Operators*, Nucl. Phys. **B129** (1977) 66–88.

[122] A. Gonzalez-Arroyo, C. Lopez, and F. J. Yndurain, *Second Order Contributions to the Structure Functions in Deep Inelastic Scattering. 1. Theoretical Calculations*, Nucl. Phys. **B153** (1979) 161–186.

[123] E. G. Floratos, C. Kounnas, and R. Lacaze, *Higher Order QCD Effects in Inclusive Annihilation and Deep Inelastic Scattering*, Nucl. Phys. **B192** (1981) 417.

[124] S. Moch, J. A. M. Vermaseren, and A. Vogt, *The three-loop splitting functions in QCD: The non-singlet case*, Nucl. Phys. **B688** (2004) 101–134, [`hep-ph/0403192`].

[125] A. Vogt, S. Moch, and J. A. M. Vermaseren, *The three-loop splitting functions in QCD: The singlet case*, Nucl. Phys. **B691** (2004) 129–181, [`hep-ph/0404111`].

[126] A. D. Martin, R. G. Roberts, W. J. Stirling, and R. S. Thorne, *Parton distributions incorporating QED contributions*, Eur. Phys. J. **C39** (2005) 155–161, [`hep-ph/0411040`].

[127] W. Hollik and D. Stockinger, *Regularization and supersymmetry-restoring counterterms in supersymmetric QCD*, Eur. Phys. J. **C20** (2001) 105–119, [`hep-ph/0103009`].

[128] W. Hollik *et. al.*, *Renormalization of the minimal supersymmetric standard model*, Nucl. Phys. **B639** (2002) 3–65, [`hep-ph/0204350`].

[129] C. G. Bollini and J. J. Giambiagi, *Lowest order divergent graphs in nu-dimensional space*, Phys. Lett. **B40** (1972) 566–568.

[130] J. C. Collins, *Renormalization. An introduction to renormalization, the renormalization group, and operator product expansion*, . Cambridge, Uk: Univ. Pr. (1984) 380p.

[131] W. Siegel, *Supersymmetric Dimensional Regularization via Dimensional Reduction*, Phys. Lett. **B84** (1979) 193.

[132] W. Siegel, *Inconsistency of Supersymmetric Dimensional Regularization*, Phys. Lett. **B94** (1980) 37.

[133] D. Stockinger, *Regularization by dimensional reduction: Consistency, quantum action principle, and supersymmetry*, JHEP **03** (2005) 076, [`hep-ph/0503129`].

[134] M. Bohm, H. Spiesberger, and W. Hollik, *On the One Loop Renormalization of the Electroweak Standard Model and Its Application to Leptonic Processes*, Fortsch. Phys. **34** (1986) 687–751.

[135] A. Denner, *Techniques for calculation of electroweak radiative corrections at the one loop level and results for W physics at LEP-200, Fortschr. Phys.* **41** (1993) 307–420, [`arXiv:0709.1075`].

[136] T. Fritzsche, *Berechnung von Observablen zur supersymmetrischen Teilchenerzeugung an Hochenergie-Collidern unter Einschlußhöherer Ordnungen.* PhD thesis, Universität Karlsruhe, 2005.

[137] W. A. Bardeen, A. J. Buras, D. W. Duke, and T. Muta, *Deep Inelastic Scattering Beyond the Leading Order in Asymptotically Free Gauge Theories, Phys. Rev.* **D18** (1978) 3998.

[138] G. 't Hooft, *Dimensional regularization and the renormalization group, Nucl. Phys.* **B61** (1973) 455–468.

[139] I. I. Y. Bigi, Y. L. Dokshitzer, V. A. Khoze, J. H. Kuhn, and P. M. Zerwas, *Production and Decay Properties of Ultraheavy Quarks, Phys. Lett.* **B181** (1986) 157.

[140] **Tevatron Electroweak Working Group** Collaboration, *Combination of CDF and D0 Results on the Mass of the Top Quark*, 2009.

[141] U. Langenfeld, S. Moch, and P. Uwer, *Measuring the running top-quark mass, Phys. Rev.* **D80** (2009) 054009, [`arXiv:0906.5273`].

[142] S. Moch, U. Langenfeld, and P. Uwer, *The top-quark's running mass, PoS* **RADCOR2009** (2010) 030, [`arXiv:1001.3987`].

[143] W. Hollik and H. Rzehak, *The sfermion mass spectrum of the MSSM at the one-loop level, Eur. Phys. J.* **C32** (2003) 127–133, [`hep-ph/0305328`].

[144] S. Heinemeyer, W. Hollik, H. Rzehak, and G. Weiglein, *High-precision predictions for the MSSM Higgs sector at $O(\alpha(b)\alpha(s))$, Eur. Phys. J.* **C39** (2005) 465–481, [`hep-ph/0411114`].

[145] S. Heinemeyer, H. Rzehak, and C. Schappacher, *Proposals for Bottom Quark/Squark Renormalization in the Complex MSSM*, `arXiv:1007.0689`.

[146] S. Bethke, *The 2009 Wolrd Average of $\alpha_s(M_Z)$, Eur. Phys. J.* **C64** (2009) 689–703, [`arXiv:0908.1135`].

[147] T. Appelquist and J. Carazzone, *Infrared Singularities and Massive Fields, Phys. Rev.* **D11** (1975) 2856.

[148] W. Bernreuther and W. Wetzel, *Decoupling of heavy quarks in the minimal subtraction scheme, Nucl. Phys.* **B197** (1982) 228.

[149] F. Bloch and A. Nordsieck, *Note on the Radiation Field of the electron, Phys.Rev.* **52** (1937) 54–59.

[150] T. Kinoshita, *Mass singularities of Feynman amplitudes*, *J.Math.Phys.* **3** (1962) 650–677.

[151] S. Catani and M. Seymour, *A General algorithm for calculating jet cross-sections in NLO QCD*, *Nucl.Phys.* **B485** (1997) 291–419, [`hep-ph/9605323`].

[152] S. Catani, S. Dittmaier, M. H. Seymour, and Z. Trocsanyi, *The Dipole formalism for next-to-leading order QCD calculations with massive partons*, *Nucl.Phys.* **B627** (2002) 189–265, [`hep-ph/0201036`].

[153] S. Dittmaier, A. Kabelschacht, and T. Kasprzik, *Polarized QED splittings of massive fermions and dipole subtraction for non-collinear-safe observables*, *Nucl.Phys.* **B800** (2008) 146–189, [`0802.1405`].

[154] Z. Kunszt and D. E. Soper, *Calculation of jet cross-sections in hadron collisions at order alpha-s**3*, *Phys. Rev.* **D46** (1992) 192–221.

[155] U. Baur, S. Keller, and D. Wackeroth, *Electroweak radiative corrections to W boson production in hadronic collisions*, *Phys.Rev.* **D59** (1999) 013002, [`hep-ph/9807417`].

[156] W. Hollik, T. Kasprzik, and B. Kniehl, *Electroweak corrections to W-boson hadroproduction at finite transverse momentum*, *Nucl.Phys.* **B790** (2008) 138–159, [`0707.2553`].

[157] Piessens, Doncker, Überhuber, Kahaner, *Quadpack – A Subroutine Package for Automatic Integration*. Springer-Verlag, 1983.

[158] R. Bellman, *Dynamic Programming*. Dover Books on Mathematics. Dover Publications, 2003.

[159] G. P. Lepage, *A New Algorithm for Adaptive Multidimensional Integration*, *J. Comput. Phys.* **27** (1978) 192.

[160] G. P. Lepage, *VEGAS: An adaptive multidimensional integration program*, . CLNS-80/447.

[161] T. Hahn and M. Rauch, *News from FormCalc and LoopTools*, *Nucl. Phys. Proc. Suppl.* **157** (2006) 236–240, [`hep-ph/0601248`].

[162] T. Hahn, *Generating Feynman diagrams and amplitudes with FeynArts 3*, *Comput. Phys. Commun.* **140** (2001) 418–431, [`hep-ph/0012260`].

[163] T. Hahn and C. Schappacher, *The implementation of the minimal supersymmetric standard model in FeynArts and FormCalc*, *Comput. Phys. Commun.* **143** (2002) 54–68, [`hep-ph/0105349`].

[164] A. X. El-Khadra and M. Luke, *The Mass of the b Quark*, *Ann. Rev. Nucl. Part. Sci.* **52** (2002) 201–251, [`hep-ph/0208114`].

[165] J. A. Aguilar-Saavedra *et. al.*, *Supersymmetry parameter analysis: SPA convention and project*, *Eur. Phys. J.* **C46** (2006) 43–60, [hep-ph/0511344].

[166] B. C. Allanach, *SOFTSUSY: A C++ program for calculating supersymmetric spectra*, *Comput. Phys. Commun.* **143** (2002) 305–331, [hep-ph/0104145].

[167] A. D. Martin, R. G. Roberts, W. J. Stirling, and R. S. Thorne, *NNLO global parton analysis*, *Phys. Lett.* **B531** (2002) 216–224, [hep-ph/0201127].

[168] J. Germer and W. J. Stirling. Private discussion.

[169] A. D. Martin, R. G. Roberts, W. J. Stirling, and R. S. Thorne, *Physical gluons and high E(T) jets*, *Phys. Lett.* **B604** (2004) 61–68, [hep-ph/0410230].

[170] S. Dittmaier and M. Kramer, 1, *Electroweak radiative corrections to W-boson production at hadron colliders*, *Phys. Rev.* **D65** (2002) 073007, [hep-ph/0109062].

[171] F. E. Paige, *SUSY signatures in ATLAS at LHC*, hep-ph/0307342.

[172] M. Chiorboli and A. Tricomi, *Squark and gluino reconstruction in CMS*, . CMS-NOTE-2004-029.

[173] K. Kawagoe, M. M. Nojiri, and G. Polesello, *A new SUSY mass reconstruction method at the CERN LHC*, *Phys. Rev.* **D71** (2005) 035008, [hep-ph/0410160].

[174] **ATLAS** Collaboration, *Early supersymmetry searches in events with missing transverse energy and b-jets with the ATLAS detector*, . ATLAS-CONF-2010-079.

[175] **Particle Data Group** Collaboration, C. Amsler *et. al.*, *Review of particle physics*, *Phys. Lett.* **B667** (2008) 1–1340.

[176] C.-N. Yang, *Selection Rules for the Dematerialization of a Particle Into Two Photons*, *Phys. Rev.* **77** (1950) 242–245.

[177] B. A. Kniehl, C. P. Palisoc, and A. Sirlin, *Elimination of threshold singularities in the relation between on-shell and pole widths*, *Phys. Rev.* **D66** (2002) 057902, [hep-ph/0205304].

[178] A. Denner, H. Eck, O. Hahn, and J. Kublbeck, *Feynman rules for fermion number violating interactions*, *Nucl. Phys.* **B387** (1992) 467–484.

[179] H. Kalka and G. Soff, *Supersymmetry. (In German)*, . Stuttgart, Germany: Teubner (1997) 444 p.

[180] M. F. Sohnius, *Introducing Supersymmetry*, *Phys. Rept.* **128** (1985) 39–204.

Acknowledgments

First of all, I would like to thank my supervisor Prof. Wolfgang Hollik for giving me the opportunity to work on such an interesting field and for his continuous support during all the stages of the thesis.

I am indebted to my colleagues Maike Trenkel and Edoardo Mirabella for their patience in answering all the questions, for all the helpful discussions, and for taking care of me especially in the early stages of this work. It was really a pleasure to work with you.

I am grateful to Max Huber and Ananda Landwehr for proofreading (parts of) this thesis. Special thanks to Sebastian Moster for all the help and useful suggestions related to LATEX.

Many thanks to Frank Daniel Steffen for keeping the IMPRS program alive, and to the secretaries of the theory institute Rosita Jurgeleit and Monika Goldammer.

Special thanks go to Thomas Hahn and Peter Breitenlohner for the computer administration and for their kindful help concerning all IT-related questions.

I would like to thank all members of the theory group of the institute and in particular my numerous office mates, Max Huber, Philipp Kostka, Martin Spinrath, Daniel Härtl, Hai Ngo Than, Jianhui Zhang, Edoardo Mirabella, Thi Nhung Dao, and Davide Pagani for creating such a nice atmosphere. Many thanks go to the PhD representatives, Maike Trenkel, Clemens Kießig, and Katja Seidel for taking care of the PhD life.

Last but not least, I would like to thank my family for giving me all the support they could give.